UNIVERSIDAD COMPLUTENSE DE MADRID
FACULTAD DE CIENCIAS QUÍMICAS
Departamento de Química Inorgánica

NEW CHROMIUM MIXED OXIDES WITH THE RUTILE, HOLLANDITE AND PEROVSKITE STRUCTURES OBTANINED AT HIGH PRESSURE AND HIGH TEMPERATURE

MEMORIA PARA OPTAR AL GRADO DE DOCTOR
PRESENTADA POR

Iván Pierrotta

Bajo la dirección de los doctores

Miguel Ángel Alario y Franco
Emilio Morán Miguélez

Madrid, 2014

New chromium mixed oxides with the rutile, hollandite and perovskite structures obtained at high pressure and high temperature

Ivan Pirrotta

Departamento de Química Inorgánica
Facultad de Ciencias Químicas
Universidad Complutense de Madrid

Directores
Prof. Miguel Ángel Alario y Franco
Prof. Emilio Móran Miguelez

Julio 2013

"I only know that I know nothing"

Socrates, 469 – 399 B.C.

Acknowledgements

This work has been performed thanks to financial support of European Union by the FP7 program and the SOPRANO project and the Comunidad de Madrid by the MATERYENER project.

Many persons gave some contribution performing this experimental work; first of all I'd like to thank my thesis directors, Prof. M.A. Alario y Franco and Prof. E. Moran Miguelez. About high pressure experiments, Ph.D. J.M. Gallardo Amores provided a fundamental contribution; Ph.D. J. Romero de Paz for magnetic measurements; a special thank to the technician staff from x-ray diffraction CAI and all technician staff of Centro de microscopia L. Bru.

A special thanks to Prof. C. Otero Diaz for fruitful conversations about crystallography and jazz, Ph.D. R. Schmidt for measurement and discussions of dielectrical properties and Ph. D. A.J. Dos Santos Garcia for his fundamental discussion about magnetic characterization. Also I'd like to thank Ph.D. students D. Muñoz Gil, J. Prado Gonjal, Subakti and S.Marik for their daily support and help during the four years of work. A special thank to Mr. Nostro and Ph. D. Osciandoclash.

New chromium mixed oxides with the rutile, hollandite and perovskite strucutres obtained at high pressure and high temperature

Abstract

Strongly correlated materials are a wide class of electronic materials that show unusual (often technologically useful) electronic and magnetic properties, such as metal-insulator transitions or half-metallicity. The essential feature that defines these materials is that the behavior of their electrons cannot be described effectively in terms of non-interacting entities.[1] Many transition metal oxides belong to this class.[2] which may be subdivided according to their behavior, e.g. high-T_c, spintronic materials, Mott insulators, spin Peierls materials, heavy fermion materials, quasi-low-dimensional materials, etc.

Among first row of transition metals, Cr element is one of those more prolific in oxidation state. In oxides, Cr(II) is rare, Cr(III) common and stable, Cr(IV) rare and metastable, Cr(V) rare and Cr(VI) common and stable. Oxides containing Cr(IV) are very few in number if compared with Cr(III) or Cr(VI) oxides or with other transition metal oxides. Moreover, in some of these Cr oxides, there is not only Cr(IV) but a mixed valence Cr(IV) / Cr (III) exists. To this date, these oxides can be fully listed as follows:

1) rutile and rutile-like structures: CrO_2,[3] Cr_nO_{2n-2} and related materials,[4] and $Cr_{1-x}V_xO_2$ solid solution (this work);

2) perovskite structures: $MCrO_3$ (with M = Ca or Sr or Pb),[5-7] $Bi_{0,5}M_{0,5}CrO_3$ (with M = Sr,[8] Pb this work);

3) hollandite structures: $K_2Cr_8O_{16}$[9] and $K_{1,2}Cr_8O_{16}$ (this work).

Studying oxides containing Cr(IV) is interesting because this cation, in particular crystal structures, can give rise to peculiar physical-chemical properties like: half-metallicity (CrO_2 and $K_2Cr_8O_{16}$), frustrated order or spin glass systems ($Bi_{0,5}Sr_{0,5}CrO_3$ and $Bi_{0,5}Pb_{0,5}CrO_3$), ferromagnetic order ($K_{1,2}Cr_8O_{16}$), antiferromagnetic order ($Cr_{1-x}V_xO_2$ solid solution and $PbCrO_3$) and "anomalous" electronic state ($CaCrO_3$ and $SrCrO_3$).

All these materials have two common features: 1) they have Cr(IV) in their structures and 2) high pressure and high temperature conditions are needed to synthesize them, an exception is the case of $Bi_{0,5}Sr_{0,5}CrO_3$ where conventional ceramic method and Cr(III) as reactant have been used. The aim of this work is the high pressure and high temperature synthesis of new materials containing Cr(IV), their structural and physical characterization.

Also a study of possible candidate materials that could be new strongly correlated systems.

Several members of the solid solution of $Cr_{1-x}V_xO_2$ with $0,126(9) \leq x \leq 0,901(9)$ have been explored, synthesized under high temperature / high pressure conditions; a structural change as function of composition have been observed when $0.499(4) \leq x \leq 0.500(6)$; from structural characterization and compositional measurement the maximum content of Cr is expected to be in the region of solid solution $x < 0,342(9)$.

Powder samples data refinements shown a rutile-like structures that can vary as function of V content from $CaCl_2$ rutile like to VO_2 (M3) structure. Moreover the presence of V in CrO_2 "induce a pressure effect" allowing the structural transition from rutile to $CaCl_2$ structure at 40 Kbar. In pure CrO_2 this transition take place at a pressure of 120 Kbar at room temperature.

Electron diffraction experiments revealed a diffuse polarize streaks that could be related with a short range order V/Cr in the structure at composition $Cr_{0.499(4)}V_{0.500(6)}O_2$; more work is to be due to establish the type of short range order responsible for this diffuse scattering.

The magnetic properties of the different samples of solid solution have been determined and show a transition from paramagnetic (PM) to antiferromagnetic (AFM) in lowering the temperature. Independently the type of structure they have, $CaCl_2$ or VO_2 (M3), all samples have an AFM magnetic order. The transition temperature T_N is linearly dependent form Cr (or V) content in the structure and the trend has been explained by the presence of increasing amounts of Cr^{3+} in the structure.

In fact, the oxidation states of the Cr and V cations in $Cr_{1-x}V_xO_2$ confirm a rather complex mixed valences set. Comparison between measured and calculated magnetic moment have been realized in order to establish the valence states; Both V and Cr cations happen to be in a mixed valence state.

Electrochemical and chemical oxidation has been successfully applied to the half-metallic ferromagnet $K_2Cr_8O_{16}$ to partly extract K ions from the hollandite tunnel. Oxidation reaction results in new potassium deficient $K_{2-x}Cr_8O_{16}$ Cr-hollandites with $x_{max} = 0.8$. Structural characterisation shows that potassium extraction (oxidation) proceeds topotactically with some noticeable changes of the tetragonal cell parameters. The partial extraction of the K tunnel cation give rise to, among other effects widely described before, an unusual thermal parameter value B_{iso}, explained by an elongated electron density distribution along the tunnel direction. Interestingly, we have observed an important change in the magnetic properties. Potassium deficient hollandites $K_{2-x}Cr_8O_{16}$ are

ferromagnetic with a Curie temperature of 250 K which is 70K higher than the one reported for the pristine material $K_2Cr_8O_{16}$ (180 K). In both samples, neutron diffraction measurements confirmed a paramagnetic -> ferromagnetic phase transition decreasing temperature, following the double exchange mechanism; moreover fitting refined magnetic momentum curves as function of temperature, by using the spin wave model, confirm the transition at high temperature for $K_2Cr_8O_{16}$ and $K_{1,2}Cr_8O_{16}$ respectively; these values are in agreement with the change in slope observed in magnetic susceptibility measurements; likely observed for T_c, these values are shifted as function of relative proportion Cr^{3+} / Cr^{4+} in the structure, this behaviour have not been observed until this date in $K_2Cr_8O_{16}$ and $K_{1,2}Cr_8O_{16}$ materials. In structural related systems, similar properties have been observed; tuning physical parameters, reversible effects on properties have reported; in our case irreversible modification of properties have induced by means of chemical and/or electrochemical modification.

The new ternary oxide with perovskite structure $Bi_{0,5}Pb_{0,5}CrO_{2,92}$ has been structural and physical characterized showing a disordered Bi^{3+} and Pb^{2+} cations arrangement and its oxygen content has been determined by means of thermogravimetric reduction method; moreover no ordering of this vacancy have been observed by HRTEM experiments.

The magnetic behaviour may be explained by a long-range canted-antiferromagnetic structure coexisting at low temperatures with a substantial glassy component; that is a re-entrant spin-glass.

Dielectrical measurements have been performed on this material, magnetoresistance (MR) effect have been detected as function of temperature and seems to be correlated with magnetic susceptibility χ; moreover the correlation between χ and MR may corroborate the notion that charge transport is by spin dependent Cr^{3+} - Cr^{4+} hopping. The low resistivity for $Bi_{0,5}Pb_{0,5}CrO_{2,92}$ allowed reliable determination of ε' values only for $T \leq 75$ K. Therefore we cannot exclude ferroelectricity with a potential high $T_C >> 75$ K. Powder neutron diffraction studies below the Neél temperature are planning to confirm the presence of long-range ordering.

The single crystal growth of $PbCrO_3$ under high pressure and high temperature have been performed, several experimental condition of pressure, temperature, reaction time, cooling rate and reactants have been scanned; moreover the role of flux have been studied for some kind of fluxes. In few cases the experimental conditions were adequate for the single crystal growth of $PbCrO_3$. However the grown single crystals had not an excellent quality,

they have been suitable to confirm composition and structure; moreover the diffraction pattern from single crystal $PbCrO_3$ evidenced that the uncommon microstructural property: a superstructure that presents a compositional modulation, previously observed in polycrystalline sample of this material. this modulation is also present in the single crystal. These evidences suggest that its microstrucutral properties can be an intrinsic property of $PbCrO_3$ rather than a local effect in microcrystals.

0) Resumen

0.1) Introducción

Entre los metales de transición de la primera serie, el elemento Cr presenta un número de estados de oxidación amplio y variado: Cr (II) raro, Cr (III) común y estable, Cr (IV) raro y metastable, Cr (V) raro, Cr (VI) común y estable). Existen un número muy pequeño de óxidos de Cr (IV) si se compara con los óxidos de Cr (III) y Cr (VI) y/o con otros óxidos de metales de transición. Además en diversos óxidos de Cr, el catión (IV) existe con valencia mixta acoplado a otros cationes de Cr (III). Hasta la fecha, estos óxidos se pueden describir como:

1) estructuras rutilo o rutilo-relacionada: CrO_2[1] y la solución solida $Cr_{1-x}V_xO_2$ (este trabajo);

2) estructura perovskita: $MCrO_3$ (con M = Ca o Sr o Pb),[2-4] $Bi_{0,5}M_{0,5}CrO_3$ (con M = Sr,[5] o Pb este trabajo);

3) estructura holandita: $K_2Cr_8O_{16}$[6] y $K_{1,2}Cr_8O_{16}$ (este trabajo).

El estudio de óxidos de Cr(IV) es interesante porque este catión, en varias estructuras cristalinas, puede dar lugar a propiedades físicas interesantes como: "half-metallicity" (comportamiento de "medio-metal") (CrO_2 y $K_2Cr_8O_{16}$), frustración del orden magnético o vidrio de espín ($Bi_{0,5}Sr_{0,5}CrO_3$ y $Bi_{0,5}Pb_{0,5}CrO_3$), orden ferromagnetico ($K_{1,2}Cr_8O_{16}$), orden antiferromagnetico (la solución solida $Cr_{1-x}V_xO_2$ y $PbCrO_3$) y anómalos estados electrónicos ($CaCrO_3$ and $SrCrO_3$).

Todos estos materiales tienen dos puntos comunes: 1) El Cr (IV) en su estructura y 2) se necesitan condiciones de alta presión y alta temperatura para ser sintetizados, una excepción es el caso de $Bi_{0,5}Sr_{0,5}CrO_3$ donde el método cerámico convencional es suficiente.

El objetivo de este trabajo, como será descrito más en detalles en los capítulos relativos a cada material, es la síntesis y caracterización de nuevos materiales conteniendo Cr (IV) a presión ambiente y preparados bajo condiciones de alta presión y alta temperatura.

0.2) Desarrollo de la investigación

0.2.1) La disolución solida $Cr_{1-x}V_xO_2$

En este trabajo, ha sido estudiada la solución solida $Cr_{1-x}V_xO_2$ con $0,1 \leq x \leq 0,9$, sintetizada bajo condiciones de alta presión y alta temperatura. Se ha observado un cambio estructural en función de la composición para $0.5 \leq x \leq 0.6$; a partir de datos de caracterización estructural y análisis composicional se ha observado que el V se substituye en $Cr_{1-x}V_xO_2$ sin formación de fases segundarias con $x > 0,3$.

El refinamiento de los datos de muestras policristalinas muestra que esta disolución solida de estructura tipo rutilo, en función del contenido en V cambia desde estructura $CaCl_2$ hasta VO_2 (M3). Además la presencia de V en CrO_2 suministra una presión química permitiendo que la transición rutilo → $CaCl_2$ tenga lugar a 40 Kbar y 900ºC en lugar de los 120 Kbar como es el caso de CrO_2 puro. El estudio por medio de microscopia electrónica de transmisión revela líneas de difracción difusa que pueden ser relacionadas con orden a corto alcance entre V/Cr para la composición $Cr_{0.5}V_{0.5}O_2$.

Se ha realizado asimismo un estudio de las propiedades magnéticas y se ha observado una transición de fase magnética dependiente de la temperatura; disminuyendo la temperatura tiene lugar una transición desde la fase paramagnética (PM) a la fase antiferromagnetica (AFM) o ferromagnetico débil (WFM); la transición estructural $CaCl_2$ -> VO_2 (M3) no influye en las propiedades magnéticas observadas, La temperatura (T_N) de transición (PM)-(AFM) es dependiente de manera lineal del contenido de los cationes Cr (o V) en la estructura y su evolución ha sido explicada por la presencia de Cr^{3+} en la estructura.

Por último, pero no de menor importancia, los estados de oxidación de los cationes Cr y V en $Cr_{1-x}V_xO_2$ se encuentran en un conjunto complejo estados de valencia mixto. La comparación entre los momentos magnético experimentales y calculados para establecer los estados de valencia para los miembros de la disolución solida objeto de este trabajo aporta resultados muy interesantes. Ambos Cr y V resultaron estar en un estado de valencia mixto, pero no necesariamente al mismo tiempo;

0.2.2) El oxido medio-metálico (half-metal) $K_{1,2}Cr_8O_{16}$

A través de diferentes técnicas experimentales se han sintetizado materiales con estructura holandita con concentración de cationes K^+ diferentes. El origen de esta rica química reside en el túnel 1D de sección 2 x 2 de octaedros de la holandita. La ocupación total de los sitios del catión K^+ se ha conseguido a través de síntesis de alta presión y alta temperatura como en de $K_2Cr_8O_{16}$ and $K_2V_8O_{16}$.

Recientemente de los materiales más interesantes con estructura holandita es $K_2Cr_8O_{16}$, cuyas propiedades de transporte han sido estudiadas por Hasegawa et al..[7] La estructura cristalina de $K_2Cr_8O_{16}$ contiene iones Cr con un valor medio de estado de oxidación por átomo de Cr de +3,75.

Además este oxido presenta una transición de fase desde paramagnético y metálico (PM-M) a ferromagnetico y metálico (FM-M) con una T_C de ~180 K y con una polarización de espín de 18 μ_B por unidad de formula a baja temperaturas. Otras investigaciones en este material han señalado que otra transición de fase tiene lugar desde la fase ferromagnetica y metal a la fase ferromagnetica y aislante a una T_{MI} ~90 K, indicando que el intervalo de carga se abre debajo la temperatura T_{MI}.

Por medio de química suave y electroquímica hemos extraído hasta 0,8 átomos de potasio por celda unidad. Nuestro interés se ha centrado en que cambios en la composición, producen leves cambios en la estructura y que ese llevan a cambios las propiedades. Las diferencias estructurales entre $K_2Cr_8O_{16}$ y $K_{1,2}Cr_8O_{16}$ son debidas a cambios en los valores de los ángulos O-Cr-O y las distancias interatómicas; ello da lugar a un mecanismo de doble intercambio Cr^{3+} - Cr^{4+} más eficiente en $K_{1,2}Cr_8O_{16}$ que en el material de partida $K_2Cr_8O_{16}$ a través de un aumento de las interacciones de los orbitales d-d.

El objetivo inicial de esta parte del trabajo es la total extracción del catión K^+ desde la estructura de $K_2Cr_8O_{16}$ a través de métodos de química suave y/o métodos electroquímicos, oxidando $K_2Cr_8O_{16}$ y aumentando el contenido de Cr^{4+}. Idealmente, la extracción total de K^+ en la estructura holandita, produciría un nuevo polimorfo de CrO_2. Como ya hemos enfatizado, Cr(IV) es un estado de oxidación muy peculiar y hasta la fecha solo existen dos polimorfos del dióxido de CrO_2: el de tipo rutilo α-CrO_2 y β-CrO_2[8] con estructura $CaCl_2$. Además el aumento de la cantidad de Cr(IV) daría lugar a cambios en las propiedades magnéticas y de transporte con respecto a la holandita original $K_2Cr_8O_{16}$. En este trabajo describimos las reacciones químicas para la oxidación del Cr^{3+} en estructura holandita y sus efectos en las propiedades magnéticas.

Las oxidaciones electroquímicas y de química suave han sido aplicadas con éxito al medio-metal $K_2Cr_8O_{16}$, consiguiendo una extracción parcial de cationes K^+. La oxidación resulto

en una nueva especie: $K_{1,2}Cr_8O_{16}$. La caracterización estructural revelo que la oxidación tuvo lugar de manera topotactica con cambios en los parámetros de la celda tetragonal. La nueva especie $K_{1,2}Cr_8O_{16}$ es ferromagnetica a baja temperatura con una temperatura de Curie, T_C = 250 K que es 70 K más alta que la reportada por el material $K_2Cr_8O_{16}$ (T_C = 180K). En ambos materiales se realizaron medidas de difracción de neutrones en función de la temperatura, lo que confirmo la transición de fase paramagnético (PM) → ferromagnetico (FM) al bajar de la temperatura, describiendo el ferromagnetismo a través del modelo del doble intercambio; en materiales isoestructurales, estas propiedades han sido también observadas;[9,10] en materiales isoestructurales, como el caso de $K_2V_8O_{16}$, se han observado efectos reversibles en las temperaturas de transición a través de medidas de susceptibilidad magnética y de resistividad eléctrica en función de la temperatura a diferentes presiones; mientras que en el caso de $K_{1,2}Cr_8O_{16}$ efectos irreversibles sobre las propiedades físicas han sido inducidas a través de modificaciones químicas o electroquímicas.

0.2.3) Nuevo candidato multiferroico: $Bi_{0,5}Pb_{0,5}CrO_3$

Entre todas las estructuras de óxidos ternarios, las perovskitas (ABO_3) representan una de las estructura más importante y estudiada en ciencias del estado sólido. Estos óxidos, dependiendo de la composición pueden tener diversas propiedades, entre otros materiales: superconductividad (e.g. $Ba_{1-x}K_xBiO_3$), magnetoresistencia colosal (e.g. $La_{1-x}Ca_xMnO_3$), ferromagnetismo de electrón itinerante (e.g. $SrRuO_3$), ferroelectricidad (e.g. $BaTiO_3$), piezoelectricidad (e.g. $PbZr_{1-x}Ti_xO_3$), conductividad iónica (e.g. $La_{0.67-x}Li_{3x}TiO_3$, $BaCeO_{3-x}$) y multiferroicismo (e.g. $TbMnO_3$).[11]

El interés en materiales multiferroicos ha crecido muy rápidamente en las últimas decadas.[12]

Un camino preferente en la investigación de nuevo candidatos para materiales multiferroicos es la combinación de cationes que tienen propiedades magnéticas con otros cationes que tienen par inerte que puede inducir polarización y/o una estructura no centrosimetricas. El caso de $BiCrO_3$ y $PbCrO_3$ son ejemplos de estas exploraciones, ambos necesitan alta presión (respectivamente 40 Kbar y 55 Kbar) y altas temperatura (800 < °C < 1000) condiciones (HP/HT) para ser sintetizados.[13-18]

La estrategia de combinar los dos cationes Bi(III) y Pb(II), ambos con par inerte, en posición A de la perovskita con un catión en la posición B, dando lugar a una perovskita $AA'B_2O_6$, nos guio en la síntesis HP/HT de una nueva fase $Bi_{0,5}Pb_{0,5}CrO_3$.

El nuevo oxido ternario con estructura perovskita $Bi_{0,5}Pb_{0,5}CrO_3$ ha sido caracterizado estructuralmente y físicamente, este oxido presenta una distribución aperiódica de los cationes Bi(III) y Pb(II) en posición A, además ningún orden de vacantes ha sido observado por microscopia de transmisión de alta resolución; el comportamiento magnético puede ser explicado a través de una estructura antiferromagnetico-canteada a largo alcance que coexiste a baja temperatura con una componente de vidrio de espín de tipo vidrio de espín re-entrante.

0.2.4) Monocristal de $PbCrO_3$

Chamberland and Moeller[19] sintetizaron muestras policristalinas de $PbCrO_3$ y sus resultados concuerdan con los de Roth y deVries, además algunos picos de difracción aparecían menos definidos utilizando también radiación monocromática; el mismo efecto has sido observado por Goodenough et al.[20] que prepararon independientemente $PbCrO_3$.

A través de difracción de neutrones a baja temperatura los mismos autores descubrieron un orden de tipo antiferromagnetico a 240 K.

Esta ampliamente descrito en la literatura que en algunas perovskitas el par inerte $6s^2$ del catión Pb^{2+} puede producir desorden en la posición de este catión, como confirmado por el alto valor del factor térmico, obtenido en refinamiento de datos de difracción;[21]

Arevalo et al. realizaron estudios estructurales y microestrucutrales, utilizando respectivamente difracción de polvo de r-X y difracción de electrones de área seleccionada, y microscopia de transmisión de alta resolución para aclarar el origen de este ensanchamiento de los máximos de difracción en $PbCrO_3$.

Los autores observaron que el oxido $PbCrO_3$ tiene una deficiencia de Pb^{2+}, que da lugar a una estructura modulada con microdominios y una textura compleja.

El ensanchamiento observado por difracción de r-X es pues debido a la compleja microestrucutra originada por la modulación composicional del átomo de Pb^{2+}, en microdominios las tres direcciones del espacio.

El crecimiento de monocristales de $PbCrO_3$ bajo condiciones de alta presión y alta temperatura ha sido realizado barriendo los parámetros de presión, temperatura, tiempo de reacción, velocidad de enfriamiento y diversos reactivos; además, el papel del fundente ha sido investigado. Solo en pocos casos las condiciones experimentales han sido las adecuadas para el crecimiento de monocristal de $PbCrO_3$. A pesar de sus buen aspecto macroscópico, la calidad de los monocristales no ha sido suficiente para confirmar las propiedades microestructurles observadas por microscopia de transmisión, y no ha sido posible llevar cabo un refinamiento aceptable para obtener un modelo analítico.

0.3) Conclusiones

La síntesis y caracterización de nuevos materiales conteniendo Cr (IV): la disolución solida $Cr_{1-x}V_xO_2$ con $0,1 \leq x \leq 0,9$, el oxido ternario con estructura holandita $K_{1,2}Cr_8O_{16}$, la perovskitas $Bi_{0,5}Pb_{0,5}CrO_3$ y el monocristal de $PbCrO_3$, han sido preparados bajo condiciones de alta presión y alta temperatura; se llevo a cabo la caracterización estructúrales y diferentes medidas físico-químicas: eléctricas y de transporte; los resultados de estas investigaciones, ampliamente descritos en los siguientes capítulos, han dado lugar a resultados muy interesantes y cumplen con los objetivos de este trabajo.

0.4) Bibliografía

1. Schwarz, K., *CrO_2 predicted as a half-metallic ferromagnet.* Journal of Physics F: Metal Physics, 1986. 16(9): p. L211.
2. Zhou, J.S., et al., *Anomalous Electronic State in $CaCrO_3$ and $SrCrO_3$.* Physical Review Letters, 2006. 96(4): p. 046408.
3. Castillo-Martinez, E., et al., *Increasing the Structural Complexity of Chromium(IV) Oxides by High-Pressure and High-Temperature Reactions of CrO_2* Inorganic Chemistry, 2008. 47(19): p. 8526-8542.
4. Roth, W.L. and R.C. De Vries, *Crystal and magnetic sturcture of $PbCrO_3$. J.Appl. Phys.*, 1967. 38: p. 951.
5. Ortega-San-Martin, L., et al., *Frustrated Orders in the Perovskite $(Bi_{0.5}Sr_{0.5})CrO_3$.* Chemistry of Materials, 2009. 21(12): p. 2436-2441.
6. Endo, T., et al., *A new compound $K_2Cr_8O_{16}$ with hollandite type structure.* Materials Research Bulletin, 1976. 11(6): p. 609-614.
7. Hasegawa, K., et al., *Discovery of Ferromagnetic-Half-Metal to Insulator Transition in $K_2Cr_8O_{16}$.* Physical Review Letters, 2009. 103(14): p. 146403.
8. Maddox, B.R., et al., *High-pressure structure of half-metallic CrO_2.* Physical Review B, 2006. 73(14): p. 144111.
9. Yamauchi, T., et al., *Electromagnetic properties of hollandite $K_2V_8O_{16}$ under pressure.* Physical Review B, 2011. 84(11): p. 115104.
10. Isobe, M., et al., *Observation of Metal–Insulator Transition in Hollandite Vanadate, $K_2V_8O_{16}$.* J. Phys. Soc. Jpn., 2006. 75: p. 073801.
11. King, G. and P.M. Woodward, *Cation ordering in perovskites.* Journal of Materials Chemistry, 2010. 20(28): p. 5785-5796.
12. Spaldin, N.A. and M. Fiebig, *The Renaissance of Magnetoelectric Multiferroics.* Science, 2005. 309(5733): p. 391-392.
13. Hill, N.A., P. Baettig, and C. Daul, *First Principles Search for Multiferroism in $BiCrO_3$.* The Journal of Physical Chemistry B, 2002. 106(13): p. 3383-3388.
14. Baettig, P., C. Ederer, and N.A. Spaldin, *First principles study of the multiferroics $BiFeO_3$, Bi_2FeCrO_6, and $BiCrO_3$: Structure, polarization, and magnetic ordering temperature.* Physical Review B, 2005. 72(21): p. 214105.
15. Niitaka, S., et al., *Crystal structure and dielectric and magnetic properties of $BiCrO_3$ as a ferroelectromagnet.* Solid State Ionics, 2004. 172(1): p. 557-559.
16. DeVries, R.C. and W.L. Roth, *High-pressure Synthesis of $PbCrO_3$.* Journal of the American Ceramic Society, 1968. 51(2): p. 72-75.

17. Arevalo-Lopez, A.M. and M.M.A. Alario-Franco, *On the structure and microstructure of $PbCrO_3$.* Journal of Solid State Chemistry, 2007. 180(11): p. 3271-3279.
18. Arevalo-Lopez, A.M., A.J. Dos santos-Garcia, and M.A. Alario-Franco, *Antiferromagnetism and Spin Reorientation in $PbCrO_3$.* Inorganic Chemistry, 2009. 48(12): p. 5434-5438.
19. Chamberland, B.L. and C.W. Moeller, *A study on the $PbCrO_3$ perovskite.* Journal of Solid State Chemistry, 1972. 5(1): p. 39-41.
20. Hagenmuller, P., *Preparative Methods in Solid State Chemistry*. 1972: Elsevier Science.
21. Baldinozzi, G., et al., *Crystal strucutre of the antiferroelectric perovskite Pb_2MgWO_6.* Acta Cryst. B, 1992. 51.

1) General introduction

1.1 Strongly correlated materials

Strongly correlated materials are a wide class of electronic materials that show unusual (often technologically useful) electronic and magnetic properties, such as metal-insulator transitions or half-metallicity. The essential feature that defines these materials is that the behavior of their electrons cannot be described effectively in terms of non-interacting entities.[1] Many transition metal oxides belong to this class.[2] which may be subdivided according to their behavior, e.g. high-T_c, spintronic materials, Mott insulators, spin Peierls materials, heavy fermion materials, quasi-low-dimensional materials, etc.

1.2 Overview about Cr(IV) and its relationship with pressure

Among first row of transition metals, Cr element is one of those more prolific in oxidation state. In oxides, Cr(II) is rare, Cr(III) common and stable, Cr(IV) rare and metastable, Cr(V) rare and Cr(VI) common and stable. Oxides containing Cr(IV) are very few in number if compared with Cr(III) or Cr(VI) oxides or with other transition metal oxides. Moreover, in some of these Cr oxides, there is not only Cr(IV) but a mixed valence Cr(IV) / Cr (III) exists. To this date, these oxides can be fully listed as follows:

1) rutile and rutile-like structures: CrO_2,[3] Cr_nO_{2n-2} and related materials,[4] and $Cr_{1-x}V_xO_2$ solid solution (this work);

2) perovskite structures: $MCrO_3$ (with M = Ca or Sr or Pb),[5-7] $Bi_{0,5}M_{0,5}CrO_3$ (with M = Sr,[8] Pb this work);

3) hollandite structures: $K_2Cr_8O_{16}$[9] and $K_{1,2}Cr_8O_{16}$ (this work).

Studying oxides containing Cr(IV) is interesting because this cation, in particular crystal structures, can give rise to peculiar physical-chemical properties like: half-metallicity (CrO_2 and $K_2Cr_8O_{16}$), frustrated order or spin glass systems ($Bi_{0,5}Sr_{0,5}CrO_3$ and $Bi_{0,5}Pb_{0,5}CrO_3$), ferromagnetic order ($K_{1,2}Cr_8O_{16}$), antiferromagnetic order ($Cr_{1-x}V_xO_2$ solid solution and $PbCrO_3$) and "anomalous" electronic state ($CaCrO_3$ and $SrCrO_3$).

All these materials have two common features: 1) they have Cr(IV) in their structures and 2) high pressure and high temperature conditions are needed to synthesize them, an exception is the case of $Bi_{0,5}Sr_{0,5}CrO_3$ where conventional ceramic method and Cr(III) as reactant have been used.

Pressure is the keystone to obtain Cr (IV) oxides that can be prepared under a wide range of high pressure and high temperature conditions: But why pressure is the keystone to obtain Cr (IV)?

Reading literature, starting from Latimer diagram, fig.1 it is possible to build a Frost diagram fig.2 for all the Cr valence states.

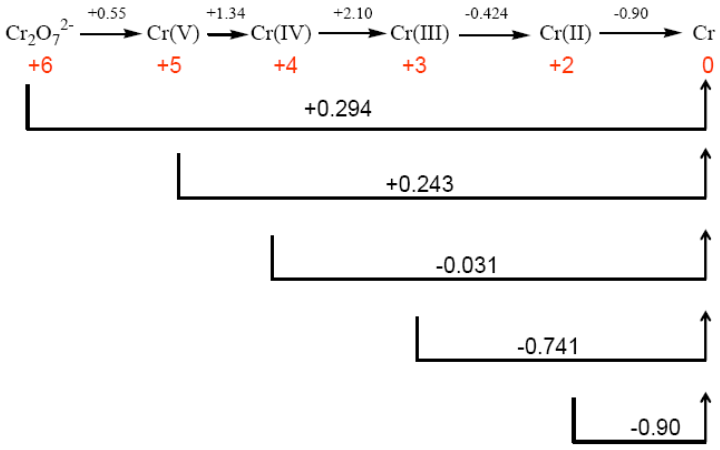

Fig. 1 The Latimer diagram for chromium in aqueous acid solution.

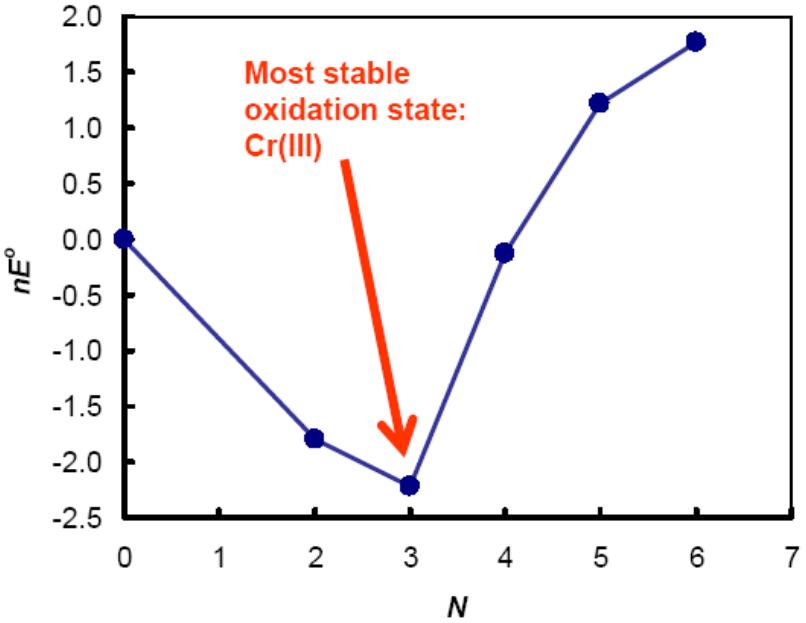

Fig. 2 The Frost diagram for the N chromium oxidation states; n represent the number of electron to reduce directly from an oxidation state to Cr metal, E° is the semireaction potencial wrote in the sense of reduction.

linking the evidences, a very well knew cases obtaining Cr (IV) are: the hydrothermal synthesis of CrO_2 from decomposition of CrO_3 where at least, conditions of 400 bars and 380-400 °C are required.[10,11]

Similar to these cases, studies of phase diagrams for $Cr(OH)_3$ - CrO_2 - Cr_2O_3 or CrOOH - CrO_2 - Cr_2O_3 of partial oxygen pressure in function of temperature, pO_2 / T (see chapter 3.1.2) have been carried out.

In all of these cases, formation of Cr(IV) is pressure dependent (partial oxygen pressure and/or autogenous pressure); the general and the redox semi-reactions equations can be write as follow:

$$2\ Cr(OH)_3 + 1/2\ O_2 \rightarrow 2\ CrO_2 + 3\ H_2O$$

$$Cr^{3+} \rightarrow Cr^{4+} + e^-$$

$$1/2\ O_2 + e^- \rightarrow O^{2-}$$

the role of pressure is narrowly linked with the electrochemical potential for the reaction

$$1/2\ O_2 + e^- \rightarrow O^{2-}$$

following the Nernst equation and fixing temperature and volume, the standard reduction potential E° are constants; the electrochemical potential for the semireaction

$$Cr^{3+} + e^- \rightarrow Cr^{4+} \text{ is:}$$

$$E_{(Cr^{3+} \rightarrow Cr^{4+})} = E°_{(Cr^{3+} \rightarrow Cr^{4+})} + (RT / F) \ln [Cr^{4+}] / [Cr^{3+}]$$

while for the oxygen $O_2 + 2e^- \rightarrow 2\ O^{2-}$:

$$E_{(1/2\ O_2 + e^- \rightarrow O^{2-})} = E°_{(1/2\ O_2 + e^- \rightarrow O^{2-})} + (RT / F) \ln\{[PO_2]^{1/2} / [PO^{2-}]\};$$

In order to take place spontaneously, the redox reaction have to be:

$$\Delta E = E_{(1/2\ O_2 + e^- \rightarrow O^{2-})} - E_{(Cr^{3+} \rightarrow Cr^{4+})} > 0 \text{ then } \Delta G < 0.$$

At room pressure, due to low O_2 concentration, the value of $\ln\{[PO_2]^{1/2} / [O^{2-}]\}$ is not high enough to reach $\Delta E > 0$. On the other hand increasing the total pressure of the system, or the oxygen partial pressure ($P_{o2} = \chi_{O2} * P_{tot}$, where χ_{O2} = O_2 molar fraction) it is possible reach condition of $\Delta E > 0$ and Cr^{4+} is themodinamically allowed to form.

In a second example Roth and De Vries obtained $PbCrO_3$ under high pressure and high temperature: below 55 Kbar reactants were present in product but above 55 Kbar $PbCrO_3$ is formed. In this case have not provided a straightforward explanation, "the electronic state of Cr(IV) ions in addition to the size effects" has indicated as responsible of the necessity of high pressure to stabilize these ions in the perovskite structure. $PbCrO_4$ (Cr(VI)) have been used successfully in high pressure high temperature synthesis of polycrystalline $PbCrO_3$ by Roth and De Vries and using the same reactant, single crystal of $PbCrO_3$ have been grown in this work; these facts reflect how pressure can influence also the redox

potential, providing experimental evidences for the narrow link existing between pressure and electrochemical potential previously described.

Whatever is (are) the mechanism(s) allowing the formation of Cr(IV), the pressure remains the crucial parameter.

1.3 High pressure technique

The High Pressure Technique was first employed in a systematic way by Percy B. Bridgman (1946's Nobel Prize) in his study of phase transformations under pressure, where he did study more than one thousand of systems. Later on it was developed by Tracy Hall in his successful work in the synthesis of diamond.[11,12] Nowadays it is commonly used in Geology and Geochemistry for the understanding of the Earth's interior as well as in the synthesis of new materials in Solid State Chemistry and Materials Science. Pressure and temperature, as thermodynamic parameters, play an important role in the preparation of novel materials. If the temperature reached during the materials synthesis is mainly determining atomic diffusion, the effects of the pressure become involved through two different approaches: 1.2.1) phase transition: for a given composition with characteristic chemical bonds, high pressure induce structural changes, and 1.2.2) system: starting from different precursors, high pressure can induce the formation of new chemical bonds promoting the synthesis of new materials unknown at normal pressure conditions.[13] Often, either of this two processes yield thermodynamically unstable materials at room conditions; however by means of quenching, the transition can be kinetically stabilized.

1.3.1 Structural transformations

The main factors that induce phase transition under high pressure conditions are:

i) The "densification effect": Considering a phase transition induced by pressure from F1 to F2 (F being a structural form), due to the compressibility, the ΔV value between the two forms is negative:

$$\Delta V = \Sigma(V/Z)_{F2} - (V/Z)_{F1}$$

Where V is the unit cell volume and Z is the number of formula units per unit cell. Under high pressure only structural transformations characterized by a negative ΔV value can take place. Therefore the increase in pressure during the synthesis leads to a more dense structure than that observed under normal conditions. As an example, we can mention the aluminosilicate $K_3AlSi_3O_9$ that, at 1450°C and 0 GPa has a density of 2.47 g/cm3 and at 10 GPa presents one of 2.68 g/cm3 (Figure 1.1a).[14]

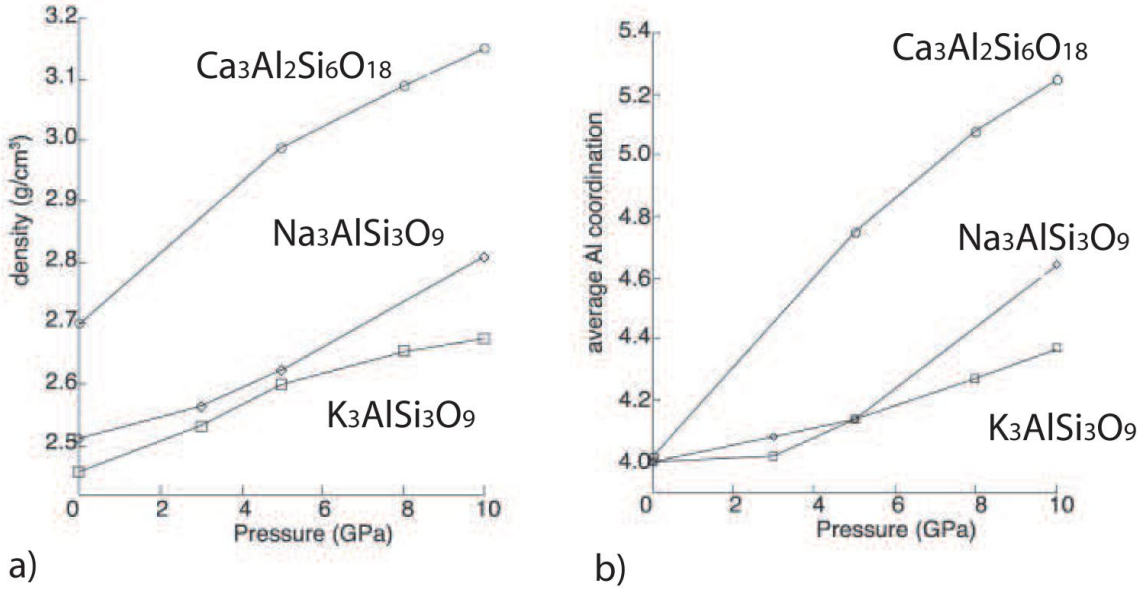

Figure 1.1: High pressure effects in aluminosilicates. a) Densification effect. b) Coordination increasing.[13]

ii) The electrostatic interactions: One of the main effects associated with the application of high pressures to a solid phase is the decrease of the average distances between atoms participating in the involved structures. For iono-covalent materials, the electrostatic repulsion between the most highly charged cations or anions is increased and this causes instability. In order to reduce these adverse effects, the structure changes to another one involving higher coordination numbers of the atoms (Figure 1.1b), usually the cations, which are harder than the anions, and this is often associated with larger interatomic distances (pressure-coordination rule and pressure-distance paradox). Yet, not all the distances become either shorter or longer, usually some increase, say [M-O], and this leads to an increase in the cationic radius and some decrease in the cation-cation or anion-anion distances. So called a well known example is the evolution of the structure versus increasing pressure of the "hexagonal" perovskites ABX_3: from the 2H structure to the 3C structure (Figure 1.2).[15]

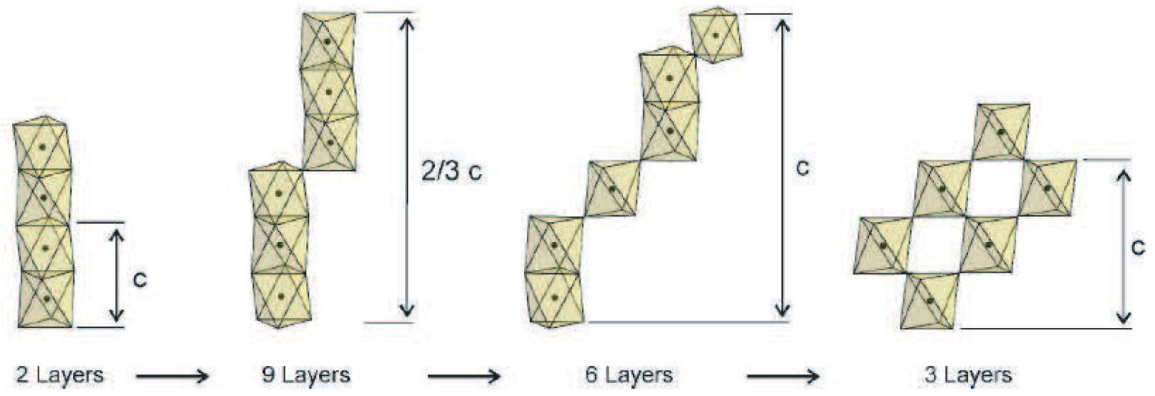

Figure 1.2: Structural evolution with pressure for some ABO_3 polytypes.

Increasing pressure changes the structure from left to right.[15]

iii) The chemical bond compressibility: The modification, by the application of pressure of the cation-anion distances can induce new structures, e.g. in the case of $SrCuO_2$, due to the difference in compressibility between the Cu-O bond and the Sr-O bond, the quasi-1D structure of $SrCuO_2$, characterized by Cu-O double chains, is transformed to a 2D structure with (CuO_2) sheets at 3 GPa and 900°C.[16]

1.3.2 Synthesis at high pressure

The synthesis under high pressure conditions depends on two sets of parameters:[17]

i) The thermodynamic effects associated with the specificities of the pressure parameter. Here three main effects can be considered:

1) reducing the formation of gas or liquid phases with Le Chatelier's rule: "Any change in status quo prompts an opposing reaction in the responding system".

2) Synthesis through the "densification effect", this effect is, in most cases accompanied by an increase of the coordination number of the anions.

3) Through the compressibility of atoms by the stabilization of new materials regarding the modification of the r_A/r_B ratio (r_A and r_B are the ionic radii of the corresponding atoms).

ii) The chemical effects associated with the enhancement of the reactivity of the precursors. The main effects regarding this are:

1)improvement of the kinetics of the chemical reactions: less time and less temperature,

2) improvement of the reactivity at the interface of liquid/solid phases,

3) the so-called "reactive pressure", e.g. stabilization of the highest oxidation states of transition metals.

1.4 Aim of the work

The aim of this work is the high pressure and high temperature synthesis of new materials containing Cr(IV), their structural and physical characterization. Also a study of possible candidate materials that could be new strongly correlated systems.

1.5 Bibliography

1. Quintanilla, J. and C. Hooley, *The strong-correlations puzzle.* Physics World, 2009. 22: p. 37.
2. Millis, A.J., *Lecture notes on "Strongly Correlated" Transition Metal Oxides.* Columbia University, 2012.
3. Schwarz, K., *CrO_2 predicted as a half-metallic ferromagnet.* Journal of Physics F: Metal Physics, 1986. 16(9): p. L211.
4. Alario Franco, M.A., J.M. Thomas, and R.D. Shannon, *Crystallographic share strucutres derived from CrO_2: An electron microscopic study.* J. Solid State Chem., 1974. 9: p. 261.
5. Castillo-Martinez, E., et al., *Increasing the Structural Complexity of Chromium(IV) Oxides by High-Pressure and High-Temperature Reactions of CrO_2* Inorganic Chemistry, 2008. 47(19): p. 8526-8542.
6. Zhou, J.S., et al., *Anomalous Electronic State in $CaCrO_3$ and $SrCrO_3$.* Physical Review Letters, 2006. 96(4): p. 046408.
7. Roth, W.L. and R.C. De Vries, *Crystal and magnetic sturcture of $PbCrO_3$. J.Appl. Phys.*, 1967. 38: p. 951.
8. Ortega-San-Martin, L., et al., *Frustrated Orders in the Perovskite $(Bi_{0.5}Sr_{0.5})CrO_3$.* Chemistry of Materials, 2009. 21(12): p. 2436-2441.
9. Endo, T., et al., *A new compound $K_2Cr_8O_{16}$ with hollandite type structure.* Materials Research Bulletin, 1976. 11(6): p. 609-614.
10. Kubota, B., *Decomposition of Higher Oxides of Chromium Under Various Pressures of Oxygen.* Journal of the American Ceramic Society, 1961. 44(5): p. 239-248.
11. Ikemoto, I., et al., *X-ray photoelectron spectroscopic studies of CrO_2 and some related chromium compounds.* Journal of Solid State Chemistry, 1976. 17(4): p. 425-430.
12. Arevalo, A., *$PbCrO_3$: synthesis a alta presion, estructura, modulacion composicional, propiedades y estudio de las disoluciones solidas con sus homologos de Ti y V.* Universidad Complutense de Madrid, 2009.
13. Bundy, F.P., et al., *Man made diamaond.* Nature, 1955. 176(4471): p. 51.
14. Bovenkerk, H.P., et al., *Preparation of Diamond.* Nature, 1959. 184(4693): p. 1094-1098.
15. Demazeau, G., et al., *Materials Chemistry under High Pressures – Some Recent Aspects.*,

Z. Naturforsch., 2006. 61b: p. 1457.

16. Allwardt, J.R., et al., *Effect of structural transitions on properties of high-pressure silicate melts: ^{27}Al NMR, glass densities, and melt viscosities.* American Mineralogist, 2007. 92(7): p. 1093-1104.

17. Goodenough, J.B., J.A. Kafalas, and J. Longo, *Handbook on the physics and chemistry of rare earths.* 1972.

2) Experimental

2.1 Synthetic techniques

2.1.1 High pressure / High temperature devices

2.1.2 “Soft Chemistry” methods for materials synthesis

2.2 Characterization techniques

2.2.1 Powder X-ray diffraction

2.2.1.a Thermodiffraction

2.2.2 Single crystal diffraction

2.2.3 Neutron diffraction

2.2.4 Electron microscopy

2.2.4.a Morphology and semi-quantitative analysis

2.2.4 b Transmission Electron Microscopy and High Resolution Transmission Electron Microscopy (TEM and HRTEM)

2.2.4 c X-ray Energy Dispersive Spectroscopy (XEDS)

2.2.5 Thermogravimetric methods: ATG/DTA TGA/DTA and Cahn balance

2.3 Quantitative analysis methods

2.4 Magnetic measurements

2.5 Electrical measurements

2.6 Software: Diffraction data refinement, model visualization, TEM image simulation, structure prediction

2.6.1 FullProf program for Rietveld Refinement

2.6.2 Model and atomic distances and angles TEM image simulation, Fast Fourier Transform

2) Experimental

2.1 Synthetic techniques

2.1.1 High pressure / High temperature devices

All the materials object of this work need high pressure and high temperature conditions to be synthesized. Synthesis have been carried out in “Conac” and “Belt” presses located in the High Pressure Laboratory of Complutense University of Madrid.
(http://www.ucm.es/info/labcoap/index.htm)

Both presses are shown in fig.1; the belt type press can work with two different pressure chambers, the largest is 17mm in length, could reach 40 Kbar of pressure, and can store 300-500 mg of reactants mixture, depending of its density. The 12.5 mm chamber can reach 80 Kbar and store 50mg of reactants mixture. The heating is generated by a graphite oven by means of Joule effect, the maximum temperature reached is 1100ºC and 1400ºC, respectively when Au and Pt crucibles are used. The reactants, grounded and mixed are pressed manually in to a crucible, it is placed inside the cylindrical graphite oven, separated by an cylinder insulator of Al_2O_3; two MgO tops are placed at the ends of the previous cylinder; two phyrophylite cones (used as quasi-hydrostatic pressure transmitter) close the new cylinder, with two teflon rings (to avoid losses of phyrophylite), from the belt plate.

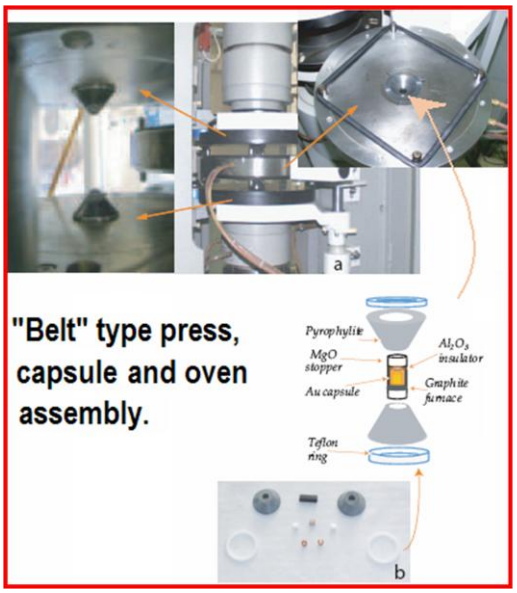

Fig.1 Belt press (right), Conac Press (left).

Once the crucible pack have been mounted, pressure is applied with a rate of 300 tons/hr, reached the value of pressure needed, the machine is then left to stabilize for 5 minutes; then heating is applied at a constant rate reaching the required temperature; then temperature is kept constant in a fixed time; at the end of this period the temperature is

switched off, the machine is left to stabilize for 5 minutes allowing the quenching of sample and finally pressure is released.

The Concac Press, has a different design; Here two plates can accommodate a toroidal $CaCO_3$ carrier where the internal volume is occupied by a cylindrical graphite furnace, Al_2O_3 insulator cylinder and Pt crucible containing the reactants mixture.

2.1.2 "Soft Chemistry" methods for materials synthesis

The methods knew as "soft chemistry" provide alternative synthetic routes for materials that cannot be synthesized by other methods in solid state chemistry.

Materials obtained by means of this technique are often metastable and reaction are usually topotactic, reactant and product maintaining the same structure. Under soft chemistry methods, several kinds of reaction can take place:

1) Cation insertion (or intercalation) / desinsertion (or deintercalation)
2) Dehydratation; Dehydroxylation
3) Hydrolisys
4) Cation interexchange
5) Redox

As well as a combination of those processes: Intercalation and/or insertion reactions are often reduction processes that can be described as follows:

$$xA^+ + xe^- + [H] \leftrightarrow A_x^+[H]^{x-} \quad 1a)$$

Where A^+ is the moving cation that can insert in the solid host's matrix material ([H]), the charge of the cation is neutralized by acquisition of an electron by [H].

Redox processes can take place at room temperature or a moderate temperature ($\approx 200^\circ C <$) in two different ways: chemical reduction a) and electrochemical b).

a) Metals in liquid ammonia, organometallic compounds (n-C_4H_9Li) or alkaline thetrahydroborates, depending of the redox potential required for reduction.
b) A cell is mounted where host material [H] is the cathod of the cell.

As pointed out by the double arrows in equation 1a) the inverse process is also possible; the deintercalation occurs (often only partially), depending of several factors, one of them is the dimensionality of the [H] crystal structure.

Deintercalation can be write as follows:

$$A_x[H](red)X_n \xrightarrow{-oxidant} xA^+ + [H](ox)X_n \quad 2a)$$

As described for the intercalation process, no structural changes occurs in the deintercalated material ($[H](ox)X_n$) too. Also deintercalated materials can be synthesized through chemical oxidation a) and electrochemical b).

a) I_2 , Br_2 , H_2O_2/H_2SO_4 , NO_2 BF_4 depending of the redox potential required for oxidation.
b) A cell is mounted where host material [H] is the anode of the cell.

In this work K^+ cations from the oxide $K_2Cr_8O_{16}$ have been deintercalated (and Cr atoms of $K_2Cr_8O_{16}$ oxidated) by means of both paths a) and b); for a) it has been realized under N_2 atmosphere with a refluxing solution of CH_3CN and NO_2BF_4 as oxidant, in a Schlenk tube mounted in a Schlenk line; for b) has been realized using a MacPile II System Biologic apparatus. More details about oxidation are reported in the experimental session of chapter 4.

2.2 Characterization techniques

Three types of radiations are used for crystal diffraction studies: X-rays, electrons and neutrons; Of these, X-rays are by far the most used technique but electron and neutron diffraction have important specific applications: by electron diffraction, the wave properties of electrons and its high scattering efficiency, it is possible to carry out experiments in the same condition of single crystal diffraction but in a micrometric scale, using crystals of few of thousands of Å; moreover, by electron diffraction it is possible having information about some symmetry properties not available with other techniques, example is existence or not of inversion center (Friedel's law it is not valid in electron diffraction). The role of neutron diffraction is clear when is mandatory to know the magnetic structure of a sample; Since neutrons possess a magnetic dipole moment they can interact with unpaired electrons of d and f orbitals, giving rise to an additional scattering effect.

2.2.1 Powder X-ray diffraction

The conventional and easiest technique to characterize the product of reaction, when polycrystalline, is the X-ray diffraction powder diffraction technique.
Diffraction measurement have been performed in CAI X-ray Diffraction of Complutense University of Madrid.
(http://www.ucm.es/info/vinvest/sic/cais/drx.htm)

Initial identification has been carried out for all samples in a Siemens D-5000 diffractometer, equipped with a Cu source ($K_{\alpha1}$=1.5405(6) Å and $K_{\alpha2}$=1.5443(9) Å). Working conditions was of 40 kV and 30 mA. The measurement scan program was in the range between $5° \leq 2\theta \leq 90°$ with a step of 0°,02' with a recording time of 0,8 sec/step. For better quality measurement of selected samples, high quality measurement have been carried out by means of a Philips X'Pert Pro Alpha 1 diffractometer equipped with a primary Ge (111) monochromator, Cu source ($K_{\alpha1}$=1.5405(6) Å) and a fast detector XCelerator. Measurement conditions was of 45 kV and 40 mA. Data collection have been made between a range $5° \leq 2\theta \leq 120°$, and a step of 0°,017' , the recording time was variable in function of each sample due to its characteristic and established from a first trial measurement, usually established that the number of counts for the highest peak was not lower than $2x10^4$ counts.

2.2.1.a Thermodiffraction

High temperature and low temperature powder X-ray diffraction

High temperature powder X-ray diffraction measurements have been performed in a X'Pert PRO MPD diffractometer with a θ — θ configuration; the samples have been placed in to an Anton Paar HTK1200 chamber. Data collection have been made between a range $5° \leq 2\theta \leq 120°$, and a step of 0°,017' , the recording time was variable as explained above.

Low temperature powder X-ray diffraction measurements have also be performed on the same diffractometer, but using a low temperature chamber Phenix of Oxford Cryosystems.

2.2.2 Single crystal diffraction

The measurements were recorded on a CCD area detector (Bruker Smart 1000, Bruker AXS, Madison, WI, U.S.A.) with graphite monochromated Mo*K*α radiation.

2.2.3 Neutron diffraction

Neutron scattering is a key technique investigating the properties of materials on atomic scale. The technique is complementary to the X-ray experiment as neutrons can interact strongly with light elements. The uniqueness of this method is based on the fact that the wavelength and energy of thermal neutrons ideally match interatomic distances and excitation energies in condensed matter; thus neutron scattering is able to directly examine the static and dynamic properties of the material. In addition, neutrons carry magnetic moment, which makes them a unique probe for detecting magnetic structures.

The Bragg equation is utilized in two different ways in two sorts of powder diffraction experiment:

1) Fixed wavelength, using a reactor source.

2) Fixed theta, using a spallation source.

The neutron diffraction device for the measurement in this work was the D1B - High resolution neutron two-axis powder diffractometer; the device was at the Laue-Langevin Institute, Grenoble, France; It is a high intensity powder diffractometer with a new steady 128° PSD covering the angular range 0.8 to 128.8º;

http://www.ill.eu/instruments-support/instruments-groups/instruments/d1b/description/instrument-layout/

2.2.4 Electron microscopy

Microstructral characterization of samples is one important point in the study of materials. All microstructural characterization of samples have been realized in the "Centro Nacional de Mircoscopia Electronica" Luis Bru in the Universidad Complutense of Madrid. (http://www.ucm.es/info/vinvest/sic/cais/bru.htm)

2.2.4.a Morphology and semi-quantitative analysis

For scanning electron microscopy (SEM) JEOL JSM 6400 has used, operating at 25 KV, with a resolution of: 3.5 nm (working distance 8 mm), 10.0 nm (working distance 39 mm); Using backscattered electron detector: with resolution of: 10.0 nm (working distance 8 mm). The device have been equipped with qualitative EDS with a resolution of e 133 eV;

2.2.4 b Transmission Electron Microscopy and High Resolution Transmission Electron Microscopy (TEM and HRTEM)

The sample preparation for electron transmission microscopy start with grinding of sample in a mortar, then the powder is dispersed in n-butanol using an ultrasonic bath; after that, a few drops of the suspension are placed in a Cu or Ni TEM grid covered by a carbon layer; once the solvent is evaporated, the grid is ready for TEM experiments.

Selected Area Electron Diffraction (SAED) experiments have been realized in a transmission microscope JEOL 2000FX with an accelerating voltage of 200 keV with a resolution between points of 0.31 nm; the microscope is equipped with a double tilting ± 45°, in two direction, sample holder and a microanalysis system for X-ray Energy Dispersive Spectroscopy (XEDS) Link ISIS 300; Further experiments have been carried out with a JEOL JEM 2100 with an accelerated voltage of 200 kV; LaB_6 electron gun; a

resolution of 0.25nm between points; STEM unit with clear field detector; CCD ORIUS SC 1000 camera (model 832); the grid of microscope can tilt in one direction ±42, or in two directions ±42/±30; or until ±80 in tomography mode; the microanalysis has realized by means of XEDS (OXFORD INCA).

Experiments of high resolution TEM have been performed in a Field Emission Gun (FEG) microscope JEOL-3000F with a accelerate voltage of 300 keV, a resolution of 0.17 nm and a spherical aberration Cs = 0.6 mm; the sample holder can rotate of ±25° in two directions and microanalysis is realized by a XEDS LINK ISIS 300. High resolution images have collected by means of a CCD multiscan camera.

For images processing Digital Micrograph Gatan software 3.10.0 (Gatan Inc. 5933 Colorado Lane Pleasantone, CA, Usa, 94588-3334) is used. By this software calculating fast Fourier transform (FFT) of experimental images is possible as well the inverse fast Fourier transform (IFFT) to obtain a calculated image from the selected diffraction packs.

Calculated images have made by Mac Tempas software (Kilaas, R. MacTempas Software, version 2.3.7; Total Resolution Inc.: Berkeley, CA, 1988), starting from lattice, space group and atomic position of desired structure.

2.2.4 c X-ray Energy Dispersive Spectroscopy (XEDS)

Cationic content of samples has been realized by every monocrystal by XEDS; Detector record photon energies emitted from the sample due to electron beam, each emission line recorded by the detector is characteristic of each element.

2.2.5 Thermogravimetric methods: ATG/DTA TGA/DTA and Cahn balance

Thermal analysis may be defined as the measurement of physical and chemical properties of materials as a function of temperature. The two main thermal analysis techniques are thermogravimetric analysis (TGA), which automatically records the change in weight of a sample as a function if either temperature or time (see fig.3); the differential thermal analysis (DTA), which measures the difference in temperature, ΔT, between a sample and an inert reference material as a function of temperature; DTA therefore detects changes in heat content.

The Cahn balance is a TGA method where a reduction of the sample take place under H_2/He atmosphere. By means of this technique it is possible to determine the sample oxygen content.

2.3 Quantitative analysis methods

Atomic absorption spectrometer has been used to measure the cationic content of bulk phase in soft chemistry synthesis; a Flame Photometer, Sherwood–Corning 410 atomic absorption spectrometer has used.

2.4 Magnetic measurements

Magnetic properties have been measured in a Magnetic Properties Measurement System-superconducting Quantum Interference Device, Quantum Design (MPMS-SQUID).

Magnetization in function of temperature has been measured warming from 2 to 300 K after a zero magnetic field cooling (ZFC) and/or after an applied magnetic field cooling (FC) using an external applied magnetic field, see relative experimental chapter for details of applied magnetic field.

Magnetization vs. applied field measurement have realized a several constant temperatures in ZFC mode. Once required temperature is reached, applied magnetic field is increased up to 5T after that decreased to -5T and increase again to close the cycle.

2.5 Electrical measurements

A QuadTech impedance analyzer was used for dielectric spectroscopy with an applied ac amplitude of 20 mV operating between 20 Hz – 1 MHz. Data were collected. To facilitate frequency (f), temperature (T) and magnetic field (*H*) dependent dielectric measurements a special sample holder was used (Janis Research Ltd., USA), which can fit into a Quantum Design PPMS measurement system providing variable *H* (up to 140 kOe) and variable *T* (10 – 320 K). The custom built probe was necessary to minimize the internal probe capacitance (≈ 0.2 pF) and maximize the internal probe resistance (≈ 10 GΩ),

which is both detrimental for reliable alternating current (ac) dielectric measurements.

The sample tray at the bottom of the probe was equipped with spring loaded drop-down pins To ensure optimal contact between the pins and the Au electrodes sputter deposited onto two opposing faces of the bulk samples.

Equivalent circuit fitting of the dielectric data collected at variable *f*, *T* and *H* was performed by employing commercial Z-View® fitting software, where each equivalent circuit model was fitted to both the real and imaginary parts of the *f*-dependent impedance data by minimizing the statistically weighted linear least-squares.

2.6 Software: Diffraction data refinement, model visualization, TEM image simulation, structure prediction

Several softwares made possible the data collection and data analysis; here report the most important software for data analysis used:

2.6.1 FullProf program for Rietveld Refinement

The Rietveld method was the method used for diffraction data analysis, by means of the FULLPROF program (Rodriguez-Carvajal, J., Physica B.(1993), 192, 55.), by means of this program it is possible also simulating powder diffraction diffractograms, starting from crystallographic information. Type of background and peak shape have been chosen separately for each diffractogram analyzed. Details about each refinement are reported in its relative experimental chapter.

2.6.2 Model and atomic distances and angles TEM image simulation, Fast Fourier Transform

After refinement a .cif file is created by FULLPROF program, that could be visualized by a wide number of software, like VESTA (http://jp-minerals.org/vesta/en/) or Crystal Maker (http://www.crystalmaker.com/), the second has been used also to calculate the interatomic distances and angles among atoms.

TEM image simulation have been realized, starting from crystallographic data of desired phase by means of Mac Tempas software, calculation have realized in a range of

-600Å < (100Å step) < -100Å of focus and 11Å < (27.4 Å step) < 93.1 Å of sample thickness; obtaining a 24 simulated images to compare with the real.

For Fast Fourier Transform, the Gatan (Gatan Inc. 5933 Colorado Lane Pleasantone, CA, Usa, 94588-3334) program have been used, more detail about this software are in the TEM experimental session.

3) The solid solution $Cr_{1-x}V_xO_2$

3.1Introduction

3.1 The Cr-O system

3.1.1 The half-metal binary oxide CrO_2: Chemistry and general aspects

3.1.2 Crystal structure and polymorphism

3.1.3 Electronic structure and transport properties

3.2 The V-O system

3.2.1 Crystal structure and polymorphism of VO_2

3.2.1a The high pressure phases of VO_2 (P > 20Kbars)

3.2.1b Transport properties and electronic structure of VO_2

3.2.2 The Magneli-Andersson phases

3.3 Some previously known solid solutions: $Cr_{1-x}M_xO_2$ and $V_{1-x}M_xO_2$ (M = transition metal) having the rutile structure

3.4 Results and discussion

3.4.1 Synthesis optimization

3.4.2 Structural characterization

3.4.2a Powder X-ray diffraction data, refinement and proposed crystallographic models

3.4.2b Discussion of structural data in $Cr_{1-x}V_xO_2$

3.4.2c Evolution of crystal parameters

3.4.2d Measurement of the $(101)_{M3}$ peak at low and high temperature

3.4.2e Electron diffraction

3.4.3Magnetic measurements

3.4.3.1 Magnetic susceptibility measurements

3.4.3.2 Magnetization measurements

3.5 Conclusions

3.6 Bibliography

3.1 The Cr-O system

3.1.1 The half-metal binary oxide CrO_2: Chemistry and general aspects

Chromium dioxide is the only stoichiometric binary oxide that is a ferromagnetic metal. It is the simplest and best studied half metal. Also chromium (IV) dioxide CrO_2 has many properties of interest to both the scientific community and industry. First suggested to be half-metallic by Schwarz,[1] CrO_2 has been studied extensively both theoretically and experimentally and has been shown to possess near 100% spin polarization at the Fermi level using superconducting point contact tunneling experiments.[2] Its half-metallic behaviour gives rise to relatively low electrical resistivity for an oxide, ~300 μΩcm,[3] and is commonly referred to as a "bad metal." CrO_2 is also ferromagnetic at room temperature with a high Curie temperature of Tc = 390 K. These two properties, along with its already wide availability, in spite of being a high pressure phase, make CrO_2 scientifically and technologically important and an ideal material for developing spintronic devices.

Concerning the synthesis, the thermal decomposition of CrO_3 under autogenus oxygen pressure in a sealed vessel in the presence of a TiO_2 substrate yields oriented thin films. Single crystal films can be produced by chemical vapor transport of CrO_3, CrO_2Cl_2, or Cr_8O_{21}.[4,5] Photodecomposition of $Cr(CO)_6$ is another route.[6] Although metastable under ambient conditions, there is a narrow stability range near 300 °C which extends to high oxygen pressure. It has been proved possible to grow small crystals and good-quality films, and produce powder which is sufficiently stable for industrial applications.[7] Acicular powder, typically 100 x 30 x 30 nm, is still used for audio or video tapes.

3.1.2 Crystal structure and polymorphism

CrO_2 has the tetragonal rutile structure illustrated in fig. 1. The space group is $P4_2/mnm$ with Cr in 2*a* sites (0,0,0); (½, ½, ½) and oxygen in 4 *f* sites (± *x*, ± *x*, 0); (½ ± *x*, ½ ± *x* , ½), where $x = 0.302$. Lattice parameters are $a = 4.421(1)$ Å and $c = 2.916(1)$ Å. Each oxygen has three chromium neighbors, and each chromium is octahedrally coordinated by oxygen with two short apical bonds (1.89 Å) and four longer equatorial bonds (1.91 Å). Octahedra sharing a common edge form ribbons parallel to **c**. Local axes are defined with *x* and *y* towards the edge-sharing oxygens, and *z* towards the apical oxygens. The Cr *d* orbitals are splitted by the octahedral crystal field (~2.5 eV) into a t_2g triplet and an e_g doublet; The t_2g orbitals are further splitted into a nonbonding d_{xy} orbit which lies in the equatorial plane of the octahedron, and a d_{yz} , d_{zx} doublet, which

form and antibonding d_{yz} x d_{zx} (π^*) combinations with respect to the oxygen *p*-orbital perpendicular to the Cr_3O triangles.[8,9]

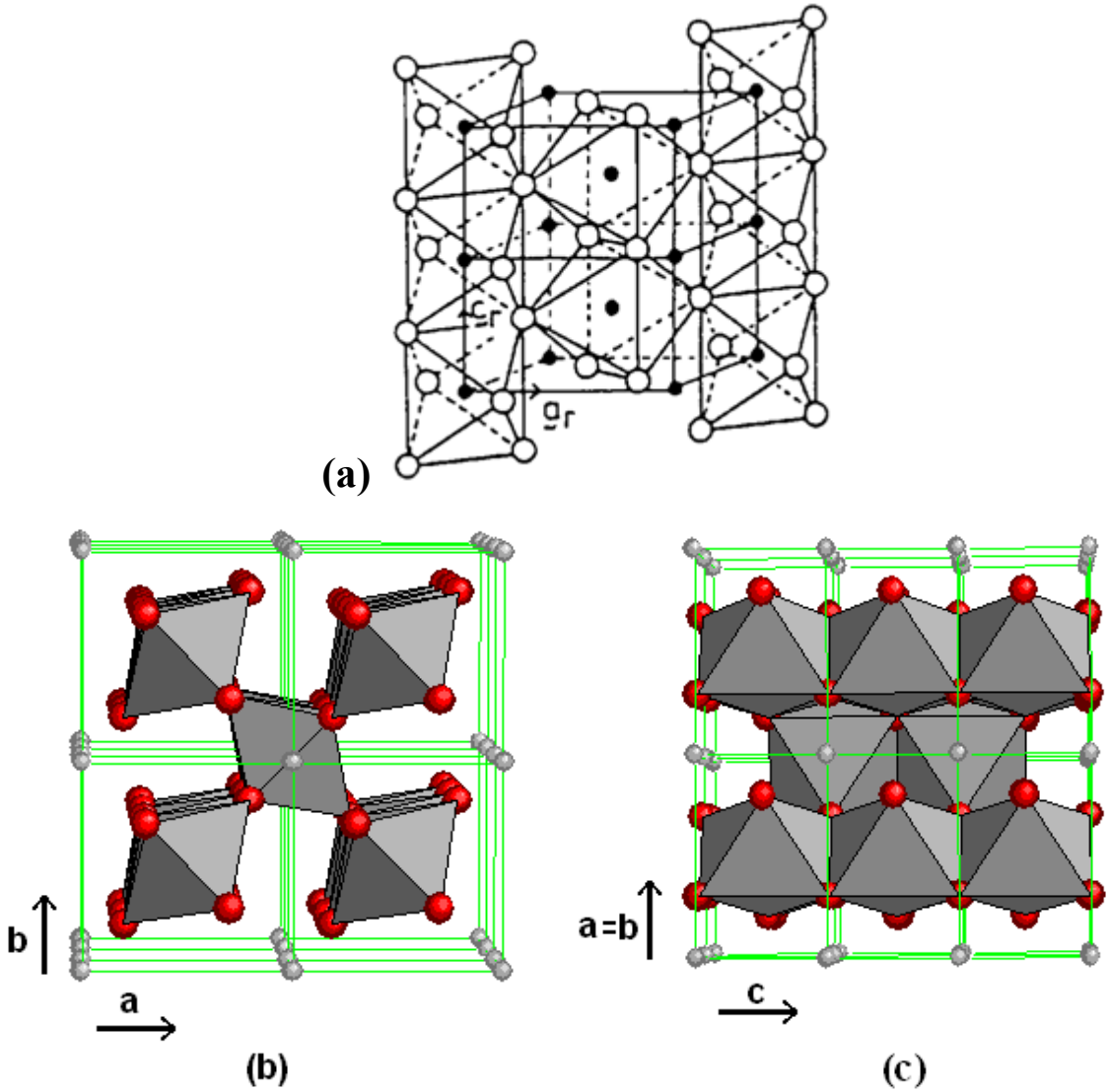

Fig. 1 a) The clinograhic representation of rutile structure; (b) The rutile structure of α-CrO_2 (*P*42 /*mnm),* $a = b = 4.421(1)$ Å, $c = 2.916(1)$ Å, at ambient conditions projected onto the *ab* plane with Cr^{+4} ions in grey and O^{-2} ions in red. (c) projected onto the *a* (or *b*) *c* plane;

Evidence for a structural phase transition from the rutile α-CrO_2, phase I, (*P*42 /*mnm*) to an orthorhombic β-CrO_2, phase II, ($CaCl_2$-like, *Pnnm*) has been studied using angle-resolved synchrotron x-ray diffraction and high sensitivity confocal Raman spectroscopy under pressure.[10] The transition to the $CaCl_2$ structure, appears to be second order; it occurs at 12±3 GPa without any measurable discontinuity in volume. At 12.8 GPa, an orthorhombic distortion was detected by the splitting of (*hkl)* diffraction lines with $h \neq k$.

The $CaCl_2$ crystal structure of β-CrO_2 consists of chains of distorted edge-sharing CrO_6 octahedra along the *c* axis with the Cr ions forming a body-centered orthorombic lattice and is shown in fig. 2.

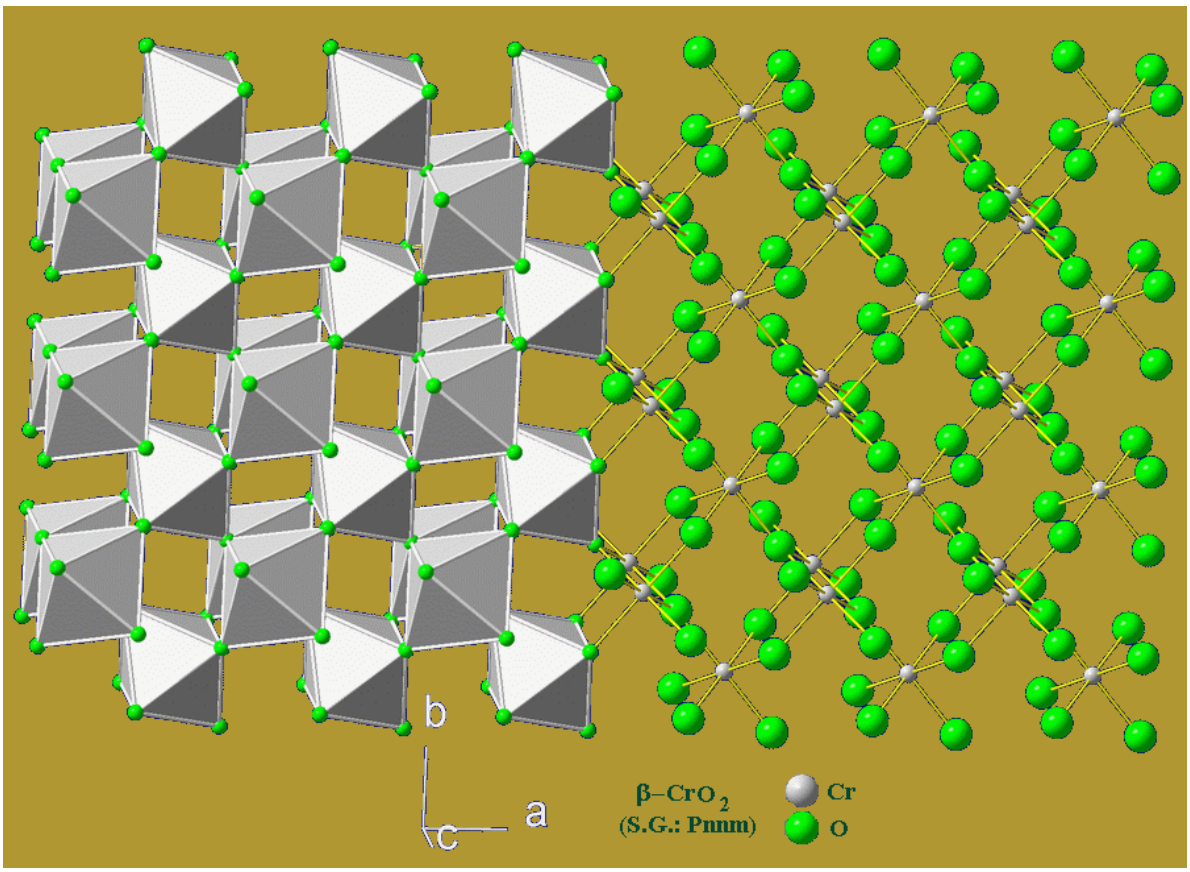

Fig. 2 Shows β-CrO_2 (*Pnnm*), *a* = 4.425 Å, *b* = 3.987 Å, and *c* = 2.683 Å.

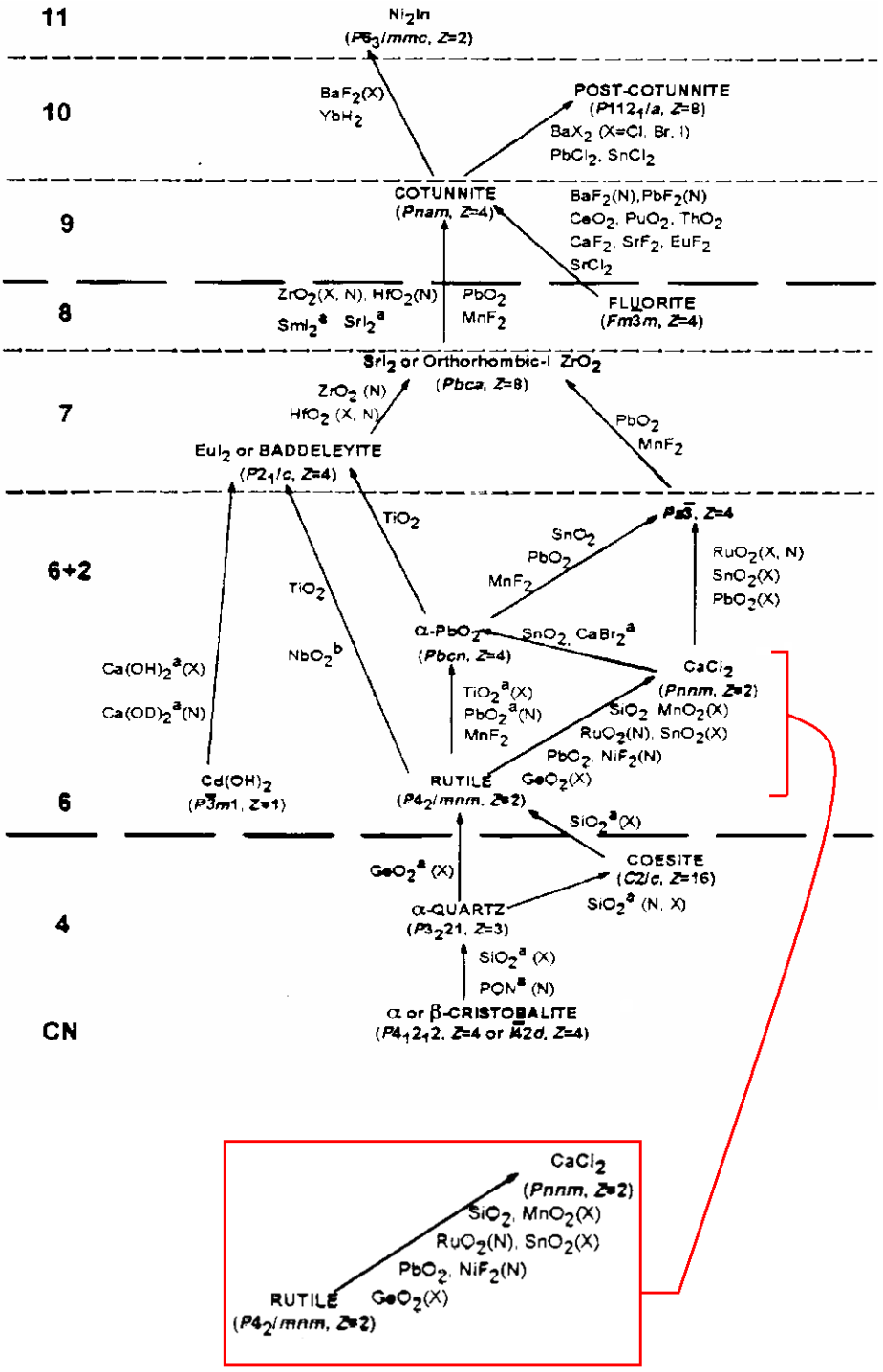

Fig. 3 Structure map of the MX_2 compounds as a function of coordination number; arrows indicate high pressure transformations (up); Detail of the region of interest in the present work (red box down); CN = coordination number; arrows = high pressure transformations, after Haines and Leger.[11]

The transition from α-CrO_2 to β-CrO_2 is consistent with the structural transition from rutile to $CaCl_2$ (*Pnnm*) crystal structures observed in other rutile-type oxides such as MnO_2,[11] RuO_2,[12] SiO_2,[13] GeO_2,[14.15] SnO_2,[16,17] PbO_2[18]. In fact the AO_2 stoichiometry is a paradigmatic example of the influence of pressure in the coordination number. As shown in the fig. 3, after Haines and Leger,[11] up to 11 near neighbours can be obtained for this composition in binary oxides in non-molecular solid state chemistry.

In $CaCl_2$, linear strands of edge-sharing octahedra are present; observing along [001], the strands are joined by common octahedra vertices, see fig. 4.

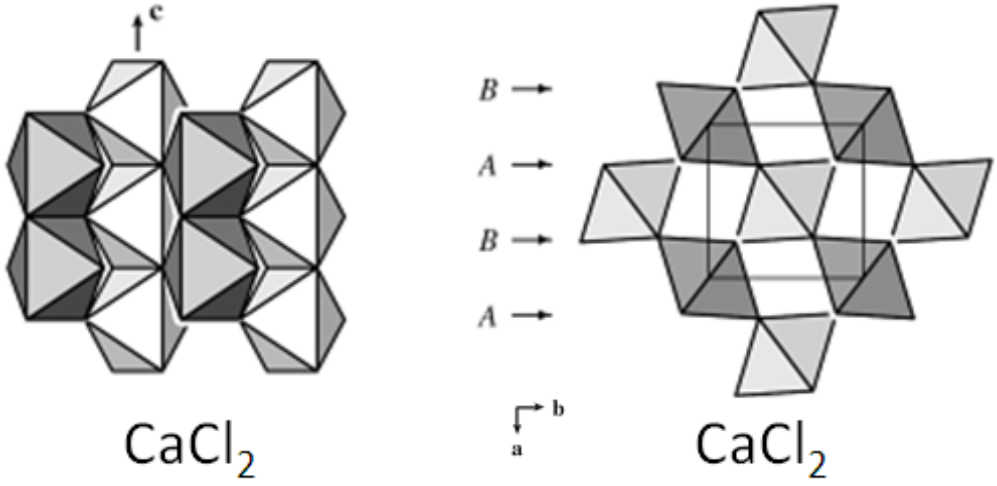

Fig. 4 $CaCl_2$ structure, view perpendicular to the hexagonal layers (left); view along the strands of edge-sharing octahedra, the hexagonal layers are marked by A and B.

$CaCl_2$ is a hexagonal closest-packing of O atoms frequently ascribed to the rutile-type. However, the deviations of rutile from this kind of packing are quite significant; Every O atom is no longer in contact with twelve other O atoms, but with eleven; moreover, the 'hexagonal' layers are considerably corrugated.

All attempts substituting a transition metal M with chromium in a rutile structure MO_2 have been made using reactants having Cr^{3+} instead of Cr^{4+}; the reason is that CrO_2 is not stable at high temperature and room pressure, so that it cannot be used in conventional ceramic synthesis;

At room pressure, it decomposes around 400º C, following the reaction:

$$2\ CrO_2 \rightarrow Cr_2O_3 + ½\ O_2.$$

This decomposition has been studied by Alario and Sing,[12] the phase diagrams as function of T, P_{O2} in fig.5 (left)[12] shows the range of existence of Cr^{4+}, where could be stabilized and synthesized; the phase is metastable, then once it forms at required conditions, temperature and pressure could be released and CrO_2 is stable at ambient conditions. The phase diagram of fig.5 (right), after Kubota et. al,[13] represents the chromium–oxide system as function of pressure and temperature; higher pressure stabilizes the CrO_2 phase. Same system has been studied by Ikemoto and al.[14] and other authors.[15-18]

Salinas et al.[16] carried out a study about the thermal decomposition and reduction of CrO_2 to CrOOH.

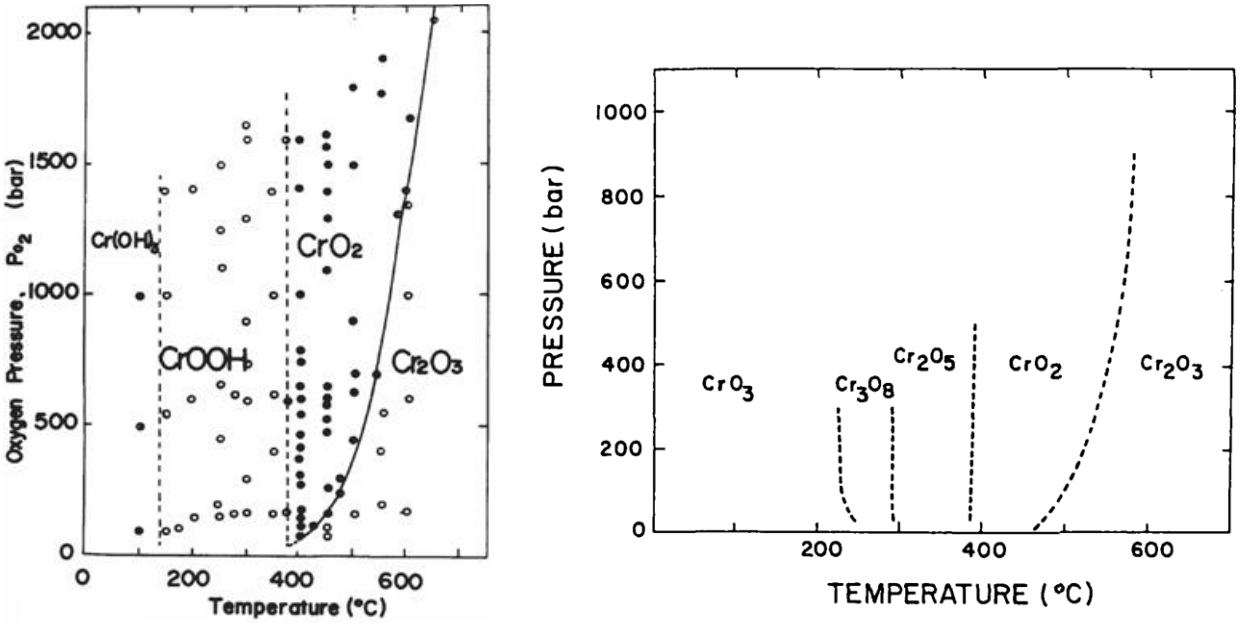

Fig. 5 To the left, the phase diagram showing the interrelationship of $Cr(OH)_3$ and its products at temperature and high oxygen pressure; water product is omitted in the diagram. To the right, the low pressure – low temperature phase diagram in the chromium-oxide system. The dashed lines represent the approximate phase boundaries for the different phases observed.

3.1.3 Electronic structure and transport properties

The formal electronic configuration is $(t_2g^{\,2})^{\uparrow}$ for Cr^{4+}, and $2p^6$ for O^{2-} although there is some $O^{2-} \rightarrow Cr^{4+}$ charge transfer and strong mixing of oxygen hole and chromium electron states at E_F.[19] The Cr *d* levels lie close to the top of the O 2*p* band. The Fermi level lies in the half-full $d_{yz} \pm d_{zx}$ band.

A dozen of Local Spin Density Approximation (LSDA) and Local Spin Density Approximation + the orbital specific screened Coulomb interaction (LSDA + U) calculations, beginning with that of Schwarz[1] have refined the picture. There is a large peak in the paramagnetic density of states at E_F, but almost every calculation confirms that the spin–split band structure is that of a type IA half metal, with a spin gap $\Delta_{\downarrow} > 1$ eV, and a spin–flip gap Δ_{SF} of a few tenths of an eV. All the calculations yield a moment very close to 2 μ_B/formula. The Curie temperature of CrO_2 is usually reported to lie around 392 K. The temperature dependence of the magnetization well below T_C follows a Bloch $T^{3/2}$ law.[18,19] The localized S = ½, d_{xy} core is exchange coupled to the (d_{yz} + d_{zx}) conduction electrons by an on-site Hund's rule interaction $J_H \sim 1$ eV to form S = 1 atomic spins, which then interact by double-exchange and ferromagnetic superexchange interactions. The paramagnetic moment deduced from the Curie–Weiss susceptibility above T_C slightly exceeds that expected for S = 1.[20]

The electrical conductivity determined on single crystals or high quality films shows residual resistivity ρ_0 of ~1028 Vm.[21] Below 50 K, CrO_2 is a rather good metal, with a resistivity that is practically independent of temperature.[22,25]

Core-electron and valence-band regions of crystalline CrO_2, CrOOH, Cr_2O_3, and $K_2Cr_2O_7$ have been studied by XPS spectrum; the valence band region of CrO_2 is interpretable in terms of Goodenough's band-structure model.[12]

The only way doping CrO_2 with V^{4+} is by solid state reaction using high temperature / high pressure conditions and perhaps by high pressure hydrothermal methods.

In this work we attempted to scan the whole $Cr_{1-x}V_xO_2$ solid solution trying to replace Cr^{4+} by V^{4+}. A study of crystallographic shear and other phases intermediate between CrO_2 and Cr_2O_3 appear in previous work of Alario et al.[17]

3.2 The V-O system

3.2.1 Crystal structure and polymorphism of VO_2

Above 340 K VO_2 crystallizes in the rutile crystal structure based on a simple tetragonal lattice with space group $P4_2/mnm$ (D^{14}_{4h}), as shown before for CrO_2 in fig. 1a,b. Using single crystal diffraction experiments McWhan et al.[21] determined the tetragonal lattice constants a_r = 4.554(6) Å and c_r = 2.851(4) Å and the positional parameters. With respect to the vanadium sites the VO_2 structure is based on a body-centered tetragonal lattice, where each metal site is surrounded by an oxygen octahedron. Octahedra at the center and the corners of a rutile unit cell are rotated by 90° around the rutile c-axis. This reduces the lattice symmetry from body-centered tetragonal to simple tetragonal and causes the unit cell to contain two formula units. In this structure, octahedra form chains along the rutile c-axis. Within the chains neighbouring octahedra share edges, whereas corner and center chains are connected via corners. Next to the filled oxygen octahedra the rutile comprises the same amount of empty octahedra, half are empty and half are occupied, this forms tunnels which are very important in the chemistry of rutile type solids; which likewise form chains along the rutile c-axis. Hence VO_2 is based on a three dimensional network of oxygen octahedra half filled with vanadium atoms. Each octahedron has orthorhombic symmetry, but deviations from tetragonal and even cubic symmetry are small. One observes two different V-O distances, where the apical distance appears twice within each octahedron and the equatorial distance is found four times.[22]

At 340 K, VO_2 experiences one of the more studied, if not the most MIT due to a first order phase transition; it is accompanied by structural distortions leading to the monoclinic M1 phase, which is based on a simple monoclinic lattice with space group $P2_1/c$ (C^5_{2h}).[23] Despite very similar gross features, distinct differences distinguish rutile and monoclinic VO_2.

First, a characteristic metal-metal pairing along the c_{rut}-axis (rut= rutile) is present in the monoclinic structure, which modifies the V-V distances (2.851(3) Å in the rutile case) and gives rise to alternating values of 2.619(1) Å and 3.164(2) Å. Second, a zigzag-type displacement of the metal atoms evolve diagonally in reference to the rutile z-axis (along c). The shift direction alternates along a_{rut} and c_{rut} but not along b_{rut}. Due to the zigzag type distortions two different apical V-O bond lengths of 1.77 Å and 2.01 Å are observed. In addition, the V-V pairing results in two short (1.86 Å and 1.89 Å) and two long (2.03 Å and 2.06 Å) equatorial distances in each oxygen octahedron. If VO_2 undergo uniaxial stress along the rutile (110) axis or if doped with some percent of chromium (III) or aluminum (III) yields two additional insulating phases: the monoclinic (M2) and triclinic T phase.[24-26]

In the M1 phase V-V pairing and zigzag-type lateral displacements of the metal atoms affect each vanadium chain. In contrast, in the (M2) phase half of the chains dimerize and the other half show zigzag-type deviations. The T phase is intermediate since the dimerized (M2) chains start to tilt and the zigzag chains generate a dimerization until eventually the (M1) structure is reached.

3.2.1a The high pressure phases of VO_2 (P > 20Kbars)

In 1973, Chamberland[27] conducted a series of experiments under high pressures and temperatures on the (M1) V_2O_4 monoclinic form; two new varieties were obtained:

* M2, monoclinic, C2/m space group;

* M3, monoclinic, P2/m space group;

The unit cell dimensions for the unmodified monoclinic (M1) phase are: a = 9.083(3) Å, b = 5.763(5) Å, c = 4.532(1) Å, and β = 91°.3(1)'. The new vanadium dioxide (M2) exhibited a structural transition and an abrupt, reversible change in resistivity (approx. 4 orders of magnitude) at 66°C similar to that observed in MI-type VO_2. Controlled substitution of V^{5+} for V^{4+} in the structure led to yet another monoclinic (M3) phase. This phase is closely related to the (M2) phase. The (M3) unit cell dimensions are:

a = 4.506(4) Å, b = 2.899(2) Å, c = 4.617(3) Å, and β = 91°.7(9)', having the space group P 2/m. The substitution of V^{3+} yielded only monoclinic (M1) derivatives. The modified products have various semiconductor to metal transition temperatures which have been described by the authors like "which depend on the type and amount of substitution and defect structure".[28]

Fig. 6 represent the structural models, based on crystal data ab-initio structures, of (M2) and (M3), the atomic coordinates are shown in tab.1; they have been elaborated and adjusted to fit their experimental powder patterns. The (M2) structure exhibits two different infinite parallel strings of [V-O_6] edge shared octahedra, interconnected by apices like in the rutile structure, but the oxygens are quasi-hexagonally close packed. Vanadium atoms are situated in distorted oxygen octahedra, the V-O bond lengths ranging from 1.66(1) Å to 2.15(2) Å and with the characterisitic V^{4+}-V^{4+} pairing: d_{V1-V1} = 2.70(1) Å and d_{V2-V2} = 2.89(2) Å in (M2).

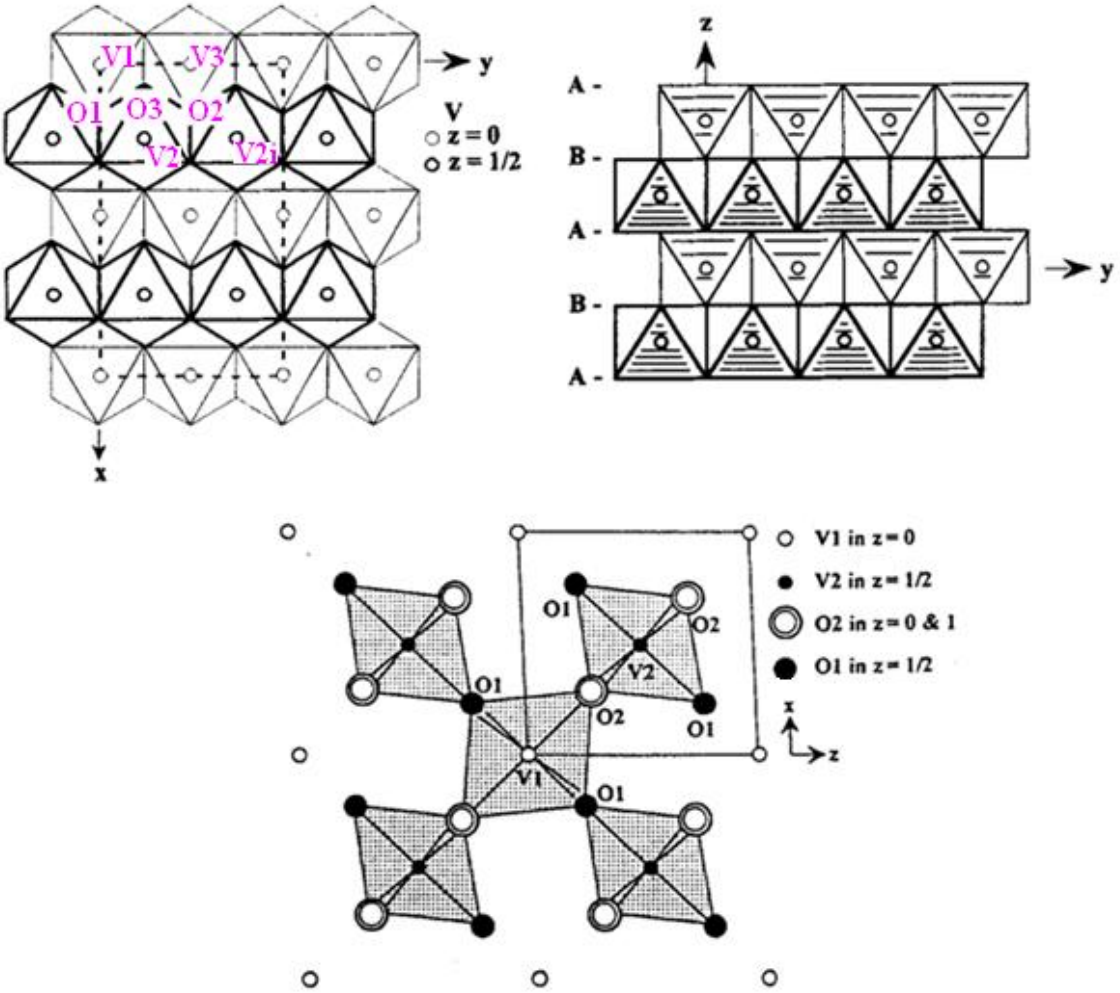

Fig. 6 The structural model of VO_2 (M2) (up) and (M3) (down): View of (M2) along c axis (left up), along the a axis (right up); View of (M3) along b axis (down).

Tab.1 Atoms coordinates and Wyckoff position for VO_2 (M2) and (M3) polymorph.

(M2) VO_2

Atoms	Wyckoff site	x	y	z
V1	2a	0	0.265	0
V2	4f	0.24	0	0.507
V3	2b	0.24	0	0.507
O1	4i	0.136	0.235	0.307
O2	4i	0.122	0	0.779
O3	8j	0.108	0.5	0.798

(M3) VO_2

Atoms	Wyckoff site	x	y	z
V1	1a	0	0	0
V2	1h	0.5	0.5	0.5
O1	2n	0.761	0.5	0.206
O2	2m	0.726	0	0.704

In the (M2) variety, octahedra are distorted; The average V-O bond values d_{V1-O} = 1.970(5) Å and d_{V2-O} = 1.92(2) Å are within the classical range for V^{4+}: mean d_{V-OAp} = 1.933(1) Å at 360K, 1.935(1) Å at 470 K;
mean d_{V-OEq} = 1.921(1) Å at 360K, 1.924(1) Å at 470 K.[28]
The distortion drive to bond angles, 85°.6' < O-V1-O < 94°.9', Ol-Vl-Ol = 169°.1' and O3-V1-O2 = 179°.2'(x 2) for the former and 84°.4' < O-V2-O < 95°.1', O4-V2-O3 = 176°.1' and Ol-V2-Ol = 175°,1'(x 2) for the latter.
The linear string of [$V1O_6$] octahedra sharing edges along [0l0] exhibits two different d_{V1-V1i} distances: 2,70 Å and 3.06 Å (with subscript V1i represents the next near neighbour vanadium atom in octahedral), clearly linked with the formation of V^{4+}-V^{4+} pairs. In the string the minimum distance should be exactly b/2, i.e. 2.882(2) Å; In (M3) the V-O distances range from 1.75(4) Å to 2.l0(6) Å and $d_{VI-V1} = d_{V2-V2}$ = 2.90(5) Å.[28]
In (M3) VO_2 the two V^{4+} columns show identical V-V distances, equal to the b parameter, i.e. 2.899 Å, close to the critical value and explain the smaller jump of the conductivity at the transition. Octahedra exhibit small volume differences with average bond distances d_{V1-O} = 2.07 Å and d_{V02-O} = 1.92 Å.
It has been shown that the structures of (M2) and (M3) VO_2, determined on the base of the powder pattern, via trial and error methods combined with Rietveldt refinements, allow to give a quantified basis on the V-O bonding and more especially at the level of the V^{4+}-V^{4+} pairing, which explain at their phase transitions on heating, around 65-70°C, the abrupt change of their electric properties.
Applying a pressure of 65 Kbars and temperatures from 500°C up to 1200°C on the (M1) form of vanadium dioxide, Chamberland[27] obtained the powder and some crystals of the (M2) form. (M2) VO_2, was clearly identified by its original X-ray powder pattern; the study of the issued single crystals, even not good enough for structural determination, allowed to precise cell dimensions and possible space groups C2/m, Cm or C2.
The resistance of the single crystals showed a sharp discontinuity on heating around 66°C (similar to that of (M1) VO_2 type), semiconducting behaviour changing to metallic one.
The (M2) polymorph is close to the structure described by Marezio et al. for $V_{0.975}Cr_{0.025}O_2$,[24,29,30] therefore the V^{4+} pairing seems to induce less distortion, the corresponding distances being 2.54 Å and 3.26 Å in one string and 2.93 Å in the other.
These V-V interatomic distances, clearly showing the presence of homopolar V^{4+} pairs, explain the electric properties of (M2) VO_2, characterized by a drastic decrease of resistance by more than a 10^{-4} factor at 66°C.[31]

As described by the Goodenough model,[8] the R_c value calculated as the critical separation of V^{4+} for localized vs itinerant *3d* electron behaviour in oxides is R_c = 2.94 Å. The homopolar pairs break up at the phase transition temperature, when the (M2) structure type transforms into the rutile one; then the metallic conduction via t_{2g} bands takes place, in a similar way of the one occurring in the (Ml) to (R) VO_2 phase transition.

3.2.1b Transport properties and electronic structure

The sharpness of the phase transition is characterized by an abrupt change in electrical conductivity and infrared transmission characteristics, making it a good for sensor and switching applications.

The electronic structure of metallic VO_2 has been probed by optical measurements revealing the lowest empty V *3d* levels 2.5 eV above the top edge of the O *2p* bands.[32] Ultraviolet and x-ray photoelectron spectroscopy show a 8.5 eV wide occupied band, directly below the Fermi energy.[33]

The valence band splits up into low and high binding regions with widths of 1.5 eV and 6 eV, respectively. While the low binding contributions are attributed to the V 3d states, the broader part of the valence band mainly traces back to O *2p* states. According to oxygen K-edge x-ray absorption spectroscopy unoccupied V *3d* bands extend from the Fermi energy to 1.7 eV and from 2.2 eV to 5.2 eV.[34]

For monoclinic VO_2 photoelectron spectroscopy shows a sharpening accompanied by an energetical downshift of the occupied V *3d* bands. Shin et al. reported a band gap of 0.7 eV for the insulating phase.[35]

Theoretical approaches towards understanding the MIT and the simultaneous structural transformations range from Peierls[36,37] to Mott–Hubbard[38,39] schemes. Possible driving forces are lattice instabilities, electron-phonon interaction, and electronic correlations.

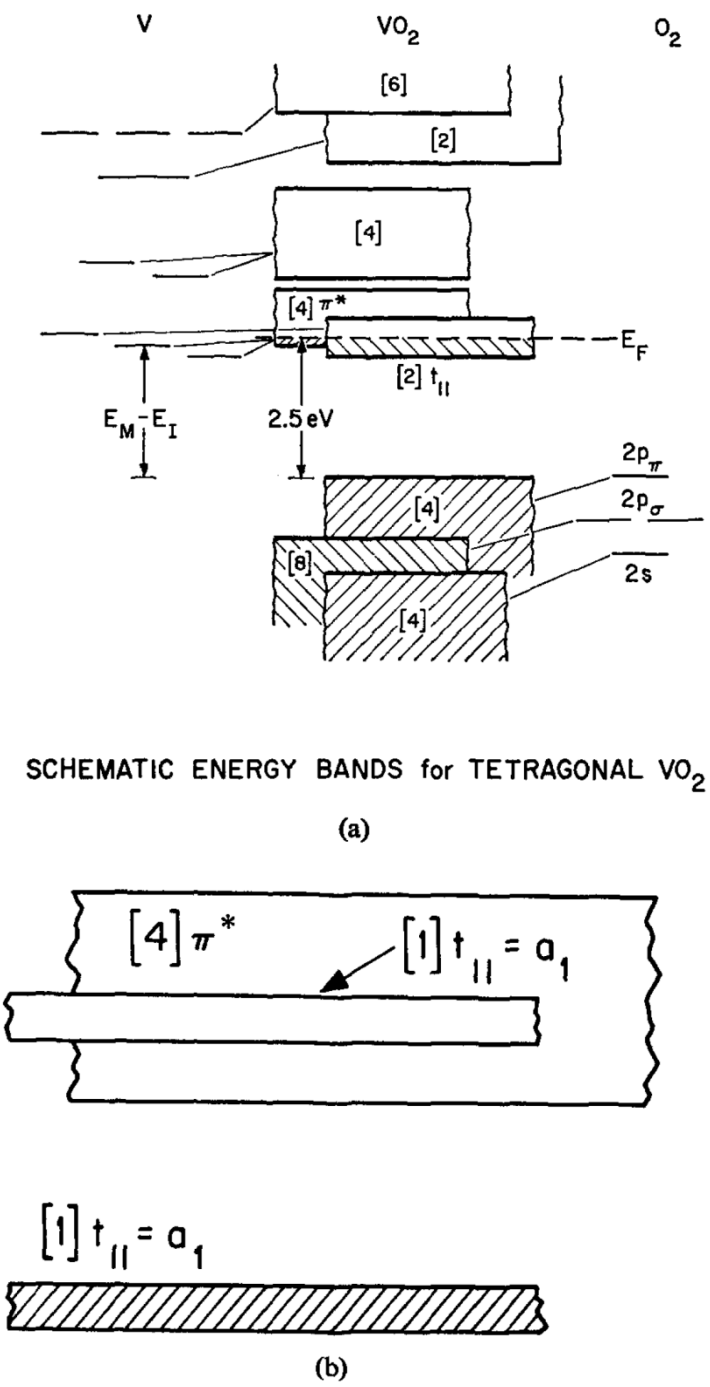

Fig. 7 One electron energy bands for VO_2. Numbers in brackets refer to numbers of orbitals per formula unit VO_2. (a) $T > T_t$ (b) $T < T_t$. After Goodenough.[40]

Fig. 7 shows an energy band scheme, proposed by Goodenough for both metallic and insulating VO_2.[47] Starting with electrostatic onsiderations he placed the O *2p* states well below the V *3d* states. Octahedral crystal field splitting leads to lower V *3d* t_{2g} and higher V *3d* e_g levels, where the former are located in the vicinity of the Fermi level and split into $d\|$ (oriented parallel to the rutile c-axis) and π^* states. In the monoclinic case metal-metal pairing causes the $d\|$ band to split into filled bonding and empty antibonding states. Due to antiferroelectric zigzag-type displacements of the metal atoms, the π^* bands shift to

higher energies. Shin et al. found the $d\|$ band splitting to amount to 2.5 eV and the π^* bands to rise by 0.5 eV.[41]

In contrast to the Goodenough scheme Zylbersztejn and Mott proposed an MIT mechanism based on strong electron-electron correlations.[42]

According to these authors especially the one-dimensional $d\|$ band is affected by correlations rather than by electron-lattice interaction. In the metallic phase, correlations are efficiently screened by the π^* electrons, but screening is reduced below the phase transition as the π^* bands are subject to an energetical upshift. Thus the narrow $d\|$ bands become susceptible to strong Coulomb repulsion and undergo a Mott-transition – opening a correlation gap. Recently, the MIT of VO_2 was explained in terms of a Peierls instability of the one-dimensional $d\|$ band, embedded in a background of the remaining V *3d* t_{2g} states.[43,44]

The vanadium atoms in VO_2 are shifted from the center to their oxygen octahedra. This relative shift affects the bonding between V *3d* and O *2p* states as it influences the orbital overlap. Thus an antiferroelectric distortion of the [V-O_6] octahedra is inherent in the monoclinic (M1) phase of VO_2.

3.2.2 The Magneli-Andersson- phases Chemistry and general aspects

The vanadium oxides comprise compounds with different formal vanadium valency states, which go from two in VO, three in V_2O_3, four in VO_2 to five in V_2O_5. In addition to these configurations, mixed valent compounds can be synthesized. Amongst the latter, one can mention the so-called Magneli-Anderson phases, intermediate between VO_2 and V_2O_3, that can be defined by the general stoichiometric formula:

$$V_nO_{2n-1} = V_2O_3 + (n-2)VO_2 \text{ where } 3 \leq n \leq 9,$$

They are of special interest since give rise to a homologous series of compounds with closely related crystal structures, and non less interesting transport and magnetic properties.

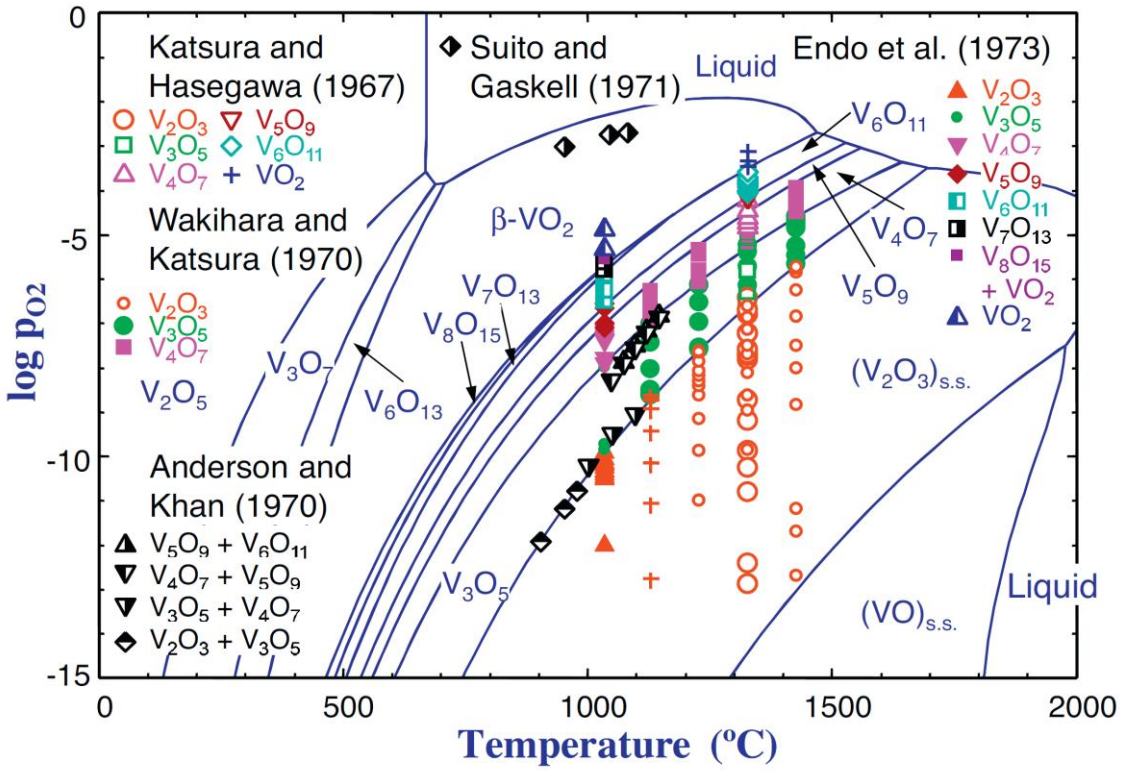

Fig. 8 Calculated phase diagram of V-O system with oxygen partial pressure as y-axis, along with available experimental data;[26]

Fig. 8 shows the phase diagram of the V-O system as a function of temperature and oxygen partial pressure; the phase diagram is complex and includes the relations among the different Magneli phases.

Obviously composition is another fundamental variable; the phase diagram in fig. 9 shows the variation of composition as function of temperature;

As a function of temperature each Magneli phase undergoes a metal-insulator transition (MIT), except for V_7O_{13}, which is metallic at all temperatures. The MITs are of first order and are accompanied by distinct structural transformations. Tab. 2 summarizes transition temperatures, inferred from electrical resistivity measurements by Kachi et al.,[45] and formal oxidation state, varying from +3.33 in V_3O_5 to +3.78 in V_9O_{17}.

Tab.2 The metal-insulator transition temperaure and formal oxidation state for the non molecular V_nO_{2n-1} series.

Compound V_nO_{2n-1}	Formal oxidation state	MIT temperature
V_3O_5	3.33	430 K
V_4O_7	3.50	250 K
V_5O_9	3.60	135 K
V_6O_{11}	3.67	170 K
V_7O_{13}	3.71	metallic
V_8O_{15}	3.75	70 K
V_9O_{17}	3.78	—

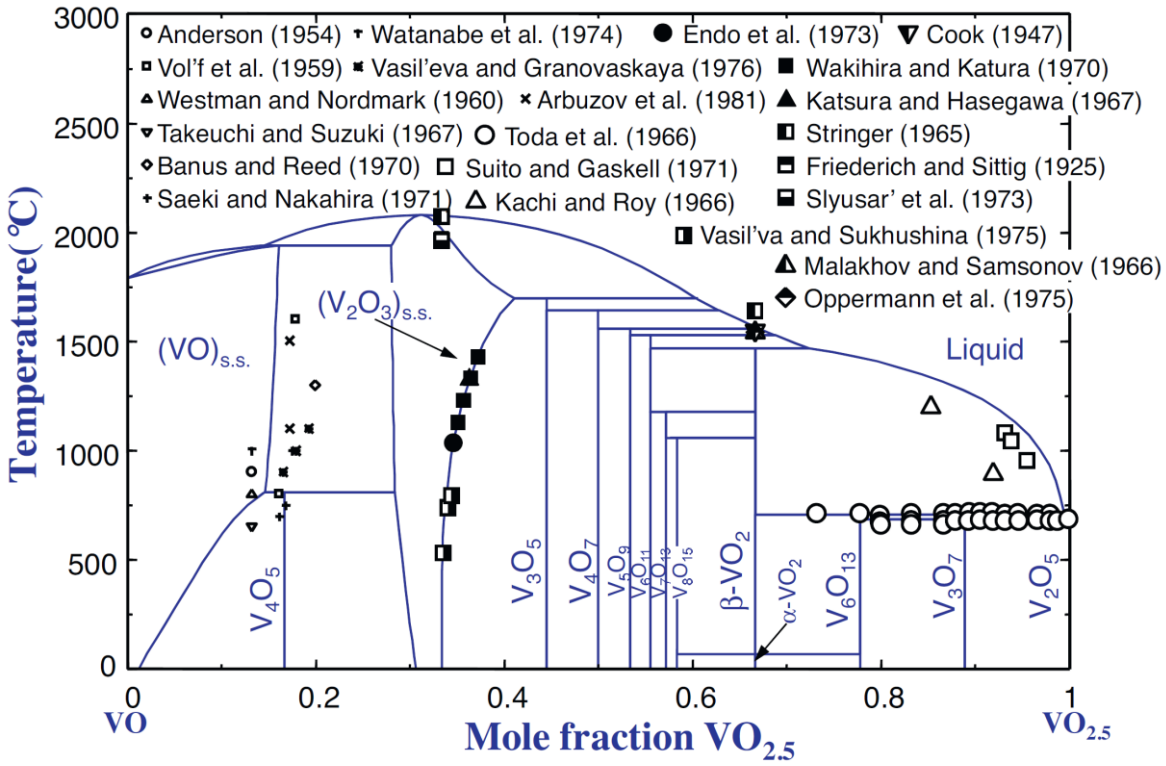

Fig. 9 Calculated phase diagram of the VO-$VO_{2.5}$ system along with available experimental data.[26]

As the Magneli phases are characterized by vanadium atoms in mixed valent states, the electronic properties are expected to be influenced by charge ordering.[45]

Fig. 10 illustrates the behaviour of the MIT temperatures listed in tab.2 as a function of the vanadium oxygen ratio. We recognize a broad minimum centered at the ratio corresponding to V_7O_{13}. Interestingly, the MITs of the vanadium Magneli phases are coupled to an anomaly in the magnetic susceptibility, which closely resembles the characteristics of a transition from a paramagnetic to an antiferromagnetic state.

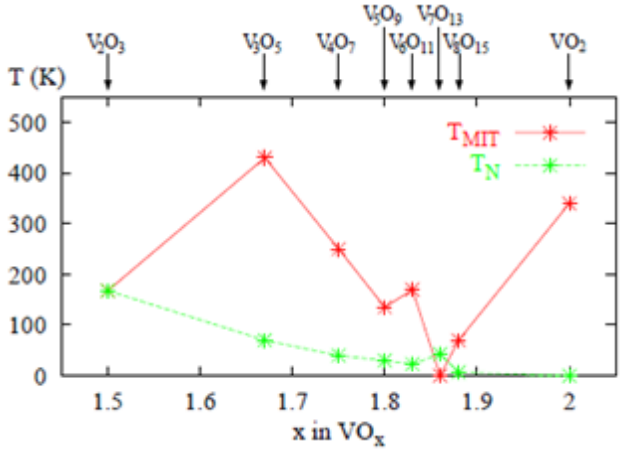

Fig. 10 Plot of MIT temperatures listed in table 2 as a function of the vanadium oxygen ratio.

Nonetheless, the anomaly is not accompanied by long range magnetic order. While the MIT temperature of VO_2 increases on the application of pressure, V_2O_3 reveals the opposite trend. The Magneli phases reflect a similar behaviour with the sesquioxide as their transition temperatures decrease with growing hydrostatic pressure.[46,48]

Moreover, Canfield et al.[49] reported on unifying aspects emerging in the Magneli series on the application of pressure. They observed for both V_8O_{15} and $(V_{0.98}Cr_{0.02})_8O_{15}$ a transition from a paramagnetic-metal (PM phase) to an antiferromagnetic-metal (AFM phase) and further to a paramagnetic-insulator (PI phase). Consequently, the PM-AFM transition present for V_7O_{13} at atmospheric pressure should not be regarded anomalous for the Magneli series. While the PM-AFM transition is found in V_8O_{15} only above 9 Kbar, it is always present for the chromium doped system. The magnetic transition exhibits the same pressure dependence in all three cases (−0.75 K/ Kbar). Since the MIT temperature decreases at a larger rate, the AFM modification is stabilized for sufficiently high pressures.

Examples of chromium doped V_3O_7, V_6O_{13} and V_8O_{15} are not present in literature at this date. As mentioned before, in the case of V Magneli phases, some new doped Cr Magneli phase related $(Cr_xV_y)_nO_{2n-1}$ (where: x + y = n) could exist. Our present work concerns the HP/HT synthesis of members of solid solution $Cr_{1-x}V_xO_2$; one can anticipate that these conditions should be favorable for a possible synthesis of new doped Cr Magneli phase related $(Cr_xV_y)_nO_{2n-1}$. However intriguing theory, the structural characterization of our samples did not provide evidence about the possible existence of new doped Cr Magneli phase related $(Cr_xV_y)_nO_{2n-1}$ (where: x + y = n).

3.3 Some previously known solid solutions: $Cr_{1-x}M_xO_2$ and $V_{1-x}M_xO_2$ (M = transition metal) having the rutile structure

Several examples have been reported in the literature of Cr^{3+} doping in rutile, trirutile or rutile-like structure, since the ionic radius of Cr^{3+} (0.62Å) is close to the one of Ti^{4+} (0.61Å) for octahedral oxygen coordination.[50-52] The rutile-type structure with a statistical i.e. disordered distribution of cations is knownn: for example, for $CrMO_4$ (M = Sb, Nb,Ta).[53] A solid solution of $CrV_{1-x}Sb_xO_4$ (x = 0 - 1) with rutile-type structure has also been synthesized.[54] Depending on the Cr/M ratio in $Cr_xM_{1-x}O_2$ systems, different rutile-structure derivative can be formed. $CrMO_4$ (M = Mo[55], W[56] has a monoclinic distorted rutile-like structure with M^{5+} stabilized by the formation of M–M pairs with metallic bonds.

In the system $Cr_xMo_{1-x}O_2$ four different rutile-related phases were found: a monoclinic MoO_2-type for $0 < x < 0.12$, a solid solution with a tetragonal rutile-structure for $0.12 < x < 0.36$,[57,58] a monoclinic distorted rutile for $0.36 < x < 0.5$ ($CrMoO_4$-type), and a trirutile structure for $x = 0.667$.[59] The mixed dioxides $Cr_xMo_{1-x}O_2$ in the range of $0.0 < x < 0.5$ demonstrate ferromagnetic behaviour with Curie temperatures below 200 K. The experimental effective magnetic moment of $Cr_xMo_{1-x}O_2$ ($0.0 < x < 0.5$) in the paramagnetic region is in good agreement with the calculated spin-only values of Cr^{3+} and indicates no significant contribution from the Mo ions. $CrMoO_4$ is antiferromagnetic with a Neél temperature of 100 K, similar to isostructural $CrWO_4$,[60] which has an antiferro-paramagnetic transition between 40 and 45 K. Ternary oxides in the system Cr–Re–O have been less intensively investigated, although the systems offer an additional degree of freedom due to the ability of the Re ion to adopt formal oxidation states between +4 and +7 in complex oxides with different resulting properties. Both end members CrO_2[61] and the monoclinic modification of ReO_2,[62] have a rutile-like structure. A new modification of ReO_2 with rutile structure was also recently reported.[62] Sleight[63] has reported on Cr_2ReO_6, prepared under high-pressure high-temperature conditions, and proposed for this compound a tri-rutile structure. This suggestion was based on the similarities of the cell metric and diffraction patterns with analogous tungsten compounds, but neither a structure refinement was performed, nor physical properties were investigated.

Villeneuve et al.[30] reported a phase diagram for the system $V_{0.9}Cr_{0.1}O_2$ which is based on magnetic susceptibility, electrical resistivity, and powder x-ray diffraction measurements.[30] Adding Cr, they found a sequence of phases with increasing temperature of monoclinic to orthorhombic to tetragonal (rutile) with the insulator-to-metal transition being associated with the latter crystallographic transition. The metallic phase is more dense than the insulating phase, in contrast to pure VO_2 where the insulator is slightly more dense. This implies that the metal-insulator transition temperature of Cr-doped VO_2 will decrease with increasing pressure.[24,65] As crystals of VO_2 doped with 2 4-at. % Cr were available from the earlier studies of Mac-Chesney and Guggenheim, a complete determination of the crystal structure of the intermediate phase was undertaken and measurements of the pressure dependence of the transition temperature were made.[65]

3.4 Results and discussion

3.4.1 Synthesis optimization

The optimal conditions for the synthesis of the solid solution $Cr_{1-x}V_xO_2$, using α-CrO_2 (a = b = 4.421(1) Å, c = 2.916(2), (Tetragonal) S.G.:P42/mmm (nº 136)) and VO_2 (a = 5.751(7) Å, b = 4.537(8) Å, c = 5.382(5) Å, β = 122°.6(4)' (Monoclinic) S.G.: P21/c (n° 14)), have been found to be 900 ºC and 40 Kbars; Indeed VO_2 at high pressure (P > 65 Kbar) transforms into the (M3) monoclinic phase (a = 4.506(4) Å, b = 2.899(2) Å, c = 4.617(3) Å, and β = 91°.7(9)', S.G.: P 2/m (n°10)).

The single phase range is in the region 0,1 < x < 0,7. Starting from nominal composition $Cr_{0,7}V_{0,3}O_2$, small secondary phases of Cr_2O_3 have been detected by means of x-ray diffraction. Decreasing the V substitution in $Cr_{1-x}V_xO_2$, in $Cr_{0,8}V_{0,2}O_2$ and $Cr_{0,9}V_{0,1}O_2$ samples secondary phases of Cr_2O_3 (a = 4.958(7) Å, c = 13.59(4) Å, (Rhombohedral), S.G.: R-3c (n° 167)) and VO_2 (a = 5.751(7) Å, b = 4.537(8) Å, c = 5.38285) Å, β = 122°.6(4)' (Monoclinic) S.G.: P21/c (n° 14)) have been observed in the product by means of X-ray powder diffraction.

3.4.2 Structural characterization

As can be easily seen from fig. 11 and 12, the peaks are shifted as function of composition. Two different regions can be defined in the solid solution $Cr_{1-x}V_xO_2$: the shift of the $(110)_{\beta\text{-}CrO2}$ peak, in the range $0 \geq x \geq 0{,}500(6)$, follows the Vergard's law underlined by the line on fig. 11; up to x = 0,500(6) there is not symmetry change, V replaces Cr in CrO_2 keeping the tetragonal structure. Above that, for compositions richer in vanadium

x > 0,500(6) a structural change takes place, the symmetry becomes monoclinic, the $(110)_{\beta\text{-}CrO2}$ peack splits in a doublet of $(-101)_{M3\text{-}VO2}$ and $(101)_{M3\text{-}VO2}$. Also these peaks distanced each others increasing V substitution until x = 0.847(1), again following the Vergard's law; when x = 0.901(9) is reached the separation between these two peaks has a small contraction. In fig.11 the diffraction pattern for (M3) VO_2, i.e. x = 1 at high pressure, is calculated on the basis of data reported in literature.[36]

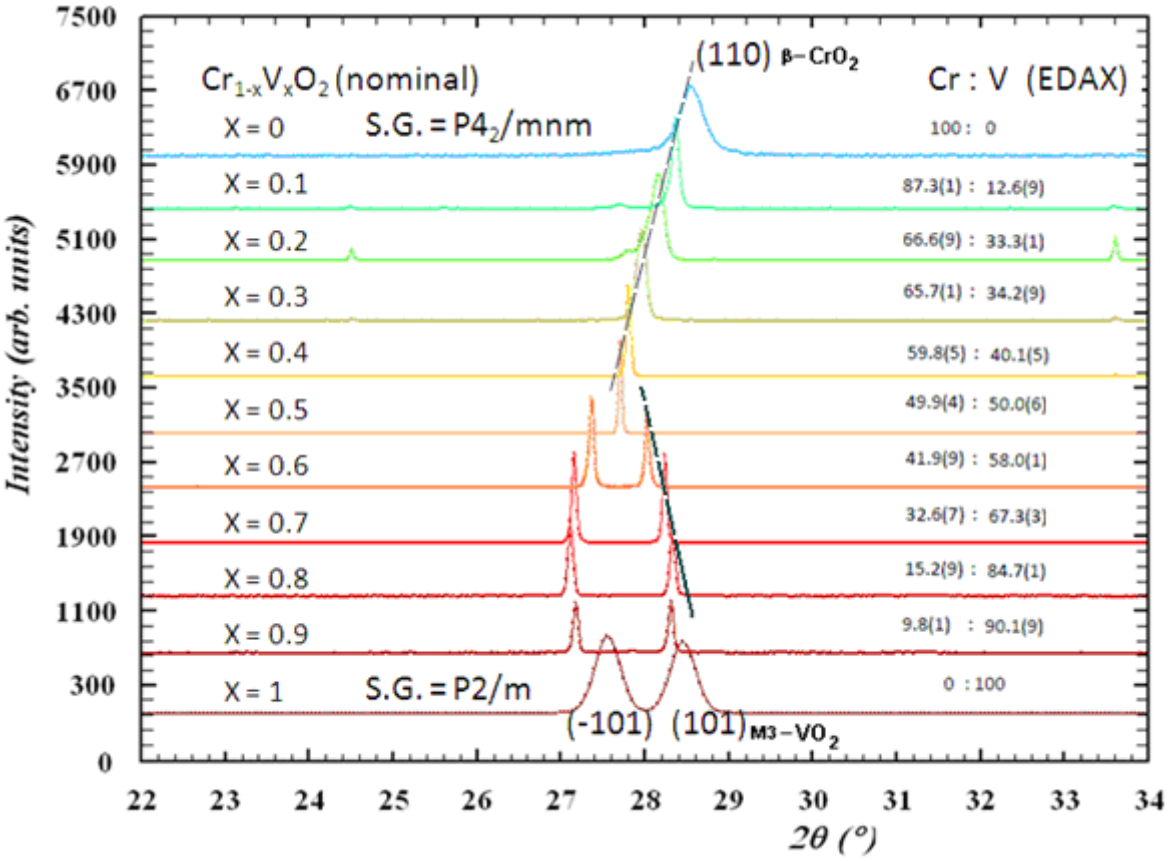

Fig. 11 Details of PWD-XRD of all members of solid solution $Cr_{1-x}V_xO_2$ between 22 and 34 2θ degrees as function of composition.

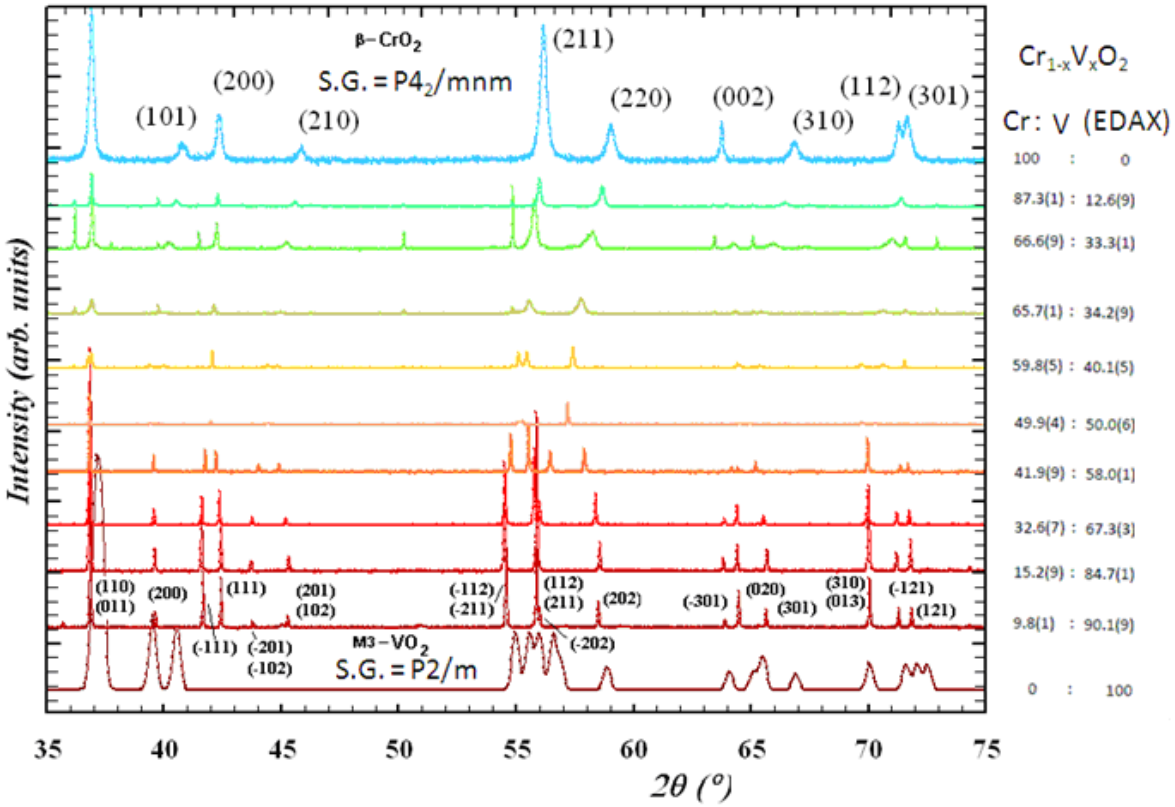

Fig. 12 Details of PWD-XRD of all members of solid solution $Cr_{1-x}V_xO_2$ between 35 and 75 2θ degrees as function of composition.

Differences among diffractograms observed in Fig. 11 tuning composition, $Cr_{1-x}V_xO_2$, have been investigated in more detail, after pattern matching, indexing and refinement of crystallographic data for all phases and is described in what follows. A representation of remaining parts of the complete x-ray diffraction patterns appear in figure 12. Vergard's law is confirmed in the whole patterns. Yet some Cr_2O_3 did appear as secondary phases starting from $x \leq 0.326(7)$. The peak displacement indicate that some more V can still enter in the $Cr_{1-x}V_xO_2$ rutile-like (M3) structure.

In an attempt to increase the substitution of V in the Cr rich region of the solid solution $Cr_{1-x}V_xO_2$, some experiments at higher pressure have been performed. However, in spite of increasing pressure, we were not able to isolate a Cr rich member of solid solution $Cr_{1-x}V_xO_2$ free of secondary phases.

Further details about the region between $Cr_{0,657(1)}V_{0,342(9)}O_2$ and $Cr_{0,873(1)}V_{0,126(9)}O_2$ will be discussed in 3.4.2a below

3.4.2a Powder X-ray diffraction data, refinement and proposed crystallographic models

All the compositions of solid solution have been structurally characterized by Rietveld refinement. The corresponding data of the x-ray powder diffraction are shown in the tables 3, 4 and 5; the table 3 shows the refined lattice parameters, space group, observed agreement factors, calculated and measured composition (refinement and EDAX respectively) and structural model for all compositions.

For clarity, only the plots for $Cr_{0,59(8)}V_{0,40(2)}O_2$ (nominal composition $Cr_{0,6}V_{0,4}O_2$) and $Cr_{0,41(9)}V_{0,58(1)}O_2$ (nominal composiotion $Cr_{0,4}V_{0,6}O_2$) refinements of are shown, respectively in fig. 13 and fig. 14. The plots for other compositions have been reported in appendix 1. The refinements of all samples show a satisfactory matching between calculated and experimental data; the values of χ^2, reported in tab. 3, are between a minimum of 2,2 ($Cr_{0,59(8)}V_{0,40(2)}O_2$) and a maximum of 6,6 ($Cr_{0,336(7)}V_{0,673(3)}O_2$). Also generally in the refinements the value of R_p is in agreement with the theoretical R expected (R_{exp} = pure statistical disagreement factor),

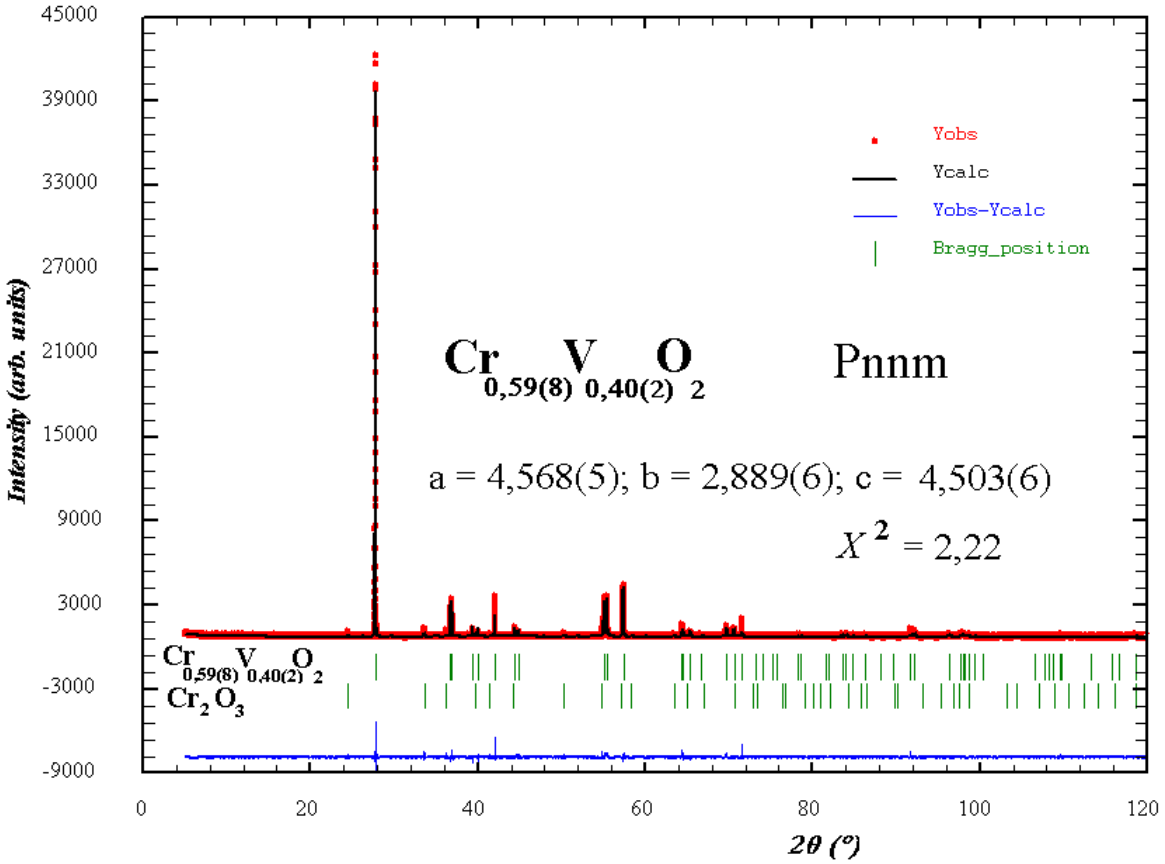

Fig. 13 Graphical result of the Rietveld refinement of $Cr_{0,59(8)}V_{0,40(2)}O_2$ rutile; X-ray powder data at 298 K. The experimental data is presented as points and the calculated profile as solid line. The observed profile is plotted at the bottom. Vertical bars are the allowed Bragg reflections $Cr_{0,59(8)}V_{0,40(2)}O_2$ (up) Cr_2O_3 (down). Formula show quantitative easurements by EDAX.

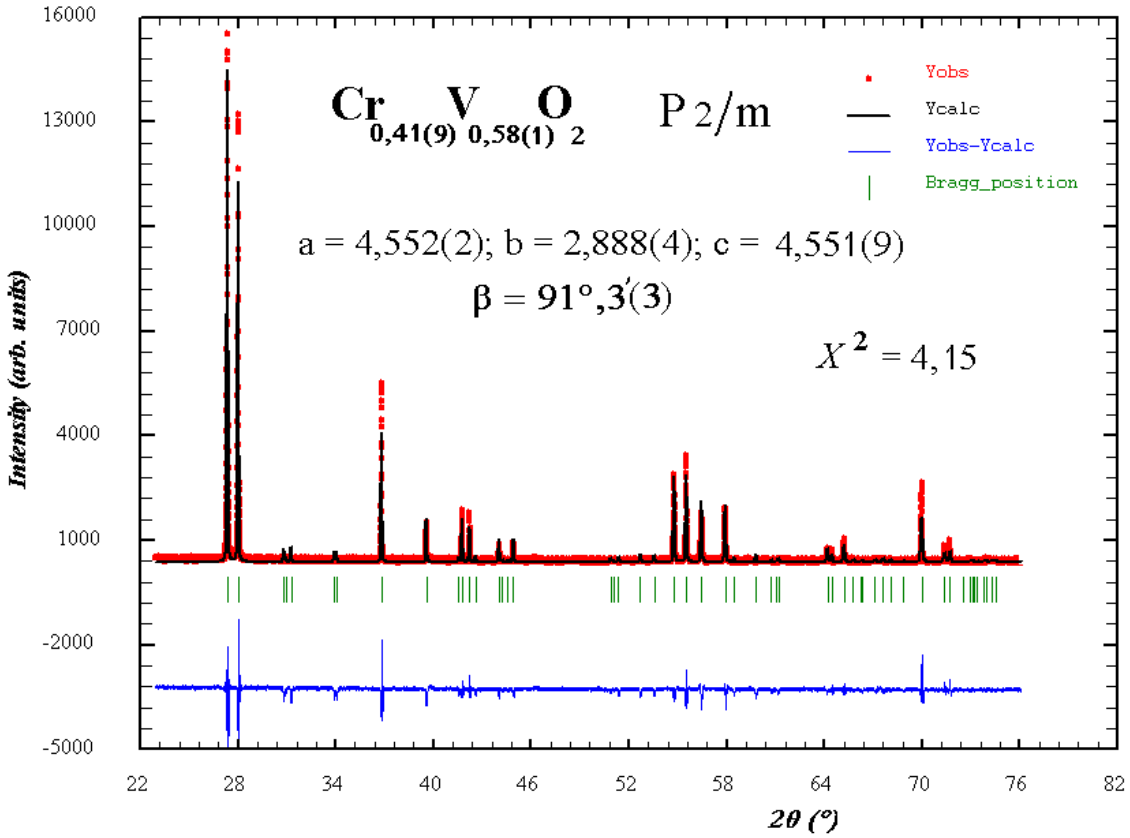

Fig. 14 Graphical result of the Rietveld refinement of $Cr_{0,41(9)}V_{0,58(1)}O_2$ rutile; X-ray powder data at 298 K. The experimental data is presented as points and the calculated profile as solid line. The observed profile is plotted at the bottom. Vertical bars are the allowed Bragg reflections. Formula show quantitative easurements by EDAX.

excepted the case of $Cr_{0,33(6)}V_{0,67(4)}O_2$ (nominal $Cr_{0,3}V_{0,7}O_2$) where disagreement between the two values can be distinguished (see tab.3).

The R_{wp} factors have acceptable values for the refined phases, one of the highest value is observed for $Cr_{0,49(9)}V_{0,50(1)}O_2$ (nominal $Cr_{0,5}V_{0,5}O_2$) having a R_{wp} = 10.0: it appears to be related to a high preferential orientation; the preferential orientation has been taken into account during the refinement and several attempts to minimize R_{wp} value have been made; the best result is shown in fig. 14.

However relative high values of R_{wp} in $Cr_{0,49(9)}V_{0,50(1)}O_2$ and R_p in $Cr_{0,33(6)}V_{0,67(4)}O_2$ exist, the χ^2 values and R_p (in $Cr_{0,49(9)}V_{0,50(1)}O_2$) or R_{wp} (in $Cr_{0,33(6)}V_{0,67(4)}O_2$) provide a good agreement factors for refined data.

The symmetry change as function of composition has been discussed qualitatively in 3.4.1; when $x \geq 0.6$ the structure decrease in symmetry from Pnnm (nº58) to P2/m (nº10) (see tab. 3);

3.4.2b Discussion of structural data in $Cr_{1-x}V_xO_2$

On the basis of these events, we can propose two different models for two different region of the solid solution: for $x \leq 0{,}500(6)$ and for $x \geq 0{,}580(1)$.

Each of them belong to rutile or rutile-like structures.

First of all we have to consider the crystal structure of high pressure phase of CrO_2: as already described in paragraph 3.1.2; the structural model proposed for β-CrO_2 is rutile-like with a $CaCl_2$ structure. As pointed out in fig. 4, the structural modification observed is common for rutile structures under high pressures: they transform from a (6) fold coordinated structure to a (6+2) fold coordinated one $CaCl_2$-like. In a first approximation these pressure-induced structural transitions may be understood in view of a topological packing of hard spheres, i.e., an increase in density and a small variation of coordination number.[10,72]

The phase transition α-CrO_2 → β-CrO_2 occurs at 12.8 GPa (128 Kbar) but in the $Cr_{1-x}V_xO_2$, presence of V cations, $0.500(6) \geq x \geq 0$ in the structure induce a "chemical pressure effect" decreasing needed pressure down to 40 Kbar and 900ºC.

In the region comprised between $Cr_{0,419(9)}V_{0,580(1)}O_2$ to $Cr_{0,098(1)}V_{0,901(9)}O_2$, samples have the VO_2 (M3) structure previously reported in literature;[36]

The structural model for phases between $Cr_{0,879(1)}V_{0,126(9)}O_2$ and $Cr_{0,499(4)}V_{0,500(6)}O_2$ are shown in fig 15, while the model for phases between $Cr_{0,419(9)}V_{0,580(1)}O_2$ and $Cr_{0,098(1)}V_{0,901(9)}O_2$ are shown in fig 16.

Tab. 3 Refined lattice parameters, agreement factors, symmetry, space group. secondary phases, composition (EDAX and refinement) and structural model for each composition of the solid solution $Cr_{1-x}V_xO_2$.

Composition Nominal	Composition Measured	EDAX V : Cr	a	b	c	V	α	β	γ	X^2	Rp	Rwp	Rexp
VO_2 (M3)	VO_2	100 : 0	4.617	2.899	4.506	60.3(1)	90	91.7(9)	90	*J.sol.state chem. 7 377 1973			
$V_{0.9}Cr_{0.1}O_2$	$Cr_{0.098(1)}V_{0.901(9)}O_2$	90.1(9) : 9.8(1)	4.553(2)	2.889(0)	4.553(1)	59.8(4)	90	92.2(9)	90	4.39	4.16	6.36	3.04
$V_{0.8}Cr_{0.2}O_2$	$Cr_{0.152(9)}V_{0.847(1)}O_2$	84.7(1) : 15.2(9)	4.555(3)	2.891(1)	4.554(2)	59.9(2)	90	92.4(5)	90	4.95	4.27	6.09	2.74
$V_{0.7}Cr_{0.3}O_2$	$Cr_{0.336(7)}V_{0.673(3)}O_2$	67.3(3) : 32.6(7)	4.553(6)	2.891(1)	4.553(6)	59.9(4)	90	92.1(8)	90	6.67	9.22	10.5	1.57
$V_{0.6}Cr_{0.4}O_2$	$Cr_{0.419(9)}V_{0.580(1)}O_2$	58.0(1) : 41.9(9)	4.552(2)	2.888(4)	4.551(9)	59.8(3)	90	91.3(3)	90	4.15	6.34	9.38	4.61
$V_{0.5}Cr_{0.5}O_2$	$Cr_{0.499(4)}V_{0.500(6)}O_2$	50.0(6) : 49.9(4)	4.568(7)	2.886(2)	4.532(8)	59.7(7)	90	90	90	4.18	9.37	10.8	5.28
$V_{0.4}Cr_{0.6}O_2$	$Cr_{0.598(5)}V_{0.401(5)}O_2$	40.1(5) : 59.8(5)	4.568(5)	2.889(6)	4.503(6)	59.4(5)	90	90	90	2.22	3.71	5.26	3.53
$V_{0.3}Cr_{07}O_2$	$Cr_{0.657(1)}V_{0.342(9)}O_2$	34.2(9) : 65.7(1)	4.520(3)	2.887(3)	4.495(1)	58.6(7)	90	90	90	2.64	5.01	7.16	4.4
$V_{0.2}Cr_{0.8}O_2$	$Cr_{0.666(9)}V_{0.333(1)}O_2$	33.3(1) : 66.6(9)	4.469(1)	2.893(0)	4.480(4)	57.9(2)	90	90	90	6.08	3.45	5.84	2.37
$V_{0.1}Cr_{0.9}O_2$	$Cr_{0.873(1)}V_{0.126(9)}O_2$	12.6(9) : 87.3(1)	4.440(6)	2.904(7)	4.449(2)	57.3(9)	90	90	90	3.26	3.48	4.83	2.68
β–CrO_2	CrO_2	0 : 100	4.425	3.987	2.683	47.3(3)	90	90	90	*Phys. Rev. B 73 144111 (2006)			
α–CrO_2	CrO_2	0 : 100	4.423(5)	4.423(5)	2.918(7)	57.1(1)	90	90	90	2.62	2.41	3.21	2.09

Composition Nominal	Composition Measured	symm	S.G. (nº)	Secondary phases	Strucutral model
VO_2 (M3)	VO_2	monoc	P2/m (10)	—	VO_2 (M3)
$V_{0.9}Cr_{0.1}O_2$	$Cr_{0.098(1)}V_{0.901(9)}O_2$	monoc	P2/m (10)	no	VO_2 (M3)
$V_{0.8}Cr_{0.2}O_2$	$Cr_{0.152(9)}V_{0.847(1)}O_2$	monoc	P2/m (10)	no	VO_2 (M3)
$V_{0.7}Cr_{0.3}O_2$	$Cr_{0.336(7)}V_{0.673(3)}O_2$	monoc	P2/m (10)	no	VO_2 (M3)
$V_{0.6}Cr_{0.4}O_2$	$Cr_{0.419(9)}V_{0.580(1)}O_2$	monoc	P2/m (10)	no	VO_2 (M3)
$V_{0.5}Cr_{0.5}O_2$	$Cr_{0.499(4)}V_{0.500(6)}O_2$	orth	Pnnm (58)	no	b-CrO2 rutile ($CaCl_2$)
$V_{0.4}Cr_{0.6}O_2$	$Cr_{0.598(5)}V_{0.401(5)}O_2$	orth	Pnnm (58)	Cr_2O_3	b-CrO2 rutile ($CaCl_2$)
$V_{0.3}Cr_{07}O_2$	$Cr_{0.657(1)}V_{0.342(9)}O_2$	orth	Pnnm (58)	Cr_2O_3, VO_2 (?)	b-CrO2 rutile ($CaCl_2$)
$V_{0.2}Cr_{0.8}O_2$	$Cr_{0.666(9)}V_{0.333(1)}O_2$	orth	Pnnm (58)	Cr_2O_3, VO_2	b-CrO2 rutile ($CaCl_2$)
$V_{0.1}Cr_{0.9}O_2$	$Cr_{0.879(1)}V_{0.126(9)}O_2$	orth	Pnnm (58)	Cr_2O_3, VO_2	b-CrO2 rutile ($CaCl_2$)
β–CrO_2	CrO_2	orth	Pnnm (58)	—	b-CrO2 rutile ($CaCl_2$)
α–CrO_2	CrO_2	tetr	$P4_2/mnm$ (136)	—	rutile

Tab. 4 Wyckoff positions, atomic coordinates, isotropic thermal factor, and calculated occupancy for each composition under exam.

composition	atoms	site	X	Y	Z	B	occ
VO2 (M3)	V1	1a	0	0	0		
	V2	1h	0.5	0.5	0.5		
	O1	2n	0.761(1)	0.5	0.206(2)		
	O2	2m	0.726(1)	0	0.704(2)		
$Cr_{0,098(1)}V_{0,901(9)}O_2$	V1	1a	0	0	0	0.9(6)	0.37(3)
	Cr1	1a	0	0	0	0.9(6)	0.03(2)
	V2	1h	0.5	0.5	0.5	2.4(6)	0.36(5)
	Cr2	1h	0.5	0.5	0.5	2.4(6)	0.05(4)
	O1	2n	0.744(9)	0.5	0.179(4)	1	1
	O2	2m	0.756(9)	0	0.684(3)	1	1
$Cr_{0,152(9)}V_{0,847(1)}O_2$	V1	1a	0	0	0	0.0(5)	0.4
	Cr1	1a	0	0	0	0.0(5)	0.1
	V2	1h	0.5	0.5	0.5	0.1(0)	0.4
	Cr2	1h	0.5	0.5	0.5	0.1(0)	0.1
	O1	2n	0.827(0)	0.5	0.251(1)	0.3(2)	1
	O2	2m	0.7019(1)	0	0.713(3)	0.9(4)	1
$Cr_{0,336(7)}V_{0,673(3)}O_2$	V1	1a	0	0	0	1	0.35
	Cr1	1a	0	0	0	1	0.15
	V2	1h	0.5	0.5	0.5	1	0.35
	Cr2	1h	0.5	0.5	0.5	1	0.15
	O1	2n	0.836(8)	0.5	0.213(2)	1	1
	O2	2m	0.672(4)	0	0.727(3)	1	1
$Cr_{0,419(9)}V_{0,580(1)}O_2$	V1	1a	0	0	0	2.4(2)	0.3
	Cr1	1a	0	0	0	2.4(2)	0.19(9)
	V2	1h	0.5	0.5	0.5	2.2(9)	0.3
	Cr2	1h	0.5	0.5	0.5	2.2(9)	0.19(9)
	O1	2n	0.779(3)	0.5	0.163(9)	0	1
	O2	2m	0.717(7)	0	0.688(1)	0	1
$Cr_{0,499(4)}V_{0,500(6)}O_2$	Cr	2a	0	0	0	1.7(2)	0.5
	V	2a	0	0	0	0.7(2)	0.5
	O	4f	0.312(0)	0.28(6)	0	1	1
$Cr_{0,598(5)}V_{0,401(5)}O_2$	Cr	2a	0	0	0	0.2(1)	1.18(4)
	V	2a	0	0	0	0.2(1)	0.78(4)
	O	4f	0.308(8)	0.296(6)	0	1	4
$Cr_{0,657(1)}V_{0,342(9)}O_2$	Cr	2a	0	0	0	1	0.7
	V	2a	0	0	0	1	0.3
	O	4f	0.299(0)	0.291(4)	0	0	2
$Cr_{0,666(9)}V_{0,333(1)}O_2$	Cr	2a	0	0	0	1.9(8)	0.79(5)
	V	2a	0	0	0	1.9(8)	0.19(5)
	O	4f	0.309(7)	0.307(7)	0	0	2
$Cr_{0,873(1)}V_{0,126(9)}O_2$	V	2a	0	0	0	0.2(0)	0.21(3)
	Cr	2a	0	0	0	0.2(0)	1.8(8)
	O	4f	0.305(5)	0.3001(4)	0	1	4
CrO2 β-CrO_2	Cr	2a	0	0	0	1	1
	O	4f	0.301(4)	0.301(4)	0	1	1

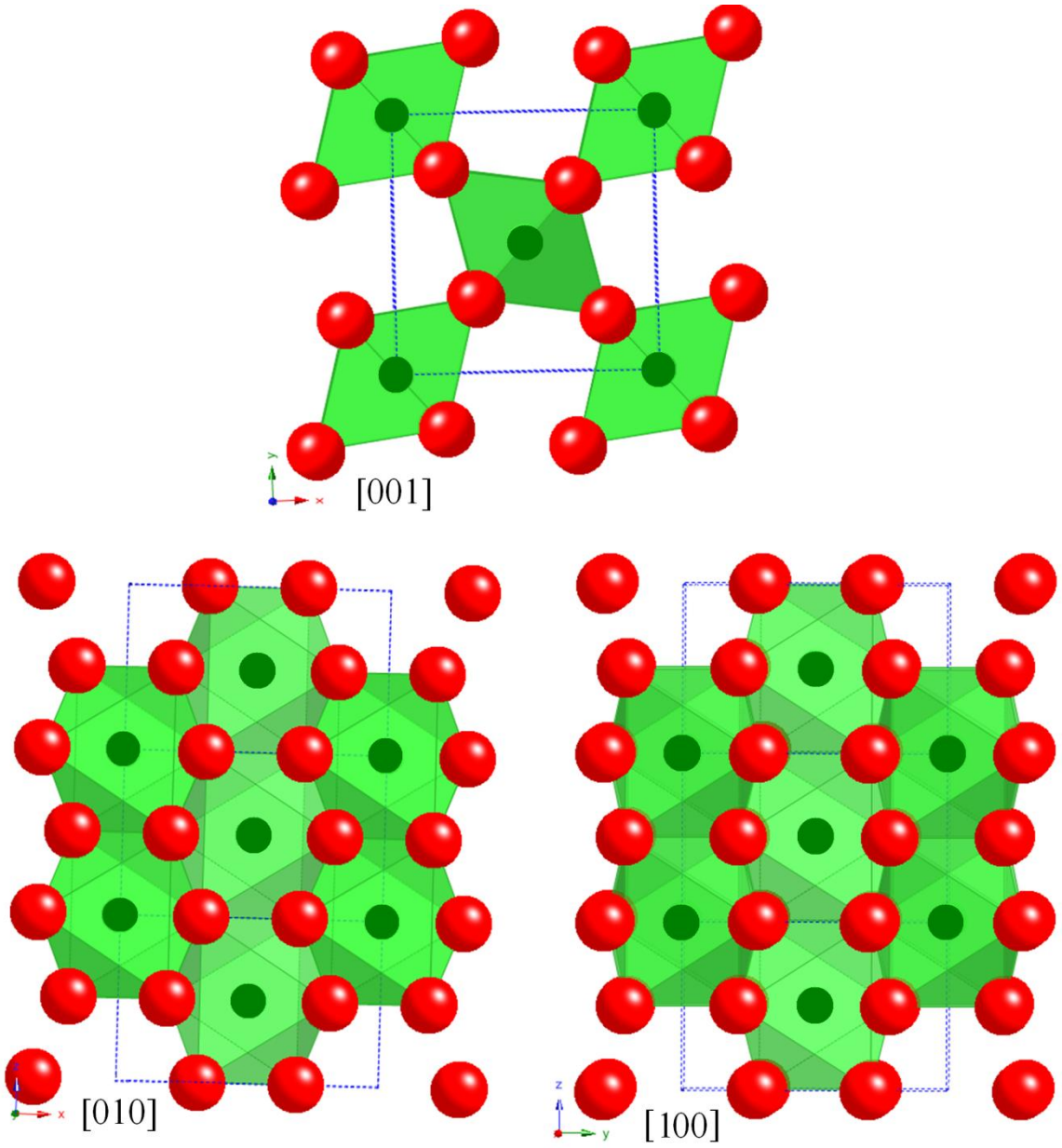

Fig. 15 The structural model $CaCl_2$ type for the phases of solid solution $Cr_{1-x}V_xO_2$ with $0.126(9) < x < 0.500(6)$. Green spheres represent V (or Cr) in 2a Wyckoff position (0 0 0), oxygen atoms in red.

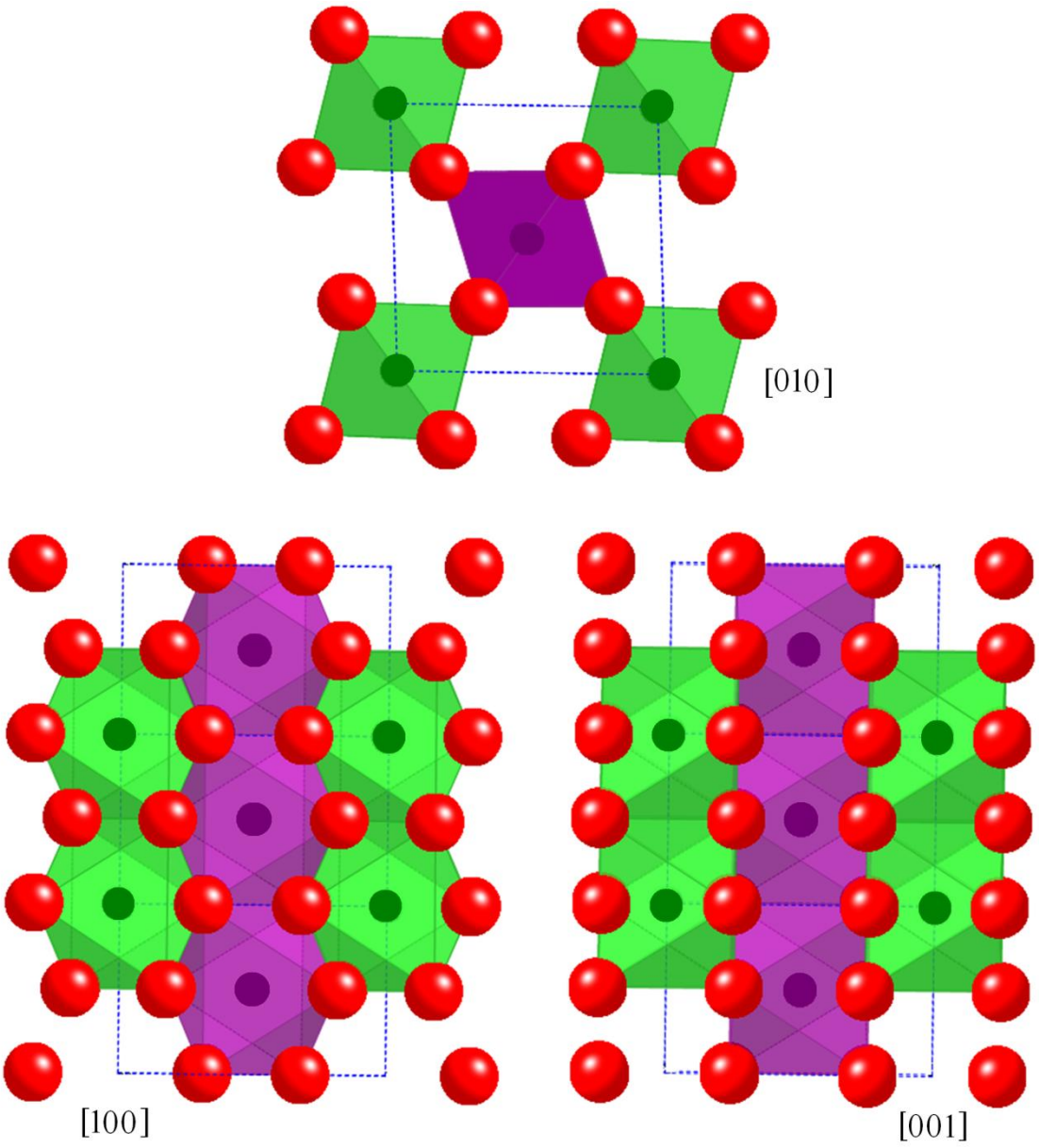

Fig. 16 The structural model VO_2 (M3) type for the phases of solid solution $Cr_{1-x}V_xO_2$ with 0.580(1) < x < 0.901(9); Green spheres represent V (or Cr) in 1a Wyckoff position (0 0 0), while purple spheres represent V (or Cr) in 1h Wyckoff position (½ ½ ½), oxygen atoms in red.

3.4.2c Evolution of crystal parameters

Fig. 17 shows the evolution of structural parameters a, b, c plotted as a function of composition, the refined lattice parameters of members of the solid solution studied in this work together with the data of VO_2 (M3), α-CrO_2 and β-CrO_2 reported in literature. Error bars are not visible in most of the plots in fig.18 and 19, because these values are in the range of 10^{-4} in the case of the lattice parameters; however they are visible in the angle vs. composition plot in fig. 19 because errors are in the range of 10^{-2}.

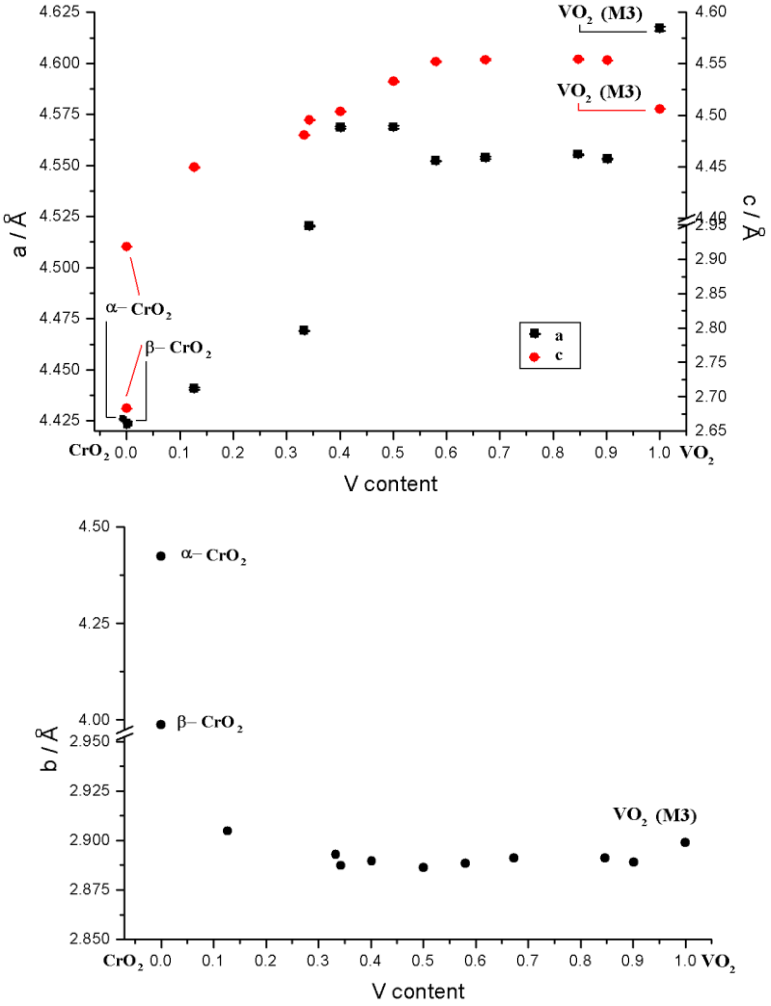

Fig. 17 The evolution of structural parameters *a* and *c* (up) and *b* (down), plotted as a function of composition.

The value of the *a* lattice parameter increases until it reaches a value of x = 0,401(5). Increasing the V substitution x ≥ 0,580(1) a small contraction is observed with no changes.

The value of *c* parameter increases when 0,126(9) > x > 0,580(1), then value does not change increasing V substitution.

The value of the *b* parameter remains practically unchanged except for a small contraction with 0,126(9) > x > 0,342(9).

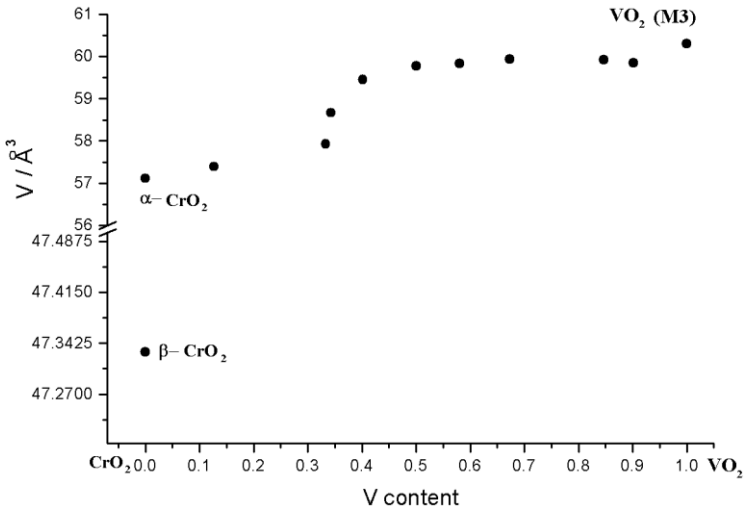

Fig. 18 The plots of volume V as function of composition for the members of solid solution studied in this work and data of VO_2 (M3), α-CrO_2 and β-CrO_2 reported in literature.

The volume as function of substitution, shown in fig.18, obviously reflects the effect of the lattice parameters. Its value increase as a function of V substitution in a similar way the *a* and *c* recall that *b* is almost independent of V concentration.

Summarizing, the parameters *a*, *c* and the volume increase remarkably in the Cr based solid solution while they remain almost constant when x ≥ 0,580(1); the *b* parameter is practically unaffected.

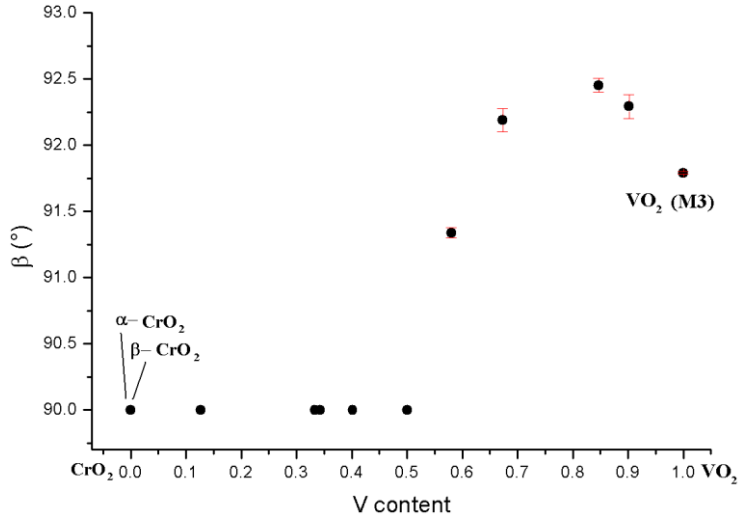

Fig. 19 The plots of refined lattice parameters angle (β) and volume V as function of composition for the members of solid solution studied in this work and data of VO_2 (M3), α-CrO_2 and β-CrO_2 reported in literature.

The monoclinic angle for the VO_2 (M3) structure increases from x > 0,500(6) to x = 0,847(1) and then is constant. Among the plots represented in fig. 18, the most uncommon is plot of the β angle values as function of composition; increasing the V content

$x \geq 0{,}580(1)$ the β angle value reaches a maxima with $x = 0{,}847(1)$ then the angle width decrease in $x = 0{,}901(9)$; this unusual parabolic trend should be related to variation of cation-cation distance in members of $Cr_{1-x}V_xO_2$ solid solution.

With this in mind, a study of the distances reported in tab. 5 has been carried out; several plots of distances and angles values as function of composition have been represented; among all data, distances M1-M1 and M2-M2 shown in fig.20 (positions of Cr or V cations in 1a and 1h sites respectively), have a similar parabolic trend observed in the same range of composition as observed in fig.19; this indicate that this parabolic trend of β is a consequence of the evolution of the M-M distances.

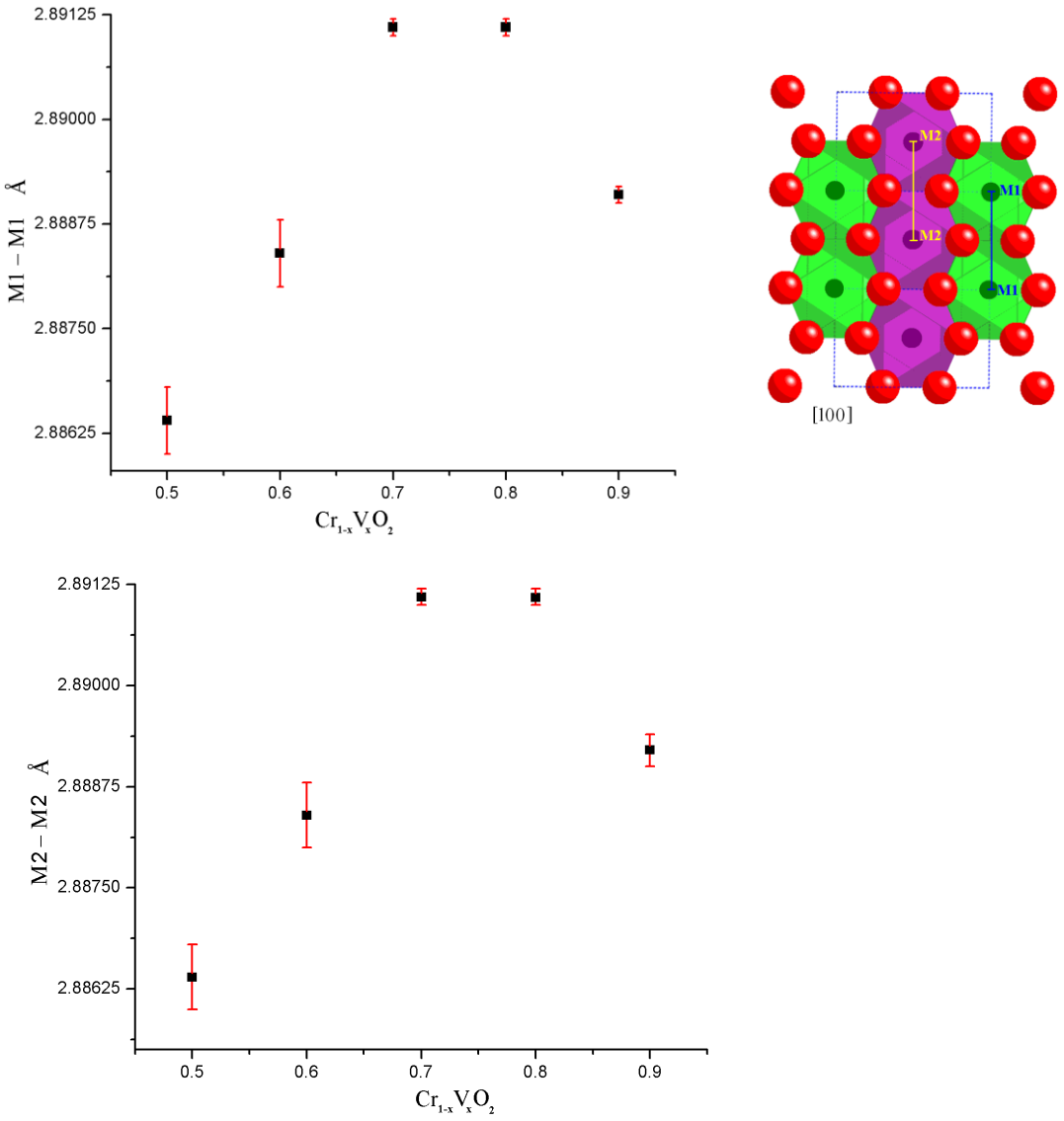

Fig.20 Plots of distances M1-M1 (up) and M2-M2 (down), positions of Cr (or V) cations are in 1a and 1h sites respectively, the model shows the distance between atoms in M1 and M2 position respectively for VO_2 structures.

As pointed out from fig.20, there is a correspondence between distance M1-M1 and M2-M2 and the β angle moving on composition in the monoclinic region. For this reason we think that the cation-cation distances could play a crucial role in the evolution of the β angle; Thought no further linear correspondences have been observed in the study of tab.5, we cannot exclude other effects, for example the interatomic distances are cationic radius and charge dependent; moreover magnetic characterization section will show, from magnetic susceptibility vs. temperature measurements, that both Cr and V are in mixed valence in $Cr_{1-x}V_xO_2$ (Cr^{4+} and Cr^{3+}; V^{4+} and V^{5+}); these two aspects (cationic radius and charge) in relationship with the relative proportion on Cr / V in the structure could give explaination the observed trend for the β angle. More work is planned to establish the origin of this behaviour.

Tab. 5 Metal-metal, metal oxygen distances (Å) and metal-oxygen-metal angles (°) for each composition under exam (continued next page).

VO2 (M3)							
	Distances (Å)						
V1-V1	2.9						
V1-V2	3.49						
V2-V2	2.9	Angle values					
V1-O1 (x4)	2.1	not reported in literature					
V1-O2 (x2)	2						
V2-O1 (x2)	1.75						
V2-O2 (x4)	2						

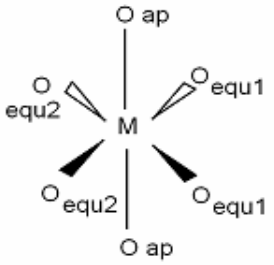

$Cr_{0,098(1)}V_{0,901(9)}O_2$		M= Cr, V					
	Distances (Å)			Angles (°)			
M1-M1	2.889(1)	Oe1-M1-Oe1	88.7(3)	Oe1-M2-Oe1	88.3(2)	M1-O1-M'1	89.9(2)
M1-M2	3.476(0)	Oe1-M1-Oe2	91.2(6)	Oe1-M2-Oe2	91.6(7)	M1-O1-M2	78.3(4)
M2-M2	2.889(2)	Oap-M1-Oap	180.0(1)	Oap-M2-Oap	180.0(1)	M1-O2-M'1	106.2(4)
M1-O1 (x4)	2.044(2)	Oap-M1-Oeq	90.3(2)	Oap-M2-Oeq	90.1(5)	M1-O2-M2	131.8(4)
M1-O2 (x2)	1.778(5)					M2-O1-M'2	123.3(7)
Mean M1-O	1.911					M2-O2-M'2	91.2(9)
M2-O1 (x2)	1.872(2)						
M2-O2 (x4)	2.020(2)						
Mean M2-O	1.946						

$Cr_{0,152(9)}V_{0,847(1)}O_2$		M= Cr, V					
	Distances (Å)			Angles (°)			
M1-M1	2.891(1)	Oe1-M1-Oe1	83.9(1)	Oe1-M2-Oe1	86.3(1)	M1-O1-M'1	91.2(0)
M1-M2	3.479(1)	Oe1-M1-Oe2	96.0(8)	Oe1-M2-Oe2	93.6(8)	M1-O1-M2	131.9(3)
M2-M2	2.891(1)	Oap-M1-Oap	180.0(1)	Oap-M2-Oap	180.0(1)	M1-O2-M'1	110.2(4)
M1-O1 (x4)	2.023(2)	Oap-M1-Oeq	90.2(2)	Oap-M2-Oeq	90.0(5)	M1-O2-M2	131.9(3)
M1-O2 (x2)	1.850(2)					M2-O1-M'2	95.9(7)
Mean M1-O	1.936					M2-O2-M'2	95.9(7)
M2-O1 (x2)	1.911(1)						
M2-O2 (x4)	1.945(5)						
Mean M2-O	1.928						

$Cr_{0,336(7)}V_{0,673(3)}O_2$		M= Cr, V					
	Distances (Å)			Angles (°)			
M1-M1	2.891(1)	Oe1-M1-Oe1	88.0(3)	Oe1-M2-Oe1	81.9(4)	M1-O1-M'1	98.5(3)
M1-M2	3.479(2)	Oe1-M1-Oe2	91.9(6)	Oe1-M2-Oe2	98.0(5)	M1-O1-M2	130.3(1)
M2-M2	2.891(1)	Oap-M1-Oap	180.0(1)	Oap-M2-Oap	180.0(1)	M1-O2-M'1	112.8(9)
M1-O1 (x4)	1.908(2)	Oap-M1-Oeq	90.4(2)	Oap-M2-Oeq	90.1(7)	M1-O2-M2	130.8(3)
M1-O2 (x2)	1.906(1)					M2-O1-M'2	98.0(5)
Mean M1-O	1.907					M2-O2-M'2	98.0(5)
M2-O1 (x2)	2.044(1)						
M2-O2 (x4)	1.914(5)						
Mean M2-O	1.979						

$Cr_{0,419(9)}V_{0,580(1)}O_2$		M= Cr, V					
	Distances (Å)			Angles (°)			
M1-M1	2.888(4)	Oe1-M1-Oe1	85.5(4)	Oe1-M2-Oe1	83.7(5)	M1-O1-M'1	97.6(4)
M1-M2	3.476(0)	Oe1-M1-Oe2	94.4(5)	Oe1-M2-Oe2	96.2(5)	M1-O1-M2	130.0(5)
M2-M2	2.888(4)	Oap-M1-Oap	180.0(1)	Oap-M2-Oap	180.0(1)	M1-O2-M'1	112.5(4)
M1-O1 (x4)	1.918(8)	Oap-M1-Oeq	90.4(8)	Oap-M2-Oeq	90.1(2)	M1-O2-M2	131.8(5)
M1-O2 (x2)	1.886(4)					M2-O1-M'2	97.9(8)
Mean M1-O	1.902					M2-O2-M'2	96.2(4)
M2-O1 (x2)	2.010(4)						
M2-O2 (x4)	1.939(6)						
Mean M2-O	1.975						

Tab. 5(continued) Metal-metal, metal oxygen distances (Å) and metal-oxygen-metal angles (°) for each composition under exam (second part).

$Cr_{0,499(4)}V_{0,500(6)}O_2$	M= Cr, V				
	Distances (Å)	Angles (°)			
M1-M1	2.886(4)	Oe1-M1-Oe1	89.5(1)	M1-O1-M'1	131.5(6)
M1-O1 (x4)	1.937(2)	Oe1-M1-Oe2	90.4(8)		
M1-O1 (x2)	1.929(8)	Oap-M1-Oap	180.0(1)		
Mean M-O	1.933	Oap-M1-Oeq	90.4(8)		

$Cr_{0,598(5)}V_{0,401(5)}O_2$	M= Cr, V				
	Distances (Å)	Angles (°)			
M1-M1	2.889(7)	Oe1-M1-Oe1	97.5(5)	M1-O1-M'1	131.1(5)
M1-O1 (x4)	1.920(9)	Oe1-M1-Oe2	82.4(4)		
M1-O1 (x2)	1.942(8)	Oap-M1-Oap	180.0(1)		
Mean M-O	1.931	Oap-M1-Oeq	89.8(6)		

$Cr_{0,657(1)}V_{0,342(9)}O_2$	M= Cr, V				
	Distances (Å)	Angles (°)			
M1-M1	2.887(3)	Oe1-M1-Oe1	89.9(8)	M1-O1-M'1	132.1(2)
M1-O1 (x4)	1.947(4)	Oe1-M1-Oe2	89.9(8)		
M1-O1 (x2)	1.880(9)	Oap-M1-Oap	180.0(1)		
Mean M-O	1.914	Oap-M1-Oeq	90.0(1)		

$Cr_{0,666(9)}V_{0,333(1)}O_2$	M= Cr, V				
	Distances (Å)	Angles (°)			
M1-M1	2.893(1)	Oe1-M1-Oe1	100.2(3)	M1-O1-M1	129.8(8)
M1-O1 (x4)	1.885(4)	Oe1-M1-Oe2	79.7(6)		
M1-O1 (x2)	1.955(4)	Oap-M1-Oap	180.0(1)		
Mean M-O	1.920	Oap-M1-Oeq	89.8(3)		

$Cr_{0,873(1)}V_{0,126(9)}O_2$	M= Cr, V				
	Distances (Å)	Angles (°)			
M1-M1	2.904(8)	Oe1-M1-Oe1	99.6(1)	M1-O1-M1	130.1(9)
M1-O1 (x4)	1.901(4)	Oe1-M1-Oe2	80.3(9)		
M1-O1 (x2)	1.915(8)	Oap-M1-Oap	180.0(1)		
Mean M-O	1.908	Oap-M1-Oeq	89.9(2)		

	beta CrO2		
	Distances (Å)	Angles (°)	
Cr-Cr	2.91(8)	Cr-O1-Cr	130.4(6)
Cr-O (x4)	1.91(8)		
Cr-O (x2)	1.88(3)		
Mean Cr-O	1.900		

3.4.2d Measurement of the $(101)_{M3}$ peak at low and high temperature

In order to investigate the eventual existence of temperature dependent structural phase transitions, such as in VO_2 itself, thermodiffraction measurements have been carried out for $Cr_{0,499(4)}V_{0,500(6)}O_2$ (Pnnm nº58, β-CrO_2 structure) and $Cr_{0,419(9)}V_{0,6580(1)}O_2$ (P 2/m nº10, (M3) VO_2 structure) from 13 K to room temperature and form room temperature to 423 K. These measurements did not reveal any temperature dependent phase transition; on the other hand a shift to lower value of 2θ (a higher value in d-spacing) increasing the temperature is observed from 13 K up to 423 K; The plots reported in fig. 21; it show the measurement of the $(101)_{M3}$ peak for $Cr_{0,419(9)}V_{0,6580(1)}O_2$ at low and at high temperature; Both measurements have Cu K_α 1 and K_α 2 wavelenght contributions due to setting of measurement device, this is more evident in low temperature measurement.

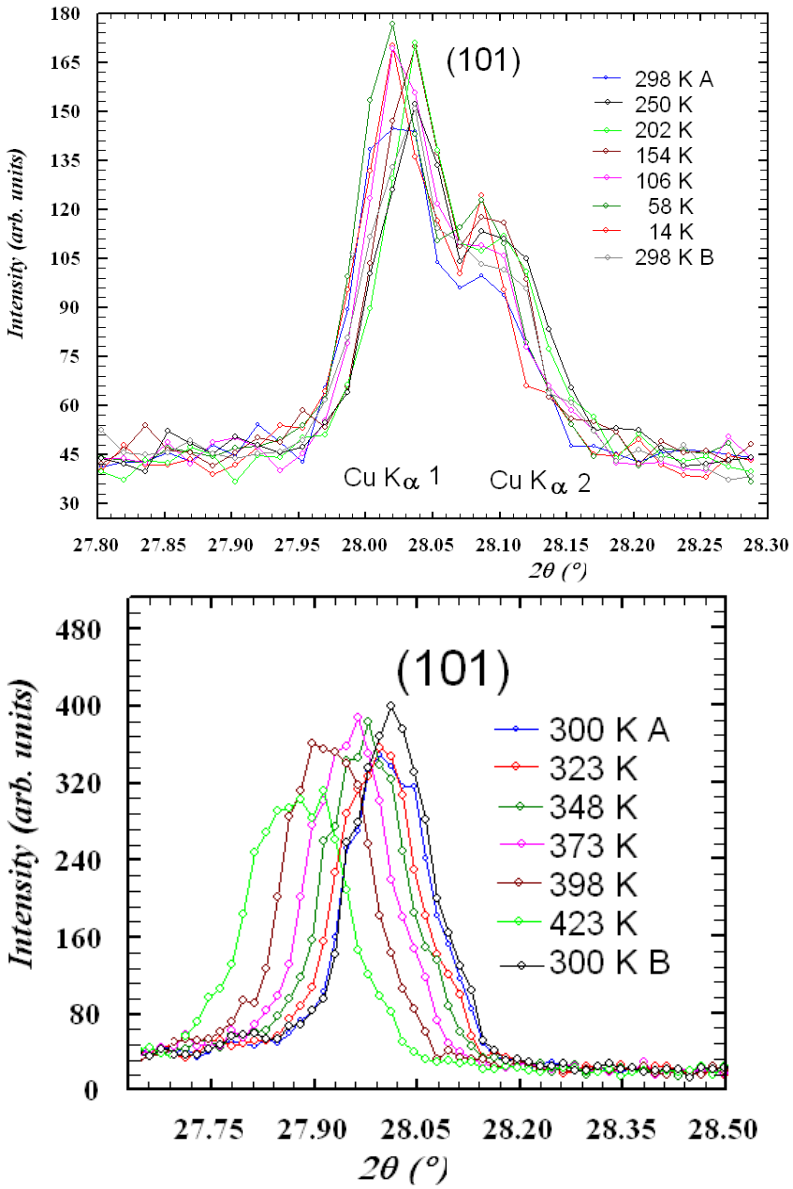

Fig. 21 Thermodiffraction experiments of $Cr_{0,419(9)}V_{0,6580(1)}O_2$, for direction (101) at high (up) and low temperature (down); Cu K_α 1 and K_α 2 wavelenght contributions are present in the measurements; shift to lower value of 2θ (a higher value in d-spacing) is observed increasing the temperature.

this contribution behaviour is more evident in high temperature thermodiffraction measurement than in low temperature; the magnitude of the shift is small and is related to the thermal expansion/contraction effect. The variation of the corresponding d-spacing for the $(101)_{M3}$ peak it has measured and plotted as a function of temperature as shown in fig. 22. Moving to higher temperature than ambient condition a small linear increasing of d-spacing is observed in the sample, according to the thermal expansion.

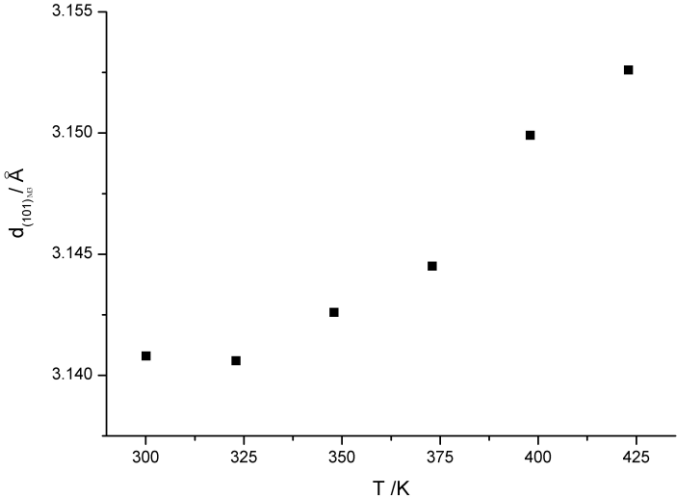

Fig. 22 Plot representing the change of value of $d_{(101)\ M3}$ as function of temperature, it is visible the linear evolution of d-spacing due to the thermal expansion.

3.4.2e Electron diffraction

Electron diffraction experiments have been performed for the composition $Cr_{0,499(4)}V_{0,500(6)}O_2$; Several crystals have been analyzed; after confirming the composition by EDAX, the observed SAED patterns show orthorhombic symmetry. The corresponding d spacings agree with data obtained from Rietveld refinement of x-ray diffraction.

Figures 23 a) b) and 24 show the SAED pattern corresponding, respectively, to the [001], [110] and [-113] zone axis of $Cr_{0,499(4)}V_{0,500(6)}O_2$ unit cell a = 4.568(7), b = 2.886(2) and c = 4.532(8) orthorhombic S.G. Pnnm (nº58).

It is worth to note that in the [-113] zone axis, bands like sharp reflections transversal and crossed dark bands can be observed. These “lines”, identified as structured diffuse scattering, have been observed and identified in previous works in the literature: for example oxyfluoride like Elpasoite $K_3MoO_3F_3$,[58] NbO_2F,[59] (both of them members of the perovskite family) and FeOF [60,61] another rutile type structure.

These strong (virtually continuous) lines of polarized diffuse intensity are clearly visible running approximately along the $g_{(110)}$ and $g_{(-110)}$ directions in reciprocal space. The transverse polarized character of the diffuse streaking (i.e., the fact that the intensity of the

diffuse streaking is always strongest when looking out along directions of reciprocal space perpendicular to the direction of streaking itself) implies that the associated atomic shifts must also be largely transverse polarized; i.e., the atomic shifts giving rise to the diffuse streaking along $g_{(-110)}$ direction in the reciprocal space must be largely due to the atomic shifts along and $g_{(1-10)}$ and vice versa.[61]

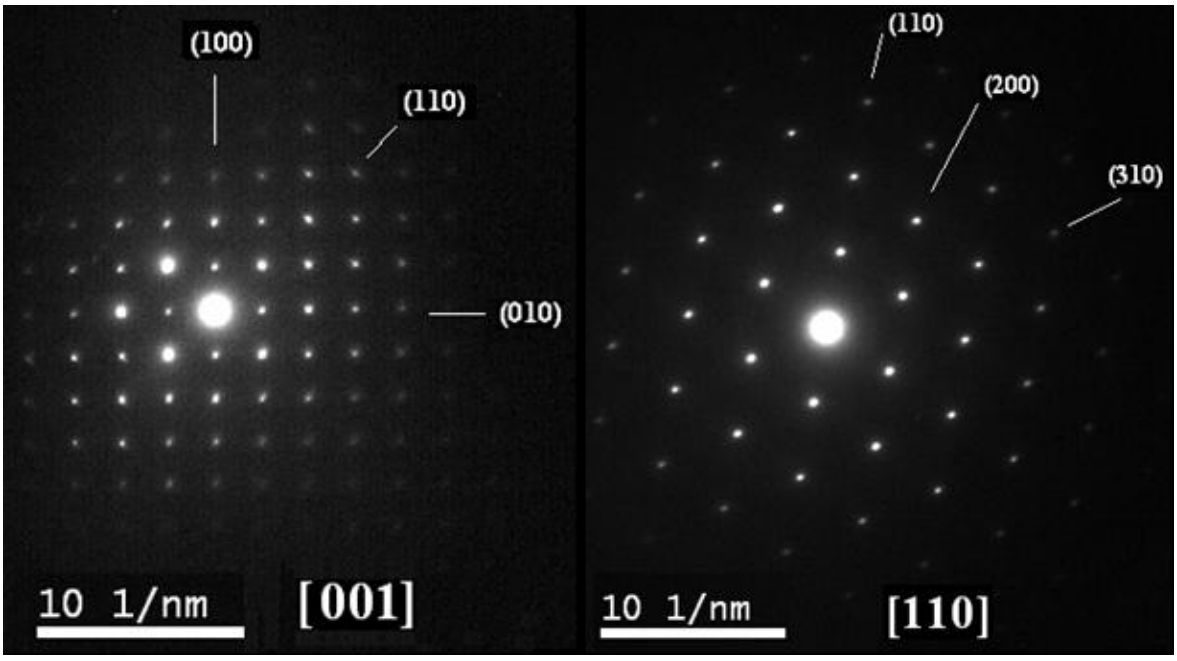

Fig.23 a) (up) Selected area electron diffraction patterns for [001] zone axis for $Cr_{0,499(4)}V_{0,500(6)}O_2$; and fig. 23 b) (down) for [110]; Characteristic extinction condition can be easily obscured at more major zone axis orientations.

The final important feature to notice about fig. 24 is that there is clearly an extinction condition operating in that the diffuse streaking run through all parent rutile reflections, ($h + k + l$) odd, diffuse streaks run through the (110) reflection but not through the neighboring reflections. This characteristic extinction condition can be easily obscured at more major zone axis orientations such as [001] itself or [110] as can be observed in fig. 23 a), b). This essentially body centered extinction condition is absolutely characteristic of the diffuse streaking and strongly suggests that atomic displacements of the Cr and V atoms must be largely responsible. The relationship between diffuse streaking and atomic displacement has been evidenced in literature by Whiters et. Al and Vlasse *et al.*.[58-61] In our case evidence supporting that the diffuse streacking is due to a substantial atomic displacement, is supported by the high values of the refined B_{iso} in many of the refined phases (see tab. 4). The nature of this displacement can be attribuited due to some kind of short range order between Cr-V in to the structure; however this short range order does not form any modulation, because no satellite reflection have been observed in SAED patterns, contrary to what happens, for example, in the case of FeOF.[61]

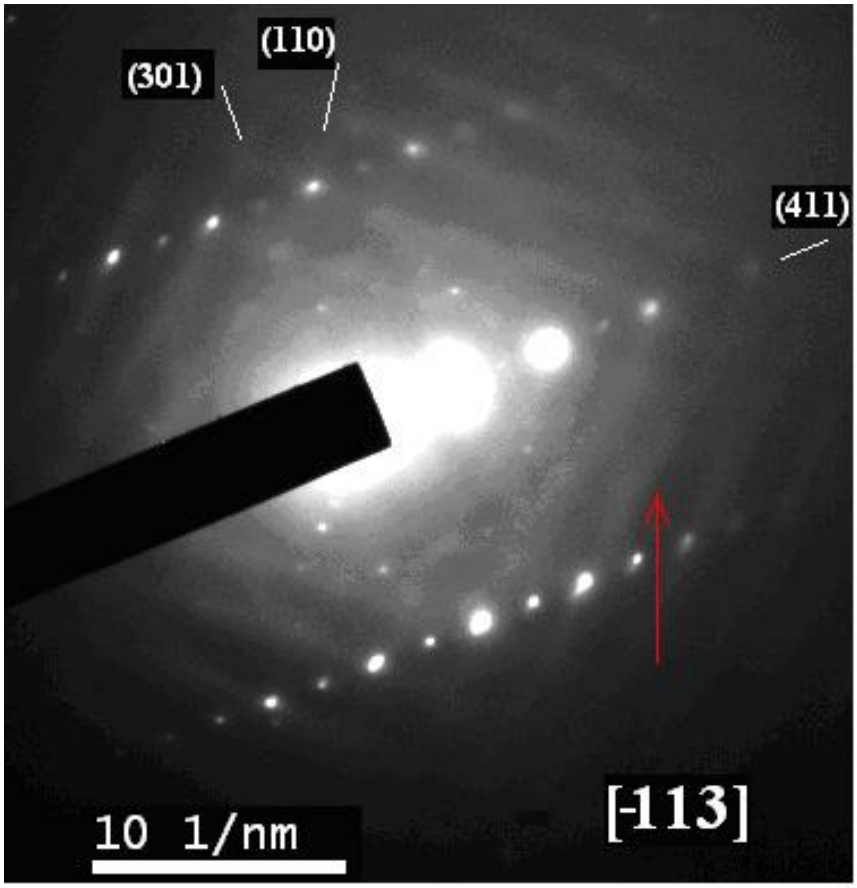

Fig. 24 Selected area electron diffraction patterns for [-113] zone axis for $Cr_{0,499(4)}V_{0,500(6)}O_2$; diffuse streaking has been related with transverse polarized character due to an low range order between Cr and V cations.

3.4.3 Magnetic measurements

3.4.3.1 Magnetic susceptibility measurements

The magnetic characterization of the $Cr_{1-x}V_xO_2$ samples have been carried out in the compositional range between $Cr_{0,098(1)}V_{0,901(9)}O_2$ and $Cr_{0,666(9)}V_{0,333(1)}O_2$. As it has pointed out in the structural characterization section, it is important to stress that some residual amounts of Cr_2O_3 (T_N = 307 K)[62] have been detected in the x-ray diffraction profiles in $Cr_{065(7)}V_{342(9)}O_2$ and in compositions with higher Cr content. Fig. 25 represents the temperature dependence of the magnetic susceptibility from 50 K to 2 K at 1000 Oe. Upon cooling below 160 K, the susceptibility deviates increasingly from the Curie-Weiss behaviour. Then the susceptibility shows a sharp increase followed by the onset of a net maximum at 23 K for the $Cr_{065(7)}V_{342(9)}O_2$ oxide. It can be seen, on fig. 27, that both ZFC and FC branches start to diverge at this temperature, which is a clear indication of presence of weak ferromagnetic correlations (WFM). Interestingly, there already exist a clear evolution of the transition temperature with the Cr-content. The Curie temperature of CrO_2 usually reported to lie in the range 392 K,[63] further decrease to only 23 K by the insertion of 30% of vanadium in the parent oxide. A progressive vanadium doping leads to an expected decreasing of the magnetic correlations and concomitantly to this, the Curie temperature vanishes to 4 K for the $Cr_{0,098(1)}V_{0,901(9)}O_2$ oxide and finally ends in a paramagnetic behaviour for VO_2. All ZFC/FC measurement for all compositions are reported in appendix.

Table 6 summarize the temperature evolution of the Curie temperature for the studied samples. Figure 26 shows the temperature dependence of the reciprocal susceptibility for all the samples. In these plots only zero field cooling (ZFC) measurements are shown for a better visualization.

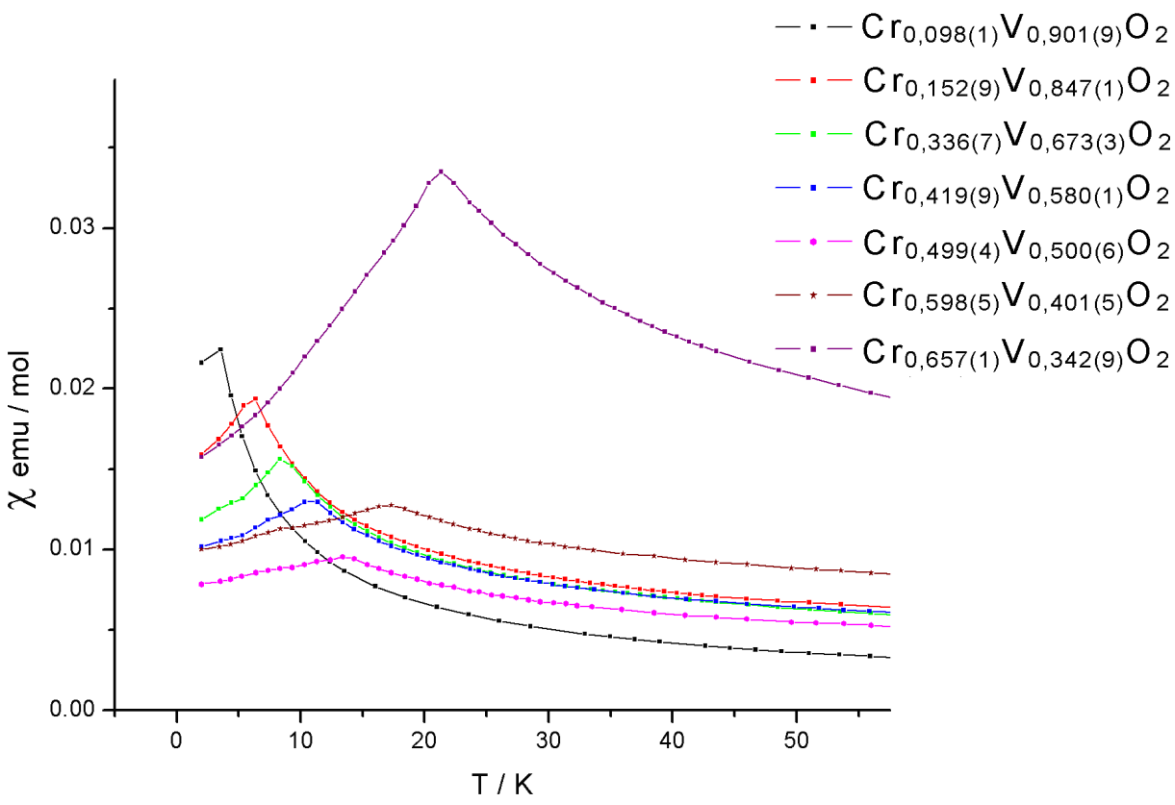

Fig. 25 The magnetic susceptibility plot for all measured members of solid solution.

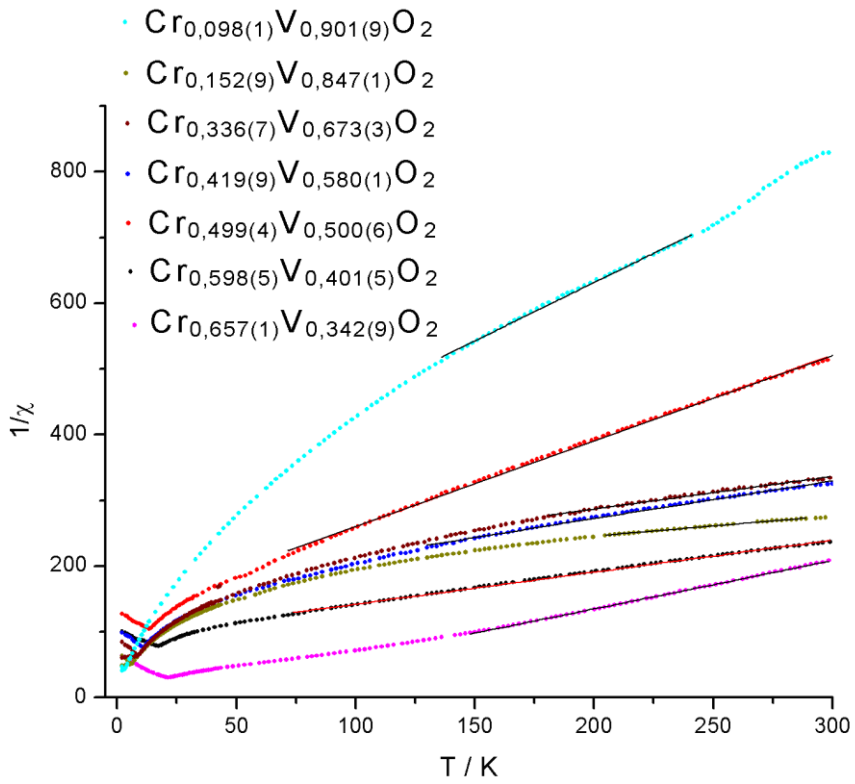

Fig. 26 The inverse of the magnetic susceptibility plot for all measured members of solid solution.

The fitted parameters of the1/χ of curves versus temperature in fig. 26 have been made by the Curie-Weiss law: $1 / \chi = C / (T - \theta)$ (where C is the Curie constant and θ is the Weiss temperature);

The θ values reported in tab. 6 are negative from $Cr_{0,598(5)}V_{0,401(5)}O_2$ to $Cr_{0,098(1)}V_{0,901(9)}O_2$ indicating a WFM (or canted AFM) phase below the transition temperature; however in the case of $Cr_{0,657(1)}V_{0,342(9)}O_2$ the θ value is positive indicating a possible ferrimagnetic phase likely to be due to a high amount of Cr^{4+}.

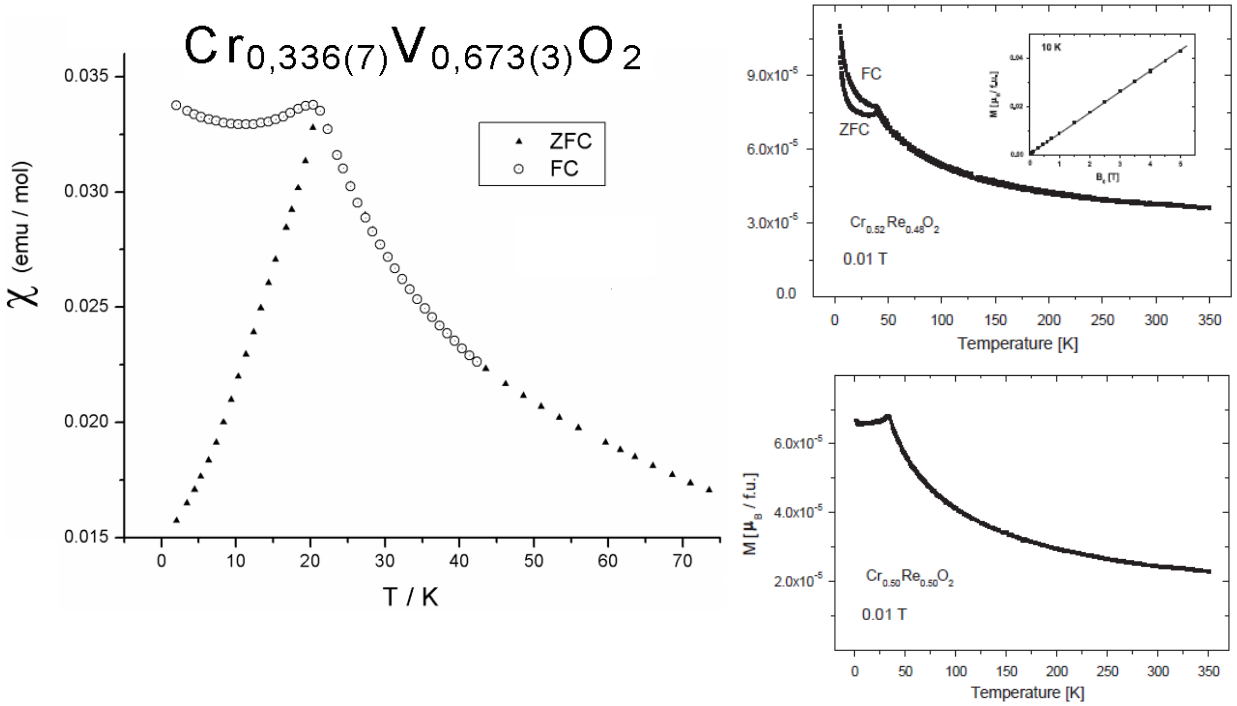

Fig. 27 ZFC/FC measurement for $Cr_{0,657(1)}V_{0,342(9)}O_2$ (left) compared with members of $Cr_{1-x}Re_xO_2$ solid solution (Mikhailova et al.); All three samples have rutile-like structure and similar AFM behaviour.

Observing ZFC / FC measurement of all our samples the behaviour observed is similar to $Cr_{0,657(1)}V_{0,342(9)}O_2$ providing further evidence for an AFM low temperature phase; moreover different systems like $Cr_{1-x}Re_xO_2$[54-56] solid solution with rutile-like structure showed similar magnetic behaviour and have been identified as AFM at low temperature. Mikhailova et al.,[55] calculated the effective paramagnetic moments, $\mu_{eff(cal)}$, for $Cr_xRe_{1-x}O_2$ based on the simple ionic model with Cr^{+3} and Re ions in oxidation states between +6 and +4; by taking just the spin-only contribution from Cr^{3+} into account:

μ_{eff} (cal) = g √ (S(S+1) x) where g = 2, S = 3/2 and x is the Cr content in the compound.[55]

The measured paramagnetic moments for $Cr_xRe_{1-x}O_2$ was much smaller than the calculated effective ones, indicating an electronic configuration, different from the above described model. This was in contrast to $Cr_xMo_{1-x}O_2$, where a good agreement between $\mu_{eff(exp)}$ and $\mu_{eff(cal)}$, was observed for this simple approximation.[51] A partial transfer of electrons could be proposed to explain the lower magnetic moments: $Cr^{+3} + Re^{+6} \rightarrow Cr^{+4} + Re^{+5}$ and

$Cr^{+3} + Re^{+5} \rightarrow Cr^{+4} + Re^{+4}$. However, an intermediate state with a delocalization of some electrons is more probable and should be reflected in the electronic structure.[55]

As shown in tab. 6 and fig. 28, $Cr_{0,657(1)}V_{0,342(9)}O_2$ shows a T_N at 21.34 K, increasing the V content, the T_N value shift to lower temperature but still an AFM phase at low temperature is observed. In opposite to this is the behaviour of VO_2: in vanadium dioxide a discontinuity around 341 K has been observed: a jump to lower susceptibility keeping a paramagnetic phase.[32,39] The behaviour observed in fig. 28 and the difference between $Cr_{0,879(1)}V_{0,126(9)}O_2$ and VO_2 can be attributed to the presence of Cr^{3+} in the structure of the former.

Tab.6 The parameter of linear fitting using Curie-Weiss law, Curie and Weiss constants, magnetic moment μ, T_N and χ (T_N).

$Cr_{1-x}V_xO_2$	1 / C	−θ / C	C	μ	θ	T n / K	χ (Tn)
VO_2	VO_2	Paramag. -> Paramag.				T 341	
$Cr_{0,098(1)}V_{0,901(9)}O_2$	1.65909	301.7006	0.60274	2.19589	-181.847	3.55	0.022
$Cr_{0,152(9)}V_{0,847(1)}O_2$	0.32206	180.6757	3.10501	4.98398	-561.0001	6.36	0.019
$Cr_{0,336(7)}V_{0,673(3)}O_2$	0.48095	191.662	2.07922	4.07845	-398.5071	8.34	0.015
$Cr_{0,419(9)}V_{0,580(1)}O_2$	0.50519	175.265	1.97945	3.9794	-346.9289	10.85	0.012
$Cr_{0,499(4)}V_{0,500(6)}O_2$	1.26543	139.2714	0.79025	2.51435	-110.0586	13.4	0.0095
$Cr_{0,598(5)}V_{0,401(5)}O_2$	0.49329	92.64776	2.02721	4.02711	-187.816	17.3	0.0127
$Cr_{0,657(1)}V_{0,342(9)}O_2$	0.74617	-14.1203	1.34018	3.27436	18.9237	21.34	0.033
α-CrO_2	α-CrO_2	Paramag. -> Ferromag.				T_c 392	

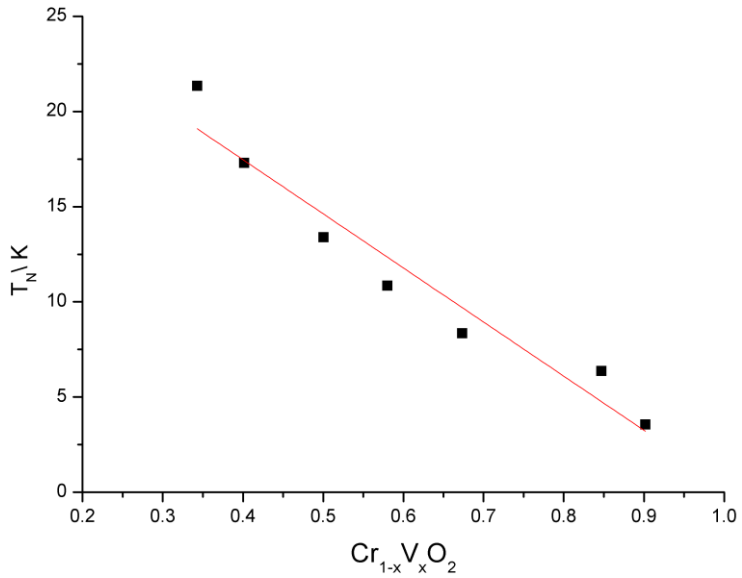

Fig. 28 Plot of composition as function of transition temperature for measured samlples; the transition temperature T_N decrease linearly increasing V content.

In an ideal solid solution between CrO_2 (IV) a d^2 and VO_2 (IV) a d^1, substitution of V with Cr (or V with Cr) is obviously expected to change the electronic properties, but under the present high pressure and temperature conditions, the oxidation state can indeed change as well. In order to establish the oxidation states of V and Cr and theirs relative amounts,

effective magnetic moments (μ_{eff}) have been calculated and compared with the experimental ones; the results shown in tab. 7 and also plotted in fig.29; The calculation of the oxidation states have been carried out starting from two fundamental considerations:

1) The structure of the phase is rutile or rutile-like as defined in the crystallographic characterization with a stoichiometry of $M_{1-x}M'_xO_2$.

2) The possible oxidation states were depending of reactants and reaction conditions, Cr (III) and (IV) and V (III), (IV) and (V).

Fig.29 Experimental (Exp) and calculated (calc1, calc2 and calc V^{4+}, Cr^{4+}) vs. point of the solid solution.

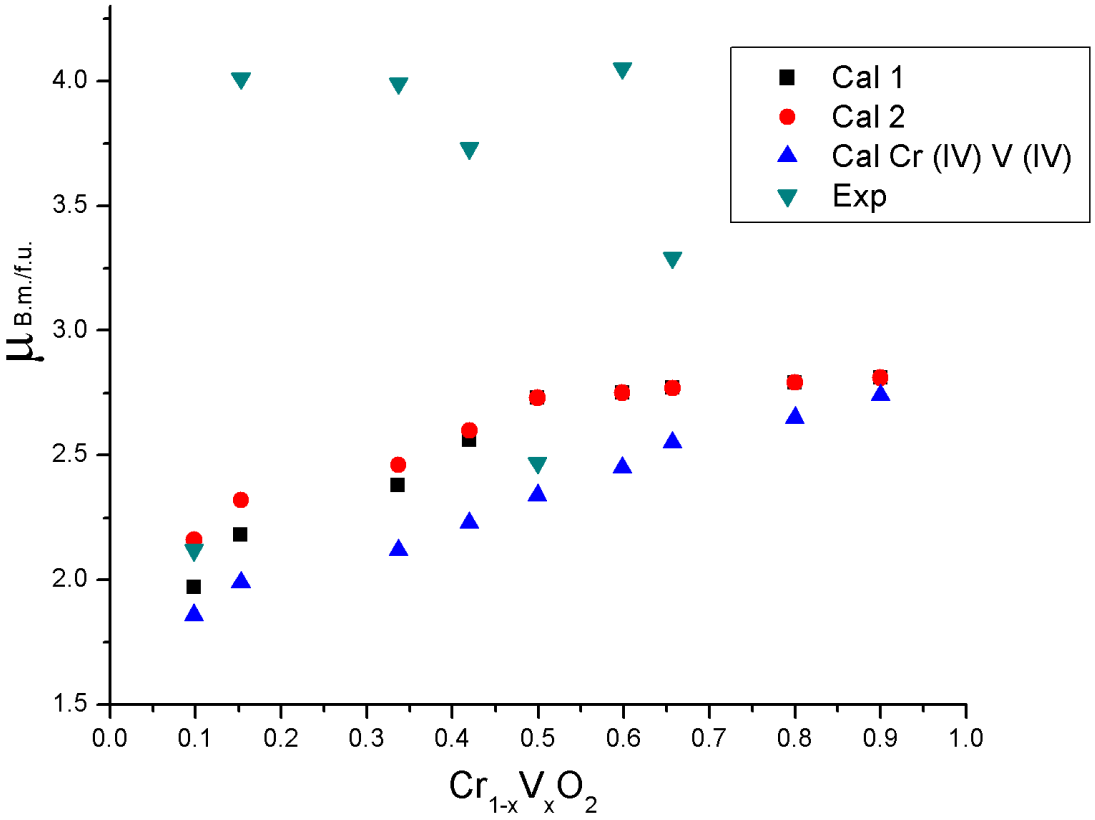

Tab. 7 Results of different calculation of magnetic moment (μ) based on composition and oxidation states taking in to account different mixed valences composition and compared with experimental magnetic moment.

oxid. state 3+	4+	5+	Composition (nominal)	Mixed valences	Composition (measured)
0.3	0.4	0.5	$Cr_{0,9}V_{0,1}O_2$	$0.1V5^+ + 0.1\ Cr3^+ + 0.8Cr4^+$	$Cr_{0,873(1)}V_{0,126(9)}O_2$
0.6	0.8	1	$Cr_{0,8}V_{0,2}O_2$	$0.2V5^+ + 0.2\ Cr3^+ + 0.6Cr4^+$	$Cr_{0,666(9)}V_{0,333(1)}O_2$
0.9	1.2	1.5	$Cr_{0,7}V_{0,3}O_2$	$0.3V5^+ + 0.3\ Cr3^+ + 0.4Cr4^+$	$Cr_{0,657(1)}V_{0,342(9)}O_2$
1.2	1.6	2	$Cr_{0,6}V_{0,4}O_2$	$0.4V5^+ + 0.4\ Cr3^+ + 0.2Cr4^+$	$Cr_{0,598(5)}V_{0,401(5)}O_2$
1.5	2	2.5	$Cr_{0,5}V_{0,5}O_2$	$0.5V5^+ + 0.5\ Cr3^+$	$Cr_{0,499(4)}V_{0,500(6)}O_2$
1.8	2.4	3	$Cr_{0,4}V_{0,6}O_2$	$0.4V5^+ + 0.2V4^+ + 0.4Cr3^+$ or $0.5V5^+ + 0.1V3^+ + 0.4Cr3^+$	$Cr_{0,419(9)}V_{0,580(1)}O_2$
2.1	2.8	3.5	$Cr_{0,3}V_{0,7}O_2$	$0.3V5^+ + 0.4V4^+ + 0.3Cr3^+$ or $0.5V5^+ + 0.2V3^+ + 0.3Cr3^+$	$Cr_{0,336(7)}V_{0,673(3)}O_2$
2.4	3.2	4	$Cr_{0,2}V_{0,8}O_2$	$0.2V5^+ + 0.6V4^+ + 0.2Cr3^+$ or $0.5V5^+ + 0.3V3^+ + 0.2Cr3^+$	$Cr_{0,152(9)}V_{0,847(1)}O_2$
2.7	3.6	4.5	$Cr_{0,1}V_{0,9}O_2$	$0.1V5^+ + 0.8V4^+ + 0.1Cr3^+$ or $0.5V5^+ + 0.4V3^+ + 0.1Cr3^+$	$Cr_{0,098(1)}V_{0,901(9)}O_2$
				Calculation 1 Calculation 2	

Composition (measured)	μ cal 1	μ cal 2	μ cal Cr(IV) V(IV)	μ exp
$Cr_{0,873(1)}V_{0,126(9)}O_2$	2.81		2.74	-
$Cr_{0,666(9)}V_{0,333(1)}O_2$	2.79		2.65	-
$Cr_{0,657(1)}V_{0,342(9)}O_2$	2.77		2.55	3.29
$Cr_{0,598(5)}V_{0,401(5)}O_2$	2.75		2.45	4.05
$Cr_{0,499(4)}V_{0,500(6)}O_2$	2.73		2.34	2.47
$Cr_{0,419(9)}V_{0,580(1)}O_2$	2.56	2.6	2.23	3.73
$Cr_{0,336(7)}V_{0,673(3)}O_2$	2.38	2.46	2.12	3.99
$Cr_{0,152(9)}V_{0,847(1)}O_2$	2.18	2.32	1.99	4.01
$Cr_{0,098(1)}V_{0,901(9)}O_2$	1.97	2.16	1.86	2.12

The comparison between experimental and calculated values provided a good matching only in the case of $Cr_{0.499(5)}V_{0.500(6)}O_2$; The case of $Cr_{0.098(1)}V_{0.901(9)}O_2$ provided a calculated value near to the experimental one, however the fitted region could not reside in the paramagnetic region due to a magnetic transition observed at temperature higher than 250 K. The calculated magnetic moment of other members of solid solution differ very much from experimental values, if observed in detail the fitted regions are not linear, they have a wide curvature angle, this imply that the fitted regions are not in the paramagnetic region. CrO_2 is an half-metal ferromagnet and VO_2 undergo to an insulator-metal transition decreasing the temperature; when composition of members of solid solution is far from the composition $Cr_{0.5}V_{0.5}O_2$, the metallic (and half-metal) contribution of VO_2 and CrO_2 respectively can influence the magnetic susceptibility measurement increasing the value of susceptibility.

To confirm this, resistivity vs. temperature measurements of these samples are needed. Future electrical measurements could represent a possible solution for this problem and are planned as a future work in this system.

3.4.3.2 Magnetization measurements

Measurements of magnetization (M) vs. applied field (H) from $Cr_{0,098(1)}V_{0,901(9)}O_2$ to $Cr_{0,598(5)}V_{0,401(5)}O_2$ have been performed at 5 K; as reported in fig.30 the coercive field is dependent of Cr (or V) content in the structure; The hysteresis curves in fig 30 shown very low coercive field at higher value of vanadium substitution, in agreement with the WFM (or AFM) magnetic order; however a small coercive field it has been observed increasing the Cr content, this could be explained as an increase of M-O-M interaction in the oxide.

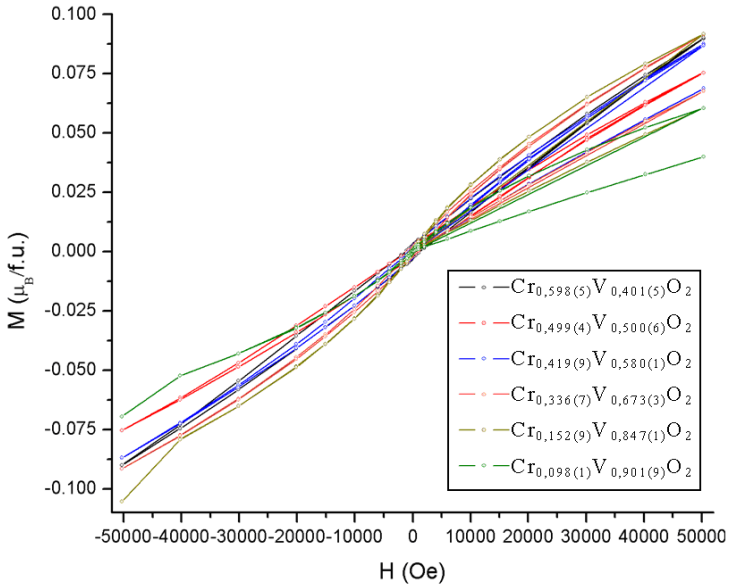

Fig. 30 The hysteresis measurement at 5 K, as a function of composition, for samples suitable for magnetic measurement (up);

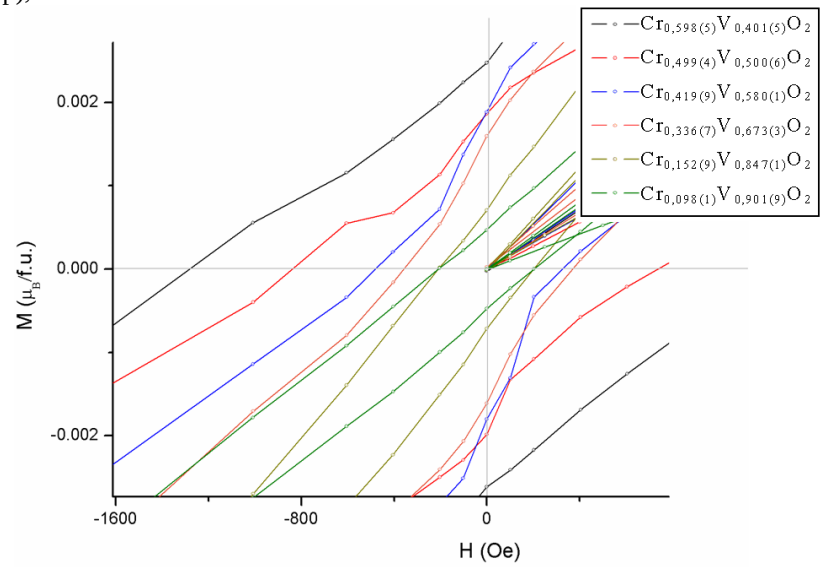

Fig 31 The zoomed part of the plot in fig.30, it shows the increment of coercive field as a function of the amount of Cr^{4+} in to the structure (down).

3.5 Conclusions

Several members of the solid solution of $Cr_{1-x}V_xO_2$ with $0,126(9) \leq x \leq 0,901(9)$ have been explored, synthesized under high temperature / high pressure conditions; a structural change as function of composition have been observed when $0.499(4) \leq x \leq 0.500(6)$; from structural characterization and compositional measurement the maximum content of Cr is expected to be in the region of solid solution $x < 0,342(9)$.

Powder samples data refinements shown a rutile-like structures that can vary as function of V content from $CaCl_2$ rutile like to VO_2 (M3) structure. Moreover the presence of V in CrO_2 "induce a pressure effect" allowing the structural transition from rutile to $CaCl_2$ structure at 40 Kbar. In pure CrO_2 this transition take place at a pressure of 120 Kbar at room temperature.

Electron diffraction experiments revealed a diffuse polarize streaks that could be related with a short range order V/Cr in the structure at composition $Cr_{0.499(4)}V_{0.500(6)}O_2$; more work is to be due to establish the type of short range order responsible for this diffuse scattering.

The magnetic properties of the different samples of solid solution have been determined and showed a transition from paramagnetic (PM) to antiferromagnetic (AFM) in lowering the temperature. Independently the type of structure they have, $CaCl_2$ or VO_2 (M3), all samples have an AFM magnetic order. The transition temperature T_N is linearly dependent form Cr (or V) content in the structure and the trend has been explained by the presence of increasing amounts of Cr^{3+} in the structure.

Comparison between measured and calculated magnetic moment have been realized in order to establish the valence states; only in the case of $Cr_{0.499(5)}V_{0.500(6)}O_2$ agreement is observed between calculated and experimental values of magnetic moments; the mismatching in the other members of solid solutions is probably due to that fitted region is not in a real linear trend that means the sample is not in a paramagnetic state at measured temperatures, moreover V doping can decrease the T_{M-I} transition of $Cr_{1-x}V_xO_2$, the analyzed samples became metallic justifying the high value of Curie constant observed.

3.6 Bibliography

1. Schwarz, K., *CrO_2 predicted as a half-metallic ferromagnet.* Journal of Physics F: Metal Physics, 1986. 16(9): p. L211.
2. Ji, Y., et al., *Determination of the Spin Polarization of Half-Metallic CrO_2 by Point Contact Andreev Reflection.* Physical Review Letters, 2001. 86(24): p. 5585-5588.
3. Allwardt, J.R., et al., *Effect of structural transitions on properties of high-pressure silicate melts: ^{27}Al NMR, glass densities, and melt viscosities.* American Mineralogist, 2007. 92(7): p. 1093-1104.
4. Li, X.W., et al., *Magnetoresistance and Hall effect of chromium dioxide epitaxial thin films.* J. Appl. Phys., 1999. 85: p. 5585-5587.
5. Ivanov, P.G., S.M. Watts, and D.M. Lind, *Epitaxial growth of CrO_2 thin films by chemical-vapor deposition from a Cr_8O_{21} precursor.* Journal of Applied Physics, 2001. 89(2): p. 1035-1040.
6. Dowben, P.A., et al., *Fabrication of ferromagnetic and antiferromagnetic chromium oxides by organometallic chemical vapor deposition.* Journal of Applied Physics, 1990. 67(9): p. 5658-5660.
7. Chamberland, B.L., *The chemical and physical properties of CrO_2 and tetravalent chromium oxide derivatives.* Critical Reviews in Solid State and Materials Sciences, 1977. 7(1): p. 1-31.
8. Goodenough, J.B., *Metallic oxides.* Progress in Solid State Chemistry, 1971. 5(0): p. 145-399.
9. Sorantin, P.I. and K. Schwarz, *Chemical bonding in rutile-type compounds.* Inorganic Chemistry, 1992. 31(4): p. 567-576.
10. Maddox, B.R., et al., *High-pressure structure of half-metallic CrO_2.* Phys. Rev. B, 2006. 73: p. 144111.
11. Haines, J., J.M. Leger, and S. Hoyau, *Second-order rutile-type to $CaCl_2$-type phase transition in β-MnO_2 at high pressure.* Journal of Physics and Chemistry of Solids, 1995. 56(7): p. 965-973.
12. Franco, M.A.A. and K.S.W. Sing, *The interconversion of orthorhombic chromium oxy-hydroxide and chromium dioxide.* Journal of thermal analysis, 1972. 4(2): p. 47-52.
13. Kubota, B., *Decomposition of Higher Oxides of Chromium Under Various Pressures of Oxygen.* Journal of the American Ceramic Society, 1961. 44(5): p. 239-248.

14. Ikemoto, I., et al., *X-ray photoelectron spectroscopic studies of CrO_2 and some related chromium compounds.* Journal of Solid State Chemistry, 1976. 17(4): p. 425-430.
15. Shibasaki, Y., et al., *Synthesis of CrO_2 by oxidation of $Cr(OH)_3$.* Materials Research Bulletin, 1970. 5(12): p. 1051-1058.
16. Salinas, A., R.S. Puche, and M.A. Alario-Franco, *Thermal decomposition and reduction of CrO_2 to CrOOH.* Thermochimica Acta, 1984. 74(1-3): p. 273-279.
17. Alario Franco, M.A., J.M. Thomas, and R.D. Shannon, *Crystallographic share strucutres derived from CrO_2: An electron microscopic study.* J. Solid State Chem., 1974. 9: p. 261.
18. Barry, A., Ph. D. Thesis, University of Dublin, 1999.
19. Blundell, S., *Magnetism in condensed matter.* 2001.
20. Watts, S.M., et al., *Evidence for two-band magnetotransport in half-metallic chromium dioxide.* Physical Review B, 2000. 61(14): p. 9621-9628.
21. McWhan, D.B., et al., *X-ray diffraction study of metallic VO_2.* Physical Review B, 1974. 10(2): p. 490-495.
22. Morin, F.J., *Oxides Which Show a Metal-to-Insulator Transition at the Neel Temperature.* Physical Review Letters, 1959. 3(1): p. 34-36.
23. Marezio, M., et al., *Structural Aspects of the Metal-Insulator Transitions in Cr-Doped VO_2.* Physical Review B, 1972. 5(7): p. 2541-2551.
24. Pouget, J.P., et al., *Electron Localization Induced by Uniaxial Stress in Pure VO_2.* Physical Review Letters, 1975. 35(13): p. 873-875.
25. Chamberland, B.L., *New defect vanadium dioxide phases.* Journal of Solid State Chemistry, 1973. 7(4): p. 377-384.
26. Galy, J. and G. Miehe, *Ab initio structures of (M2) and (M3) VO_2 high pressure phases.* Solid State Sciences, 1999. 1(6): p. 433-448.
27. Porta, P., et al., *Chromium dioxide: High pressure synthesis and bond lengths.* Materials Research Bulletin, 1972. 7(2): p. 157-161.
28. Villeneuve, G., et al., *Proprietes physiques et structurales de la phase $Cr_xV_{1-x}O_2$.* Materials Research Bulletin, 1971. 6(2): p. 119-130.
29. West, K., et al., *Ferromagnetism in Rutile Structure Cr Doped VO_2 Thin Films Prepared by Reactive-Bias Target Ion Beam Deposition.* Journal of Superconductivity and Novel Magnetism, 2008. 21(2): p. 87-92.
30. Verleur, H.W., A.S. Barker, Jr., and C.N. Berglund, *Optical Properties of VO_2 between 0.25 and 5 eV.* Physical Review, 1968. 172(3): p. 788-798.

31. Goering, E., et al., *LEED and photoemission study of the stability of VO_2 surfaces.* Physical Review B, 1997. 55(7): p. 4225-4230.
32. Muller, O., et al., *Metal-Insulator Transition of VO_2. A XANES Investigation of the O K Edge of VO_2.* J. Phys. IV France, 1997. 7(C2): p. C2-533-C2-534.
33. Shin, S., et al., *Vacuum-ultraviolet reflectance and photoemission study of the metal-insulator phase transitions in VO_2, V_6O_{13}, and V_2O_3.* Physical Review B, 1990. 41(8): p. 4993-5009.
34. Peierls, R.E., *Quantum Theory of Solids.* 1955.
35. Gruner, G., *The dynamics of charge-density waves.* Reviews of Modern Physics, 1988. 60(4): p. 1129-1181.
36. Gebhard, F., *The Mott Metal-Insulator Transition.* Springer, Berlin, 1997.
37. Mott, N.F., *Metal-Insulator Transition.* Reviews of Modern Physics, 1968. 40(4): p. 677-683.
38. Zylbersztejn, A. and N.F. Mott, *Metal-insulator transition in vanadium dioxide.* Physical Review B, 1975. 11(11): p. 4383-4395.
39. Eyert, V., *The metal-insulator transitions of VO_2: A band theoretical approach.* Annalen der Physik, 2002. 11(9): p. 650-704.
40. Eyert, V., *Octahedral Deformations and Metal-Insulator Transition in Transition Metal Chalcogenides.* Habilitation thesis, Univeritat Augsburg, 1998.
41. Kachi, S., K. Kosuge, and H. Okinaka, *Metal-insulator transition in V_nO_{2-1}.* Journal of Solid State Chemistry, 1973. 6(2): p. 258-270.
42. Kang, Y.-B., *Critical evaluation and thermodynamic optimization of the VO-$VO_{2.5}$ system.* Journal of the European Ceramic Society. 32(12): p. 3187-3198.
43. Canfield, P.C., J.D. Thompson, and G. Grüner, *Unifying Trends Found for the V_NO_{2N-1} Series by the Application of Hydrostatic Pressure.* Phys. Rev. B, 1990. 40: p. 4850.
44. Wells, A.W., *Inorganic Chemistry.* Clarendon Press, Oxford, 1984.
45. Baur, W.H., *The rutile type and its derivatives.* Crystallogr. Rev., 2007. 13: p. 65-117.
46. Shannon, R., *Revised effective ionic radii and systematic studies of interatomic distances in halides and chalcogenides.* Acta Crystallographica Section A, 1976. 32(5): p. 751-767.
47. Tojo, T., Q. Zhang, and F. Saito, *Mechanochemical synthesis of rutile-type $CrMO_4$ (M=V, Sb) and their solid solutions.* Journal of Solid State Chemistry, 2006. 179(2): p. 433-437.

48. Gleitzer, C., *Solid state chemistry of the trivalent metal molybdates.* Journal of the Less Common Metals, 1977. 51(2): p. 215-224.
49. Doumerc, J.-P., et al., *Proprietes magnetiques d'echantillons polycristallins de $CrWO_4$.* Materials Research Bulletin, 1976. 11(6): p. 673-680.
50. Sundholm, A., et al., *Metal-Metal Bonding in a Mixed Chromium Molybdenum Oxide Phase of Rutile Structure.* Acta Chem. Scand., 1958. 12: p. 1343-1344.
51. Shimony, Y. and L. Ben-Dor, *Trivalent chromium in the solid solution system $Cr_xMo_{1-x}O_2$.* Materials Research Bulletin, 1980. 15(2): p. 227-232.
52. Collomb, A., et al., *Synthese de quelques oxydes mixtes de type $A^{6+}B_2^{3+}O_6$ en milieu hydrothermal sous tres haute pression.* Journal of Solid State Chemistry, 1978. 23(3-4): p. 315-319.
53. Correa, H.P.S., et al., *Refinement of monoclinic ReO_2 structure from XRD by Rietveld method.* Braz. J. Phys., 2004. 34: p. 1208-1210.
54. Ivanovskii, A.L., et al., *Structure and electronic properties of new rutile-like rhenium (IV) dioxide ReO_2.* Physics Letters A, 2005. 348(1-2): p. 66-70.
55. Mikhailova, D., et al., *$Cr_xRe_{1-x}O_2$ oxides with different rutile-like structures: changes in the electronic configuration and resulting physical properties.* Journal of Solid State Chemistry, 2009. 182(6): p. 1506-1514.
56. Sleight, A.W., *New ternary oxides of pentavalent and hexavalent rhenium of the type $AReO_4$ or A_2ReO_6.* Inorganic Chemistry, 1975. 14(3): p. 597-599.
57. MacChesney, J.B. and H.J. Guggenheim, *Growth and electrical properties of vanadium dioxide single crystals containing selected impurity ions.* Journal of Physics and Chemistry of Solids, 1969. 30(2): p. 225-234.
58. Withers, R.L., et al., *Oxygen/fluorine ordering, structured diffuse scattering and the local crystal chemistry of $K_3MoO_3F_3$.* J.Solid State Chem., 2003. 170: p. 211-220.
59. Brink, F.J., R.L. Withers, and L. Noran, *An Electron Diffraction and Crystal Chemical Investigation of Oxygen/Fluorine Ordering in Niobium Oxyfluoride, NbO_2F.* Journal of Solid State Chemistry, 2002. 166(1): p. 73-80.
60. Brink, F.J., R.L. Withers, and J.G. Thompson, *An Electron Diffraction and Crystal Chemical Investigation of Oxygen/Fluorine Ordering in Rutile-Type Iron Oxyfluoride, FeOF.* Journal of Solid State Chemistry, 2000. 155(2): p. 359-365.
61. Vlasse, M., J.C. Massies, and G.r. Demazeau, *The refinement of the crystal structure of iron oxyfluoride, FeOF.* Journal of Solid State Chemistry, 1973. 8(2): p. 109-113.

62. Greedan, J.E., *Magnetic oxides in Encyclopedia of Inorganic Chemistry.* R. Bruce King, Ed Jhoj Wiley and sons, 1994.
63. Coey, J.M.D. and M. Venkatesan, *Half-metallic ferromagnetism: Example of CrO_2.* JOURNAL OF APPLIED PHYSICS, 2002. 91(10): p. 8345-8350.

Driving Curie temperature towards room temperature in the half-metallic ferromagnet $K_2Cr_8O_{16}$ by soft redox chemistry

4.1 Introduction

The hollandite structure was reported for the first time by Byström and Byström[1] for oxides with general formula $A_x(B_{8-y}B'_y)O_{16}$, where A = K^+, Cs^+ or Ba^{2+}, and B and B' are either a divalent or a trivalent cation, such as Mg^{2+}, Al^{3+}, Ti^{3+}. Besides, a cation with mixed oxidation state in a defined ratio of tri- and tetravalent state can also occupy the hollandite framework. For instance several Ti-based hollandites are known where both Ti^{3+} and Ti^{4+} coexist.[2] In some of these cases a rich soft redox chemistry has been discovered including lithium insertion and topotactical oxidation.[3,4]

Synthetic techniques have provided hollandite compounds with various K^+ ion concentrations. Hollandites with lower K concentration were obtained through a soft-chemical process, that is the extraction of a part of K ions in conjunction with the oxidation of framework metals.[4-6] On the other hand, full occupation of K sites has been attained by high-pressure synthesis in the cases of $K_2Cr_8O_{16}$[7] and $K_2V_8O_{16}$[8]. The origin of such rich chemistry is to be found in the 1D tunnel structure of hollandite.

It can be described as formed by linear pairs of edge-sharing octahedra (fig. 1). Four of these pairs are cross-linked by oxygen vertices in the a-b plane. This structural motif extends along the c-direction by infinite chains of edge-sharing octahedra making up an open tunnel framework, in which smaller 1 X 1 rutile-like tunnels alternate with larger 2 x 2 tunnels along the *ab* plane with all tunnels running parallel to the c-direction. Only the larger 2 x 2 tunnel space is usually partially occupied by alkali ions.[9] The cation occupation inside the framework of hollandite structure for transition metal oxides was widely studied in the past. Depending on the B and B' framework cations, a different cationic occupation of tunnels has been observed.[7,8,10-12]

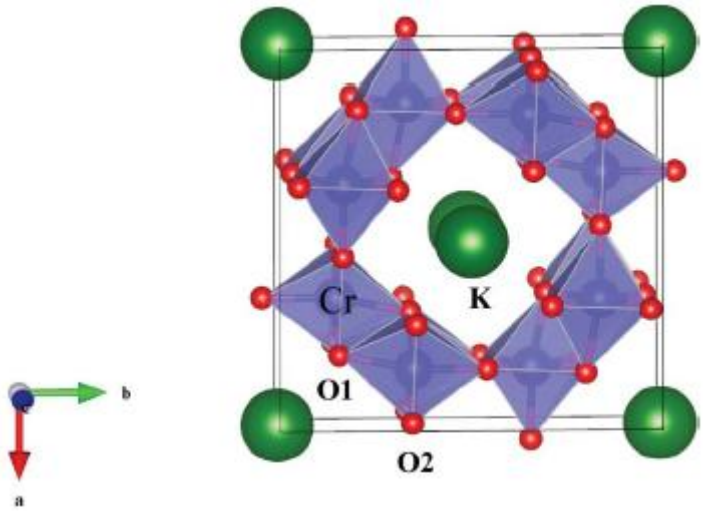

Fig.1 Schematic representation of the structure of $K_2Cr_8O_{16}$ hollandite.

In the case of Mn-hollandite oxides, $A_xMn_8O_{16}$ (A = Ba, Pb, etc.),[13-16] extensive investigations have addressed different applications, e.g. ionic conductors, positive electrodes and oxidation catalysts, though less attention has been paid to their magnetic and electronic properties. This may be because hollandite materials which are prepared through soft chemistry are poorly crystallised materials. Recently, some hollandite oxides, containing for example ruthenium, $Ba_{1.33}Ru_8O_{16}$ $BaRu_6O_{12}$ and vanadium,[17] $Bi_xV_8O_{16}$ ($1.6 < x < 1.8$),[18] were found to show anomalous electronic properties inherent to the quasi-one-dimensional double chains of MO_6 (M = Ru or V) octahedra. Low dimensionality, promoting quantum spin fluctuations or geometric frustration, has been proposed as the origin of these electronic properties.

One of the most interesting materials having hollandite structure is $K_2Cr_8O_{16}$, which transport properties of have been studied by Hasegawa et al..[19] The crystal structure of $K_2Cr_8O_{16}$ is assumed to contain Cr ions in a mixed-valent state of Cr^{4+} (d2) : Cr^{3+} (d3) ratio of 3:1, in order to keep charge balance; where Cr has a mixed valence of +3.75.

This oxide shows a phase transition from paramagnetic metal to ferromagnetic metal with a Tc onset of ca. 180 K and with spin polarization of 18 μ_B per formula unit (f.u.) at low temperatures. In addition to this phase transition, it has also been reported that another phase transition occurs from ferromagnetic metal to ferromagnetic insulator at T(MI) of ca. 90 K, suggesting that the charge gap opens below T(MI). Recent structural investigations have demonstrated that this metal-insulator transition (MIT) is accompanied by a structural transition from the tetragonal I4/m phase to a monoclinic $P2_1/\alpha$ phase.[20] Herein we present an investigation of the high pressure hollandite $K_2Cr_8O_{16}$.

This hollandite was described for the first time by Endo et al. in 1976.[21] They obtained for the first time a polycrystalline sample of $K_2Cr_8O_{16}$ with a monoclinic structure (a = 13.820 Å; b = 2.941 Å; c = 9.772 Å and β = 135°) with C2/m symmetry and reported a Tc = 225 K at a magnetic field of 1 T. Some years later, Tamada et al.[7] obtained $K_2Cr_8O_{16}$ as a single crystal material with cell parameters a = b = 9.7627(4) Å and c = 2.9347(6) Å and α = β = γ = 90°; having tetragonal symmetry and space group I4/m. On the other hand, Hasegawa et al. obtained a powder sample with the same crystallographic parameters and reported a T_C = 180 K at H = 0.1T. The difference in T_C values reported by Hasegawa (T_C = 180 K at H = 0.1 T) and Endo (T_C = 225 K at H = 1 T) has been justified as an overestimation of T_C in Endo's measurement due to the rather high magnetic field applied.[19] Ternary oxides containing transition metal like V or Cr having hollandite structure have got a renewed interest; several studies on their physical properties have been carried out.[19-24] More in detail $K_2V_8O_{16}$,[22] $Rb_xK_{1-x}V_8O_{16}$,[23] and $K_2Cr_8O_{16}$[19-21] showed coexistence of metal-insulator (M-I) transition and paramagnetic-ferromagnetic transition in the same range of temperature; Nevertheless shifts on T_{M-I} or T_c transitions as function of different thermodinamic parameters: pressure and composition, have been observed in the case of $K_{1,2}Cr_8O_{16}$ and $Rb_xK_{1-x}V_8O_{16}$; concerning these phenomena an unique and satisfying explanation has not been provided yet. Previous authors focused their attention on this structure because hollandite should be described as a 1-D material, the case of $K_2V_8O_{16}$ or a quasi 1-D material, the case of $K_2Cr_8O_{16}$, where spin dimerization could occurs; the M-I transition has been explained by means of a Peierls mechanism.[20]

In the case of $K_2Cr_8O_{16}$, density of states (DOS) calculations evidenced a double exchange coupling between Cr-Cr atoms taking place along the c direction of unit cell; it occurs between the double chains via corner shared oxygens instead of the Cr atoms in the double chains into the ab plane.[20] Our hypothesis is that changes in structure drive changes in properties: differences in the structures between $K_2Cr_8O_{16}$ and $K_{1,2}Cr_8O_{16}$, due to changes in O-Cr-O angles and interatomic distances, provide an easier Cr^{3+} - Cr^{4+} double exchange

mechanism in $K_{1,2}Cr_8O_{16}$ by means of an improved interactions of d-d orbitals. $K_2Cr_8O_{16}$ is unique in its formal valence arising from the presence of 2 Cr^{3+} and 6 Cr^{4+} per formula. Note that though Cr^{3+} is stable in a wide range of reducing to ordinary oxidizing atmosphere, Cr^{4+} is produced only under more extreme conditions, in particular at a high oxygen pressure of 0.1 GPa. Therefore, Cr^{4+} hardly coexists with Cr^{3+} in general. The aim of this work was the extraction of K^+ ions from the structure by soft-chemical and electrochemical oxidation of $K_2Cr_8O_{16}$, in order to increase the content of Cr^{4+}. Ideally total extraction may produce a new polymorph of CrO_2 with the hollandite structure, though in any case the mere increase of Cr^{4+} amount through topotactical reactions will produce changes in the magnetic and transport properties of the referred chromium hollandite. In this work the chemical reactions to oxidise Cr^{3+} and the effect on both the structure and the magnetic properties are reported.

4.2 Experimental

The pristine material $K_2Cr_8O_{16}$ was prepared by high pressure and high temperature techniques. A Conac Press 28 with a capacity of 0.3 cm3 was used for the several attempts undertaken at different experimental conditions of pressure and temperature. Following the results reported by Hasegawa et al.[19] a mixture of $K_2Cr_2O_7$ and Cr_2O_3 in 1:3 ratio was treated in a Pt crucible at pressures from 55 to 65 kbar and temperatures from 1100. to 1250 C for 1 h. Extraction of K^+ and expected oxidation of Cr $^{3+}$ to Cr $^{4+}$ was accomplished by low temperature reactions using either electrochemical methods or soft-chemistry reactions. For the former coin cells (type CR2032) with the following configuration: Li|$LiPF_6$/EC:DMC 1:1|$K_2Cr_8O_{16}$ were assembled in an Ar filled glove box. Positive electrode pellets with 8mm diameter were made by pressing mixtures of typically

ca. 25 mg of $K_2Cr_8O_{16}$ (70%) with conductive carbon (Super-S, 25%) and poly-tetrafluoroethylene (PTFE) (5%) as the binder. This pressed amount typically yielded ~1mmthick electrodes. Li metal was used as the negative electrode. It was separated from the positive electrode by a disk made of a glass fibre (Aldrich) soaked with the $LiPF_6$-based electrolyte. Cells were run under in both galvanostatic and potentiostatic mode using a MacPile II System (Biologic) apparatus. For the former, a constant current density of 0.05 mA cm-2 was applied from the rest potential (ca. 3.3 V) to 4.8 V. After the first charge the cell was discharged by reversing the current in order to check reversibility. For potentiostatic experiments the potential was stepwise changed at a step rate

of ±10 mV, and the cell left to relax for 0.5 h before a new potential step was again applied. Electrochemical experiments have provided information on the potential range

where the different oxidative-reductive process take place. The information has been used to choose the proper oxidant to carry out the reaction chemically, in order to provide samples suitable for the structural, chemical and magnetic characterization. An oxidative chemical reaction aiming for the extraction of K^+ ions from $K_2Cr_8O_{16}$ was carried out following "soft chemistry" procedures and Schlenk techniques. The oxidant used was NO_2BF_4, $E_0 = (NO_2^+/NO_2) = 4.7$ V vs. Li^+/Li. Due to the strong oxidant power of NO_2BF_4 it was handled under Ar atmosphere. According to the following chemical equation, eqn(1)

$$K_2Cr_8O_{16} + x\ NO_2BF_4 \rightarrow K_{2-x}Cr_8O_{16} + x\ KBF_4 + x\ NO_2 \quad (1)$$

stoichiometric amounts of NO_2BF_4 and $K_2Cr_8O_{16}$ were weighed in a glove box under an Ar atmosphere and placed in a Schlenk tube together with 15 mL dry CH_3CN. However, to enforce the extraction of K^+ by increasing the potential of the reaction several experiments were carried out increasing the molar ratio $K_2Cr_8O_{16}$: NO_2BF_4, in particular 1:1, 1:2.5, 1:4; or treating the sample several times with the same molar ratio to refresh oxidant. In all cases the mixture was then left stirring for 10 days at 60° C. Afterwards, the powder was washed with a convenient organic solvent like: Dimethylsulfoxide (DMSO), Propylencarbonate (PC) or Dimethylcarbonate (DMC) used to dissolve KBF_4, after that separated by decanting and centrifuging. The solutions were also kept for further analysis. X-ray diffraction patterns were recorded on a Bruker D8 high-resolution X-ray powder diffractometer, equipped with a position sensitive detector (PSD) MBraun PSD-50M, using monochromatic Cu-Ka (l = 1.54056 Å) radiation obtained with a germanium primary monochromator. Data were collected in the range $2\Theta = 10–100$ with a step width 0.020 2Θ over a total exposure time period of 16 h. Powder X-ray diffraction patterns were also obtained using an X'PERT MPD (Panalytical) instrument with a Cu monochromator (Cu-Ka1 = 1.54056 Å). The powder diffraction data were analyzed by the Rietveld method, using the FullProf program.[25] Potassium content in both pristine and chemically oxidised materials was determined by EDS microanalysis in the respective powders. To confirm the extent of the extraction reaction, potassium content of the aforementioned solutions obtained after the chemical oxidation procedure was also analysed by means of a Flame Photometer, Sherwood–Corning 410 atomic absorption spectrometer, using a 1000 ppm KCl standard solution for straight calibration, and an average amount of extracted K^+ ions was determined. Unfortunately this method did not yield very reproducible results. Furthermore, the potassium content determined by this method was always lower when compared to results obtained from EDS, which is most probably due to the fair solubility of KBF_4 even in the high permittivity solvents used (DMSO, PC,DMC). In fact, X-ray diffraction patterns of samples washed with DMSO, PC or DMC still exhibited

characteristic diffraction lines of KBF_4 indicating that complete elimination of this salt was not achieved. Finally magnetization vs. temperature, M(T), was measured for $K_{2-x}Cr_8O_{16}$ and $K_2Cr_8O_{16}$ using a SQUID Quantum Design XLMPM. A constant field of H = 1 x 10^3 Oe was applied M(H) at different temperature values of 5, 50, 100, 150, 250, 300 K.

4.3 Results and discussion

Fig. 2 Shows the x-ray diffraction pattern of the powder obtained by the high pressure synthesis carried out in the conditions described in the experimental part. The pattern has been fully indexed by using the cell previously described for $K_2Cr_8O_{16}$, space group I4/m. The Figure also shows the graphical result of the Rietveld refinement in the mentioned space group.

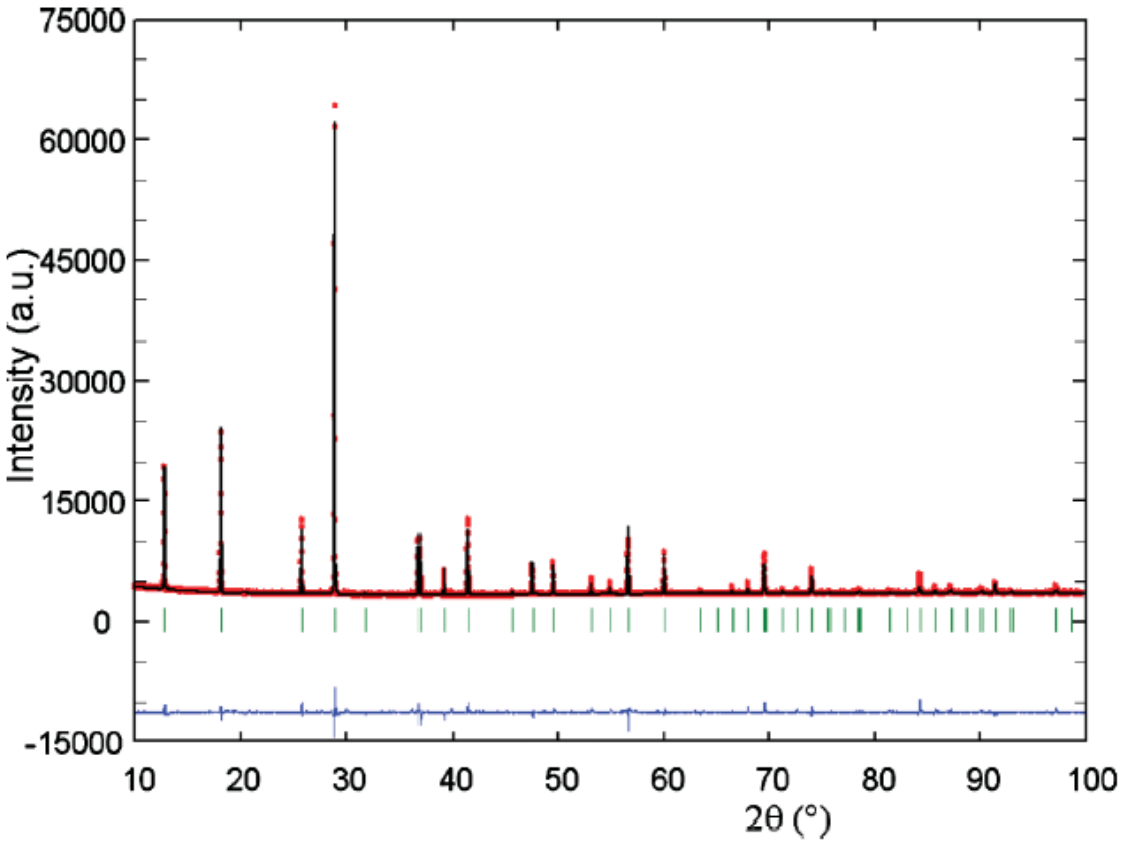

Fig. 2 Graphical result of the Rietveld refinement of $K_2Cr_8O_{16}$ hollandite using X-ray powder data. Experimental data are presented as points and the calculated profile as solid line. The observed difference profile is plotted at the bottom. Vertical bars are the allowed Bragg reflections for space group I4/m.

Structure refinement of the powder data converged to the final R factors R_{wp} = 3.1%; R_p = 2.0%; χ^2 = 3.60 and R_{Bragg} = 5.7%. Our refined cell parameters a = 9.7471(2) Å; c = 2.9291(1) Å agree with earlier reports, though they are slightly smaller than those reported for single crystal data (a = 9.7627(4) Å; c = 2.9347(6) Å).[7] This single phase $K_2Cr_8O_{16}$ material has been used as parent to undertake both electrochemical and chemical oxidation.

4.3.1 Electrochemical oxidation

Fig. 3a shows the first charge of a lithium cell bearing $K_2Cr_8O_{16}$ as the active material of the positive electrode. Data were obtained under near equilibrium conditions (+10 mV/12 h) in potentiostatic mode. It can be seen that a typical S-shaped voltage profile is developed between the rest potential of the cell, 3.2 V, and 4.6 V involving the extraction of 0.6 K^+/formula unit. The extra capacity observed above ca. 4.6 V is most probably related to parasitic reactions, such as decomposition due electrolyte oxidation.

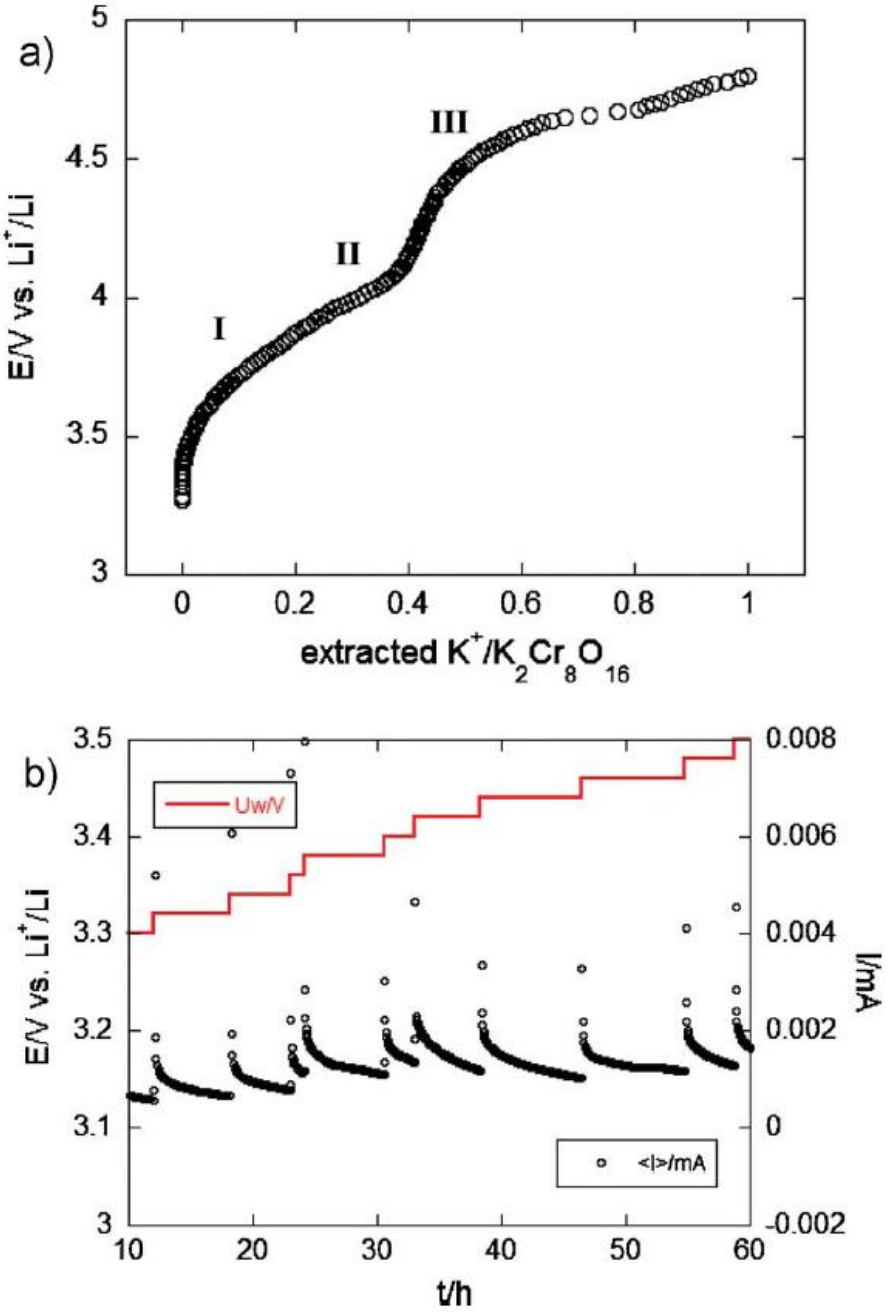

Fig. 3 a)First charge for a cell Li|LiPF6/EC:DMC 1:1|$K_2Cr_8O_{16}$. From the rest potential to 4.6 V the observed amount of extracted K^+ is 0.6 yielding $K_{1.4}Cr_8O_{16}$. Above 4.6 V decomposition of the $LiPF_6$ electrolyte is likely occurring and the total value of extracted potassium is not reliable. b) Relaxation of current corresponding to the charge of a Li Li-electrolyte $K_2Cr_8O_{16}$ cell run under potentiodynamic conditions (potential step: +20 mV; max 10 h at each potential) plotted as I–t representation.

Below 4.6 V three different regions, labelled I, II and III can be assigned to the formation of two solid solutions and one biphasic domain. In region I and III the compositional range of the solid solutions is described by $K_{2-x}Cr_8O_{16}$ with $0 < x < 0.25$ and $0.4 < x < 0.6$, respectively. In between those two regions both phases coexist in a two-phases domain (labelled II). This domain is characterised by the presence of a pseudo-plateau in the V–x profile. Accordingly to this data set it is possible to obtain a highly K-depleted hollandite with a composition $K_{1.4}Cr_8O_{16}$. Nevertheless, we have found that the compositional range determined by electrochemical methods is very dependent on the experimental conditions. Thus, when voltage is changed just a little faster, the observed amount of extracted potassium decreases. This is likely due to the slow kinetics of lithium diffusion through the hollandite structure. In this connection Fig. 3b shows the relaxation of current after a voltage increase of +20 mV. It can be seen that even after 10 h the current is still far from reaching zero (equilibrium condition). In any case, based on the closest data to equilibrium, obtained from the slowest experiment undertaken shown in Fig. 3a (+10 mV/12) we have estimated that NO_2BF_4 would be an optimum oxidant (E_0 = (NO_2^+/NO2) = 4.7 V vs. Li^+/Li) to carry out the extraction of potassium by chemical methods in order to obtain a sizeable amount of material. Furthermore, the chemically prepared sample would be free of carbon and binder and hence would be appropriate for a better structural, chemical and magnetic characterisation. We tried to discharge the cells in order to investigate the reversibility of the electrochemical process. The result (not shown) was a sharp drop of voltage as soon as the current was reversed after reaching the endpoint of charge. This indicates that neither the extracted K^+ nor lithium ions from the negative electrode can be inserted into the hollandite structure under the described experimental conditions. The X-ray diffraction patterns of both pristine and electrochemically oxidised samples are presented in Fig. 4.

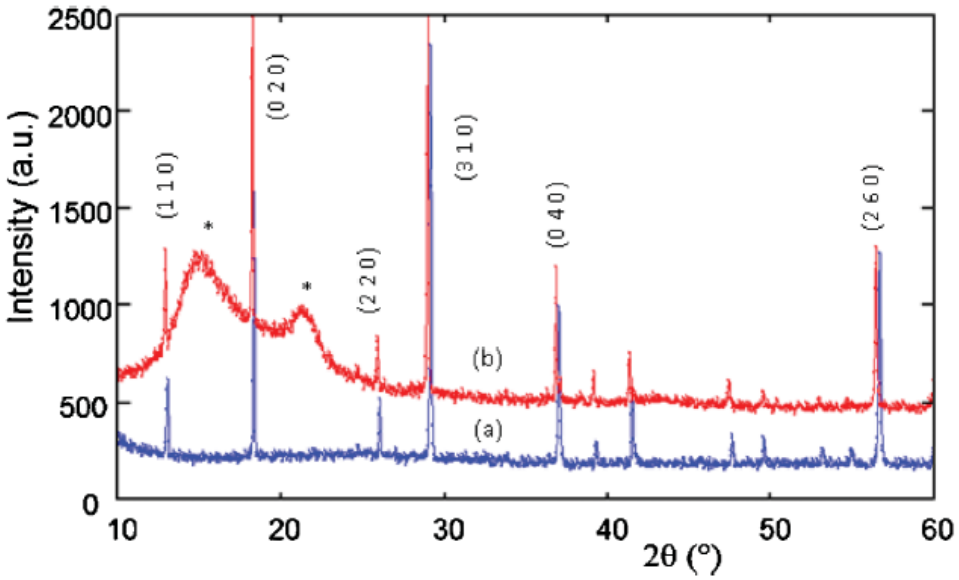

Fig. 4 X-ray patterns of a) pristine $K_2Cr_8O_{16}$ and b) electrochemically oxidised $K_{2-x}Cr_8O_{16}$ ($x \approx 0.6$). Peaks coming from the air-tight holder used for the measurement of the oxidized sample are marked with asterisks (*).

To prevent contact with air, a "home-made, air-tight" holder that uses a commercial plastic as transparent window, has been used for collecting the X-ray pattern of the oxidised sample. The Bragg positions observed for the oxidised samples match with those of the pristine as expected for a topotactic oxidation reaction. As far as quality of data allows, no extra peaks related to second phase products are observed. The potassium extraction from $K_2Cr_8O_{16}$ hollandite is accompanied by an anisotropic variation of the tetragonal cell parameters (see Table 1).

Tab. 1 Basic structural parameters for several $K_{2-x}Cr_8O_{16}$ hollandites studied in this work.

Sample	*a*/Å	*c*/Å	Vol/Å^3
$K_2Cr_8O_{16}$ single crystal[9]	9.7627(4)	2.9347(6)	279.70(6)
$K_2Cr_8O_{16}$ (powder, this work)	9.7471(2)	2.9291(1)	278.29(1)
$K_{1.4}Cr_8O_{16}$ (electrochemically)	9.7999(7)	2.9235(12)	280.77(12)
$K_{1.2}Cr_8O_{16}$ (chemically, 3 times treatment with NO_2BF_4)	9.7744(2)	2.9093(1)	277.95(1)

The concomitant increase of the a-axis is well observable by the systematic displacement of (hk0) and (0k0) Bragg peaks to lower 2q angles (see Fig. 4). At the same time the short c-axis decreases (see Table 1). Furthermore, the X-ray pattern of the electrochemically extracted hollandite shows some changes in intensities with respect to the parent, in particular concerning the (020) and (110) reflections. This may be related in part to a lower occupation of the potassium site, but is probably due to preferred orientation effects, which are likely introduced by the uniaxial pressing of the powder composite to obtain pellets suitable for the electrochemistry study.

4.3.2 Chemical oxidation

Some of the experimental conditions used to obtain several K deficient $K_{2-x}Cr_8O_{16}$ hollandites by means of a chemical oxidation/extraction procedure are shown in Table 2. The average remaining potassium content has been determined by two techniques: XEDS microanalysis and refinement of K site occupation factor from X-ray data. Both EDS and the ensuing results from X-ray diffraction indicate that potassium has been effectively extracted.

Tab. 2 Several $K_{2-x}Cr_8O_{16}$ hollandites obtained using different oxidant: $K_2Cr_8O_{16}$ molar ratio for chemical K^+ extraction, chemical formula of hollandites and values of ferromagnetic transition temperature (T_c).

Sample	NO_2BF_4:$K_2Cr_8O_{16}$	Formula (EDS)	Formula (X-ray)[a]	T_c/K
1	0:1	$K_{1.9(2)}Cr_8O_{16}$	$K_{2.0(3)}Cr_8O_{16}$	175
2	1:1	$K_{1.2(2)}Cr_8O_{16}$	—	250
3	2.5:1	$K_{1.2(2)}Cr_8O_{16}$	—	250
4	4:1	$K_{1.2(3)}Cr_8O_{16}$	$K_{1.2(3)}Cr_8O_{16}$	250
5	2:1 (3 times)	$K_{1.2(2)}Cr_8O_{16}$	—	250
6	electrochemically	$K_{1.4}Cr_8O_{16}$	—	not determined

[a] Rietveld refinement of X-ray data. Only K site occupation was refined.

The same results but with low reproducibility (see experimental section) were obtained from the analysis of potassium in solution by atomic absorption. X-EDS results included in Table 2 correspond to the average potassium content achieved over 25 analysis including the parent as reference. The standard deviation for the measurements performed on five samples was 1.6 (sample n.3) $< \sigma <$ 2.8 (sample n.4) showing an acceptable correlation among the content of K^+ in all microcrystals measured. As it is shown in Table 2 the increase of oxidant to hollandite ratio from1:1 to 4:1 does not produce a higher degree of extraction. Even the use of a 2:1 ratio but refreshing the oxidant 3 times did not give a product with a less K^+ content, and was not possible go further in K^+ extraction. X-ray data confirm that under these conditions the hollandite framework structure is still kept upon K^+ removal while K^+ analysis points to the formation of $K_{2-x}Cr_8O_{16}$ ($x \sim 0.8$).

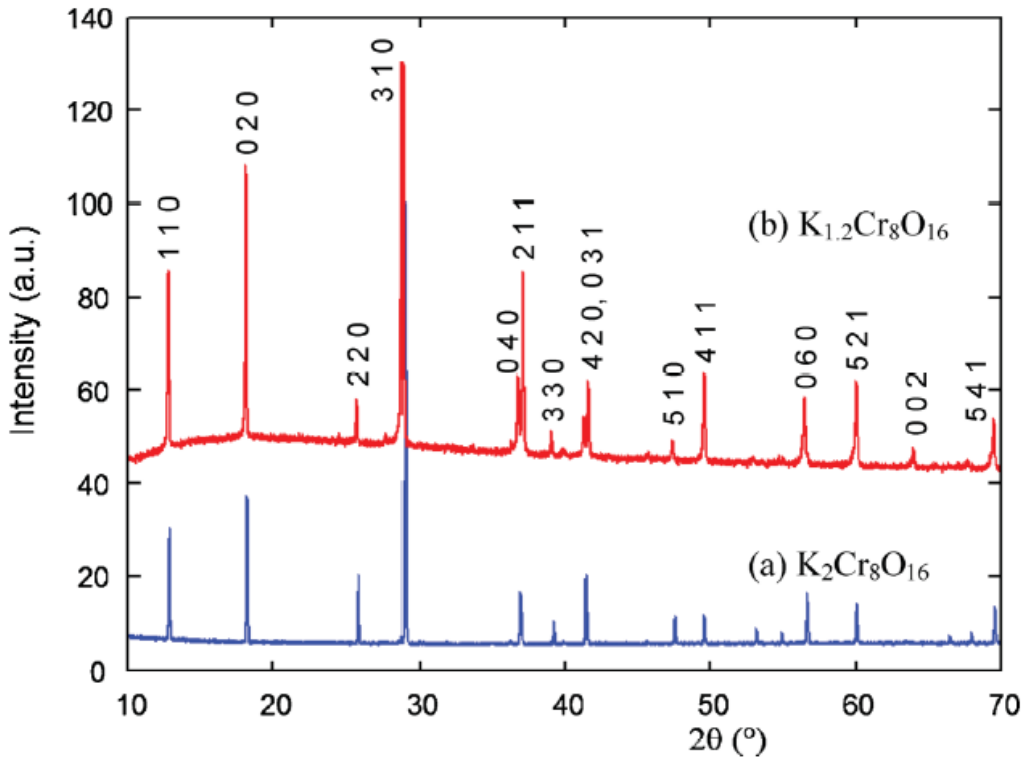

Fig. 5 X-ray patterns of (a) pristine $K_2Cr_8O_{16}$ and (b) the chemically oxidised product $K_{2-x}Cr_8O_{16}$ (x = 0.8) using NO_2BF_4 as the oxidant.

As it can be observed in the X-ray diagram shown in Fig. 5 the obtained product a) preserved the hollandite structure (Bragg reflections are very close to that of starting $K_2Cr_8O_{16}$) and b) has a high purity and crystallinity and hence is very suitable for a more detailed structural characterisation.

The results of chemical potassium extraction are in agreement with those obtained using electrochemical K^+ extraction (Fig. 4), proving the concordance and validity of both extraction methods. The highest value of extraction from the fully occupied $K_2Cr_8O_{16}$ that can be achieved under the experimental conditions used in this work (both chemically and electrochemically) is 0.8 K/formula, yielding the hollandite $K_{1.2}Cr_8O_{16}$ having a partial cationic tunnel occupation.

However, complete depletion of K^+ from the $K_2Cr_8O_{16}$ hollandite structure has not been achieved (accompanied by the complete oxidation of Cr^{3+} to Cr^{4+}). Instead, the average oxidation state has been increased from 3.75 in $K_2Cr_8O_{16}$ to 3.85 in $K_{1.2}Cr_8O_{16}$. Results from EDS evidence the existence of microcrystals with very low K concentration (less than 0.5 K per formula), albeit we have not been able to obtain a homogeneous sample with such a low potassium contents. Whether the difficulty to achieve full K extraction is related only to kinetics aspects or also to the instability of a hypothetical hollandite with composition CrO_2, remains unknown. Note that hollandite oxides $A_nB_8O_{16}$ usually have n < 2 and thus, $K_2Cr_8O_{16}$ is an unique system since n = 2. Note that the full tunnel occupancy

with high contents of K^+ cations is probably related to the high pressure conditions used for its synthesis. However, almost full depletion of the tunnel cation has been achieved in some other cases as for example $K_xTi_8O_{16}$[4] showing that a certain quantity of A^+ cation is not always needed to maintain the hollandite.

4.3.3 Thermogravimetric analysis

Several speculations about presence of water (or solvent) by absortion or crystallization molecules along [001] hollandite tunnels have been made; In order to explore this possibility, TGA for both samples have been performed in a TGA balance under N_2, the measurements are reported in fig. 6.

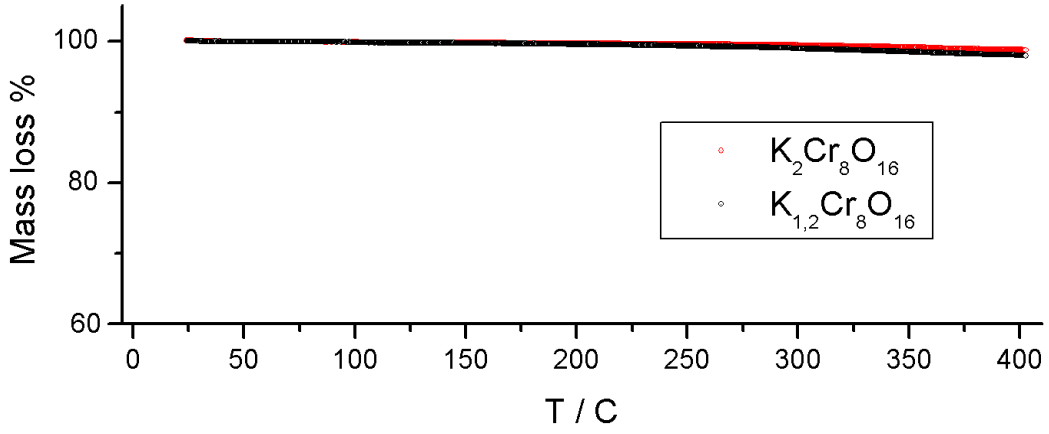

Fig. 6 Plot of TGA for both $K_{1,2}Cr_8O_{16}$ and $K_2Cr_8O_{16}$.

The maximum percentage of weight loss have been reached at the maximum temperature, 400 ºC and was of 2% for $K_{1,2}Cr_8O_{16}$ and 1% for $K_2Cr_8O_{16}$; these values of temperature seems to be rather high for a loss of crystallization water; more no evidence of any discontinuity, or characteristic plateaux, related to a loss of crystallization molecules have been observed; from TGA easurements we could exclude any presence of water in tunnels for $K_{1,2}Cr_8O_{16}$ and $K_2Cr_8O_{16}$ hollandites.

4.3.4 Structure refinement of $K_{2-x}Cr_8O_{16}$

Refined cell parameters of chemically prepared $K_{1.2}Cr_8O_{16}$: a = b =9.7744(2) Å;
c = 2.9093(1) Å are close to those obtained for a sample prepared by electrochemical oxidation (see Table 1). As already stated above, the unit cell parameters show an anisotropic variation with decreasing potassium content. However, as a consequence of the opposite variation of a and c parameters,

the unit cell volume remains practically unchanged. Interestingly a similar anisotropic behaviour has been reported for isotype $K_xV_8O_{16}$ (x = 2 and 1.8) hollandites .[8]

The structural data reported for a $K_2Cr_8O_{16}$ single crystal have been used as initial model for the structure refinement of $K_{1.2}Cr_8O_{16}$ using the space group I4/m with the K channel ion occupying the special position (2b).[9] Site occupancies of atoms, including the K ion, were fixed to 1.0 according to the fully occupied hollandite structure. The graphical result of the Rietveld refinement of $K_{1.2}Cr_8O_{16}$ is depicted in Fig.7.

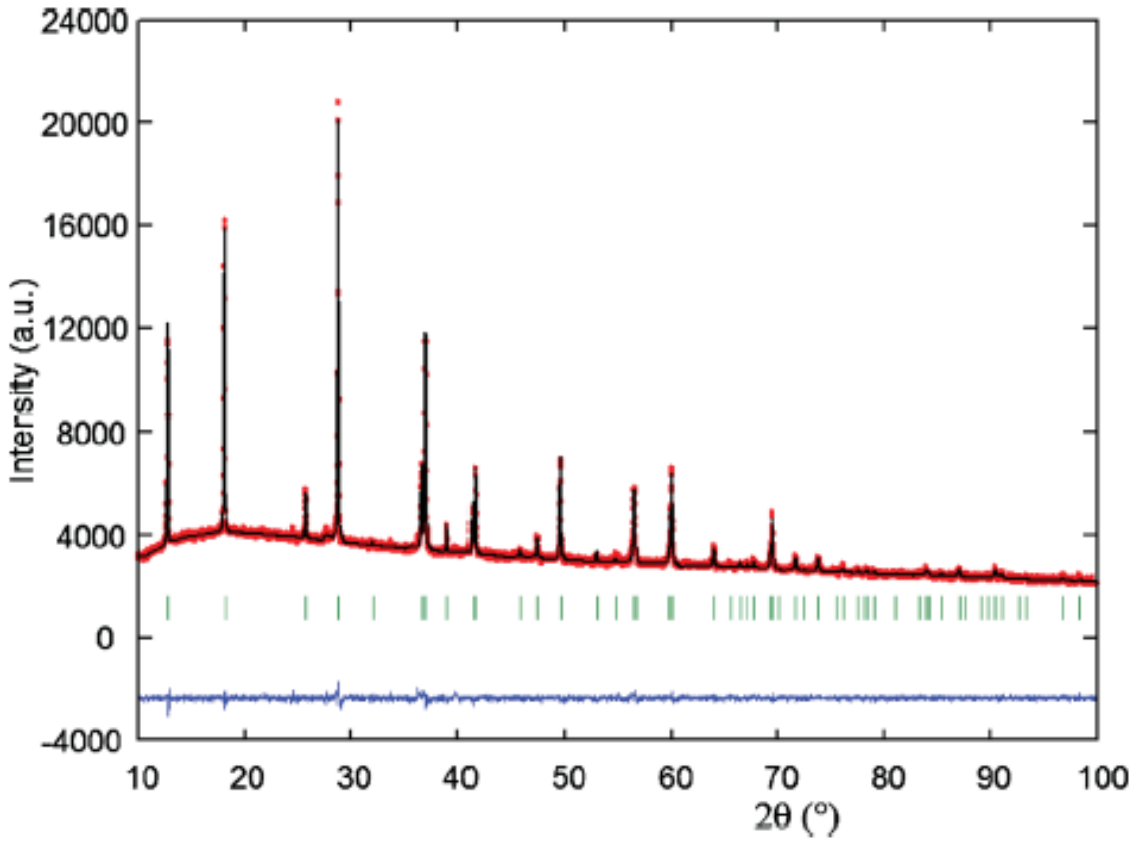

Fig. 7 Graphical result of the Rietveld refinement of $K_{1.2}Cr_8O_{16}$ hollandite. Experimental data are presented as points and the calculated profile as solid line. The observed difference profile is plotted at the bottom. Vertical bars are the allowed Bragg reflections for space group I4/m.

Background correction was done by means of linear interpolation between given points, while the peak shape for the hollandite phase was best described with a pseudo-Voigt function. After refining overall scale factor, cell parameters and zero shift, atomic positional coordinates of Cr, O(1), O(2) atoms and isotropic thermal B factors were refined. At this stage, the occupancy of the tunnel cation K was refined to $R_p = 0.017$, $R_{wp} = 0.021$, $R_{Bragg} = 0.036$, $\chi^2 = 1.42$, yielding the composition $K_{1.2(3)}Cr_8O_{16}$. This composition is equivalent to a 60% tunnel occupancy and is in good agreement with the K composition determined by X-EDS microanalysis. The main results of the structure refinement and selected atomic distances are listed in Tables 3 and 4, respectively. K^+ extraction leads to a lower occupation of the cation tunnel site of hollandite.

Tab. 3 Atomic coordinates, temperature factors and occupancy for $K_{1.2}Cr_8O_{16}$.

	Position	*x*	*y*	*z*	B_{iso}[a]	Occupancy
K	*2b*	0	0	0.5	3.00(6)	0.18(4)
Cr	*8h*	0.3489(3)	0.1660(4)	0	0.63(6)	1.0
O(1)	*8h*	0.1604(4)	0.1962(3)	0	0.26(4)	1.0
O(2)	*8h*	0.5461(4)	0.1721(3)	0	0.74(6)	1.0
	$\beta_{anisotropic}$ (K) $\beta_{11} = \beta_{22} = 0.0152$, $\beta_{33} = 0.3032$					

[a] B_{iso} are defined by $B_{iso} = 4/3\ \Sigma_i\Sigma_j\ \beta_{ij}a_ia_j$.

The relation between the tunnel cation occupancy and the value of the K temperature factor has been pointed out in earlier works. Abriel et al.[8] observed that the U_{33} coefficient of the anisotropic temperature factor of K in $K_{1.8}V_8O_{16}$ and $Tl_{1.74}V_8O_{16}$ showed high values of 0.26 and 0.252, respectively, which were significantly higher than the 0.122 reported for the fully occupied $K_2V_8O_{16}$ hollandite.

Tab. 4 Interatomic distances (Å) and bond angles (°) for Cr-hollandites, data of the fully occupied $K_2Cr_8O_{16}$ have been included for comparison.

	$K_{1.2}Cr_8O_{16}$	$K_2Cr_8O_{16}$
Distances KO_{12} polyhedron		
K–O(1)	2.871(4) × 8	2.875(2) × 8
K–O(2)	3.241(3) × 4	3.310(2) × 4
Mean K–O	2.990	3.020
Distances CrO_6 octahedron		
Cr–O(1)	1.851(6)	1.932(4)
Cr–O(1)′	1.987(4) × 2	1.964(3) × 2
Cr–O(2)′	1.883(4) × 2	1.912(3) × 2
Cr–O(2)	1.918(6)	1.871(4)
Mean Cr–O	1.918	1.926
O(1′)–O(1′); O(2′)–O(2′)	2.909(2)	2.935(2)
O(1′)–O(2′)	2.534(6)	2.529(3)
Angles CrO_6 octahedron		
O(1)–Cr–O(2)	167.4(4)	169.0(3)
O(1)′–Cr–O(2)′	81.76(15)	75.8(2)
O(1)′–Cr–O(1)′	94.1(2)	101.9(3)
O(2)′–Cr–O(2)′	101.2(3)	105.6(3)

From X-ray diffraction structure analysis it can be schematically established that in many inorganic crystals the value of √U ranges between 0.05 and 0.2 Å, although a value as high as 0.5 Å (equivalent to $B_{iso} \sim 20$ Å^2 with the relation $B_{iso} = 8\pi^2 \cdot U_{iso}$) has been reported.[26]
Temperature factor for K atom in $K_{1.2}Cr_8O_{16}$ has been first refined isotropically and then also anisotropically. Refinement resulted in a $B_{iso} = 3.00(6)$Å^2 (√U= 0.19Å).
This value is significantly higher $K_{2-x}Cr_8O_{16}$ than that determined for $K_2Cr_8O_{16}$

(B_{iso} = 1.0 Å^2; √U = 0.1 Å), in accordance with the lower K content in $K_{1.2}Cr_8O_{16}$ hollandite. These findings agree with earlier reports on the K temperature factor of $K_{2-x}V_8O_{16}$ hollandite.[7,10] The anisotropic displacement of the electron density of K along the tetragonal c-axis in the KO_{12} tunnel polyhedron is shown in Fig. 8. K extraction and increase of oxidation state of Cr have also an influence on Cr–O bond distances and O–Cr–O angles. The Cr– O(1') and Cr–O(2) distances listed in Table 3 and illustrated in Fig. 9 increase upon K extraction, whereas the Cr–O(1) and Cr–O(2') distances decrease. As a whole a modest shortening of the average Cr–O distance occurs upon K^+ extraction, which cannot satisfactorily account for the observed anisotropic variation of the tetragonal cell parameters. On the other hand, the pronounced decrease of O(1')–Cr–O(1') and O(2')–Cr–O(2') angles (7.8 and 4.4., respectively) leads to a significant shortening of the respective O(1')–O(1') and O(2')–O2(') distance around each Cr atom (see Table 4).

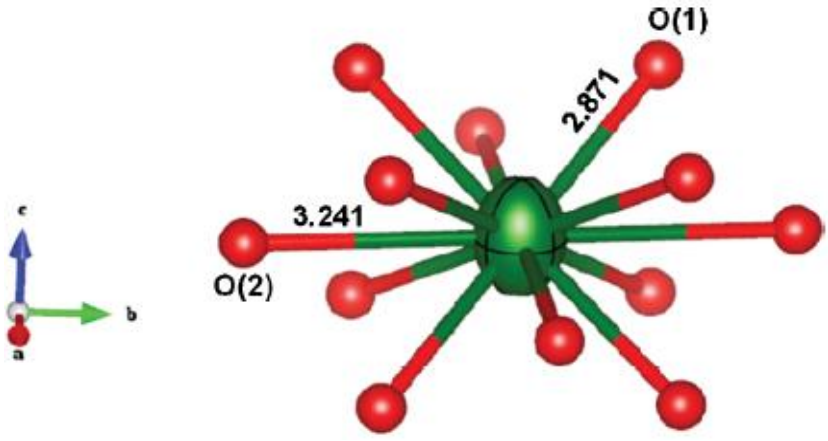

Fig. 8 K^+ ion thermal ellipsoid in the tunnel site of the $K_{1.2}Cr_8O_{16}$ hollandite coordinated by 8 O(1) + 4 O(2) oxygen atoms. Atomic distances are given in Å

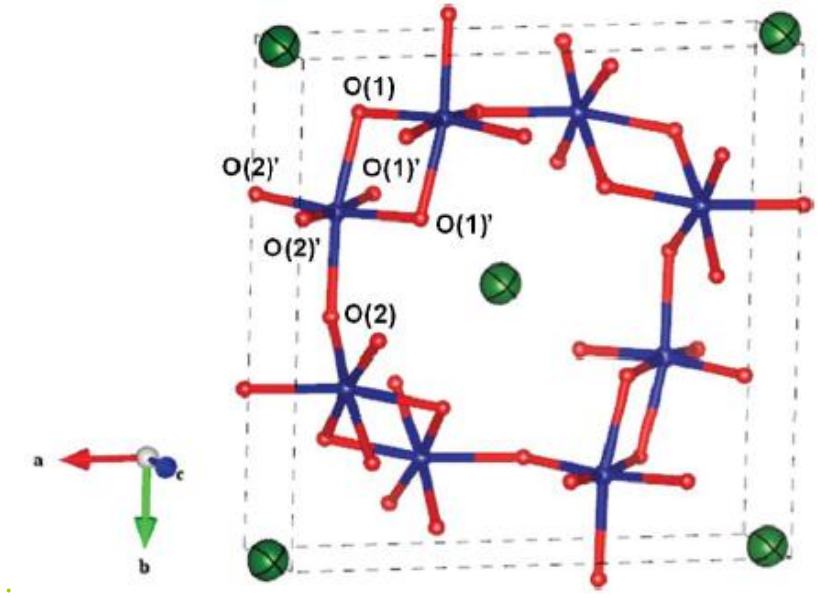

Fig. 9 Skeleton structure of $K_{2-x}Cr_8O_{16}$ hollandite showing the octahedral CrO_6 environment.

These oxygen atoms build up the edge-sharing CrO_6 octahedra blocks running along the z direction, and consequently are responsible for the shortening of the c parameter (which indeed is identical to the O(1')–O(1') distance. The aforesaid decrease of O(1')–Cr–O(1') and O(2')–Cr–O(2') angles is necessarily accompanied by an increase of the O(1')–Cr–O(2') angle, producing a significant enlargement of the corresponding O(1')–O(2') distance around each Cr atom (see Table 4). As these oxygen atoms are running parallel to the x (and y) direction, and an enlargement of the tetragonal a cell parameter is observed as consequence.

4.3.5 Magnetic characterisation

Hasegawa et al.[19] reported a ferromagnetic behavior for $K_2Cr_8O_{16}$ with a measured transition temperature Tc of 180 K at 0.1 T. Our reference sample, $K_2Cr_8O_{16}$, reproduces their measured values (180 K). Furthermore, in the present work magnetic susceptibility vs. temperature has been also measured for K^+ extracted samples.

The temperature dependence of magnetization M(T) and of the inverse molar susceptibility of three different oxidised samples (samples 2, 3 and 4 in Table 2) and the one used as reference, $K_2Cr_8O_{16}$ (sample 1 in Table 2) under a magnetic field (H) of 0.1 T are shown in Fig. 10a and 10b, respectively. For $K_2Cr_8O_{16}$ the M(T) abruptly increases with decreasing temperature at ca. 180 K and tends to saturate below 130 K, accordingly with the previously reported value of Tc.[19] Interestingly, the oxidised hollandites exhibit a ferromagnetic behaviour but the Curie temperature increases by 70 K to reach 250 K. Saturation has been observed only in two of the three oxidised samples. Samples 4 and 5 were measured in both ZFC and FC observing no changes in the magnetization curve.

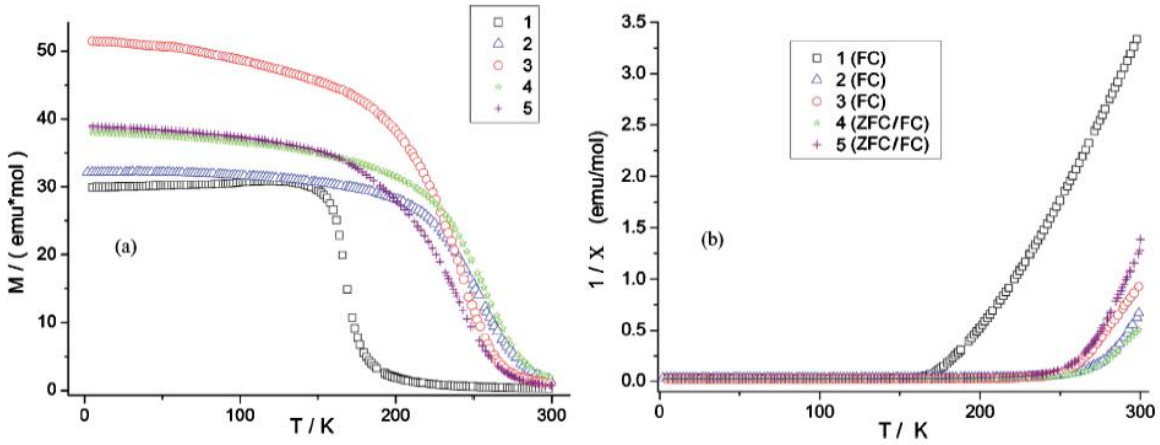

Fig. 10 Variation of magnetization (a) and inverse susceptibility (b) with temperature of $K_2Cr_8O_{16}$ (sample 1) and $K_{1.2}Cr_8O_{16}$ (samples 2–5) obtained using different experimental conditions (see experimental section for details).

In a previous work Endo et al.[21] reported on a $K_2Cr_8O_{16}$ sample with Tc = 225 K that was deduced from the M(T) curve measured at a rather high field of H = 1 T. This has been justified by Hasegawa et al.[19] like an overestimation of Tc. However in our case we have avoided that overestimation since measurements were made at 0.1 T. For several samples of $K_{1,2}Cr_8O_{16}$ magnetization have been measured, Fig.10 a) shows that they reach different values of magnetization in ferromagnetic region, keeping the same K^+ amount (then the same Cr^{4+} / Cr^{3+} ratio); this effect can be related to formation of particles with different size (rather than magnetic domains) in the samples. In fact as can shown in tab.2, each sample have been synthesized under different conditions: different amount of oxidant and different time of reaction under stirring; these two parameters have important influence on the sample particle size, influencing consequently the size of magnetic domain.

In order to determine the experimental μ_{eff} from the paramagnetic region of $K_{1,2}Cr_8O_{16}$, we needed to measure the susceptibility up to 400 K, as shown in fig.11.

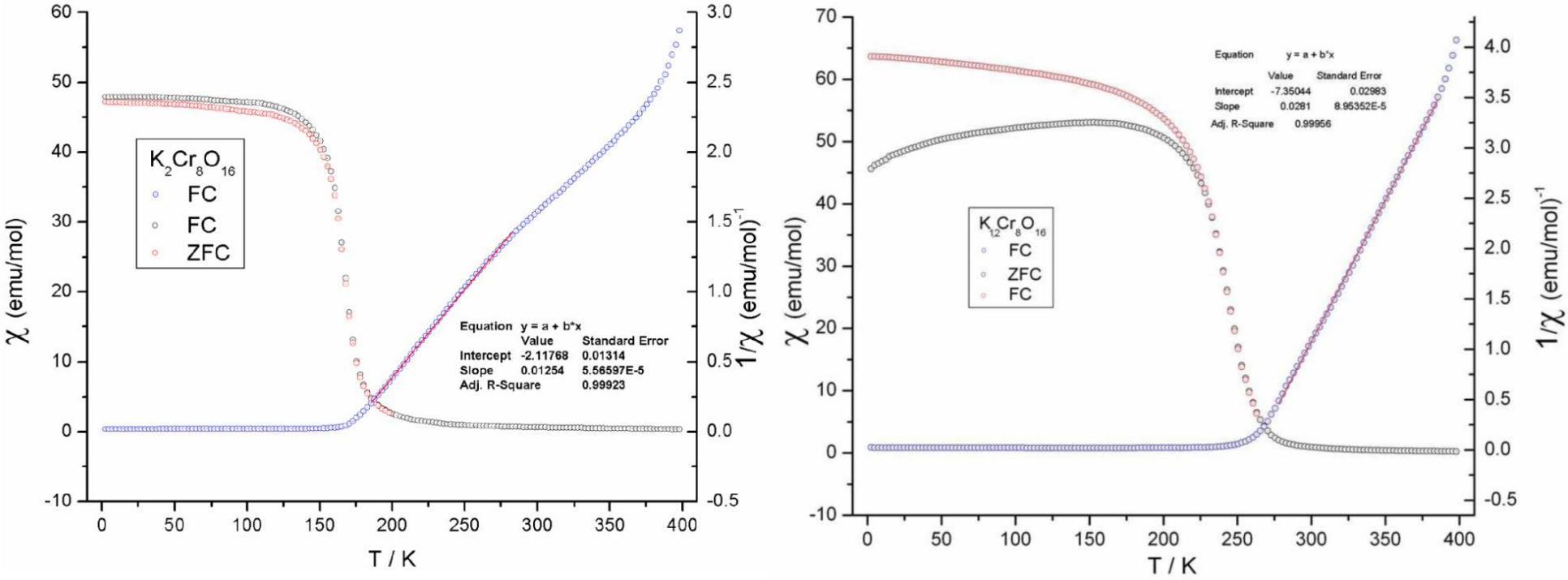

Fig. 11 shows the temperature dependence of the susceptibility for $K_2Cr_8O_{16}$ and $K_{1.2}Cr_8O_{16}$, from 400 to 2.5 K measured in the FC and ZFC mode at a 0.1 T magnetic field.

The fitting of the paramagnetic region of inverse of the susceptibility, using the inverse of the Curie Weiss law: $1/\chi = (T-\theta) / C$, with provided an effective magnetic moment of μ_{eff}= 3.16 x Cr atom and θ = 168.8(1) K, the calculated μ_{eff} for a composition 2 Cr^{3+} and 6 Cr^{4+} resulted in a calculated magnetic moment μ_{cal} = 3.13, in agreement with the experimental value. The susceptibility measurement of $K_{1,2}Cr_8O_{16}$ provided a effective magnetic moment μ_{eff} = 2.11 and a θ = 261.5(8) K; while the calculated one for a composition Cr^{3+} and 7 Cr^{4+} was μ_{cal} = 2.98, thus a slight difference between theoretical and experimental value exist. The theoretical value has been calculated on the basis of a spin free ions model where no interactions exist among other spins; this could explain the difference in values between observed and calculated. The Weiss temperature values of both materials are positive confirming a ferromagnetic behaviour in $K_2Cr_8O_{16}$ and $K_{1,2}Cr_8O_{16}$. The field dependence of magnetization M(H) for $K_{1.2}Cr_8O_{16}$ is reported in Fig. 12. The highest value of magnetization, obtained at 5 K when saturation is reached, corresponds to 13.8 μ_B/8Cr. This value is lower than 17 μ_B, which is expected for chromium atoms located in a simple octahedral crystal field. In the case of $K_2Cr_8O_{16}$ an average oxidation state of Cr +3.75 corresponding to a Cr^{3+}/Cr^{4+} ratio of 1:3 has been proposed.[19]

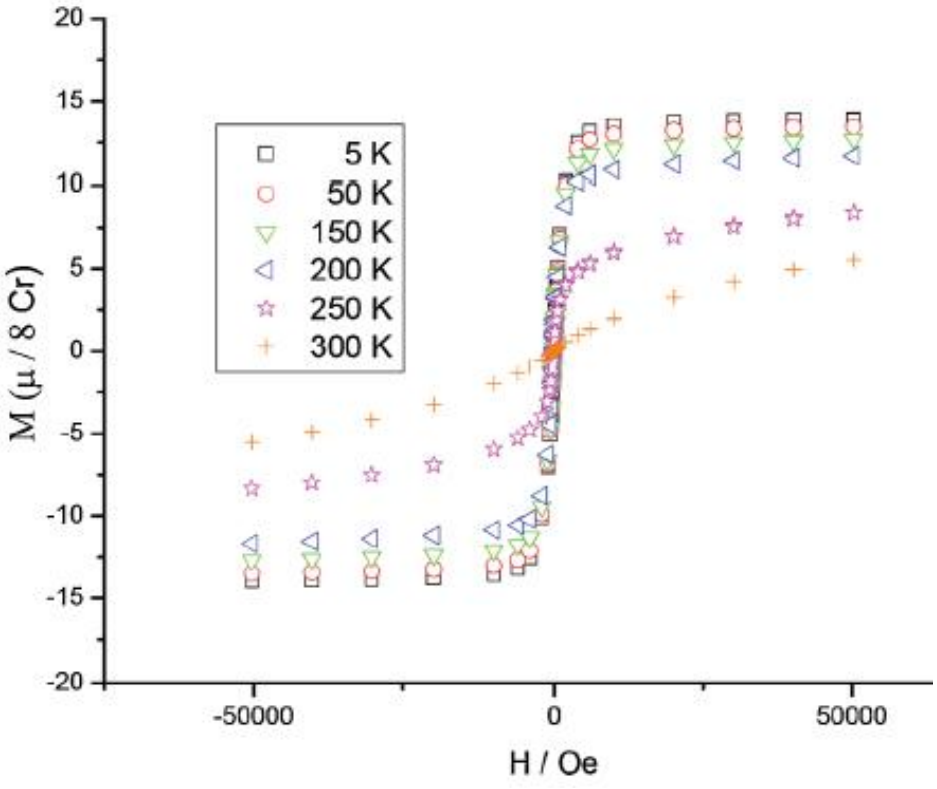

Fig. 12 Field dependence of magnetization for $K_{1.2}Cr_8O_{16}$ in the temperature range 5–300 K.

In the case of the oxidised hollandite $K_{1.2}Cr_8O_{16}$ we expect an average oxidation state of Cr +3.85, which corresponds to a Cr^{3+}/Cr^{4+} ratio of 1:7. Now we need to recall that octahedral crystal field of the cations and the tetragonal structure provide an axial field, which splits the triply degenerate metal t_{2g} orbitals into a non degenerate $t_{\parallel}$ orbital and a doubly degenerate $t_{\perp}$ orbital. While $t_{\perp}$ can form π^* bands with anion p_{π} orbitals, $t_{\parallel}$ forms cation sublattice d bands if the cation-cation distance along the c-axis is less than R_c. In CrO_2, one of the d electrons is in $t_{\parallel}$ and the other in $t_{\perp}$. While the electron in $t_{\parallel}$ is delocalized, in $t_{\perp}$ is in the π^* band formed through cation-anion-cation interaction.[27] Thus, we can explain the observed value of 13.8 μ_B by considering the distribution of electrons for each Cr atom as depicted in Fig. 13, where the contribution of Cr^{4+} and Cr^{3+} follow the same scheme afore mentioned. Thus, the calculated value, 15 μ_B /8 Cr, is closer to the observed (13.8 μ_B / 8 Cr).

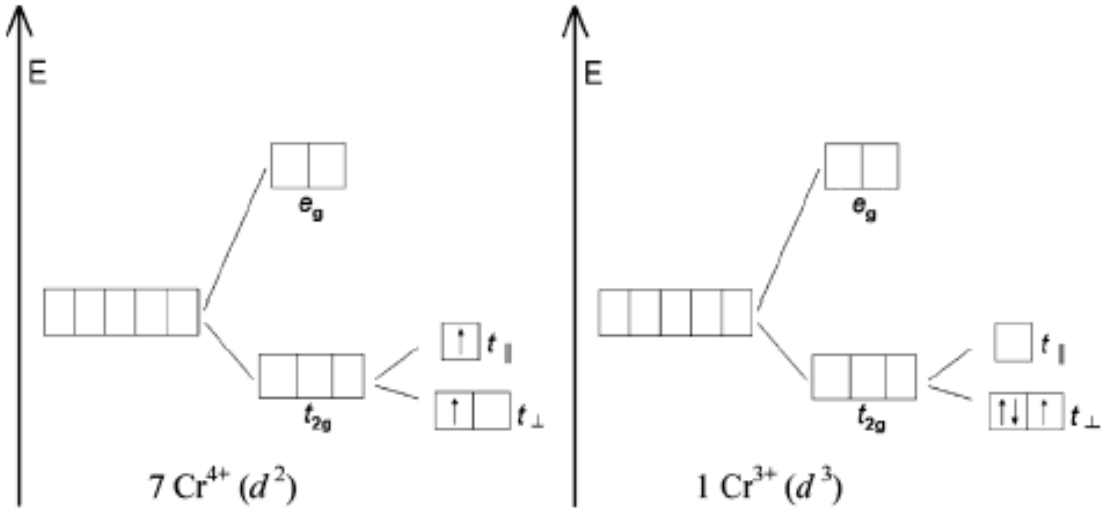

Fig. 13 Proposed crystal field arrangement for $K_{1.2}Cr_8O_{16}$.

4.3.6 Magnetic structure refinement of $K_{1,2}Cr_8O_{16}$ and $K_2Cr_8O_{16}$

The neutron diffraction measurement as a function of temperature performed for $K_{1,2}Cr_8O_{16}$ and for $K_2Cr_8O_{16}$ did not show any extra peak than nuclear reflection previously observed in powder x-ray diffraction measurements; Moreover, some peaks increased in intensity as shown in fig. 14 where 3D and 2D of neutron diffraction measurements vs. temperature for $K_{1,2}Cr_8O_{16}$ and $K_2Cr_8O_{16}$ are plotted.

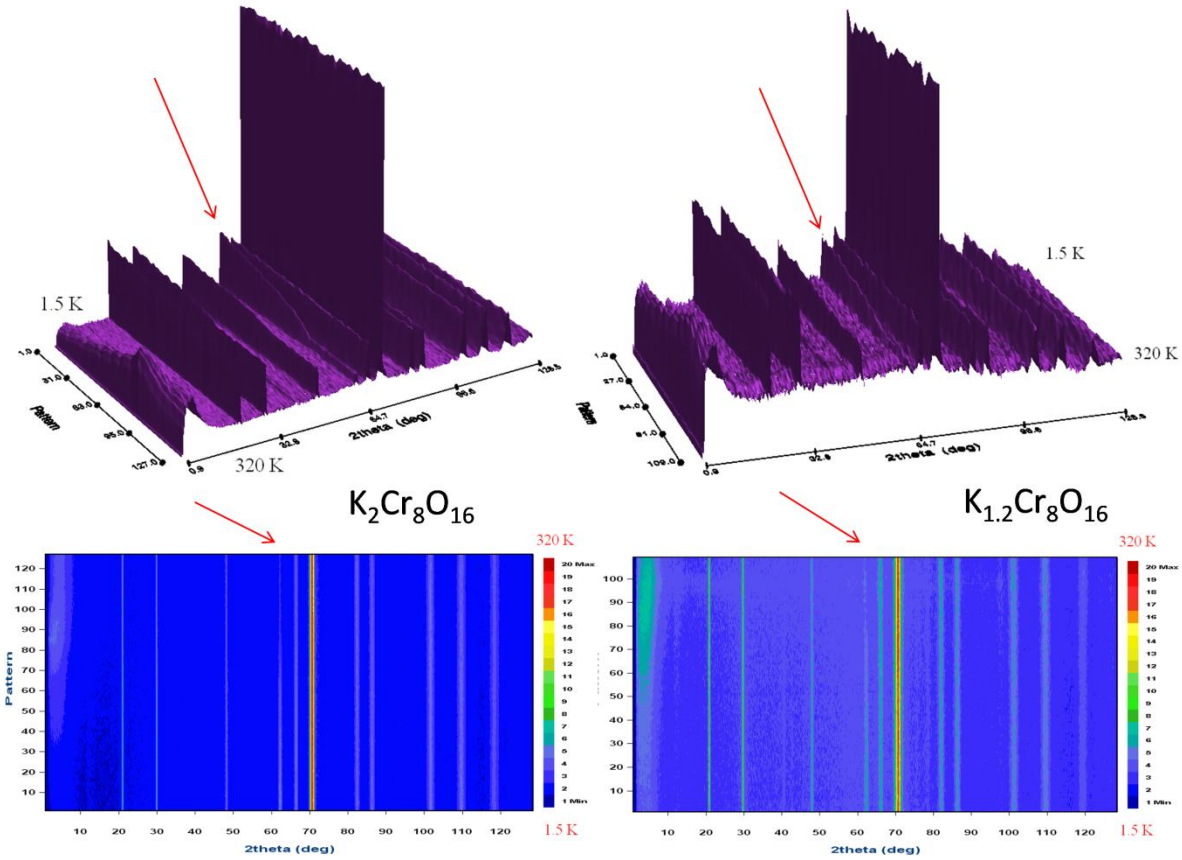

Fig.14 The thermal evolution for $K_2Cr_8O_{16}$ and $K_{1,2}Cr_8O_{16}$ between 320 K and 1.5 K; (pair up) 3D, (pair down) 2D; The red arrows indicate the evolution of intensity for a magnetic contribution to the peak due to transition in ferromagnetic state.

The Rietveld refinements of powder neutron diffraction measurements for both samples have been performed between 320 K and 1.5 K, data have been collected in D1B - High resolution neutron two-axis powder diffractometer with radiation wavelength of λ= 2,52 Å; the device was at the Laue-Langevin Institute, Grenoble, France. The refined lattice parameters of $K_{1,2}Cr_8O_{16}$ differ from $K_2Cr_8O_{16}$ in both values of temperature; At (320 K): $K_2Cr_8O_{16}$ a = b = 9.7452(5) Å, c = 2.9347(8) Å and $K_{1,2}Cr_8O_{16}$ a = b = 9.7966(5) Å, c=2.9161(7) Å; at (1.5 K): $K_2Cr_8O_{16}$ a = b = 9.7514(3) Å , c=2.9347(8) Å and $K_{1,2}Cr_8O_{16}$ a = b = 9.8145(9) Å , c = 2.9191(1) Å . In all cases a tetragonal symmetry is observed and a space group I4/m (S.G. nº 87) has been assigned. K^+ ions occupy the 2b Wyckoff

position while Cr, O1 and O2 occupy the 8h sites. Detailed summary of the lattice parameters, crystallographic data and agreement factors for both phases at the two different temperatures are reported in tab.5; The results obtained by structure refinement of powder neutron diffraction data are in full agreement with powder x-ray diffraction data refinement discussed before in the structure refinement chapters;

Tab. 5 Lattice parameters, crystallographic data and agreement factors for $K_{1,2}Cr_8O_{16}$ and $K_2Cr_8O_{16}$ at 320 K and 1.5 K.

	Powder neutron diffraction (320 K)		Powder neutron diffraction (1.5 K)	
Radiation (Å)	2.52		2.52	
Composition	K2Cr8O16	K1,2Cr8O16	K2Cr8O16	K1,2Cr8O16
Crystal system	Tetragonal	Tetragonal	Tetragonal	Tetragonal
Space group	I 4/m (n°87)	I 4/m (n°87)	I 4/m (n°87)	I 4/m (n°87)
Cell dimensions (a;b;c) (Å)	9.7452(5); 2.9347(8)	9.7966(5); 2.9161(7)	9.7514(3); 2.9347(8)	9.8145(9); 2.9191(1)
Cell Angles (α;β;γ) (°)	90.0; 90.0; 90.0	90.0; 90.0; 90.0	90.0; 90.0; 90 .0	90.0; 90.0; 90.0
Volume (Å^3)	278.71(6)	279.87(7)	279.06(9)	281.18(7)
Bragg R-Factor (%)	7.78	8.97	6.28	8.98
RF-Factor (%)	6.41	7.36	4.34	2.84
Rexp (%)	1.61	6.27	3.54	1.61
Rp (%)	3.01	2.87	4.55	6.26
χ^2	5.92	5.41	14.9	5.34

The summary of thermal parameters, atomic coordinates and occupancy for $K_2Cr_8O_{16}$ and $K_{1,2}Cr_8O_{16}$ at 320 K and 1.5 K are reported in tab. 6. In tab. 7 are reported values of distances (Å) and angles (°) for K or Cr and O, for $K_2Cr_8O_{16}$ and $K_{1.2}Cr_8O_{16}$ obtained by data refinement of x-ray diffraction and neutron powder diffraction at high and low temperatures.

The magnetic reflections can be indexed with the commensurate propagation vector k, k=(0 0 0); At low temperature, measurements of $K_{1,2}Cr_8O_{16}$ and $K_2Cr_8O_{16}$, shown in fig.15 (down right $K_{1,2}Cr_8O_{16}$, down left $K_2Cr_8O_{16}$), two peaks at 40°,45' and 72°,36'2θ° have not indexed. Attempts indexing the diffractogram, including these two peaks, provided very unusual propagation vectors k for a ferromagnet; Several indexing with different space group than I4/m, and magnetic space group I -1, have been took in to account; refinement with a space group P 1 1 21/a, previously suggested for $K_2Cr_8O_{16}$ at 20 K,[20] have been carried out; This solution has been discarded because only one peak fitted (at 72°,36'and already exists at 220 K), while the second one at 40°,45' did not fit with the calculated pattern. We can explain the existence of these two peaks as magnetic reflections from a very small amount of an unknown phases; we believe there are two small amounts of impurities formed during high pressure and high temperature synthesis; one of the impurities is removed (dissolved or decomposed during soft chemical processes), while the other is still present in $K_{1,2}Cr_8O_{16}$.

Fig. 15 Graphical result of the Rietveld refinement of $K_2Cr_8O_{16}$ (up left), $K_{1,2}Cr_8O_{16}$ (up right) at 320 K, $K_2Cr_8O_{16}$ (down left) and $K_{1,2}Cr_8O_{16}$ (down right) at 1.5 K using of powder neutron diffraction data. Experimental data are presented as points and the calculated profile as solid line. The observed difference profile is plotted at the bottom. Vertical bars are the allowed Bragg reflections for space group *I* 4/*m* (at 1.5 K) nuclear reflection in blue, magnetic reflection in red).

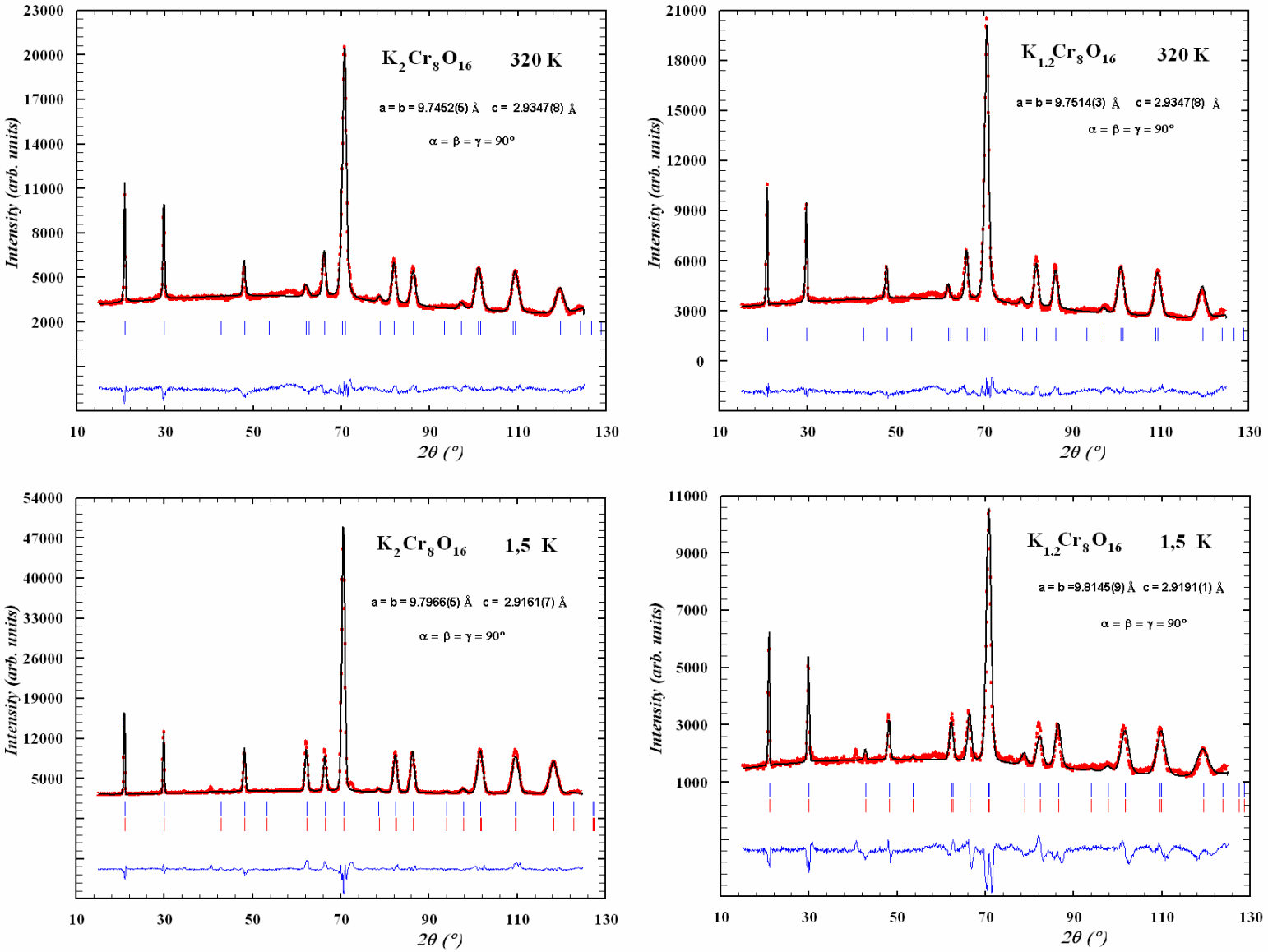

Tab. 6 Summary of thermal parameters, atomic coordinates and occupancy for $K_2Cr_8O_{16}$ and $K_{1,2}Cr_8O_{16}$ at 320 K and 1.5 K.

PWD-ND (320 K)			
K2Cr8O16		Atomic positions	
Atom	X	Y	Z
K	0	0	0.5
Cr	0.3546	0.15845	0
O1	0.1447	0.19335	0
O2	0.55462	0.16944	0
	B	Occupancy	Wickoff position
K	0.75988	0.25	2b
Cr	1.06521	1	8h
O1	0.71328	1	8h
O2	0.71328	1	8h

PWD-ND (320 K)			
K1,2Cr8O16		Atomic positions	
Atom	X	Y	Z
K	0	0	0.5
Cr	0.35161	0.15791	0
O1	0.15141	0.19682	0
O2	0.54139	0.17331	0
	B	Occupancy	Wickoff position
K	0.75988	0.2174	2b
Cr	1.06523	1	8h
O1	0.71328	1	8h
O2	0.71328	1	8h

PWD-ND (1.5 K)			
K2Cr8O16		Atomic positions	
Atom	X	Y	Z
K	0	0	0.5
Cr	0.35461	0.15845	0
O1	0.14469	0.19335	0
O2	0.55462	0.16945	0
	B	Occupancy	Wickoff position
K	0.75988	0.25	2b
Cr	1.0652	1	8h
O1	0.71328	1	8h
O2	0.71328	1	8h

PWD-ND (1.5 K)			
K1,2Cr8O16		Atomic positions	
Atom	X	Y	Z
K	0	0	0.5
Cr	0.35508	0.15937	0
O1	0.14652	0.19305	0
O2	0.54477	0.17854	0
	B	Occupancy	Wickoff position
K	0.75988	0.17935	2b
Cr	1.06523	1	8h
O1	0.71328	1	8h
O2	0.71328	1	8h

Tab. 7 Distances (Å) and angles (°) for K or Cr and O, for $K_2Cr_8O_{16}$ and $K_{1.2}Cr_8O_{16}$ obtained by data refinement of x-ray diffraction and neutron powder diffraction at high and low temperatures.

			Powder x-ray diffraction (298 K)		Powder neutron diffraction (320 K)		Powder neutron diffraction (1,5 K)		neutron (320 - 1,5 K)	
Distances	K-O_{12}	polyhedron	$K_2Cr_8O_{16}$	$K_{1.2}Cr_8O_{16}$	$K_2Cr_8O_{16}$	$K_{1.2}Cr_8O_{16}$	$K_2Cr_8O_{16}$	$K_{1.2}Cr_8O_{16}$	$K_2Cr_8O_{16}$	$K_{1.2}Cr_8O_{16}$
	K–O(1)		2.875(2) x 8	2.871(4) x 8	2.875(1) x 8	2.836(6) x 8	2.774(4) x 8	2.771(6) x 8	0.1007	0.065
	K–O(2)		3.310(2) x 4	3.241(3) x 4	3.234(1) x 4	3.226(8) x 4	3.267(7) x 4	3.161(7) x 4	-0.0336	0.0651
Mean	K–O		3.02	2.99	2.994	2.966	2.938	2.901	0.056	0.065
Distances	CrO_6	octahedron								
	Cr–O(1)		1.932(4)	1.851(6)	1.950(3)	2.00(2)	2.075(1)	2.103(1)	-0.1248	-0.1011
	Cr–O(1*)		1.964(3) x 2	1.987(4) x 2	2.051(1) x 2	2.038(1) x 2	2.060(7) x 2	2.047(1) x 2	-0.0096	-0.009
	Cr–O(2*)		1.912(3) x 2	1.883(4) x 2	1.850(1) x 2	1.868(1) x 2	1.798(7) x 2	1.886(1) x 2	0.0514	-0.018
	Cr–O(2)		1.871(4)	1.918(6)	1.870(2)	1.870(2)	1.953(1)	1.840(1)	-0.0829	0.0301
Mean	Cr–O		1.926	1.918	1.937	1.947	1.957	1.968	-0.02	-0.021
O(1*)–O(1*);	O(2*)–O(2*)		2.935(2)	2.909(2)	2.915(6)	2.916(2)	2.934(7)	2.918(4)	-0.0191	-0.0022
	O(1*)–O(2*)		2.529(3)	2.534(6)	2.560(2)	2.574(1)	2.470(8)	2.597(9)	0.0894	-0.0238
Angles	CrO_6	octahedron								
	O(1)–Cr–O(2)		169.0(3)	167.4(4)	161.5(1)	164.4(1)	167.4(7)	165.6(1)	-5.89	-1.2
	O(1*)–Cr–O(2*)		75.8(2)	81.76(15)	79.2(1)	89.3(8)	87.9(5)	84.2(6)	-8.74	5.12
	O(1*)–Cr–O(1*)		101.9(3)	94.1(2)	90.6(6)	91.4(5)	90.8(3)	90.9(4)	-0.17	0.51
	O(2*)–Cr–O(2*)		105.6(3)	101.2(3)	100.1(1)	100.3(9)	99.3(5)	104.7(8)	0.76	-4.39

The evolution of Cr magnetic moment as function of temperature is shown in Fig.16: $K_2Cr_8O_{16}$ in fig.16a) and $K_{1,2}Cr_8O_{16}$ in fig.16b next page); Magnetic momentum data at several temperatures have been refined by sequential refinement and have fitted using the so called critical law, (from the Bloch $T^{3/2}$ law), $m(T) = m(0)[1 - (T/TC)]^{\beta}$; the values of Tc obtained by fitting the curves in fig.16a) and b), have not to be confused with values from magnetic measurements (see 4.3.5 chapter and fig.11); the Tc values here reported, are referring to high temperature range (T > 300 K), in this range a transition has been detected by a change in slope of χ/T measurements in fig.11.This high temperature transitions have not been observed before in previous works for these materials; it could suggest that a different order can take place at T > 300 K. Our measurements did not scan that range of temperature and we are not able to provide more details these phenomena.

The value of m(0) represent the maximum value of magnetic moment reached by Cr atom, this occurs at lowest temperature; the critical value β for $K_2Cr_8O_{16}$ is $\beta = 0.30(9)$ that agrees with the three-dimensional Heisenberg model $\beta \approx 0.36$; less agreement exist in the case of $K_{1,2}Cr_8O_{16}$ with $\beta = 0.23$.

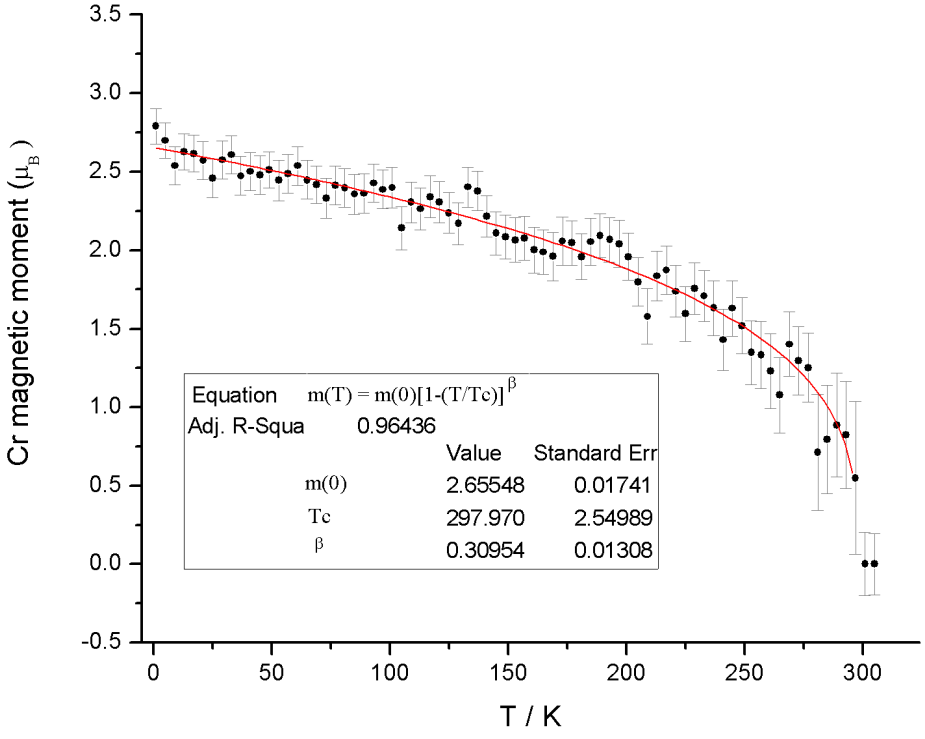

Fig.16a The evolution of Cr magnetic moment as function of temperature for $K_2Cr_8O_{16}$; The experimental data have fitted using the so called critical law, (from the Bloch $T^{3/2}$ law).

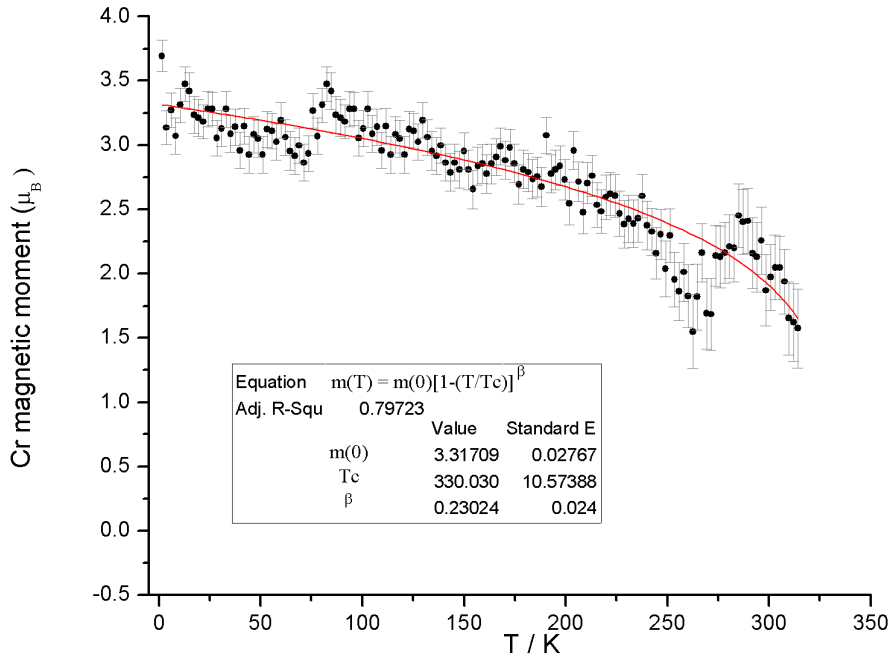

Fig.16b The evolution of Cr magnetic moment as function of temperature for $K_{1,2}Cr_8O_{16}$; The experimental data have fitted using the so called critical law, (from the Bloch $T^{3/2}$ law).

The models of magnetic structure obtained by data refinement of $K_2Cr_8O_{16}$, $K_{1,2}Cr_8O_{16}$ at 1.5 K, are in agreement with magnetic measurements of χ / T previously reported,[19] the structures are paramagnetic at high temperature and ferromagnetic below their T_c; the resulting magnetic moments coincide with the atomic position of Cr (k = 0,0,0) and they are aligned along the c axis of the structure, as can be seen in fig.17;

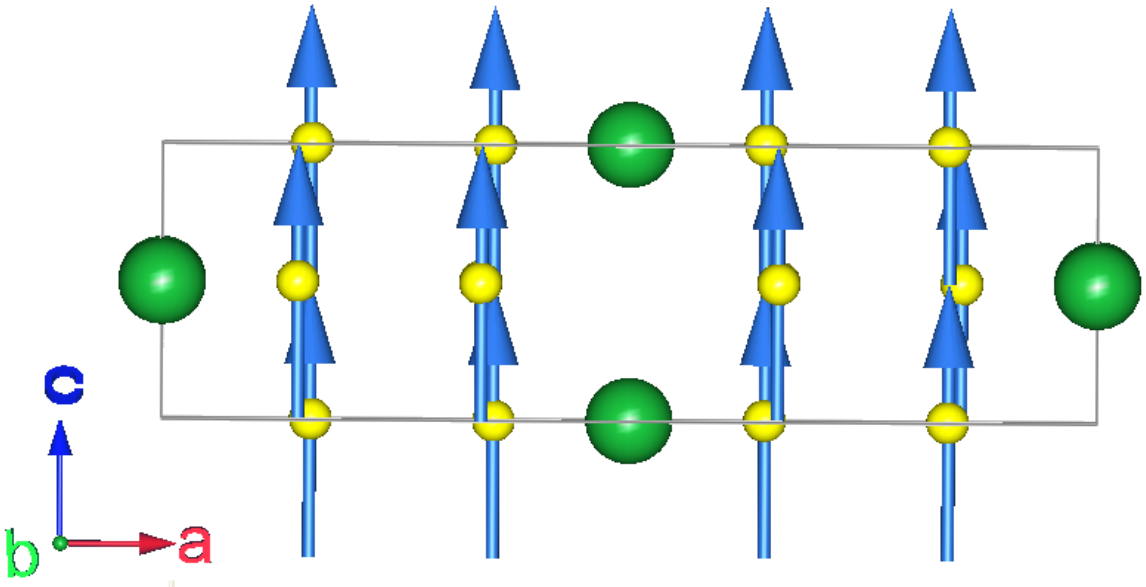

Fig. 17 View along [101] of the unit cell of $K_2Cr_8O_{16}$ (and $K_{1,2}Cr_8O_{16}$) at 1.5 K, the ferromagnetic phase; the blue arrows are the magnetic moments of Cr aligned aligned along c axis, Cr ions drawn in yellow, K^+ is represented by green spheres, oxygen anions have been hidden for clarity.

$K_2Cr_8O_{16}$ and $K_{1,2}Cr_8O_{16}$ are not the only oxides where physical properties are dependent of structural changes and oxides having similar hollandite structure like $K_{2-x}Rb_xV_8O_{16}$ [23,28]

and $K_2V_8O_{16}$ [24] show properties are, respectively chemical substitution and applied pressure dependent. These effects induce variations in the metal-insulator and ferromagnet-paramagnet transitions. Applying pressure in $K_2V_8O_{16}$, a shift of T_C at lower temperature is induced; so a negative effect is observed applying pressure; In the case of $K_{2-x}Rb_xV_8O_{16}$ the shift of metal-insulator transition and the shift of magnetic transition (the kind of magnetic phase transition have not been specified by the authors see ref. 24) increase with an expansion of the lattice (decreasing of applied pressure). A remarkable difference between K-Rb (or K) - V hollandites and K - Cr hollandites is that the shift of transition temperature is generated by change in pressure rather than a change in mixed valence; while in the K-Rb (or K) - V hollandites valence state of V ions is kept.[23] The ferromagnetic alignment have been explained by means of double exchange mechanism,[29,30] This was first explained by Zener' in the following way: (1) intra-atomic exchange is strong so that the only important configurations are those where the spin of each carrier is parallel to the local ionic spin; (2) the carriers do not change their spin orientation when moving; accordingly they can hop from one ion to the next only if the two ionic spins are not antiparallel; (3) when hopping is allowed the ground state energy is lowered (because the carriers are then able to participate in the binding). This results in a lower energy for ferromagnetic configurations. This "double exchange" is completely different from the usual (direct or indirect) exchange couplings, as pointed out by Anderson and Hasegawa.[29]In our case, one d electron t_{2g} of Cr^{3+} hop in an empty t_{2g} orbital of Cr^{4+}, as shown in fig. 18;

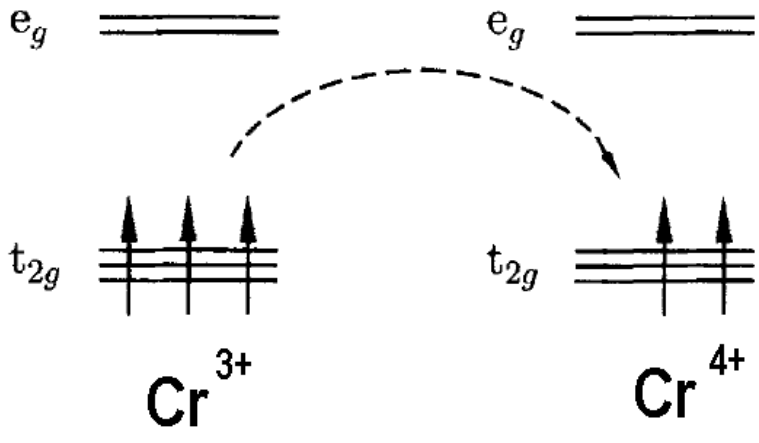

Fig. 18 The double exchange model in $K_2Cr_8O_{16}$ and $K_{1,2}Cr_8O_{16}$.

following the conditions pointed out before, filled t_{2g} orbials of Cr^{3+} should be oriented parallel to those of Cr^{4+} in $K_2Cr_8O_{16}$ and $K_{1,2}Cr_8O_{16}$.

As established in point (2), to generate ferromagnetism by the mechanism of double exchange, is fundamental the condition of not antiparallelism between orbitals involved in the exchange;[31] following Hubbard's and Goodenough works, the angle θ of the spin, hopping from Cr^{3+} and d Cr^{4+} orbitals, has to be zero (in the most favourable case) or having a very small value.[31]

Magnetic measurement revealed that in $K_{1,2}Cr_8O_{16}$ has a higher value of Tc than in $K_2Cr_8O_{16}$; this means a stronger ferromagnetic interaction between spins in $K_{1,2}Cr_8O_{16}$ than in $K_2Cr_8O_{16}$; then double exchange should have higher efficiency in $K_{1,2}Cr_8O_{16}$ than $K_2Cr_8O_{16}$; these evidences drive us to consider that the higher T_c (higher ferromagnetism) experimented in $K_{1,2}Cr_8O_{16}$ is probably due to a smaller value of the θ angle of the spin, hopping from Cr^{3+} to Cr^{4+} orbital, in $K_{1,2}Cr_8O_{16}$ than $K_2Cr_8O_{16}$; This suggest that the relative orientation between Cr^{3+} and Cr^{4+} t_{2g} orbitals, involved in hopping mechanism, is closer to a parallel configuration in $K_{1,2}Cr_8O_{16}$ rather than $K_2Cr_8O_{16}$. The change of relative orientation between d orbitals as function of composition have than a structural explanation: differences between $K_{1,2}Cr_8O_{16}$ and $K_2Cr_8O_{16}$ have been observed in O-Cr-O angles and Cr-O distances (see tab 7, last column); Then variation of O-Cr-O angles and Cr-O distances have been caused by substitution of Cr^{3+} (0,75 Å) with the smaller Cr^{4+} (0,69 Å) in the structure (confirmed by magnetic measurement and coupled to extraction of K^+ from hollandite structure.

4.4 Conclusions

Electrochemical and chemical oxidation has been successfully applied to the half-metallic ferromagnet $K_2Cr_8O_{16}$ to partly extract K ions from the hollandite tunnel. Oxidation reaction results in new potassium deficient $K_{2-x}Cr_8O_{16}$ Cr-hollandites with $x_{max} = 0.8$. Structural characterisation shows that potassium extraction (oxidation) proceeds topotactically with some noticeable changes of the tetragonal cell parameters. The partial extraction of the K tunnel cation give rise to, among other effects widely described before, an unusual thermal parameter value B_{iso}, explained by an elongated electron density distribution along the tunnel direction. Interestingly, we have observed an important change in the magnetic properties. Potassium deficient hollandites $K_{2-x}Cr_8O_{16}$ are ferromagnetic with a Curie temperature of 250 K which is 70K higher than the one reported for the pristine material $K_2Cr_8O_{16}$ (180 K). In both samples, neutron diffraction measurements confirmed a paramagnetic -> ferromagnetic phase transition decreasing temperature, following the double exchange mechanism; moreover fitting refined magnetic momentum curves as function of temperature, by using the spin wave model, confirm the transition at high temperature for $K_2Cr_8O_{16}$ and $K_{1,2}Cr_8O_{16}$ respectively; these values are in agreement with the change in slope observed in magnetic susceptibility measurements; likely observed for T_c, these values are shifted as function of relative proportion Cr^{3+} / Cr^{4+} in the structure, this behaviour have not been observed until this date in $K_2Cr_8O_{16}$ and $K_{1,2}Cr_8O_{16}$ materials. In structural related systems, similar properties have been observed; tuning physical parameters, reversible effects on properties have reported; in our case irreversible modification of properties have induced by means of chemical and/or electrochemical modification.

4.5 Bibliography

1. Bystrom, A. and A.M. Bystrom, *The crystal structure of hollandite, the related manganese oxide minerals, and α-MnO_2.* Acta Crystallographica, 1950. 3(2): p. 146-154.
2. Wadsley, A.D. and S. Andersson, *Alkali Metal Titanium Oxide Bronzes.* Nature, 1961. 192(4802): p. 551-552.
3. Andersson, S. and A.D. Wadsley, *The Crystal structure of $K_2Ti_2O_5$. Acta Chem. Scand.*, 1961. 15: p. 663.
4. Gutierrez-Florez, M.T., A. Kuhn, and F. Garcia-Alvarado, *Intercalacion electroquimica de litio en $K_{1,2}Ti_8O_{16}$ y sintesis de nuevos bronces $K_{1,2-x}Ti_8O_{16}$.* Boletin de la sociedad española de ceramica y vidrio, 1998. 37(2-3): p. 260-363.
5. Gutierrez-Florez, M.T., A. Kuhn, and F. Garcia-Alvarado, *Lithium intercalation in $K_xTi_8O_{16}$ compounds.* International Journal of Inorganic Materials, 1999. 1(1): p. 117-121.
6. Sasaki, T., M. Watanabe, and Y. Fujiki, *Structure of $K_{1.0}Ti_8O_{16}$ and $K_{0.0}Ti_8O_{16}$.* Acta Crystallographica Section B, 1993. 49(5): p. 838-841.
7. Latroche, M., et al., *New hollandite oxides: TiO_2(H) and $K_{0.06}TiO_2$.* Journal of Solid State Chemistry, 1989. 81(1): p. 78-82.
8. Tamada, O., et al., *The Crystal Structure of $K_2Cr_8O_{16}$: The Hollandite-Type Full Cationic Occupation in a Tunnel.* Journal of Solid State Chemistry, 1996. 126(1): p. 1-6.
9. Abriel, W., F. Rau, and K.J. Range, *New compounds $A_{2-x}V_8O_{16}$ (A = K,Tl) with hollandite type structure.* Materials Research Bulletin, 1979. 14(11): p. 1463-1468.
10. Xu, C.Y., et al., *Microstructural characterization of single-crystalline potassium hollandite nanowires.* Mater. Charact., 2008. 59: p. 1805-1808.
11. Vogt, T., et al., *Structural analysis of a potassium hollandite $K_{1.35}Ti_8O_{16}$.* Journal of Solid State Chemistry, 1989. 83(1): p. 61-68.
12. Fanchon, E., et al., *Commensurate ordering and domains in the $Ba_{1.2}Ti_{6.8}Mg_{1.2}O_{16}$ hollandite.* Acta Crystallographica Section B, 1987. 43(5): p. 440-448.
13. Marchand, R., L. Brohan, and M. Tournoux, *TiO_2(B) a new form of titanium dioxide and the potassium octatitanate $K_2Ti_8O_{17}$.* Materials Research Bulletin, 1980. 15(8): p. 1129-1133.
14. Ishiwata, S., et al., *Structure and magnetic properties of hollandite $Ba_{1.2}Mn_8O_{16}$* J. Phys.: Condens. Matter., 2006. 18: p. 3745-3752.

15. Brock, S.L., et al., *A Review of Porous Manganese Oxide Materials.* Chemistry of Materials, 1998. 10(10): p. 2619-2628.
16. Feng, Q., et al., *Hydrothermal soft chemical synthesis of NH^{+4} form of hollandite-type manganese oxide. J. Mater. Sci. Lett.*, 1999. 18: p. 1375.
17. Barbato, S. and J.L. Gautier, *Hollandite cathodes for lithium ion batteries. 2. Thermodynamic and kinetics studies of lithium insertion into $BaMMn_7O_{16}$ (M = Mg, Mn, Fe, Ni). Electrochim. Acta*, , 2001. 46: p. 2767.
18. Mao, Z.Q., et al., *Quantum phase transition in quasi-one-dimensional $BaRu_6O_{12}$.* Phys. Rev. Lett., 2003. 90: p. 186601.
19. Waki, T., et al., *Metal–Insulator Transition in $Bi_xV_8O_{16}$: ^{51}V NMR Study. J. Phys. Soc. Jpn.*, 2004. 73: p. 275.
20. Hasegawa, K., et al., *Discovery of Ferromagnetic-Half-Metal to Insulator Transition in $K_2Cr_8O_{16}$.* Physical Review Letters, 2009. 103(14): p. 146403.
21. Toriyama, T., et al., *Peierls Mechanism of the Metal-Insulator Transition in Ferromagnetic Hollandite $K_2Cr_8O_{16}$.* Physical Review Letters. 107(26): p. 266402.
22. Endo, T., et al., *A new compound $K_2Cr_8O_{16}$with hollandite type structure.* Materials Research Bulletin, 1976. 11(6): p. 609-614.
23. Komarek, A.C., et al., *Dimerization and Charge Order in Hollandite $K_2V_8O_{16}$.* Physical Review Letters. 107(2): p. 027201.
24. Isobe, M., S. Koishi, and Y. Ueda, *Rb-substitution effect on the metal-insulator transition of hollandite vanadate, $K_2V_8O_{16}$.* Journal of Physics: Conference Series, 2008. 121(3): p. 032007.
25. Isobe, M., et al., *Observation of Metal–Insulator Transition in Hollandite Vanadate, $K_2V_8O_{16}$.* J. Phys. Soc. Jpn., 2006. 75: p. 073801.
26. Rodriguez-Carvajal, J., *Recent advances in magnetic structure determination by neutron powder diffraction.* Physica B: Condensed Matter, 1993. 192(1-2): p. 55-69.
27. Giacovazzo, C., et al., *Fundamentals of Crystallography, 2^{nd} edition,*. IUCR, Oxford science pubblication, New York, 2002.
28. Rao, C.N.R. and B. Raveau, *Transition Metal Oxides.* Wiley-VCH pubblishers, New York, 1995.
29. Yamauchi, T., et al., *Electromagnetic properties of hollandite $K_2V_8O_{16}$ under pressure.* Physical Review B, 2011. 84(11): p. 115104.
30. Andeson, P.W. and H. Hasegawa, *consideration on double exchange. Phys. Rev. B*, 1955. 84: p. 115104.

31. Blundell, S., *Magnetism in condensed matter*. 2001.
32. Goodenough, J.B., *Magnetism and the Chemical Bond*. Interscience Wiley, New York, 1963.

High pressure synthesis and study of the solid solution $Bi_{1-x}Pb_xCrO_3$ with special interest to x = 0,5, the lone-pair electron $Bi_{0,5}Pb_{0,5}CrO_{3-\delta}$ perovskite

5.1 Introduction

Among all ternary oxide structures, perovskite ABO_3 represents one of the most important and studied structures in solid state sciences. These oxides, depending on their composition, can have several interesting properties: superconductivity (e.g. $Ba_{1-x}K_xBiO_3$), colossal magnetoresistance (e.g. $La_{1-x}Ca_xMnO_3$), itinerant electron ferromagnetism (e.g. $SrRuO_3$), ferroelectricity (e.g. $BaTiO_3$), piezoelectricity (e.g. $PbZr_{1-x}Ti_xO_3$), ionic conductivity (e.g. $La_{0.67-x}Li_{3x}TiO_3$, $BaCeO_{3-x}$) and multiferroic behavior (e.g. $TbMnO_3$), among others materials.[1] The interest in multiferroic materials has grown very fast in the last decades.[2] A preferred path in the strategy for new candidates as multiferroic materials, is the combination of cations having magnetic properties in the B position with other cations having lone pairs in the A position that could induce polarized and/or non-centrosymmetric structures. The cases of $BiCrO_3$ and $PbCrO_3$ are examples of those explorations, both needing high pressure (respectively 40 Kbar and 55 Kbar) and high temperature ($800 < ºC < 1000$) conditions (HP/HT) to be synthesized.[3-8] $BiCrO_3$ synthesized under a high pressure from 35 to 55 Kbar, has been largely studied in the past. It undergoes a structural phase transition at 410 K. Low and high temperature phases have perovskite structures with triclinic and monoclinic symmetries, respectively. $BiCrO_3$ shows a parasitic ferromagnetic ordering at 123 K. Concerning the electrical properties of $BiCrO_3$, it has been reported that the structural phase transition from a noncentrosymmetric to a centrosymmetric structure occurred at about 420 K, involving the anomaly of the dielectric permittivity;[5] A parasitic ferromagnetic ordering occurs at 114 K. Therefore they have confirmed that $BiCrO_3$ has an electric polarization and exhibits parasitic ferromagnetism simultaneously.

$PbCrO_3$ has been synthesized and characterized for the first time by Roth and De Vries;[6] they found for this perovskite a cubic symmetry (a = 4,00Å), and an antiferromagnetic structure with a T_N=240 K. Recently a deeper investigation about microstructure, magnetic and electrical properties has been carried out by Arevalo and al., who reported evidences about a modulation of Pb^{2+} where occupational and displacive modulation coexist; further magnetic measurements validated the AFM behaviour and revealed a new temperature-driven spin reorientation starting at 185 K and ending at 62 K in this phase.[7,8] These authors correlated that behaviour with the A cation modulation previously observed. This strategy of combining two cations in the A position having lone pairs with a magnetic cation in the B position leading to an $AA'B_2O_6$ perovskite, drove us to the HP/HT synthesis of a new phase $BiPbCr_2O_6$ (or $Bi_{0,5}Pb_{0,5}CrO_3$) which structural and physical characterizations are reported in this chapter.

5.2 Experimental Section

The oxide $BiPbCr_2O_6$ was prepared by means of HP/HT conditions, using a Belt-type press. Stoichiometric amounts of α-PbO, Bi_2O_3, Cr_2O_3 and CrO_2 according to the reaction:

$$\alpha\text{-PbO} + Bi_2O_3 + Cr_2O_3 + CrO_2 \rightarrow BiPbCr_2O_6$$

have been grounded, intimately mixed in an agate mortar and placed in a Pt crucible; The synthesis has been performed at 1000°C and 70 Kbar and different reaction times of 8', 15' and 30' have been tested.

Powder X-ray diffraction patterns were recorded on a Panalytical model X'Pert PRO MPD Alfa1 diffractometer, using monochromatic Cu-Ka (λ = 1.54056 Å) radiation obtained with a germanium primary monochromator. Data were collected in the range 2θ = 5.0 - 120.0, with a step of 0.017 (2θ) over a total exposure time period of 12 h. The powder diffraction data have been indexed by TREOR and DICVOL softwares;[9,10] and analyzed by the Rietveld method, using the FullProf-Suite program as well as the simulated pattern.[11, 12]

Low temperature thermodiffraction measurements have been performed in a range of 14 – 298 K in a X'Pert PRO – TT diffractometer, with a Cu source (Kα1 = 1.54056 Å and Kα2 = 1.54439 Å), equipped with a low temperature chamber Phenix Oxford Cryosystems.

The oxygen content was determined twice by thermogravimetric analysis (TGA) on a Cahn D-200 electrobalance in a gas mixture of H_2/He (200mbar / 400mbar) using different amounts of sample, and heating cycles as well.

Samples for transmission electron microscopy and high resolution transmission electron microscopy (TEM and HRTEM) were prepared by grinding the powder, dispersing it in n-butyl alcohol and collecting few drops of the suspension on a holey carbon-coated copper grid. Selected area electron diffraction (SAED) was performed using a JEOL JEM FX2000 microscope, equipped with a double tilt +/-45° holder, working at 200 kV. HRTEM was carried out on a JEOL JEM 3000FEG microscope, with Cs = 0.6 nm, operating at 300 kV. Both microscopes are equipped with EXDS analyzers, that have been used to determine the composition of the analyzed microcrystals. HRTEM images have been simulated by means of the Mac Tempas software varying the focus between -600 Å <(step of 100 Å) < -100 Å and the thickness between 11 < (27.4 Å) < 93.1 Å.[13]

The magnetization measurements in ZFC and FC modes of M / T between 2-300 K, M / H at 5 K between 0-5 T, AC applied field of M / T at 33, 330, 660 and 1000 Hz, DC applied field of M / T between 5-300 K at 1000 and 5000 Oe, were performed using a SQUID

Quantum Design XLMPM. Resistivity measurements have been performed with a Quantum Design PPMS. A QuadTech impedance analyzer was used for dielectric spectroscopy with an applied ac amplitude of 20 mV operating between 20 Hz – 1 MHz. To facilitate frequency (f), temperature (T) and magnetic field (*H*) dependent dielectric measurements, a special sample holder was used (Janis Research Ltd., USA), which can fit into a Quantum Design PPMS measurement system providing variable *H* (up to 140 kOe) and variable *T* (10 – 320 K).The custom built probe was necessary to minimize the internal probe capacitance (≈ 0.2 pF) and maximize the internal probe resistance (≈ 10 GΩ), which is both detrimental for reliable alternating current (ac) dielectric measurements. The sample tray at the bottom of the probe was equipped with spring loaded drop-down pins to ensure optimal contact between the pins and the Au electrodes sputter deposited onto two opposing faces of the $Bi_{0,5}Pb_{0,5}CrO_3$ bulk samples. Equivalent circuit fitting of the dielectric data collected at variable *f*, *T* and *H* was performed by employing commercial Z-View® fitting software, where each equivalent circuit model was fitted to both the real and imaginary parts of the *f*-dependent impedance data by minimizing the statistically weighted linear least-squares.

5.3 Results and discussion

5.3.1 The study of the solid solution $Bi_{1-x}Pb_xCrO_3$

The study of the solid solution $Bi_{1-x}Pb_xCrO_3$ have been performed by means of high pressure and high temperature reactions. The stoichiometry of reactants have been adjusted in order to synthesize the members of solid solution with values of x = 0,25, 0,4, 0,5, 0,6 and 0,75.

A first structural characterization by means of powder x-ray diffraction, shown in fig.1, revealed that Bi^{3+} and Pb^{2+} cannot be miscible in all proportions in the solid solution $Bi_{1-x}Pb_xCrO_3$. Moreover Pb^{2+} is more miscible in Bi^{3+} rich phase than Bi^{3+} in the Pb^{2+} rich phase.

In order to obtain the total substitution by a fixed amount of Pb^{2+} with Bi^{3+} in bismuth rich phase (and the total substitution by a fixed amount of Bi^{3+} with Pb^{2+} in lead rich phase), for the selected point of solid solution, several synthesis have been performed changing the pressure and temperature parameters. These experiments, performed at higher pressure and higher temperature than first attempts, shown that in all cases secondary phases were still presents.

The members of solid solution that shown full miscibility between Bi^{3+} and Pb^{2+} have been found to be x = 0,5 ($Bi_{0,5}Pb_{0,5}CrO_3$) and x = 0,25 ($Bi_{0,75}Pb_{0,25}CrO_3$) at the synthetic condition of 70 Kbar, 1000 ºC and a reaction time of 15 min.

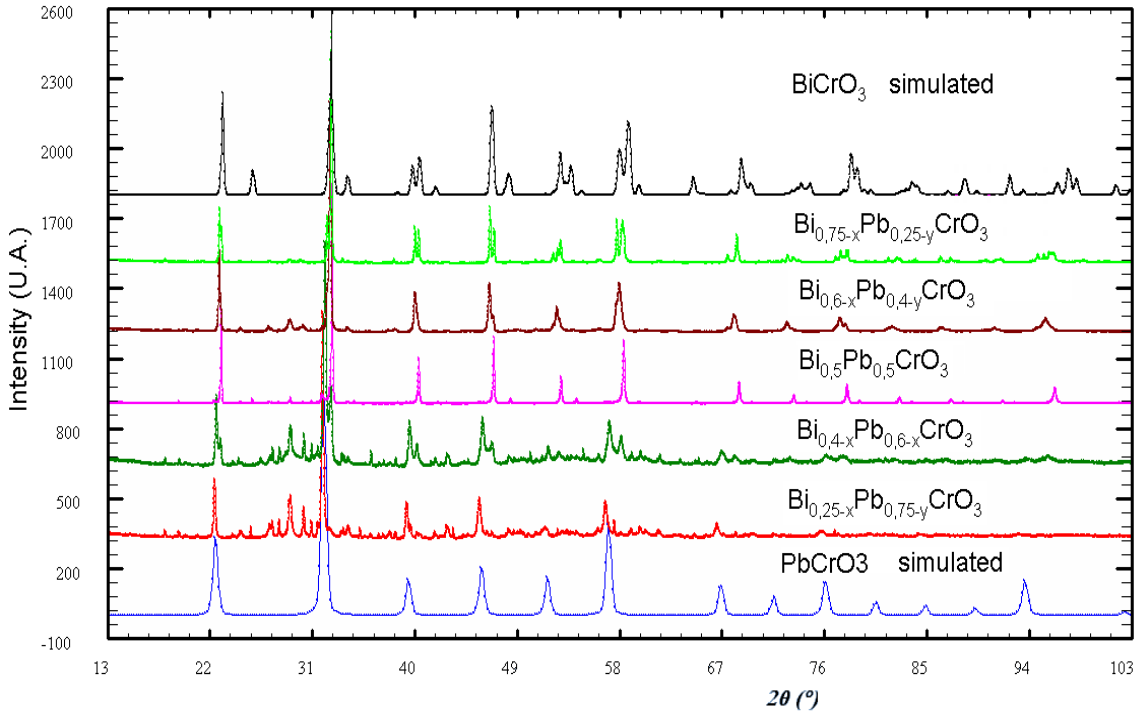

Fig. 1 The x-ray diffraction patterns of the members of solid solution $Bi_{1-x}Pb_xCrO_3$ studied in this work; does not exist a continuous miscibility along the full range of solid solution; $BiCrO_3$ and $PbCrO_3$ patterns are simulated from literature data.[3-8]

5.3.2 The case of $Bi_{1-x}Pb_xCrO_{3-\delta}$: optimization of synthesis reaction

Indeed, all three variables: Pressure, Temperature and time have to be optimized to obtain the desired composition, also that the optimum conditions are included in an ortohedron with sides P, T and t. Below the optimum, the material does not form; above, it decomposes.

Following these studies, we have found that the best conditions to form $Bi_{0,5}Pb_{0,5}CrO_3$ are 70 Kbar, 1000 ºC and a reaction time of 15 min. This can be schematized as shown in tab.1 and powder x-ray diffraction are reported in fig. 2.

Tab.1 Product of reaction in function of reaction time.

Reaction time (t / min)	Product of reaction
8'	(**)PbO + (***)Cr_2O_3 + (@)Bi2O3 + $Bi_{0,5}Pb_{0,5}CrO_3$ (majority phase)
15'	$Bi_{0,5}Pb_{0,5}CrO_3$ + small amount other Bi-Pb-Cr HP oxides
30'	$Bi_{0,5}Pb_{0,5}CrO_3$ + higher amount of Bi-Pb-Cr HP oxides than in 15' synthesis

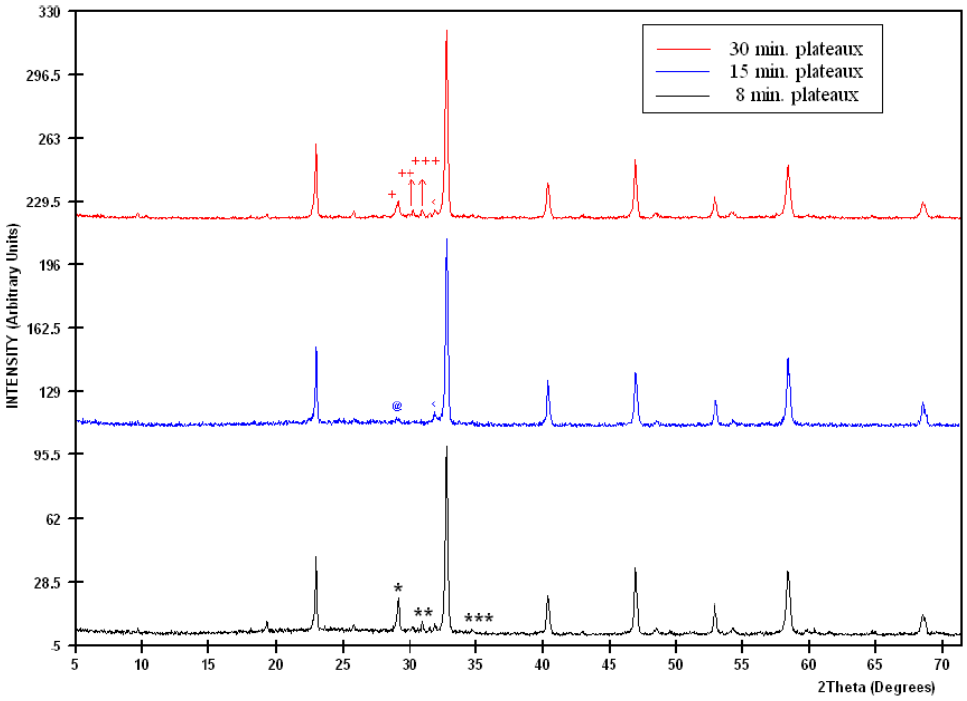

Fig.1 Comparison between different reaction time in the synthesis of $BiPbCr_2O_6$: (*) Bi_2O_3, (**)PbO, (***)Cr_2O_3; (@)Bi_2O_3, (<)$PbCrO_3$, (+)δ-Bi_2O_3, (++), (+++) unknown Bi and Cr High pressure oxides from decomposition of
$Bi_{0,5}$ $Pb_{0,5}CrO_{3-\delta}$.

5.3.3 Thermogravimetric analysis:

To determine the oxygen content of $BiPbCrO_6$, controlled reduction reactions in a Cahn balance with two different heating profiles, fig.2, have been carried out. The reduction reactions of $BiPbCr_2O_6$ under a H_2/He atmosphere which can be expressed as:

$$BiPbCr_2O_{6-x} + x/2\ H_2 \rightarrow (Bi,Pb)alloy + Cr_2O_3 + x\ H_2O\uparrow$$

The weight loss values are reported in tab. 2, values are concordant; the mean for two weight loss values is 7.43% which corresponds to x = 0,16. Therefore the correct stoichiometry of our phase is: $BiPbCr_2O_{5.84}$ ($Bi_{0,5}Pb_{0,5}CrO_{2,92}$) with an estimated contents of Cr^{4+} = 0,68 and Cr^{3+} = 1.32 and a ratio Cr^{4+} / Cr^{3+} equal to 0.51. We anticipate here that the defect in oxygen amount measured in this material does not produce ordered arrangement of vacancies, in fact no evidence of oxygen vacancy order was observed by HRTEM experiments.

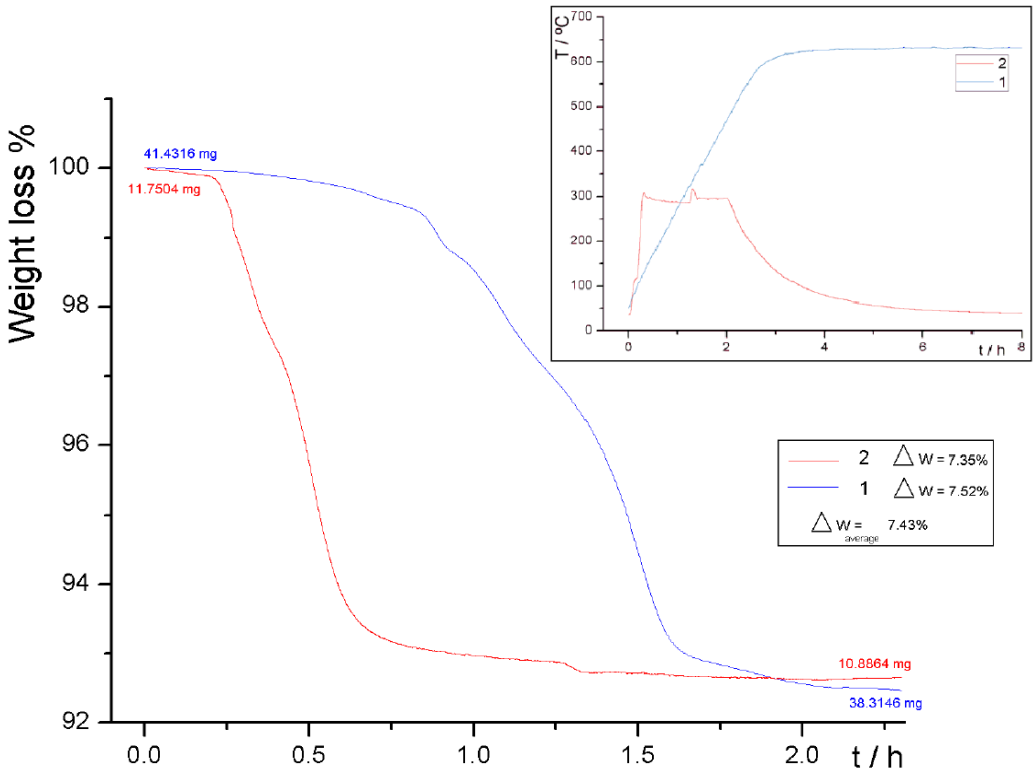

Fig. 2 Plot of $BiPbCr_2O_6$ weight loss % in function of time for controlled reduction using a Cahn balance, in the inset is shown the thermal cycle for each measurement, bottom rectangle the values for single measurement and the mean value.

Tab. 2 Thermal cycle, starting and final weight, weight loss (%) and average for the two measurements.

Thermal cycle	1	2
Starting weight (mg)	41.4316	11.7504
Final weight (mg)	38.3146	10.8864
Δ weight (%)	7.52	7.35
Average Δ weight (%)	7.43	

5.3.4 Structural characterization:

A detailed structural characterization of our samples has been made by the analysis of diffraction data from different techniques like powder x-ray diffraction, thermo- powder x-ray diffraction, transmission electron microscopy (TEM) and high resolution transmission electron microscopy (HRTEM). The structural analysis of room and low temperature phases of $Bi_{0,5}Pb_{0,5}CrO_{2,92}$ have been solved by means of Rietveld refinement of powder samples.

5.3.4a Room temperature phase: Is there any order in A position ?

The arrangement of the two different cations in the A position in a perovskite structure could be generate a disordered sorting of cations as the case of $Ca_{0,5}Pb_{0,5}CrO_3$ (S.G.:Pbnm);[14,15] or 3 kinds of order: 1)A and A' cations form in layers as in $YBaMn_2O_5$ (S.G.:P4/mmm); [16] 2) Columnar ordered like $CaFeTi_2O_6$ (S.G.: P42/nmc);[17] and 3)Rock-salt like $CaCu_3Ti_4O_{12}$ and $NaBaLiNiF_6$,
(S.G.: Fm-3m).[18-20] To define a possible order for $Bi_{0,5}Pb_{0,5}CrO_{2,92}$ we used the lattice parameters obtained indexing the experimental diffractograms; the proper symmetry and atomic positions, for each kind of order, of above mentioned oxides. For each of the three possible ordered model, a simulated diffractogram has been calculated and compared with the experimental one, all the diffractograms (experimental and calculated have been normalized before comparison), shown in fig.3;

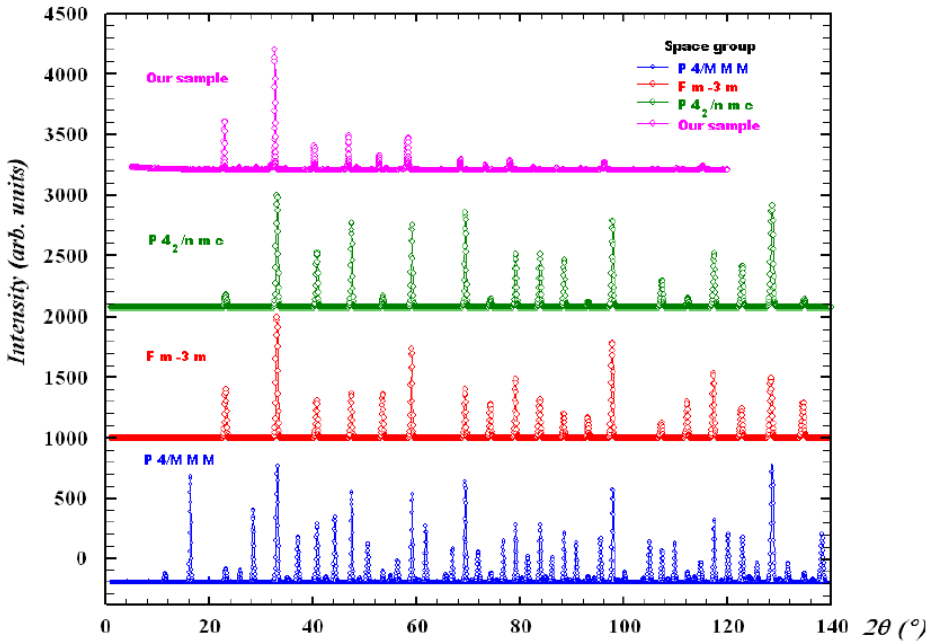

Fig. 3 Simulated diffractogram for three possible ordered models compared with the experimental one, all diffractograms normalized;

Tab. 3 Crystallographic parameters used simulating the powder x-ray diffraction for ordered structures.

Order	crystal system	Space Group	lattice parameter from index of experimnetal PWD-XR						type
			a	b	c	α	β	γ	
Columnar	Tetragonal	P 4/2 nmc	5.4112	5.4112	7.6472	90	90	90	$CaFeTi_2O_6$
Layered	Tetragonal	P 4/mmm	5.4059	5.4059	7.6475	90	90	90	$La_{0.33}NbO_3$
Salt-Rock	Cubic	F m-3m	3.8257	3.8257	3.8257	90	90	90	$NaBaLiNiF_6$

Observing fig.3 and tab.3., suddenly it appears clear that if any order exist, it should be salt-rock like. The refinement for layered and columnar order resulted to be totally unsatisfactory and has not been shown in this work. The room temperature phase refinements, provided two acceptable solutions: disordered and salt-rock ordered A cation, the graphical results are shown in respective chapters.

5.3.4b The disordered A position model: $Bi_{0,5}Pb_{0,5}CrO_{2,92}$

We have indexed the phase having an orthorhombic symmetry with a space group (S.G.) Pbnm, n° 62 and calculated the lattice parameters: a = 5.4705(6) Å, b = 5.4776(9)Å, c = 7,7420(1) Å; this is the so-called diagonal cell ~√2 ac x ~√2 ac x 2ac (a_c = 3.870(8) Å) of a perovskite structure and as starting model we did use $Ca_{0.5}Pb_{0.5}TiO_3$.[14,15] The graphical result of the fitting is shown in fig.4.

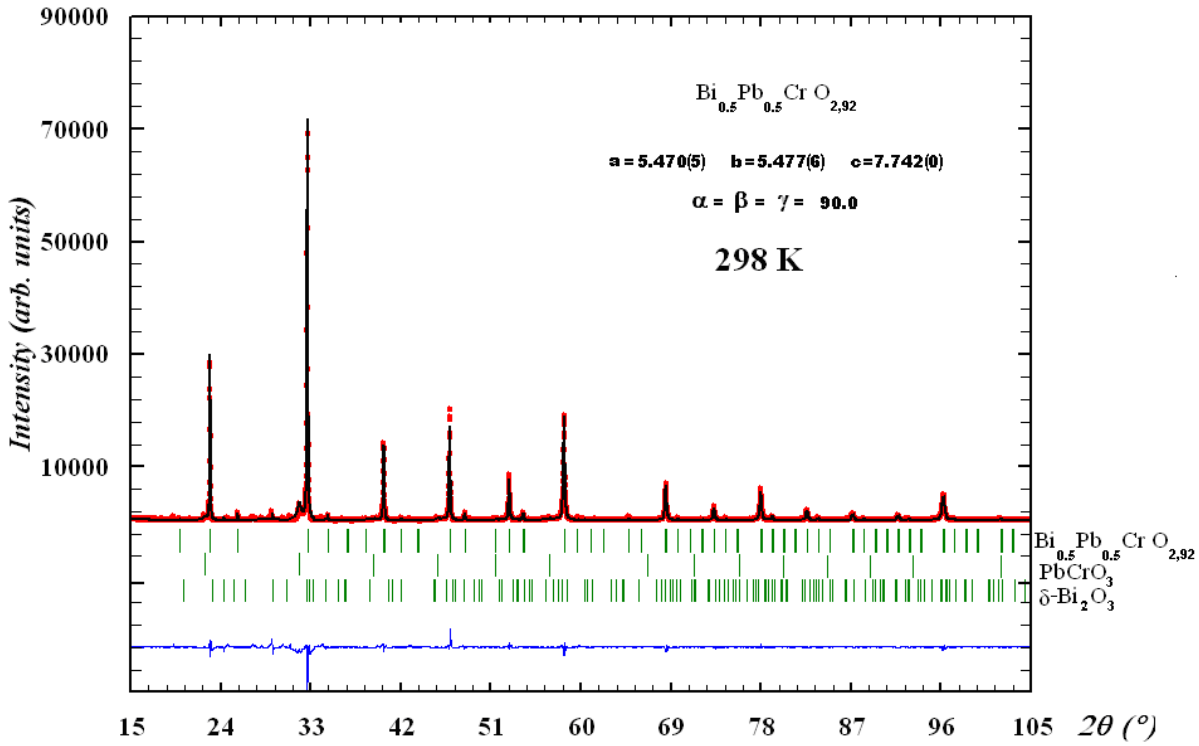

Fig. 4 Graphical result of the Rietveld refinement of $Bi_{0,5}Pb_{0,5}CrO3$ perovskite from X-ray powder data at 298 K. Experimental data are presented as points and the calculated profile as solid line. The observed difference profile is plotted at the bottom. Vertical bars are the allowed Bragg reflections for (up) $Bi_{0,5}Pb_{0,5}CrO_{2,92}$, (center) $PbCrO_3$, (down) δ-Bi_2O_3.

The summary of the crystallographic parameters are shown in tab. 4 and 8.

The Bi^{3+} and Pb^{2+} ions occupy the same crystallographic position (-0.00252, 0.52315, 0.25), see tab.4, Wyckoff position 4c (x,1/4,z for Pmna or x,y,1/4 for Pbnm); while chromium ions are in the center of a tilted octahedron surrounded by 6 oxygen atoms, the octahedra are tilted ~ 8° along the c axis in an alternating sense, corresponding to an angle Cr-O-Cr = 164°; By means of SPUDs[21,22] software, the calculated Cr-O-Cr angle results in 160°, that is in agreement with the value from the refined model. The distances Cr-O (mean Cr-O = 1.933(7) Å) fall between the limits expected for a trivalent and tetravalent chromium ions in a perovskite octahedral environment, where $<Cr^{3+}- O>$ = 1,97 Å and $<Cr^{4+}- O>$ = 1,91 Å; the mean experimental Cr-O distances spans a range from $(Ca_{0.5}Sr_{0.5})CrO_3$ < Cr-O > = 1.903(5) (P4/mmm) to $BiCrO_3$ < Cr-O >= 1.990(5) (C2/c).[23-27] Also, the octahedral tilt angles designated as φ, Φ, θ about the respective pseudo-cubic $[110]_p$, $[001]_p$ and $[111]_p$ axes, cos φ = (√2 a) / c, cos θ = a / b and cos Φ = [√2(a^2)] / (b · c), following the notations of Megaw rather than Zhao[23,24] are: φ = 2.1(5), θ = 2.9(2), Φ = 3.6(3). The model for disordered A cations is shown in fig.5.

Tab. 4 Summary of crystallographic parameters, agreement factors, thermal parameters and atomic coordinates, for orthorombic $Bi_{0,5}Pb_{0,5}CrO_{2,92}$ at 298 K.

298 K	$Bi_{0,5}Pb_{0,5}CrO_{2,92}$		
Crystal system		Orthorombic	
Space group		Pbnm nº 62	
Cell dimensions (Å)	a = 5,4705(6)	b = 5,4776(9)	c = 7,7420(1)
Cell Angles (α,β,γ) (°)	90,0	90,0	90,0
Volume (Å^3)		231.99	
Radiation (Å)	Cu	Kα1 = 1.540598	
Bragg R-Factor		3.75	
RF-Factor		3.81	
Rexp		3.14	
Rp		8.48	
	Atomic positions		
Atom	X	Y	Z
Bi	-0.00252	0.52315	0.25
Pb	-0.00252	0.52315	0.25
Cr	0	0	0
O1	0.02314	-0.00234	0.25
O2	0.23726	0.27325	0.07163
	B	Occupancy	Wickoff position
Bi	1.9053	0.515	4c
Pb	1.9053	0.485	4c
Cr	0.93984	1	4a
O1	0.97856	1	4c
O2	0	1	8d
impurities	Bragg R-Factor	RF-Factor	
$PbCrO_3$	4.42	3.84	
δ-Bi_2O_3	2.71	5.3	

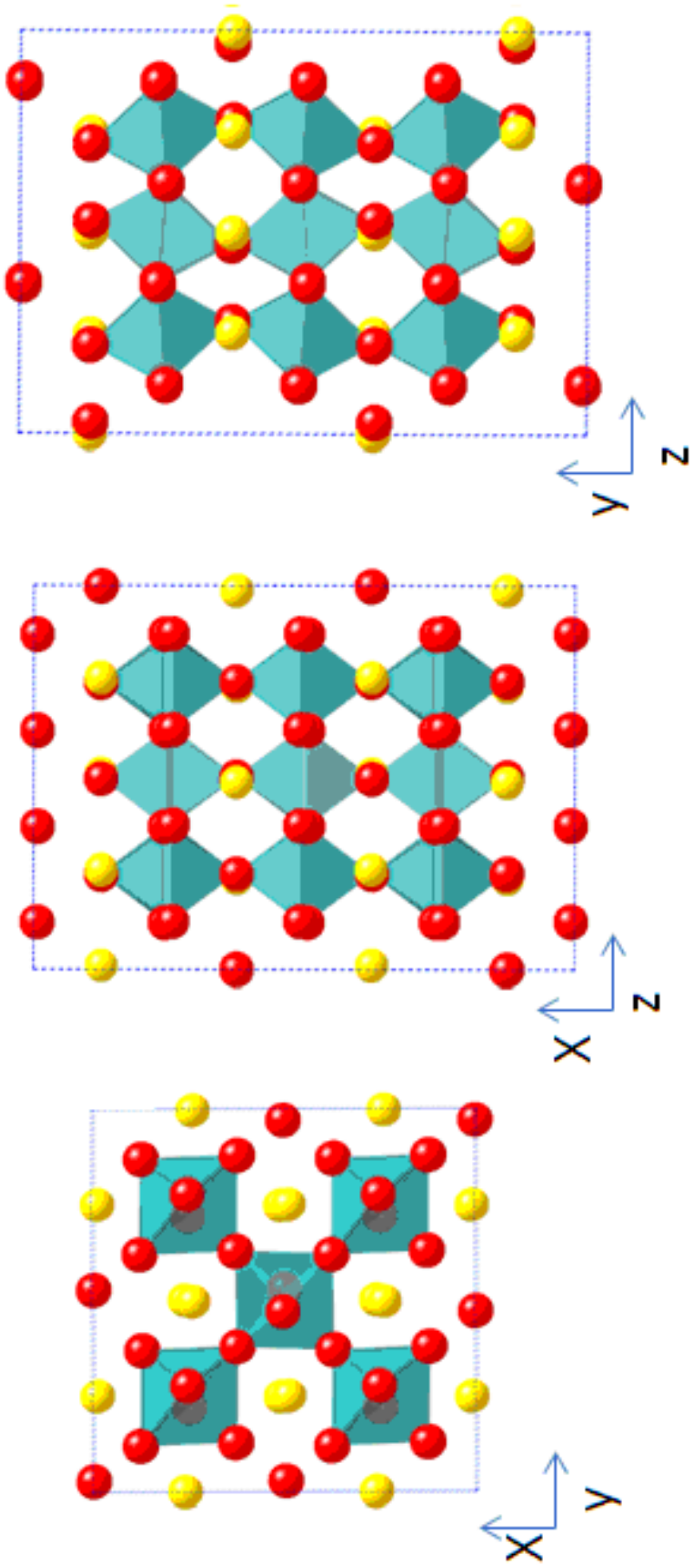

Fig. 5 The A position disordered model for orthorombic $Bi_{0,5}Pb_{0,5}CrO_3$ at 298 K.

5.3.4c The ordered A position model: $BiPbCr_2O_{5,84}$

We obtained a tetragonal unit cell a = b = 5.4747(1) Å and c = 7.7412(1) Å, a diagonal cell $\sqrt{2}a_c$ x $\sqrt{2}a_c$ x $2a_c$ (a_c = 3.870(8) Å and a S.G.: $P4_2/nmc$, nº137). The summary of crystallographic parameters and graphical result are shown in tab.5, 8 and fig.6; Differences exist between our model and the salt-rock ordered perovskite $NaBaLiNiF_6$,[17-20] however we used it as starting model because to date very few examples of A salt-rock ordered perovskites exist. The lattice parameters for $BiPbCr_2O_{5,84}$ have a metric $\sqrt{2}a_c$ x $\sqrt{2}a_c$ x $2a_c$ and a tetragonal symmetry, S.G.: $P4_2/nmc$ while for $NaBaLiNiF_6$,

$2a_c$ x $2a_c$ x $2a_c$, cubic and S.G.:Fm-3m. Attempts to refine $BiPbCr_2O_{5,84}$ salt-rock ordered, using $NaBaLiNiF_6$ parameters and symmetry did not give acceptable solutions, on the other hand we have obtained better result choosing the smaller one $\sqrt{2}a_c$ x $\sqrt{2}a_c$ x $2a_c$, obtained by the diagonal cell of a cubic one a_c x a_c x a_c. The salt-rock model proceeding form Rietveld refinement is shown in fig. 7.

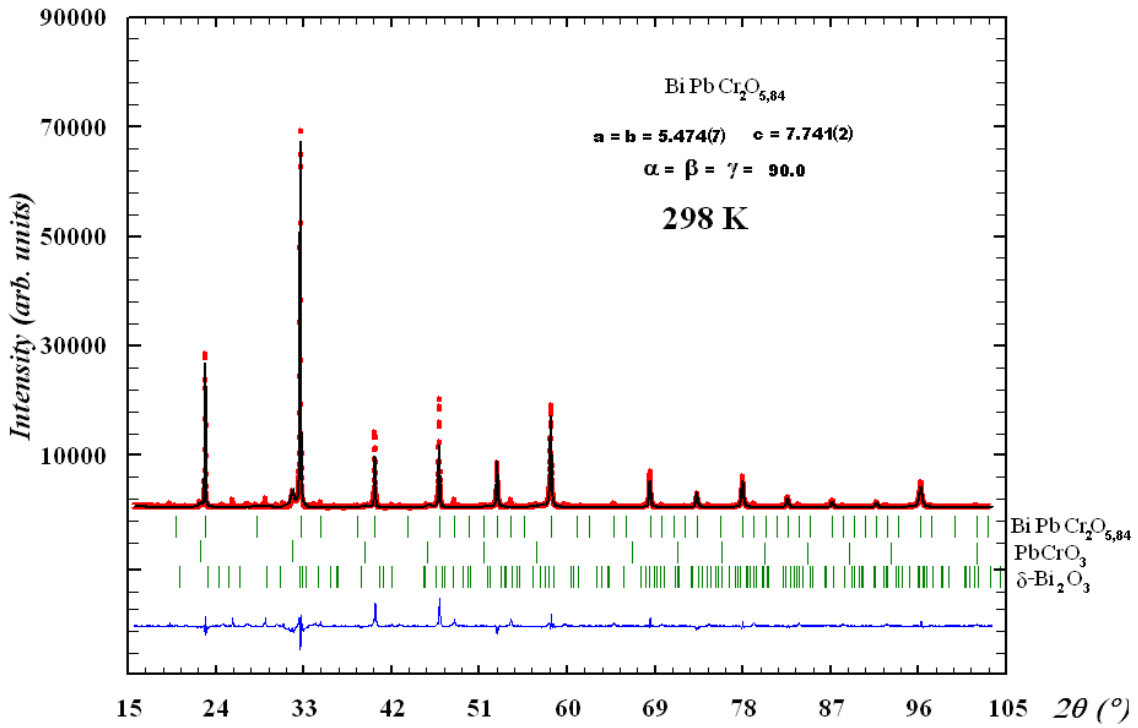

Fig. 6 Graphical result of the Rietveld refinement of $BiPbCr_2O_{5.84}$ perovskite X-ray powder data at 298 K. Experimental data are presented as points and the calculated profile as solid line. The observed difference profile is plotted at the bottom. Vertical bars are the allowed Bragg reflections for (up) $BiPbCr_2O_{5,84}$, (center) $PbCrO_3$, (down) δ-Bi_2O_3.

Tab. 5 Summary of crystallographic parameters, agreement factors, thermal parameters and atomic coordinates, for tetragonal $BiPbCr_2O_{5,84}$ at 298 K.

298 K		$BiPbCr_2O_{5,84}$	
Crystal system		Tetragonal	
Space group		P 4/2 nmc nº 137	
Cell dimensions (Å)	a = 5,4747(1)	b = 5,4747(1)	c = 7.7412(1)
Cell Angles (α,β,γ) (°)	90,0	90,0	90,0
Volume (Å^3)		232.02	
Radiation (Å)	Cu	Kα1 = 1.540598	
Bragg R-Factor		9.18	
RF-Factor		5.47	
Rexp		3.14	
Rp		7.31	
	Atomic positions		
Atom	X	Y	Z
Bi	0	0	0
Pb	0	0	0.5
Cr1	0.5	0	0.25
Cr2	0	0.5	0.25
O1	0.5	0	0
O2	0.25	0.25	0.25
	B	Occupancy	Wickoff position
Bi	0.839	0.515	2a
Pb	1.651	0.485	2b
Cr1	0.372	1	4d
Cr2	0.022	1	4d
O1	0	1	8g
O2	0	1	8e
impurities	Bragg R-Factor	RF-Factor	
$PbCrO_3$	4.31	3.25	
δ-Bi_2O_3	3.4	2.42	

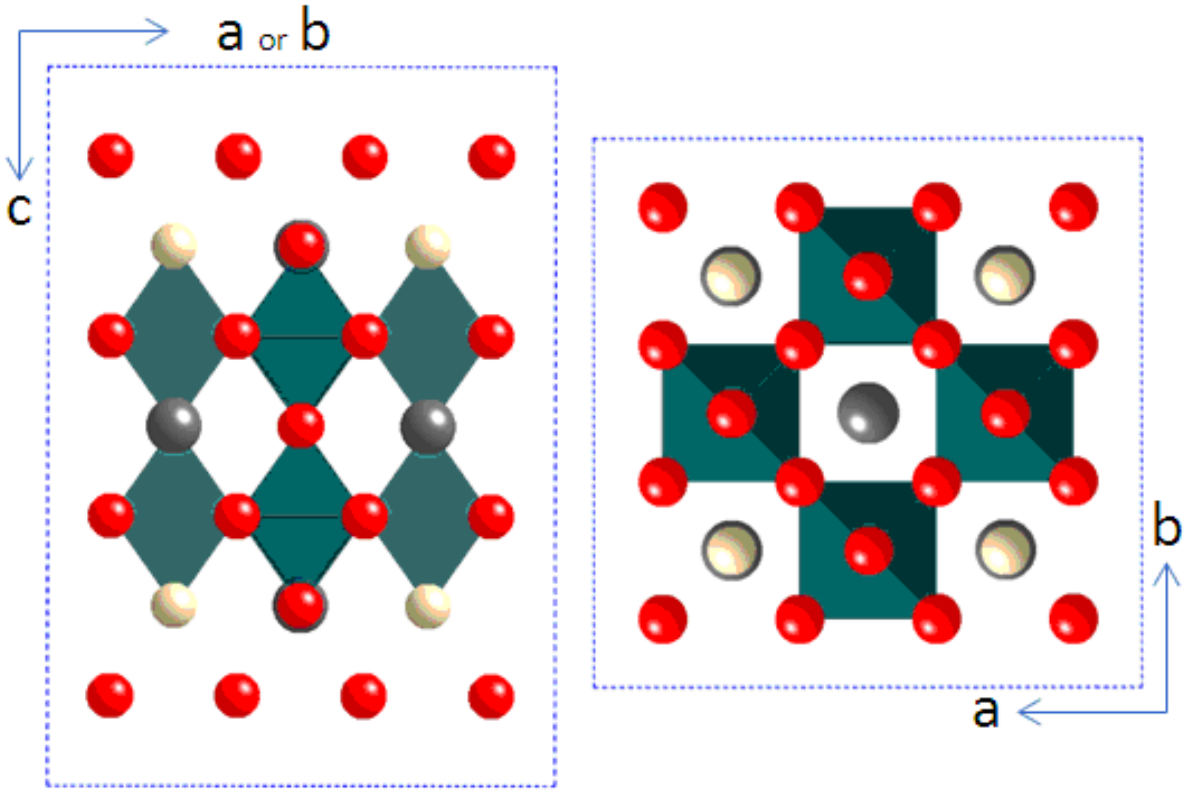

Fig. 7 The A position disordered model for tetragonal $BiPbCr_2O6$ at 298 K.

Comparing both models and the refined lattice parameters, high similarity between ordered and disordered models in terms of A and A' cations distribution exists, however differences in Rs factors, promote the random model instead of the ordered one.

The values of agreement factors (see tab. 4 and 5) are strongly influenced by known and unknown secondary phases, in fact they do not allow reaching a low value neither for the statistical expected Rexp (theoretical agreement factor in the case of an ideal fitting).

Comparing the refinement agreement factors of disordered and salt-rock ordered the first one is the model that have the best fit with experimental data, disordered:

R-Bragg = 3.75%, R-F = 3.81%, Rp = 8.48%, Rexp = 3.14%; ordered R-Bragg = 9.18%, R-F = 5.47%, Rp = 7.31%, Rexp = 3.14%.

5.3.4d HRTEM experiments, images, SAED and CBED

In order to have further evidences supporting the results provided by refinement, HRTEM experiments have been carried out. The HRTEM image in fig. 8 clearly shows the perovskite cell. No extended defects are observed indicating that the material is well crystallized. The corresponding Fourier transform of the image fits well with the diffraction pattern. In any case no distinction can be made ion the A position.

Applying Morniroli's microdiffraction method for the identification of possible space groups, the real symmetry could be determined by analysis of convergent beam electron diffraction (CBED) of principal zone axis, of the zero order Laue zone (ZOLZ) and the first order Laue zone (FOLZ).[26,27]

The CBED along $[001]_p$ experiment results are shown on fig.8 (A, blue letters) and the calculated one for an orthogonal crystal along[001] on fig. 8 (B, blue letters), we can observe a matching in the ZOLZ; It clearly shows two mirror planes m1 and m2, consistent with orthorhombic symmetry. In the case of the FOLZ, the thickness of the sample, did not allow us to observe the whole pattern. Combining the results of powder x-ray diffraction, electron diffraction and microscopy, we conclude that at room temperature $Bi_{0,5}Pb_{0,5}CrO_{2,92}$, corresponds to an orthorhombic structure, space group Pbnm (n°62), a superstructure of the perovskite with parameters $\sim a_p\sqrt{2} \times a_p\sqrt{2} \times 2a_p$, the so called diagonal cell; with a disordered arrangement of Bi^{3+} and Pb^{2+} in A position.

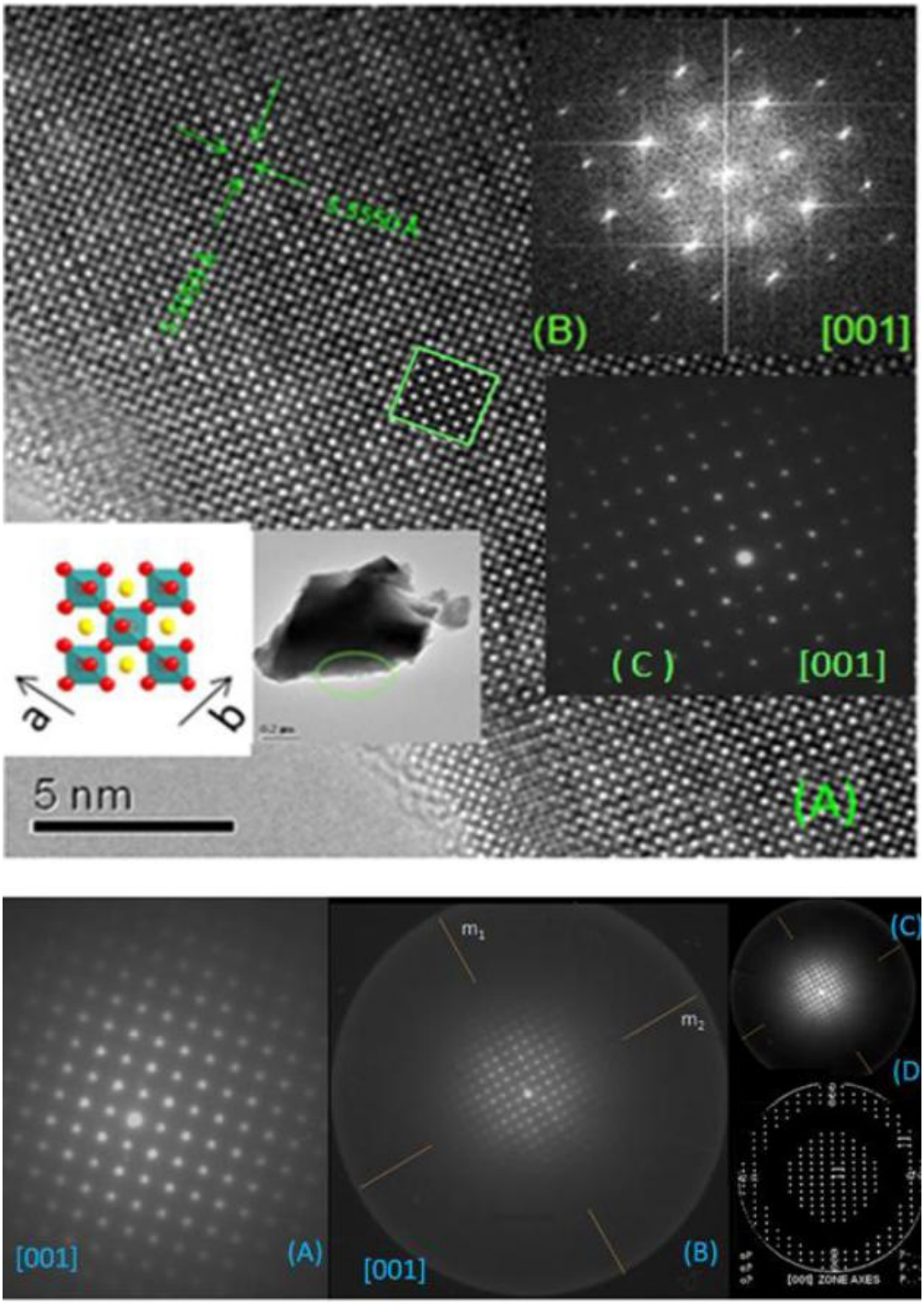

Fig. 8 Up (green letters) (A) The HRTEM image of $Bi_{0,5}Pb_{0,5}CrO_{0,92}$, (B) Fast Fourier Transform, (C) diffraction pattern; the normal arrows in (A) show the measured spacing (5.550 Å and 5.5059 Å); the green box is the calculated image using a focus of - 400 Å and a thickness of 65.8 Å. Bottom (blue letters) the CBED diffraction patterns for [001] at different camera constant: (A) 50 cm, (B) zoomed 20 cm, (C) original 20 cm and (D) calculated pattern of [001] for orthorombic symmetry.

5.3.4e Low temperature phase of $Bi_{0,5}Pb_{0,5}CrO_{2,92}$

Diffraction measurements performed decreasing temperature, showed a phase transition taking place around 150 K. In fig.9 we can clearly observe a splitting of two different peaks, (202) at 2θ = 40,31 and (204) or (312) at 2θ = 53,5 respectively.

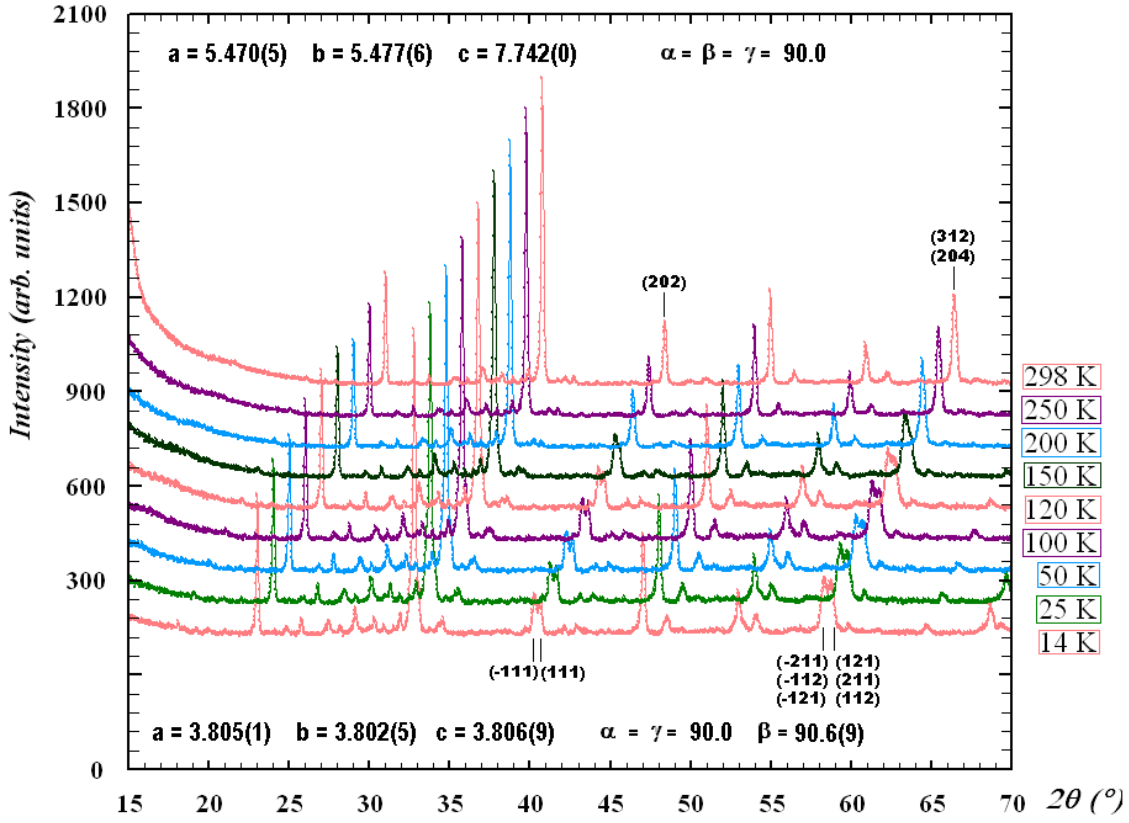

Fig. 9 The sequence of thermo-diffraction measurements of $Bi_{0,5}Pb_{0,5}CrO_{2,92}$.

The structural phase transition observed in fig.9 have been studied more in detail by refinement of $Bi_{0,5}Pb_{0,5}CrO_{2,92}$ for the measured temperatures. The several lattice parameters values a, b, and β angle as a function of temperature have been reported in tab.6; a substantial change in cell parameters can be easily observed between 150 K and 200 K.

Tab. 6 Refined cell parameters from low temperature to high temperature for $Bi_{0,5}Pb_{0,5}CrO_{2,92}$

T / K	a / Å	b / Å	c / Å	β (°)
14	3.805(1)	3.802(5)	3.806(9)	90.6(9)
25	3.855(3)	3.861(2)	3.866(8)	90.7(4)
50	3.855(3)	3.861(4)	3.866(9)	90.75(4)
100	3.855(1)	3.861(6)	3.867(5)	90.74(1)
120	3.855(7)	3.862(2)	3.867(3)	90.72(5)
150	3.858(5)	3.863(7)	3.868(5)	90.61(4)
200	5.467(1)	5.463(6)	7.740(9)	90
250	5.468(7)	5.465(2)	7.738(6)	90
298	5.470(5)	5.477(7)	7.742(5)	90

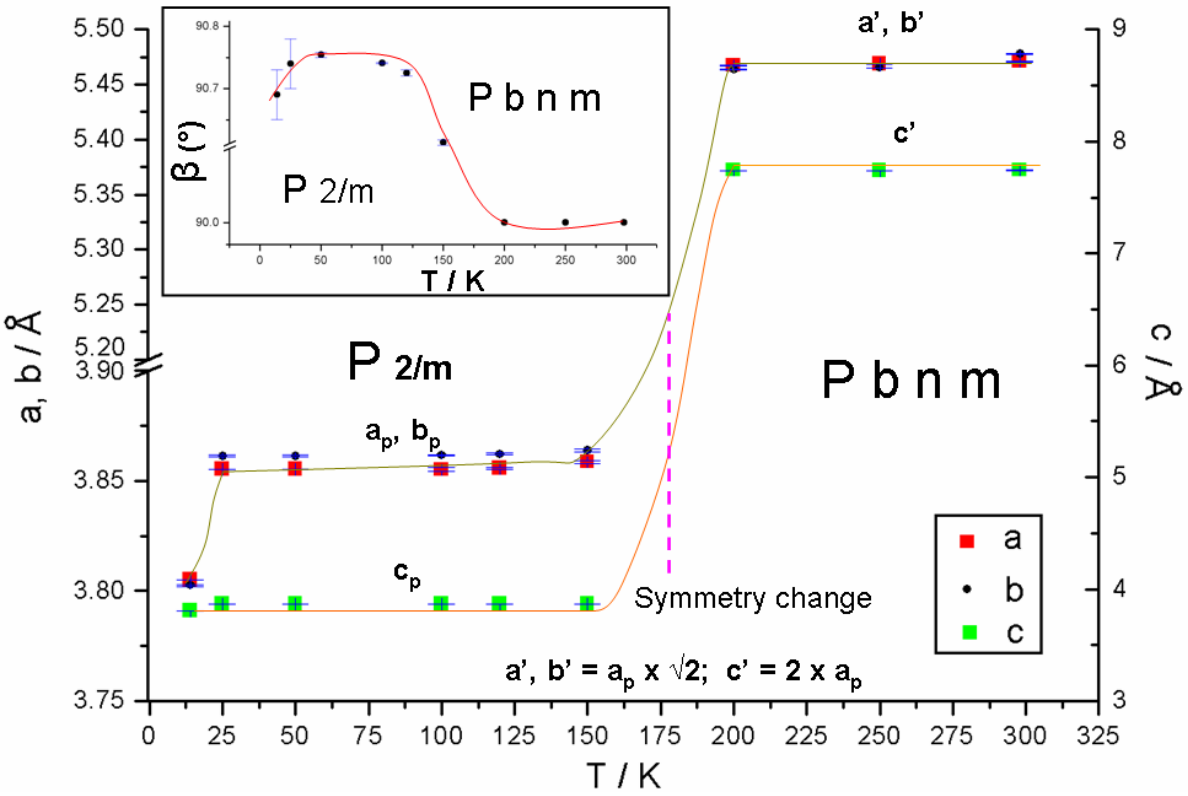

Fig. 10 The evolution of lattice parameters reported in tab.6 as function of temperature; It can be seen the change of symmetry increasing the temperature.

The variation of lattice parameters is due to a change in symmetry: from P2/m low temperature to Pbnm high temperature; this change in symmetry force to choose, at high temperature, a bigger unit cell: $\sim a_p\sqrt{2}$ x $\sim a_p\sqrt{2}$ x $\sim 2a_p$ rather than the low temperature one $\sim a_p$ x $\sim a_p$ x $\sim a_p$. The plot in fig. 10 summarize the evolution of lattice parameters reported in tab.6 as function of temperature, pointing out the increase of symmetry from low to high the temperature. The nature of this symmetry change could reside in that increasing the temperature the structure undergo to a distortion caused by octahedra tilting; this octahedra tilting force the unit cell to change its dimensions from $\sim a_p$ x $\sim a_p$ x $\sim a_p$ to
$\sim a_p\sqrt{2}$ x $\sim a_p\sqrt{2}$ x $\sim 2a_p$ (the diagonal cell): the diagonal cell is in fact the unit cell assigned by previous room temperature refinements and by electron diffraction.

This low temperature phase shows a perovskite structure where $[CrO_6]^{2-}$ octahedra are distorted and not tilted which concur for the decreasing in symmetry. Evidence of distorted octahedra come from the <Cr-O> distance values obtained by refinement of $Bi_{0,5}Pb_{0,5}CrO_{2,92}$ at 14 K: three different pairs of distances have measured, as reported in tab. 8: <Cr-O1> = 1,901(2), <Cr-O2> = 1,902(5) and <Cr-O3> = 1,9035(1)
(mean <Cr-O> =1,902), confirming the distortion of octahedra.

The observed octahedral distortion is probably generated from the repulsive electrostatic interactions of Bi^{3+} or Pb^{2+} lone pairs and the O^{2-} full filled p shell of the anionic sublattice.

A monoclinic symmetry has been assigned to the low temperature $Bi_{0,5}Pb_{0,5}CrO_{2,92}$ at 14 K, it has been refined by means of the Rietveld method and the graphical result is shown in fig.11, the model in fig. 12. The unit cell parameters are: a = 3.805(1) Å b = 3.802(5) Å c = 3.806(9) Å and β = 90°.6(9)' with a S.G. = P 2/m, n°10; Relevant crystallographic data are summarized in tab. 6, 7 and 8.

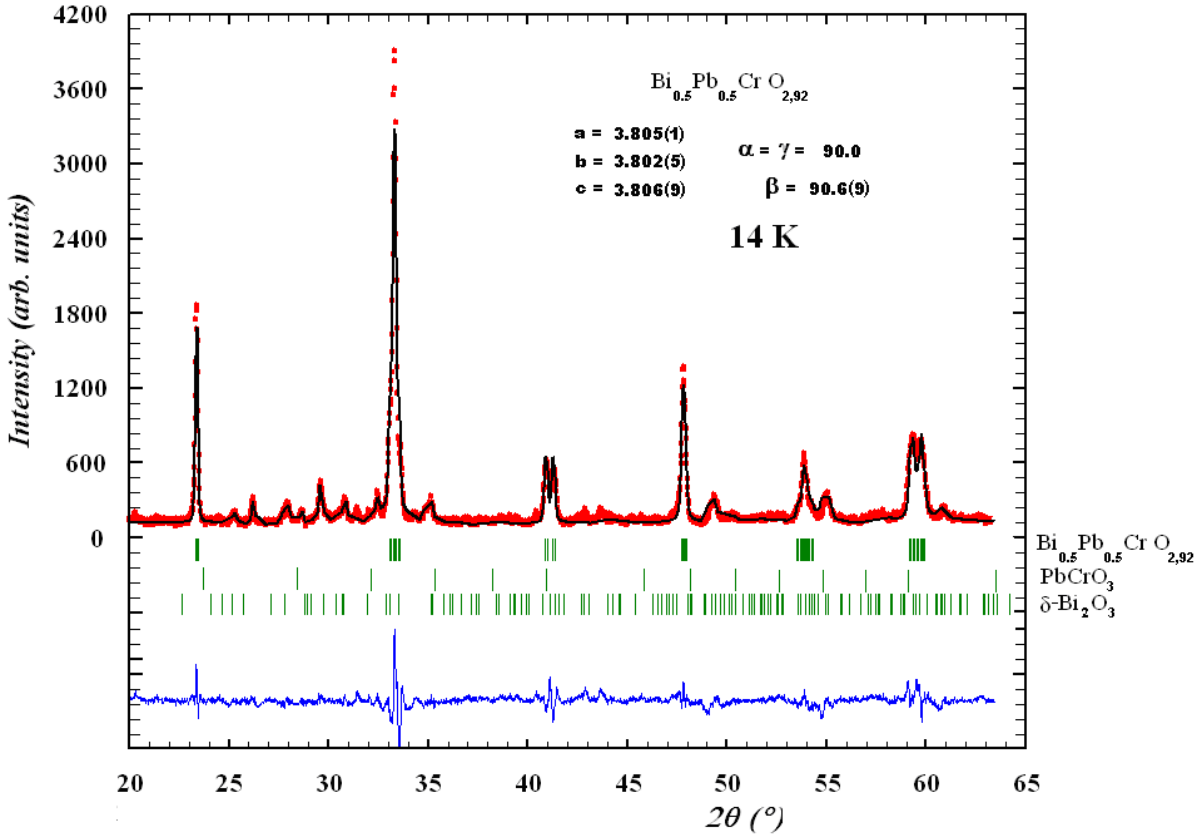

Fig. 11 Graphical result of the Rietveld refinement of $Bi_{0,5}Pb_{0,5}CrO_{2,92}$ perovskite X-ray powder data at 14 K. Experimental data are presented as points and the calculated profile as solid line. The observed difference profile is plotted at the bottom. Vertical bars are the allowed Bragg reflections for (up) $Bi_{0,5}Pb_{0,5}CrO_3$, (center) $PbCrO_3$,
(down) δ-Bi_2O_3.

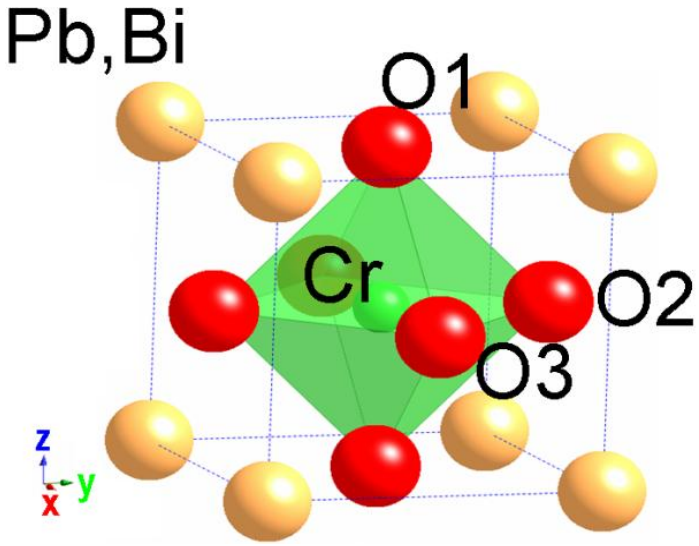

Fig. 12 The A position disordered model for orthorombic $Bi_{0,5}Pb_{0,5}CrO_{2,92}$ at 14 K; the monoclinic angle is very narrow to 90° and cannot be correct visualized in this image.

Tab. 7 Summary of crystallographic parameters, agreement factors, thermal parameters and atomic coordinates, for orthorombic $Bi_{0,5}Pb_{0,5}CrO_{2,92}$ at 14 K.

14 K		$Bi_{0,5}Pb_{0,5}CrO_{2,92}$	
Crystal system		Monoclinic	
Space group		P 2/m nº 10	
Cell dimensions (Å)	a = 3.805(1)	b = 3.802(5)	c = 3.806(9)
Cell Angles (α,β,γ) (°)	90,0	90,6(9)	90,0
Volume (Å^3)		54.98	
Radiation (Å)	Cu	Kα1 = 1.540598	
Bragg R-Factor		8.37	
RF-Factor		6.01	
Rexp		5.42	
Rp		7.05	

	Atomic positions		
Atom	X	Y	Z
Bi	0	0	0
Pb	0	0	0
Cr	0.5	0.5	0.5
O1	0.5	0	0.5
O2	0	0.5	0.5
O3	0.5	0.5	0

	B	Occupancy	Wickoff position
Bi	0.1(1)	0.4(1)	1a
Pb	0.1(1)	0.4(1)	1a
Cr	0	1	1h
O1	0	1	1g
O2	0	1	1f
O3	0	1	1e

impurities	Bragg R-Factor	RF-Factor
$PbCrO_3$	4.26	5.8
δ-Bi_2O_3	3.9	3.6

Tab. 8 Interatomic distances (Å) and bond angles (◦) for ordered $BiPbCr_2O_{5,84}$, disordered $Bi_{0,5}Pb_{0,5}CrO_{2,92}$ at 298 K and $Bi_{0,5}Pb_{0,5}CrO_{2,92}$ 14 K.

	Ordered 298 K	**Disordered 298 K**	**14 K**
Distances (Å) A-O_{12} polyhedron A= Pb or Bi	Bi-O1 = 2.743(3) x 8 Bi-O2 = 2.743(1) x 4 Pb-O1 = 2.743(2) x 8 Pb-O2 = 2.743(2) x 4	Bi,Pb-O(1) = 2.739(5) x 4 Bi,Pb-O(2) = 2.736(1) x 8	Bi,Pb-O(1) = 2.675(1) x 4 Bi,Pb-O(2) = 2.689(7) x 4 Bi,Pb-O(2´) = 2.690(3) x 4
Mean A-O	2.743	2.737	2.734
Distances (Å) CrO_6 octahedron	Cr1-O1 = 1.932(1) Cr1-O2 = 1.937(7) Cr2-O1 = 1.932(1) Cr2-O2 = 1.937(7)	Cr-O(1) = 1.932(1) x 2 Cr-O(2) = 1.937(1) x 2	Cr-O(1) = 1.9012(1) x 2 Cr-O(2) = 1.9025(4) x 2 Cr-O(3) = 1.9035(1) x 2
Mean Cr-O	1.934	1.934	1.902
Angles (°) CrO_6 octahedron	O1-Cr2-O1 = 180° O1-Cr2-O2 = 93°.384' O2-Cr2-O2 = 180°	O(1)-Cr(1)-O(1) = 180.0° O(1)-Cr(1)-O(2) = 90.0° O(2)-Cr(1)-O(2) = 180.0°	O(1)-Cr-O(2) = 89°.9(9) O(1)-Cr-O(3) = 89°.9(9) O(2)-Cr-O(3) = 89°.3(1) O(1)-Cr-O(1) = 180°.0 O(2)-Cr-O(2) = 180°.0 O(3)-Cr-O(3) = 180°.0

5.4 Magnetic measurements

The temperature dependence of the molar susceptibility χ and the reciprocal susceptibility for $Bi_{0,5}Pb_{0,5}CrO_{2,92}$ are shown in fig. 13. There exists a small divergence between ZFC and FC branches close to room temperature, this type of divergence, in this range of temperature, has be found for $PbCrO_3$ in previous work in literautre[8] and has explained due to a spin reorientation in $PbCrO_3$; By means of structural characterization, it knew the presence of small amount of $PbCrO_3$ as secondary phase, we think that the observed phenomena can be mainly attributed to the presence of the $PbCrO_3$ secondary phase.

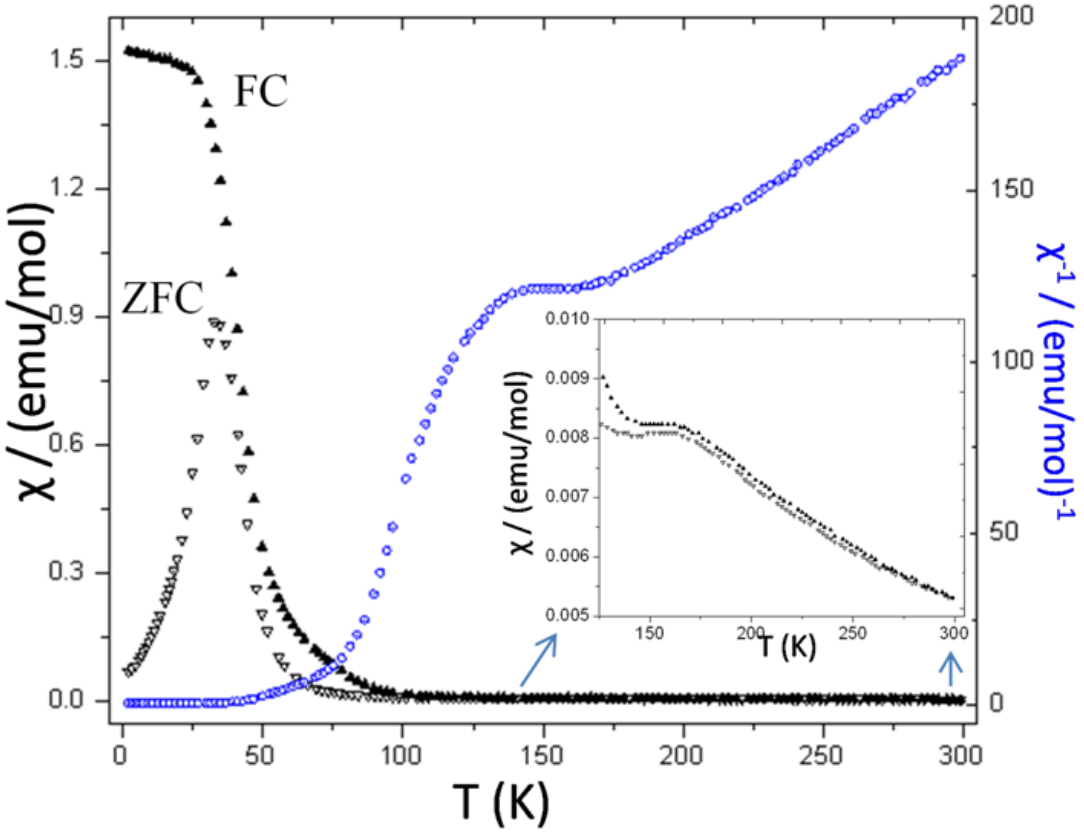

Fig. 13 The temperature dependence of the molar susceptibility χ and the reciprocal susceptibility for $Bi_{0.5}Pb_{0.5}CrO_{2,92}$; the inset shows the zoomed region indicated by arrows.

The Curie-Weiss paramagnetic behaviour is not observed in any region of the temperature range although attempts for linear fittings of the reciprocal susceptibility in the temperature range 200 < T < 300 resulted on an effective magnetic moment of $3.88\mu_B$ and a Weiss temperature θ = -69.19 K. This value is close to the theoretical magnetic moment of $3.55\mu_B$ resulting from a 1 : 2 Cr^{4+} / Cr^{3+} ratio: a mixed-valence scenario according to the thermogravimetric analysis. A further temperature decrease shows the onset of a magnetic transition at ~150 K (see fig. 13 at inset) associated with the observed structural changes from the orthorhombic high temperature phase to the monoclinic one. Below this temperature, it can be observed a net maximum at ~35 K in the ZFC branch associated to the presence of long-range antiferromagnetic interactions. It is also interesting to note that,

the ZFC and FC susceptibilities strongly diverge below the Neél temperature revealing a substantial glassy contribution to the spin order. A small hysteresis is seen in the 5 K field dependent magnetization loop fig. 14 with a remanence as small as 0.08 μ_B and a coercive field of 300 Oe, confirming the presence of a small ferromagnetic contribution.

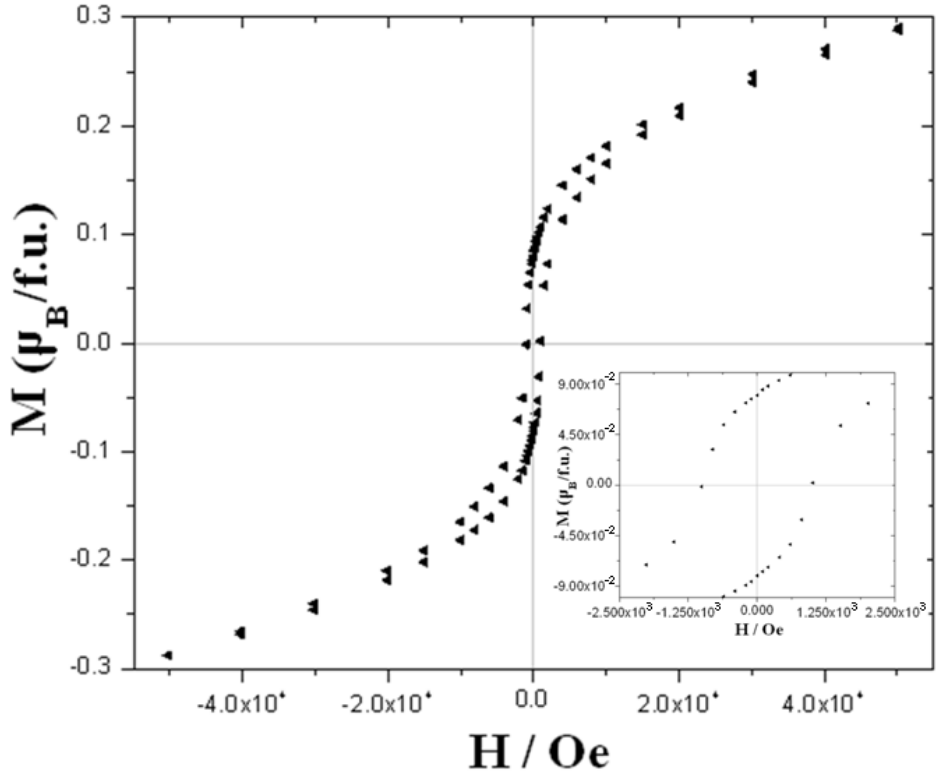

Fig. 14 Field dependence of magnetization for $Bi_{0.5}Pb_{0.5}CrO_{2,92}$ at 5 K.

Then, long-range AFM ordering (probably with a small canting angle) occurs below 35 K; however, AC-susceptibility measurements, fig. 15 show that a substantial glassy component is also present.

There exists a progressive shift of the cups with the frequency which is a direct probe of the spin relaxation time commonly observed in canonical spin-glasses. In light of these observations, we suggest that this material shows a re-entrant spin glass behavior; that is, the coexistence of ferromagnetism (or WFM) and spin-glass order.[28-29]

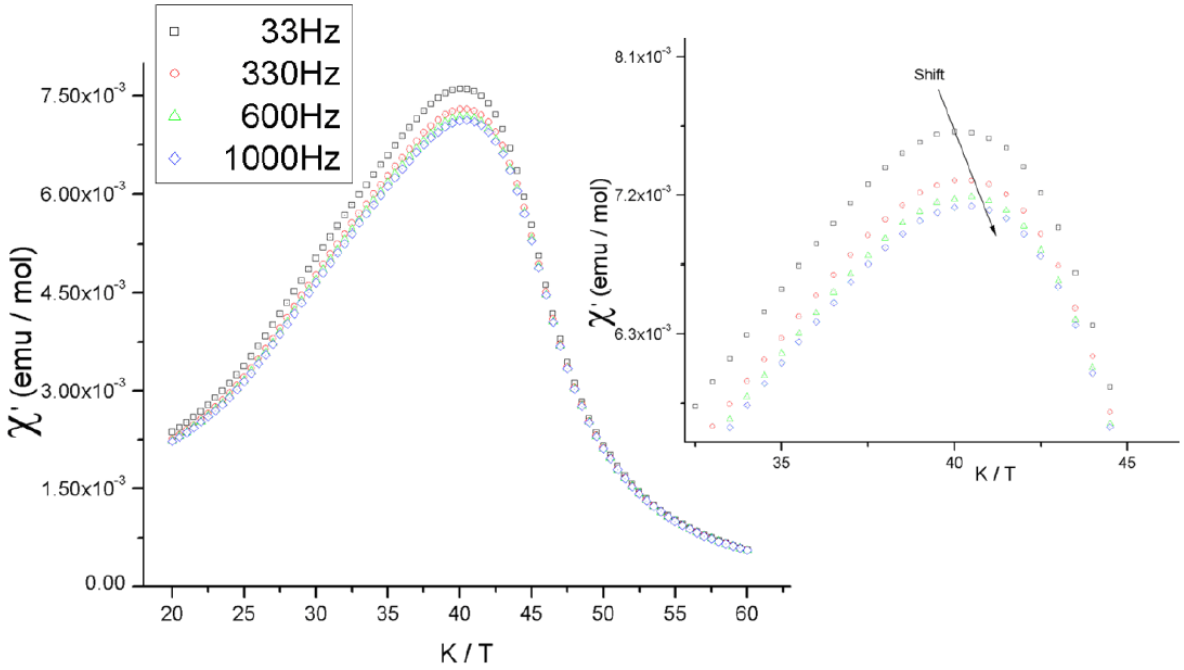

Fig. 15 Real component of AC-susceptibility for $Bi_{0.5}Pb_{0.5}CrO_{2,92}$ as function of temperature measured using frequency range 33 Hz to 1 KHz, in the inset shows a little shift to high temperature increasing the frequency of the applied field.

The origin of this behavior can be understood from the presence of different Cr-O-Cr superexchange magnetic pathways. Antiferromagnetic Cr^{3+}-O-Cr^{3+} super-exchange interactions are expected between the t_{2g}^3 Cr^{3+} ions leading to a G-type AFM-ordering as it has also been observed for $BiCrO_3$;[5] otherwise, the t_{2g}^2 Cr^{4+} ions can lead to both Cr^{3+}-O-Cr^{+4} and Cr^{4+}-O-Cr^{4+} antiferromagnetic and ferromagnetic (weak!) interactions.[30] This behavior has also been observed in the closely related $(Bi_{0.5}Sr_{0.5})CrO_3$ oxides;[27] it seems that the insertion of Pb^{2+} ions in the G-type $BiCrO_3$ perovskite leads to the presence of Cr^{3+}-O-Cr^{+4} and Cr^{4+}-O-Cr^{4+} *weak* interactions leading to magnetic local disordering and indeed to magnetic frustration but, there are still enough *strong* Cr^{3+}-O-Cr^{3+} super-exchange interactions to maintain the long range antiferromagntic ordering.

5.5 Dielectric measurements

The aim of the study of solid solution $Bi_{1-x}Pb_xCrO_3$ and in particular $Bi_{0,5}Pb_{0,5}CrO_{2,92}$ was to investigate on them as a possible candidates for multiferroic. Concerning physical properties, $Bi_{0,5}Pb_{0,5}CrO_{2,92}$ could be a possible candidate for multiferroic if its electric properties, like resistance and the dielectric constant, are influenced by presence of an applied magnetic field *H*.

The electrical properties expected to be *H* dependent are that like magnetoresistance (MR) and magnetocapacitance (MC) measured as function of temperature.

In order to do this the use of *f*, *T* and *H* dependent dielectric spectroscopy allows us detection of and discrimination between (MR) and (MC) effects in the $Bi_{0,5}Pb_{0,5}CrO_{2,92}$ samples. It has been pointed out previously that such discrimination is a non-trivial task, because pure MR of a second dielectric relaxation can cause changes in capacitance. All existing dielectric relaxations within one sample need to be identified and separated first. The *f*–dependent dielectric data taken at a fixed *T* may be fitted to an adequate equivalent circuit model based on standard parallel resistor-capacitor RC elements, where each relaxation corresponds to one RC element and multiple relaxations are reflected by a series connection of RC elements.

A magnetic field *H* can then be applied and the MC of each equivalent circuit capacitor and the MR of each circuit resistor need to be determined separately for the specific *H*-range. This procedure is followed here, where MC and MR are defined as

MC = [*C*(H=0)-*C*(H)]/*C*(0) and MR = [*R*(H=0)-*R*(H)]/*R*(0) respectively.

It is well established that one ideal parallel resistor – capacitor RC element can describe the impedance of an ideal Debye dielectric relaxation. This model works particularly well for insulators, where the capacitor describes the ability of the material to store charge and the parallel resistor describes the leakage current due to some un-trapped charge carriers bypassing the ideal charge storage element. However, in polycrystalline ceramics the grain boundaries often emerge as an additional extrinsic relaxation and the macroscopic impedance is then well represented by a series of two RC elements.

The dielectric relaxations identified in $Bi_{0,5}Pb_{0,5}CrO_{2,92}$ ceramics presented in this work were all found to be non-ideal (non-Debye) and could not be fitted with ideal RC elements. To still fit the data to an adequate equivalent circuit model such non-ideality in one specific dielectric relaxation was accounted for by using a constant-phase element (CPE) in parallel or instead of an ideal capacitor in the respective RC element. The CPE capacitance obtained from the equivalent circuit fits can be converted into a real capacitance given in [Farad] using a standard procedure. In a non-ideal R-CPE or R-CPE-C circuit the CPE

behaviour can be associated with the broadening of the distribution of relaxation times τ. In an ideal RC element τ is given by $\tau = RC = \rho\varepsilon_0\varepsilon$ and the CPE constitutes a semi-empirical parameter to reflect increasing width of the distribution of τ.

Figure 16 shows plots of imaginary vs real part of the impedance (Z'' vs Z') collected at 30 K at H = and H = 50 kOe. One semicircle appears and each spectrum, where the semicircle center seems to be suppressed below the x-axis (Z'-axis).

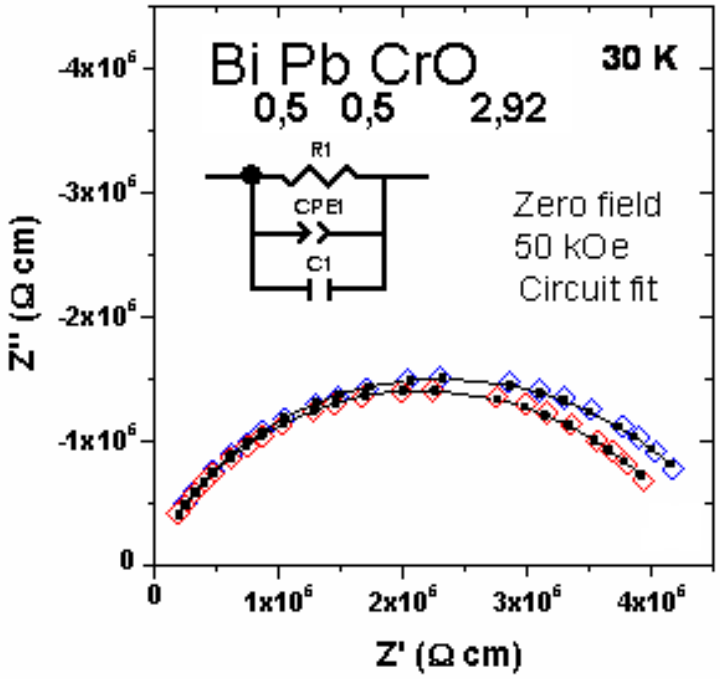

Figure 16 The plots of imaginary vs real part of the impedance (Z'' vs Z') collected at 30 K at H = and H = 50 kOe.

The appearance of only one semicircle implies good homogeneity of the sample and separated grain boundary (GB) response is not obvious. We associate this with the high-pressure synthesis, which may facilitate such homogeneity. The suppression of the semicircle center is indicative of non-ideal dielectric response as accounted for by the parallel CPE in the equivalent circuit fig.16 inset. Using the non-ideal R-CPE-C circuit shown, good agreement between data and model is obtained. The semicircle diameter corresponds to the resistivity values, which are in the range of $5 \cdot 10^6$ Ωcm at 30 K. These are rather low numbers and may be interpreted as a result of Cr^{3+} - Cr^{4+} hopping. The different semicircle diameter for H =0 and H = 50 kOe indicates a small MR effect, which we associate with a slight spin-dependence of the Cr^{3+} - Cr^{4+} hopping.

The non-ideality of the $Bi_{0,5}Pb_{0,5}CrO_{2,92}$ dielectric response as manifested by suppressed Z'' vs Z' semicircles fig.16 is also shown in the plot of dielectric permittivity ε' vs f fig.17, where ε' shows a strong f-dependence. This can be directly associated with the typical CPE-behavior and is indeed well represented by the equivalent circuit fit.

No H-dependence of ε' is obvious and MC effects as a manifestation of possible MEC effects are not indicated.

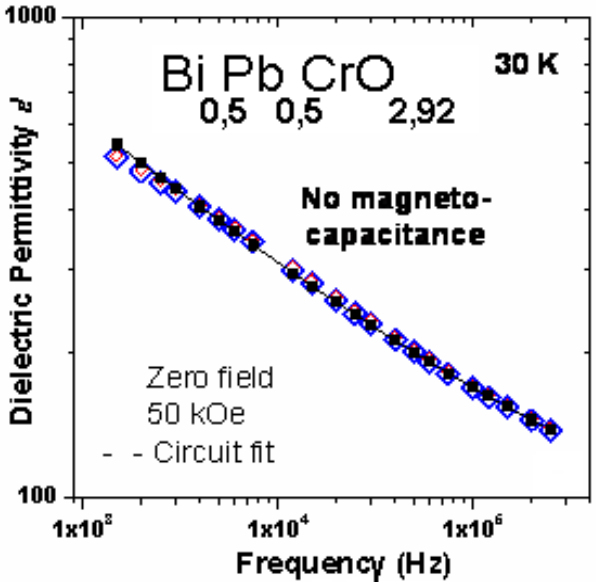

Fig. 17 The plot of dielectric permittivity ε' vs f.

On the other hand, the MR detected is perceptible and shows a clear trend with T Fig.18 and seems to be correlated to some extent with the $Bi_{0,5}Pb_{0,5}CrO_{2,92}$ magnetism, i.e. the χ vs T curve Fig.13 shows a similar trend as MR vs T in Fig.18. Since the $Bi_{0,5}Pb_{0,5}CrO_{2,92}$ magnetism is expected to be dominated by the Cr cations, the correlation between χ and MR may corroborate the notion that charge transport is by spindependent Cr^{3+} - Cr^{4+} hopping.

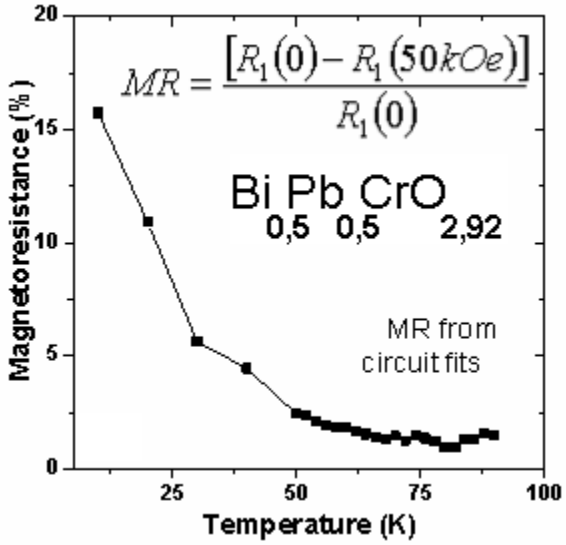

Fig. 18 The plot of magnetoresistance as function of temperature.

Fig. 19 shows the trends of ε' vs T for H = 0 and H = 50 kOe. Again, no MC is indicated and the T-dependence of ε' is generally quite weak. In the presence of Bi^{3+} and Pb^{2+} lone-pair electrons ferroelectricity may be expected, displaying the typical peak in ε' vs T near T_C but hardly any T-dependence is observed here. It should be noted though that the low resistivity of $Bi_{0,5}Pb_{0,5}CrO_{2,92}$ allowed reliable determination of ε' values only for $T \leq 75$ K. Therefore, we cannot exclude ferroelectricity with a potential high T_C » 75 K.

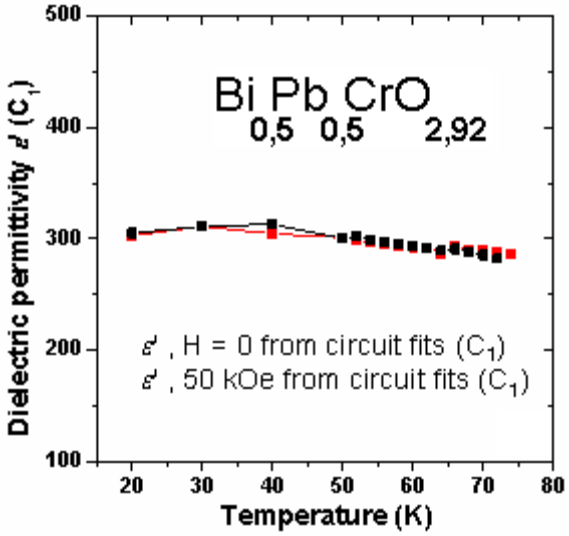

Fig. 19 The trends of ε' vs T for H = 0 and H = 50 kOe.

The T-dependence of resistivity ρ determined from the resistor R1 in the equivalent circuit fits is shown in fig.20 (left) on Arrhenius axes. $Bi_{0,5}Pb_{0,5}CrO_{2,92}$ shows the typical signs of semiconductivity, where the non-linearity of the Arrhenius-plot indicates a strong T-dependence of the activation energy E_A.

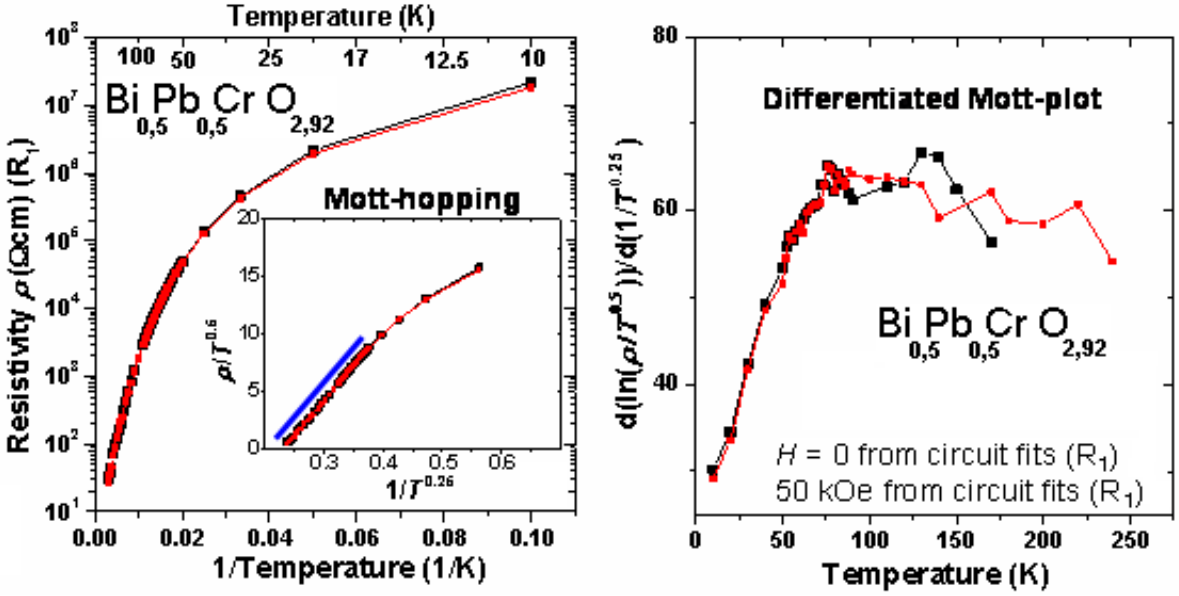

Fig. 20 The plot of resistivity ρ as function of temperature (left), by the plot of variation of ln ρ / $T^{0,25}$ vs. temperature (right) describe if the material follows the Mott variable-range hopping (VRH) model.

For $T \geq 60$ K the E_A values are in the range of 25 – 50 meV, whereas a stronger variation is observable for $T < 60$ K where E_A increases from ≈ 4 meV at 10 K to ≈ 25 meV at 60 K. Such E_A values are all rather low as compared to compounds with nominal Cr^{3+} valence and the rather good semiconductivity may therefore be associated with the mixed Cr^{3+} / Cr^{4+} valence.

From the fig.20 (left) inset it can be seen that the ρ-T data can in fact be linearized for $T > 60$ K as indicated by the blue solid line, if the data is plotted on $\rho / T^{0.5}$ vs $1/T^{0.25}$ axes for Mott-type variable-range hopping (VRH) charge transport. At $T < 60$ K such VRH behavior seems to be modified though due to a deviation off the linear behavior on the Mott-axes, which is confirmed by the differentiated Mott-plots shown in fig.20 (right). This change in trend of the charge transport may again be correlated with the onset of the Cr-magnetism at $T < 60$ K.

5.6 Conclusions

The new ternary oxide with perovskite structure $Bi_{0,5}Pb_{0,5}CrO_{2,92}$ has been structural and physical characterized showing a disordered Bi^{3+} and Pb^{2+} cations arrangement and its oxygen content has been determined by means of thermogravimetric reduction method; moreover no ordering of this vacancy have been observed by HRTEM experiments.

The magnetic behaviour may be explained by a long-range canted-antiferromagnetic structure coexisting at low temperatures with a substantial glassy component; that is a re-entrant spin-glass.

Dielectrical measurements have been performed on this material, magnetoresistance (MR) effect have been detected as function of temperature and seems to be correlated with magnetic susceptibility χ; moreover the correlation between χ and MR may corroborate the notion that charge transport is by spin dependent Cr^{3+} - Cr^{4+} hopping. The low resistivity for $Bi_{0,5}Pb_{0,5}CrO_{2,92}$ allowed reliable determination of ε' values only for $T \leq 75$ K. Therefore we cannot exclude ferroelectricity with a potential high $T_C >> 75$ K.

Powder neutron diffraction studies below the Neél temperature are planning to confirm the presence of long-range ordering.

5.7 Bibliography

1. King, G. and P.M. Woodward, *Cation ordering in perovskites.* Journal of Materials Chemistry, 2010. 20(28): p. 5785-5796.
2. Spaldin, N.A. and M. Fiebig, *The Renaissance of Magnetoelectric Multiferroics.* Science, 2005. 309(5733): p. 391-392.
3. Hill, N.A., P. Baettig, and C. Daul, *First Principles Search for Multiferroism in $BiCrO_3$.* The Journal of Physical Chemistry B, 2002. 106(13): p. 3383-3388.
4. Baettig, P., C. Ederer, and N.A. Spaldin, *First principles study of the multiferroics $BiFeO_3$, Bi_2FeCrO_6, and $BiCrO_3$: Structure, polarization, and magnetic ordering temperature.* Physical Review B, 2005. 72(21): p. 214105.
5. Niitaka, S., et al., *Crystal structure and dielectric and magnetic properties of $BiCrO_3$ as a ferroelectromagnet.* Solid State Ionics, 2004. 172(1): p. 557-559.
6. Roth, W.L. and R.C. De Vries, *Crystal and magnetic sturcture of $PbCrO_3$. J.Appl. Phys.*,, 1967. 38: p. 951.
7. Arevalo-Lopez, A.M. and M.M.A. Alario-Franco, *On the structure and microstructure of $PbCrO_3$.* Journal of Solid State Chemistry, 2007. 180(11): p. 3271-3279.
8. Arevalo-Lopez, A.M., A.J. Dos santos-Garcia, and M.A. Alario-Franco, *Antiferromagnetism and Spin Reorientation in $PbCrO_3$.* Inorganic Chemistry, 2009. 48(12): p. 5434-5438.
9. Werner, P.-E., L. Eriksson, and M. Westdahl, *TREOR, a semi-exhaustive trial-and-error powder indexing program for all symmetries.* Journal of Applied Crystallography, 1985. 18(5): p. 367-370.
10. Boultif, A. and D. Louer, *Powder pattern indexing with the dichotomy method.* Journal of Applied Crystallography, 2004. 37(5): p. 724-731.
11. Rietveld, H., *A profile refinement method for nuclear and magnetic structures.* Journal of Applied Crystallography, 1969. 2(2): p. 65-71.
12. Rodriguez-Carvajal, J., *Recent advances in magnetic structure determination by neutron powder diffraction.* Physica B: Condensed Matter, 1993. 192(1-2): p. 55-69.
13. Kilaas, R., *MacTempas softwre version 2.3.7; total resolution.* 1988.
14. Ganesh, R. and E. Goo, *Dielectric and Ordering Behavior in $Pb_xCa_{1-x}TiO_3$. J. Am. Ceram. Soc.*, 1997. 80(3): p. 653.
15. Chandra, A. and D. Pandey, *Evolution of crystallographic phases in the system $(Pb_{1-x}Ca_x)TiO_3$: A Rietveld study. J. Mater. Res.*, , 2003. 57: p. 725.

16. Lufaso, M.W., et al., *Pressure- and temperature-dependent X-ray diffraction studies of $NdCrO_3$.* Journal of Alloys and Compounds, 2007. 433(1-2): p. 91-96.
17. Castillo-Martinez, E., et al., *Increasing the Structural Complexity of Chromium(IV) Oxides by High-Pressure and High-Temperature Reactions of CrO_2* Inorganic Chemistry, 2008. 47(19): p. 8526-8542.
18. Sakai, N., H. Fjellvag, and B.r.C. Hauback, *Structural, Magnetic, and Thermal Properties of $La_{1-x}Ca_xCrO_3$* . Journal of Solid State Chemistry, 1996. 121(1): p. 202-213.
19. Lufaso, M.W. and P.M. Woodward, *Prediction of the crystal structures of perovskites using the software program SPuDS.* Acta Crystallographica Section B, 2001. 57(6): p. 725-738.
20. Zaitseva, Z.A.L., A. L. DopoV., *Akad. Nauk B*, 1978. 11: p. 994.
21. Bertaut, E.F. and J. Mareschal, *Etude de la structure magnetique des chromites d'erbium et de neodyme par diffraction neutronique.* Solid State Communications, 1967. 5(2): p. 93-97.
22. Ortega-San-Martin, L., et al., *Frustrated Orders in the Perovskite $(Bi_{0.5}Sr_{0.5})CrO_3$.* Chemistry of Materials, 2009. 21(12): p. 2436-2441.
23. Megaw, H.D., *Crystal structures: A working approach.* . W.B. Saunders Co. Philadelphia, PA 1973.
24. Zhao, Y., et al., *Critical phenomena and phase transition of perovskite data for $NaMgF_3$ perovskite. Part II.* Physics of the Earth and Planetary Interiors, 1993. 76(1-2): p. 17-34.
25. Zhao, Y., et al., *Thermal expansion and structural distortion of perovskite data for $NaMgF_3$ perovskite. Part I.* Physics of the Earth and Planetary Interiors, 1993. 76(1-2): p. 1-16.
26. Morniroli, J.P. and J.W. Steeds, *Microdiffraction as a tool for crystal structure identification and determination.* Ultramicroscopy, 1992. 45(2): p. 219-239.
27. Redjaimia, A. and J.P. Morniroli, *Application of microdiffraction to crystal structure identification.* Ultramicroscopy, 1994. 53(4): p. 305-317.
28. Bréard, Y., et al., *Spin-glass state induced by cobalt substitution in $CaRuO_3$. J. Phys:CondensMatter*, 2007. 19: p. 216212.
29. Dos santos-Garcia, A.J., J. Van Duijn, and M.Ã. Alario-Franco, *Spin-glass-like behaviour in $IrSr_2RECu_2O_8$ (RE=Sm and Eu).* Journal of Solid State Chemistry, 2008. 181(12): p. 3317-3321.

30. Gabay, M. and G.r. Toulouse, *Coexistence of Spin-Glass and Ferromagnetic Orderings.* Physical Review Letters, 1981. 47(3): p. 201-204.
31. Goodenough, J.B., *Magnetism and the Chemical Bond.* Interscience Wiley, New York, 1963.

6) High pressure – high temperature single crystal growth of $PbCrO_3$

6.1 Introduction

$PbCrO_3$ perovskite was first synthesized by Roth and deVries in the late 1960s.[1]

Single-crystal and powder x-ray diffraction studies at room temperature show a cubic structure (S.G. Pm -3 m) with constant lattice a = 4.00 Å.[1] Furthermore, by means of neutron diffraction studies at 77 and 4.2 K, Roth and deVries found that this compound shows an antiferromagnetic G-type structure ($a_{mag} = 2\ a_{nucl}$) with a magnetic moment of ~1.9 μ_B per chromium atom with a Neél temperature, T_N, of about 240 K. Chamberland and Moeller[2] also synthesized $PbCrO_3$ and their structural results were in agreement with the previous ones, but in addition, reported an unusual broadening of the diffraction peaks even using monochromatic Cu Kα1 radiation. These broad lines in the x-ray powder patterns were also observed for the same compound by Goodenough et al..[3] However, in these works neither atomic concentration nor microstructural studies were considered and/or analyzed.

It is well known that the Pb^{2+} $6s^2$ lone pair in some perovskites results in disorder of this cation as confirmed by a high thermal factor in x-ray diffraction data refinements[4], and assignment to a general position by displacement of this cation.

Electron microscopy and electron diffraction are often used to solve structural details that x-ray diffraction measurement cannot resolve,[5-8] and in the case of other lead perovskites, microstructural studies have helped solve the real structures.[9]

Arevalo and al.[10] have performed a structural and microstructural study using x-ray diffraction, selected area electron diffraction (SAED) and high-resolution transmission electron microscopy (HRTEM) to elucidate the origin of the abnormal broadening of the x-ray diffraction maxima and to clarify the origin of the cubic structure of $PbCrO_3$.

They shown a lead-perovskite compound ‘‘$PbCrO_3$’’ with a Pb deficiency, resulting in a modulated structure within a complex microdomain texture reveal that this material is far from being a conventional cubic perovskite. The SAED pattern are reported in fig. 1.

The abnormal broadening of the powder x-ray diffraction lines is due to a very complex microstructure that arises from a compositional modulation of lead atoms along the three principal directions that creates three sets of microdomains.

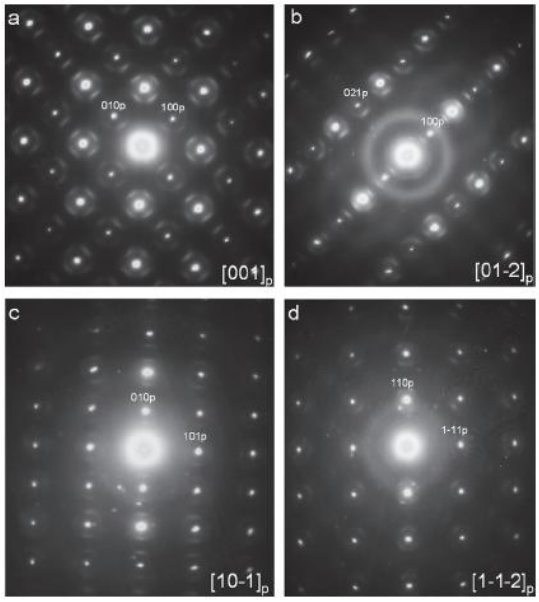

Fig. 1 SAED patterns of $PbCrO_3$ along the a) $[001]_p$, b) $[01\text{-}2]_p$, c) $[10\text{-}1]_p$ and $[1\text{-}1\text{-}2]_p$ zone axis. Subindex p refers to the basic perovskite cell.

Assuming a commensurate superstructure with an average period of 16 perovskite cells and with a phase shift of $\phi = T/3$, they proposed an orthorhombic structure model (a_p x $3a_p$ x (≈14–18)a_p) as shown in fig. 3. The calculated HRTEM images and electron diffraction patterns based on this modulated structural model, which is due to the periodic variation of the occupation factor of Pb atoms (see fig.1 and 2) agrees well with the experimental data.

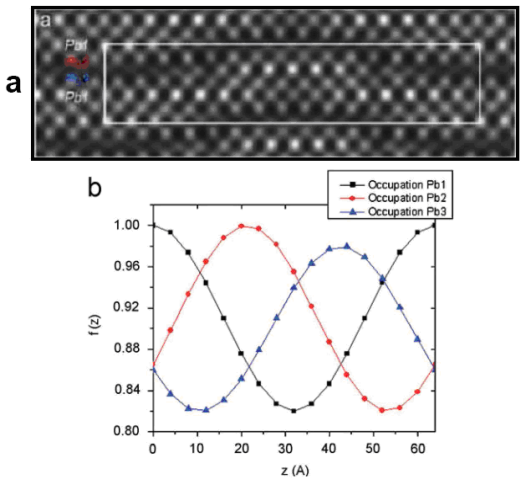

Fig. 2 (a) Calculated HRTEM image along [100]p based on (b) the occupational modulation model proposed.

The final conclusion was then that there is not really ‘‘PbCrO3’’, but $Pb_{1-x}CrO_{3-x}$ that under the present synthesis conditions has x = 0.091(5).

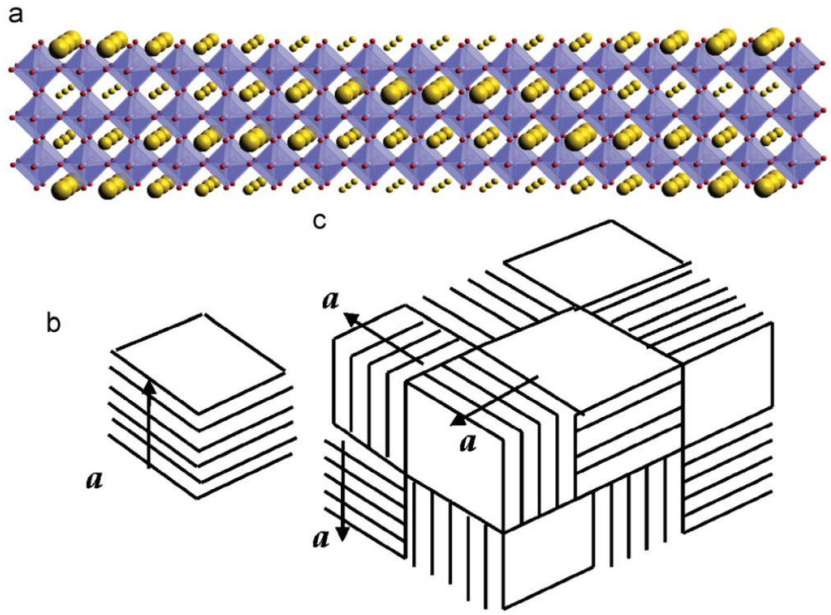

Fig. 3 (a) Model of the structure of $PbCrO_3$ obtained by electron microscopy and diffraction. The occupation factor of the Pb atoms has been scaled so as to make it more clearly visible. Lead is yellow, chromium is purple and oxygen is red (color online). (b) Single domain of a schematic representation of the microdomain texture of "$PbCrO_3$". (c) Intergrowth of domains in different orientations.

6.2 Single crystal growth and the role of fluxes

Two paths exist synthesizing $PbCrO_3$:

$$1)\ PbO + CrO_2 \rightarrow PbCrO_3$$

$$2)\ PbCrO_4 \rightarrow \sim 0.1\ PbCrO_3 + \sim 0.9\ PbCrO_4 + 0.1\ (1/2\ O_2) \uparrow$$

The path 1), in our experimentss, provided only polycrystalline product; the synthetic route 2) provided better results. Conditions of T, P, reaction time, slow cooling / quenching and reactants have been scanned by trial and error method in order to achieve the best condition growing $PbCrO_3$ single crystal, experiments and results have been summarized in tab. 1.

Tab. 1 Temperature, pressure, reaction time, slow cooling / quenching and reactants conditions for $PbCrO_3$ single crystal growth.

	Reactant	flux	T (℃)	P (Kbar)	reac time (min)	quenching	s low cooling	product	Qualty Cryst.
1	PbCrO4	--	950	55	60' at 950°C	no	to 750°C in 30'	PbCrO4 + PbCrO3	≈ 0,3 mm
2	PbCrO4	--	950	55	60' at 950°C	yes	no	PbCrO4 + PbCrO3	≈ 0,3 mm
3	PbCrO4	Pb	900	55	85'	yes	no	PbCrO4 + Pb + PbCrO3	small > 0.1 mm
4	PbCrO4	Pb	900	55	20' at 400°C, 45' at 900°C	yes	no	PbCrO4 + Pb + PbCrO3	small > 0.1 mm
5	PbCrO4	Pb	950	55	60' at 500°C, 60' 950°C	yes	no	PbCrO4 + Pb + PbCrO3	small > 0.1 mm
6	PbCrO4	Pb	950	55	60' at 400°C, 20' at 950°C	yes	no	PbCrO4 + Pb + PbCrO3	small > 0.1 mm
7	PbCrO4	2.5 Pb	950	55	60' at 400°C, 20' at 950°C	yes	no	PbCrO4 + Pb + PbCrO3	no single crys.
8	2.5 PbCrO4	Pb	950	55	60' at 400°C, 20' at 950°C	yes	no	PbCrO4 + Pb + PbCrO3	small > 0.1 mm
10	2.5 PbCrO4	Pb	950	55	20' at 900°C, 40' at 950°C	no	to 750°C in 15'	PbCrO4 + Pb + PbCrO3	small > 0.1 mm
11	PbCrO4	1.75 PbCl2	950	55	20' at 600°C, 60' at 950°C	yes	no	PbCrO4 + PbCl2	no single crys.
12	PbCrO4	PbO	950	55	20' at 900°C, 40' at 950°C	yes	no	PbCrO4 + PbO + PbCrO3	very small
13	PbCrO4	PbO + (6)	950	55	20' at 900°C, 40' at 950° C	no	to 850°C in 15'	PbCrO4 + PbO + PbCrO3	very small
14	PbCrO4	0.5 PbO	950	60	20' at 900°C, 40' at 950°C	no	to 750°C in 15'	PbCrO4 + PbO + PbCrO3	very small

Trying to improve the single crystal growth, the flux method have been applied.

PbO (11-13), $PbCl_2$ (11) and metallic Pb (3-10) have been used as flux fixing composition and scanning temperature, pressure, reaction time, slow cooling / quenching.

Using PbO as flux, very small crystals have been obtained; In the case of metallic Pb small crystals generally with dimension 0.1 mm < have been found in the product; the $PbCl_2$ seems do not improve the crystal growth; In conclusion the role of chosen fluxes did not improve the single crystal growth. The best conditions to growth $PbCrO_3$ single crystal have been found in 1) and 2): $PbCrO_4$ 60' reaction time, 950° C and 55 Kbar, obtaining a product made by a matrix of $PbCrO_4$ where some $PbCrO_3$ single crystal have been identified.

6.3 Macroscopic aspect of single crysytal

Fig. 4 a) shows examples of single crystal $PbCrO_3$ images from optical microscope, the crystals have a definite shape of prisms like truncated octahedron; Some samples have also been observed by SEM, as shown in fig. 4 b), the crystals have had an average dimension of ~70 μm.

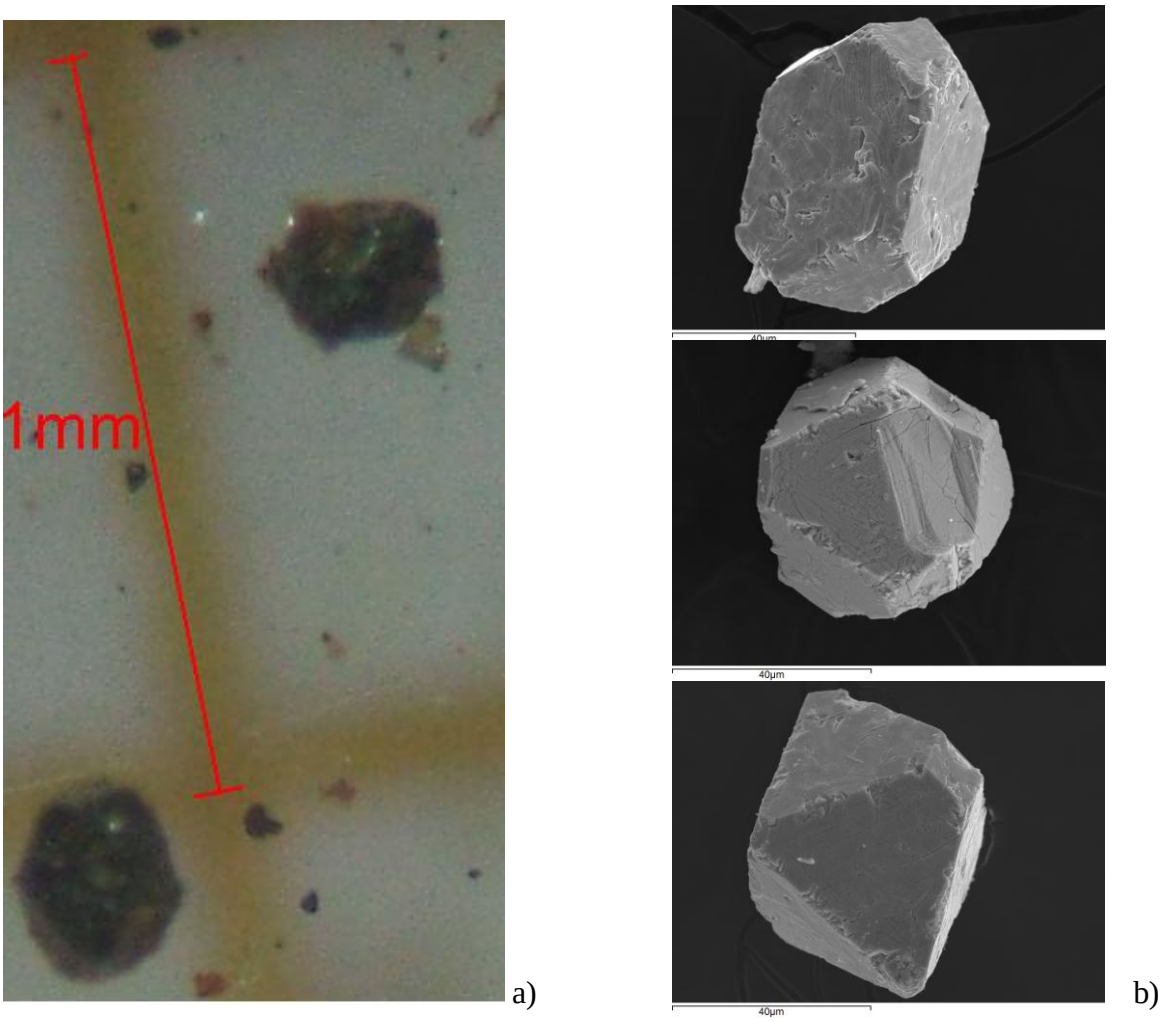

a) b)

Fig. 4 a) single crystal $PbCrO_3$ images from optical microscope,; 4 b), single crystals observed by SEM, the average dimension is ~70 μm.

The composition of many crystal have been checked by EDAX microprobe in SEM providing a result (semiquantitative) in close to ratio ~1 Pb : ~1 Cr as expected for $PbCrO_3$.

6.4 Diffraction measurement and indexing

Several samples have been tested in single crystal diffractometer, only few of them diffracted and resulted suitable for measurement. In these essays a second crystal with different lattice parameters than $PbCrO_3$ or $PbCrO_3$, (containing Pb and Cr) have been found. $PbCrO_3$ diffraction have been performed in a Bruker AXS model Smart 1000 single

crystal diffractometer equipped with a CCD area detector, using Mo λ = 0.7107; in fig. 5 is shown the diffraction pattern of [001];

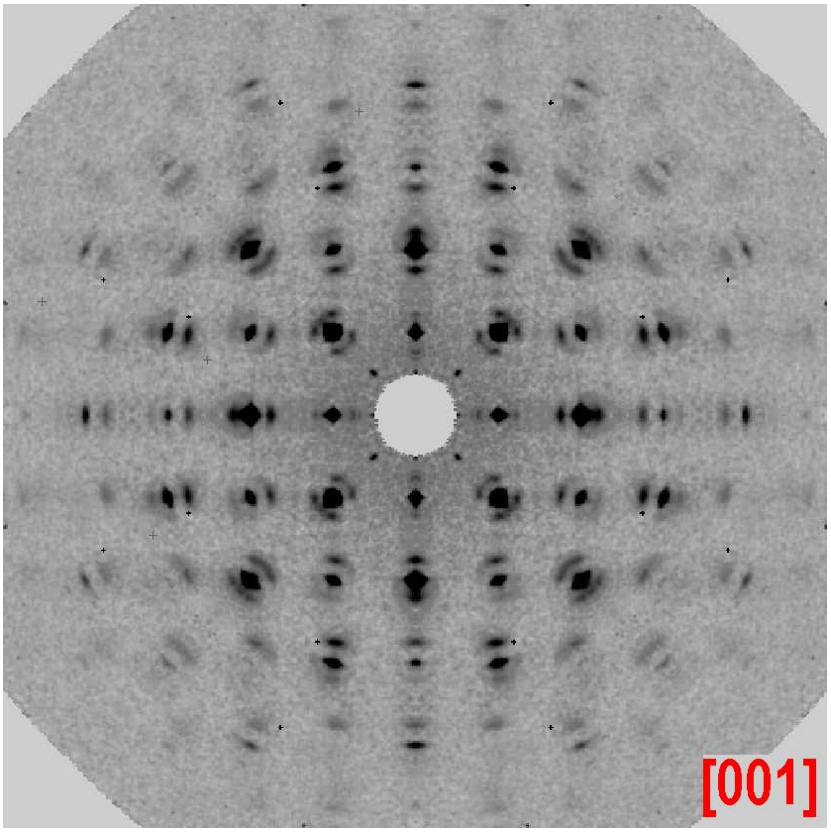

Fig. 5 The diffraction pattern of [001] for $PbCrO_3$.

The index of reflection provided the parameters (not refined) a = 4.0088(4) Å and a S.G. P m -3 m; In agreement with data previously reported in literature;[1,2,10]

Unluckily, the quality of crystals, good for a draft characterization, was not enough for a reliable structure refinement, providing Rs values always above 20%.

On the other hand the data provided are sufficient for a qualitative discussion about modulation;

Fig.6 shows the comparison between single crystal x-ray diffraction pattern (this work) and SAED from micro crystal from policrystalline sample of $PbCrO_3$ along [001] zone axis.

Comparing the two patterns is easy to see that in principal Bragg reflections a close matching exist in the streak of the satellite reflections between the two patterns. These streak satellite reflections observed by Arevalo and al.[10] have been explained as a sum of compositional and displacive modulation;

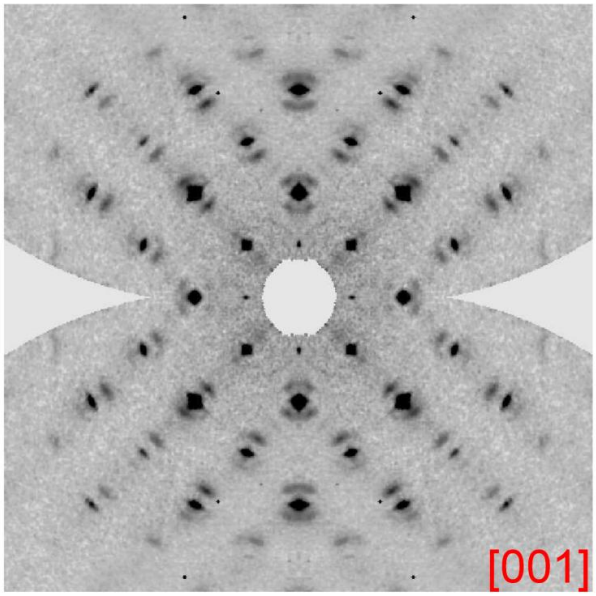

Diffraction data from difractometer of $PbCrO_3$ single crystal, reconstruction of precession camera image

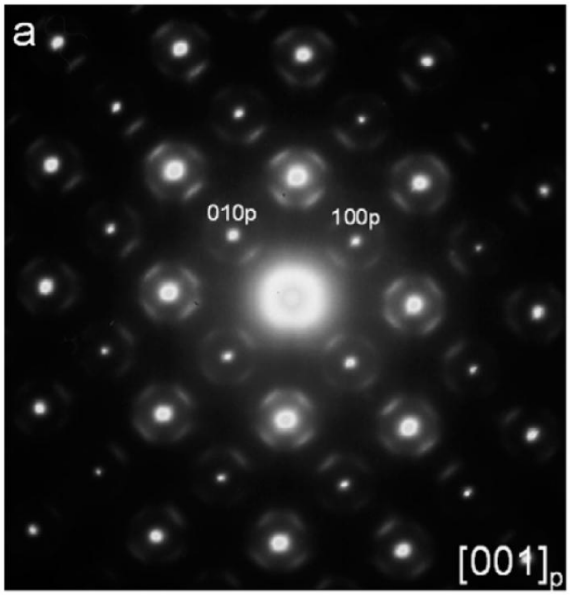

Selected Area Electron Diffraction of $PbCrO_3$

Fig.6 shows the comparison between single crystal x-ray diffraction pattern (this work) and SAED from microcrystal from policrystalline sample of $PbCrO_3$ along [001] zone axis.

6.5 The modulation in $PbCrO_3$, TEM - X-ray single crystal patterns comparison

Lead atom is considered to be located on its special position. With this assumption, a model with

$T = 16a_p$ is proposed. The modulation of the occupation factor of the Pb^{2+} cations may be expressed in general terms as

$$f(y,z) = A + B\cos^2\left(\frac{\pi z}{T} + \phi(y)\right) \qquad 1)$$

where z is the position of the Pb^{2+} cations along the direction of the modulation, T the period of the sinusoidal modulation, ϕ (y) the phase change between the different atomic planes along b sustaining the modulation, and A and B are constants to be determined. To calculate A and B, can be related by two equations.[11,12] The first one is obtained by defining the average value of the function f(z), i.e. the average occupation of the Pb^{2+} cations in the planes of the modulation:

$$\langle f(z)\rangle = \frac{1}{T}\int_0^T f(z)\,dz = \text{average occupation} \qquad 2)$$

solving the integral one obtains

$$A + B/2 = \text{average occupation} \qquad (3)$$

The second equation results from fixing the degree of occupation of the position considered as origin of the modulation, whose coordinate is z = 0, and which is normally given by the maximum value of the occupation:

$$A + B = \text{fixed degree of occupation} \quad (4)$$

Therefore, the average composition of Pb^{2+} cations in the modulation planes is required. According to EDAX analysis and considering that each layer has the same lead composition, the average occupation is equal to 0.91 so A + B/2 = 0,91 and A + B = 1, A = 0,82 and B = 0,18.

Since there is a change in phase between the planes, ϕ (y) = (T/3)y, the modulation function along one direction in the ‘‘$PbCrO_3$’’ is:

$$f(x,y) = 0.82 + 0.18\cos^2\left(\frac{\pi x}{64} + \phi(y)\right) \quad (5)$$

In the calculated electron diffraction patterns the diffuse streaks are clearly observed at $G_p \pm 1/3 <01\gamma>^*$. These ‘‘streaks’’ are composed of dots instead of continuous lines of intensity, because they are simulated only for $T = 16a_p$, whereas, the real diffraction pattern is a consequence of the disorder in the modulation with variable periodicities $T \approx 14–18a_p$. This model provides an explanation for the streaks, but not to the sheets of diffuse scattering obtained in the reconstruction of the reciprocal lattice, which arise from lack of correlation of the modulation between nearest cells. The intergrowth of three sets of microdomains justifies the presence of the other two sheets, along [010] and [001].

6.6 Conclusions

The single crystal growth of $PbCrO_3$ under high pressure and high temperature have been performed, several experimental condition of pressure, temperature, reaction time, cooling rate and reactants have been scanned; moreover the role of flux have been studied for some kind of fluxes. In few cases the experimental conditions were adequate for the single crystal growth of $PbCrO_3$. However the grown single crystals had not an excellent quality, they have been suitable to confirm composition and structure; moreover the diffraction pattern from single crystal $PbCrO_3$ evidenced that the uncommon microstructural property: a superstructure that presents a compositional modulation, previously observed in polycrystalline sample of this material. this modulation is also present in the single crystal. These evidences suggest that its microstrucutral properties can be an intrinsic property of $PbCrO_3$ rather than a local effect in microcrystals.

6.7 Bibliography

1. Roth, W.L. and R.C. De Vries, *Crystal and magnetic sturcture of $PbCrO_3$. J.Appl. Phys.* 1967. 38: p. 951.
2. Chamberland, B.L. and C.W. Moeller, *A study on the $PbCrO_3$ perovskite.* Journal of Solid State Chemistry, 1972. 5(1): p. 39-41.
3. Goodenough, J.B., J.A. Kafalas, and J. Longo, *Handbook on the physics and chemistry of rare earths.* 1972.
4. Baldinozzi, G., et al., *Crystal strucutre of the antiferroelectric perovskite Pb_2MgWO_6.* Acta Cryst. B, 1992. 51.
5. Alario Franco, M.A. and M.V. Regi, *Anion deficiency in strontium titanate.* Nature, 1977. 270: p. 706.
6. García-Martín S, et al., *Crystal structure and microstructure of some $La_{(2/3-x)}Li_{3x}TiO_3$ oxides: an example of the complementary use of electron diffraction and microscopy and synchrotron X-ray diffraction to study complex materials.* J. Am. Chem. Soc., 2004. 126(11): p. 3587-96.
7. Alario-Franco, M.A., et al., *Structural studies on A-cation-deficient perovskite-related phases. I. $ThNb_4O_{12}$, thorium/vacancy ordering in slow-cooled samples.* Acta Crystallographica Section A, 1982. 38(2): p. 177-186.
8. Baldinozzi, G., et al., *Neutron Rietveld refinement of the incommensurate phase of the ordered perovskite Pb_2CoWO_6.* Acta Crystallographica Section B, 2000. 56(4): p. 570-576.
9. Arevalo-Lopez, A.M. and M.M.A. Alario-Franco, *On the structure and microstructure of $PbCrO_3$.* Journal of Solid State Chemistry, 2007. 180(11): p. 3271-3279.
10. Senaris, M.A., et al., *Structural modulations in superconducting $La_{2-x}K_xCuO_4$.* Physica C: Superconductivity, 1997. 287, Part 2(0): p. 801-802.

7) General conclusions

The aim of this work was the high pressure and high temperature synthesis of new materials containing Cr(IV), their structural and physical characterization, also a study of possible candidate materials that could be new strongly correlated systems. Only few oxides containing Cr(IV) exist if compared with other Cr-based oxides having different oxidation states; moreover they are fewer if compared with other transition metals. In spite of these, the physical properties these oxides can have result very interesting. In the case of the solid solution $Cr_{1-x}V_xO_2$, several members of the solid solution of $Cr_{1-x}V_xO_2$ with $0{,}126(9) \leq x \leq 0{,}901(9)$ have been studied, synthesized under high temperature / high pressure conditions; a structural change as function of composition have been observed when $0.499(4) \leq x \leq 0.500(6)$; from structural characterization and compositional measurement the maximum content of Cr is expected to be in the region of solid solution $x < 0{,}342(9)$.

Powder samples data refinement shown a rutile-like structures that can vary as function of V content from $CaCl_2$ rutile like to VO_2 (M3) structure. Moreover the presence of V in CrO_2 "induce a pressure effect" allowing the structural transition from rutile to $CaCl_2$ structure at 40 Kbar. In pure CrO_2 this transition take place at a pressure of 120 Kbar at room temperature.

Electron diffraction experiments revealed a diffuse polarize streaks that could be related with a short range order V/Cr in the structure at composition $Cr_{0.499(4)}V_{0.500(6)}O_2$; more work is going to make in order to establish the type of short range order responsible for this diffuse scattering.

The magnetic properties of the different samples of solid solution have been determined and show an antiferromagnetic (AFM) (or a weak ferromagnet (WFM)) lowering the temperature. Independently the type of structure they have, $CaCl_2$ or VO_2 (M3), all samples have an AFM magnetic order. The transition temperature T_N is linearly dependent form Cr (or V) content in the structure and the trend has been explained by the presence of increasing amounts of Cr^{3+} in the structure.

In fact, the oxidation states of the Cr and V cations in $Cr_{1-x}V_xO_2$ confirm a rather complex mixed valences set. Comparison between measured and calculated magnetic moment have been realized in order to establish the valence states and a complex scenario has been found; Both V and Cr cations also could be in a mixed valence state.

The study of the half-metallic ferromagnet $K_2Cr_8O_{16}$ and the ferromagnet $K_{1,2}Cr_8O_{16}$ materials has successfully carried out by means of electrochemical and chemical oxidation

partly extract K ions from the hollandite tunnel. Oxidation reaction results in a new potassium deficient $K_{2-x}Cr_8O_{16}$ Cr-hollandites with $x_{max} = 0.8$. Structural characterisation shows that potassium extraction (oxidation) proceeds topotactically with some noticeable changes of the tetragonal cell parameters. The partial extraction of the K tunnel cation give rise to, among other effects widely described before, an unusual thermal parameter value B_{iso}, explained by an elongated electron density distribution along the tunnel direction. Interestingly, we have observed an important change in the magnetic properties. Potassium deficient hollandites $K_{2-x}Cr_8O_{16}$ are ferromagnetic with a Curie temperature of 250 K which is 70 K higher than the one reported for the pristine material $K_2Cr_8O_{16}$ (180 K). In both samples, neutron diffraction measurements confirmed a

paramagnetic -> ferromagnetic phase transition decreasing temperature, following the double exchange mechanism; moreover fitting refined magnetic momentum curves as function of temperature, by using the spin wave model, confirm the transition at high temperature for $K_2Cr_8O_{16}$ and $K_{1,2}Cr_8O_{16}$ respectively; these values are in agreement with the change in slope observed in magnetic susceptibility measurements; likely observed for T_c, these values are shifted as function of relative proportion Cr^{3+} / Cr^{4+} in the structure, this behaviour have not been observed until this date in $K_2Cr_8O_{16}$ and $K_{1,2}Cr_8O_{16}$ materials. In structural related systems, similar properties have been observed; tuning physical parameters, reversible effects on properties have reported; in our case irreversible modification of properties have induced by means of chemical and/or electrochemical modification.

The third material object of this work was the new ternary oxide with perovskite structure $Bi_{0,5}Pb_{0,5}CrO_{2,92}$, it has been structural and physical characterized showing a disordered Bi^{3+} and Pb^{2+} cations arrangement and its oxygen content has been determined by means of thermogravimetric reduction method; moreover no ordering of this vacancy have been observed by HRTEM experiments.

The magnetic behaviour may be explained by a long-range canted-antiferromagnetic structure coexisting at low temperatures with a substantial glassy component; that is a re-entrant spin-glass.

Dielectrical measurements have been performed on this material, magnetoresistance (MR) effect have been detected as function of temperature and seems to be correlated with magnetic susceptibility χ; moreover the correlation between χ and MR may corroborate the notion that charge transport is by spin dependent Cr^{3+} - Cr^{4+} hopping. The low resistivity for $Bi_{0,5}Pb_{0,5}CrO_{2,92}$ allowed reliable determination of ε' values only for $T \leq 75$ K. Therefore we cannot exclude ferroelectricity with a potential high $T_C >> 75$ K.

Powder neutron diffraction studies below the Neél temperature are planning to confirm the presence of long-range ordering.

The single crystal growth of $PbCrO_3$ under high pressure and high temperature have been performed, several experimental condition of pressure, temperature, reaction time, cooling rate and reactants have been scanned; moreover the role of flux have been studied for some kind of fluxes. In few cases the experimental conditions were adequate for the single crystal growth of $PbCrO_3$. However the grown single crystals had not an excellent quality, they have been suitable to confirm composition and structure; moreover the diffraction pattern from single crystal $PbCrO_3$ evidenced that the uncommon microstructural property. This study evidenced the difficulty on growing single crystal at high pressure.

8) Appendix

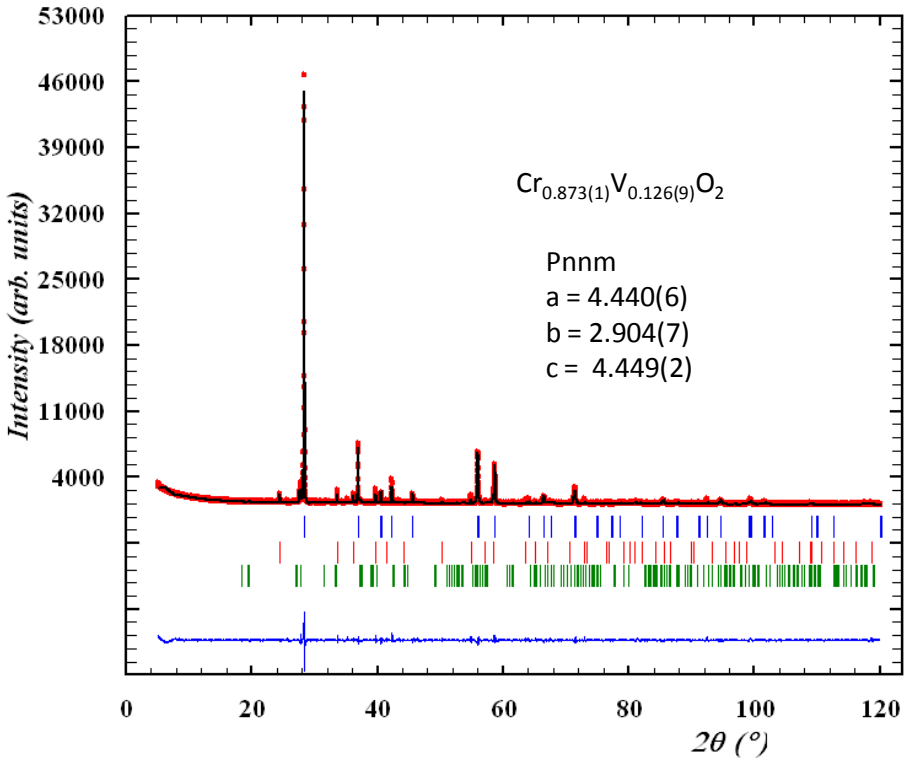

Rietveld refinement of powder x-ray data of $Cr_{0.873(1)}V_{0.126(9)}O_2$

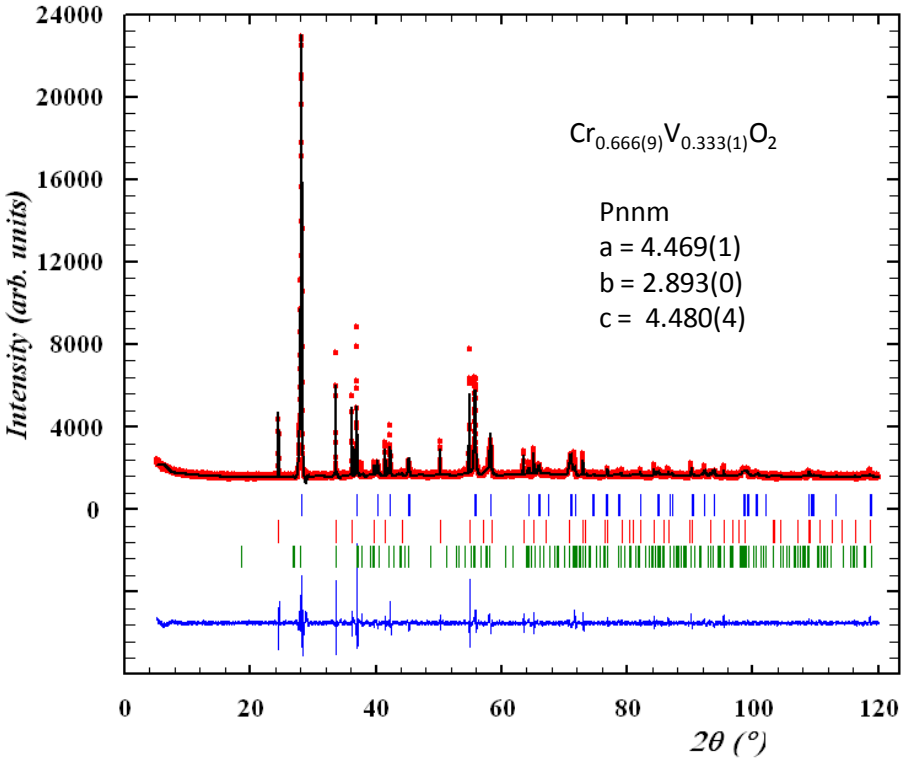

Rietveld refinement of powder x-ray data of $Cr_{0.666(9)}V_{0.333(1)}O_2$

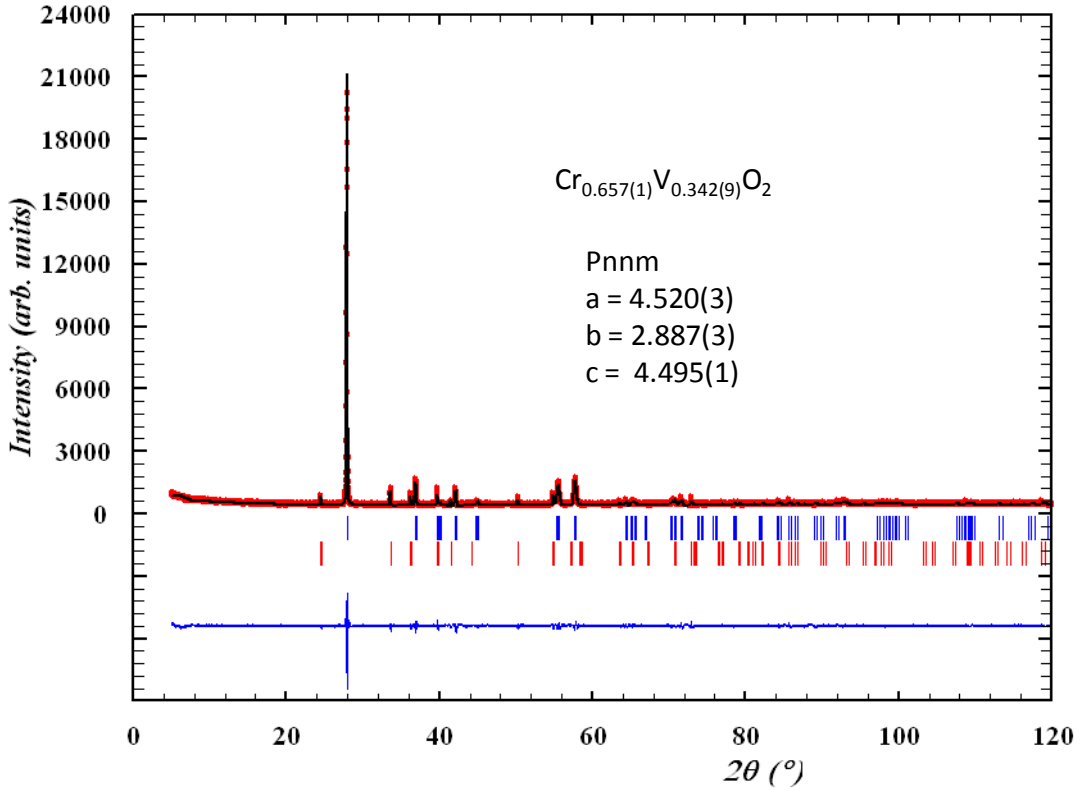

Rietveld refinement of powder x-ray data of $Cr_{0.657(1)}V_{0.342(9)}O_2$

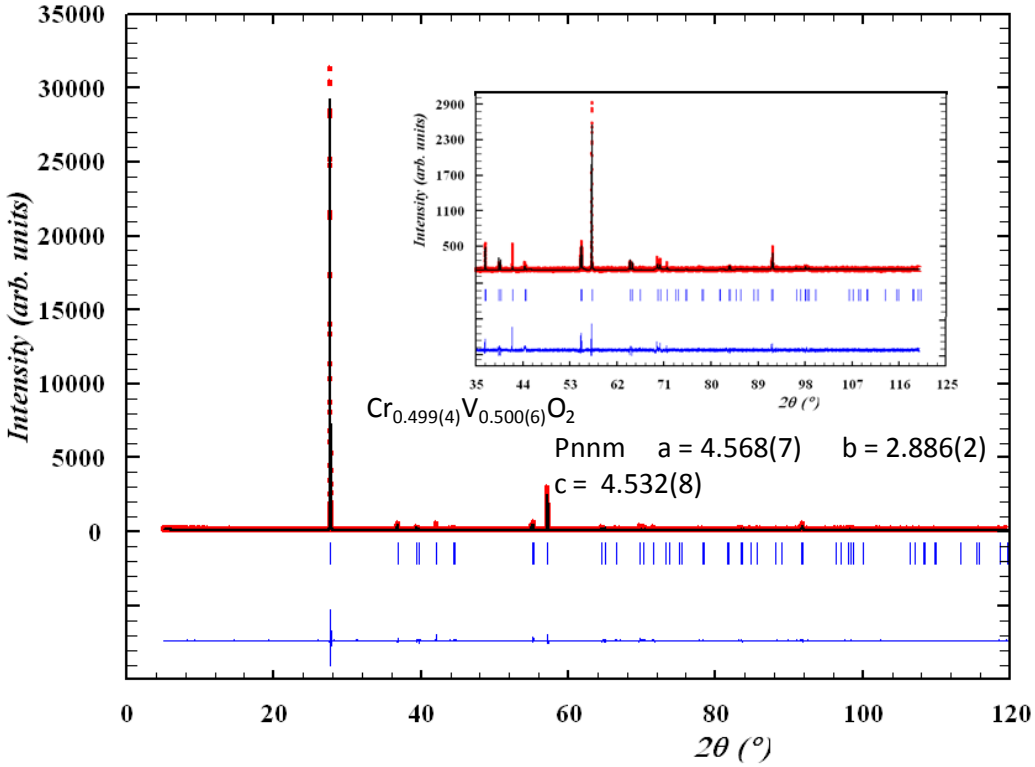

Rietveld refinement of powder x-ray data of $Cr_{0.499(4)}V_{0.500(6)}O_2$

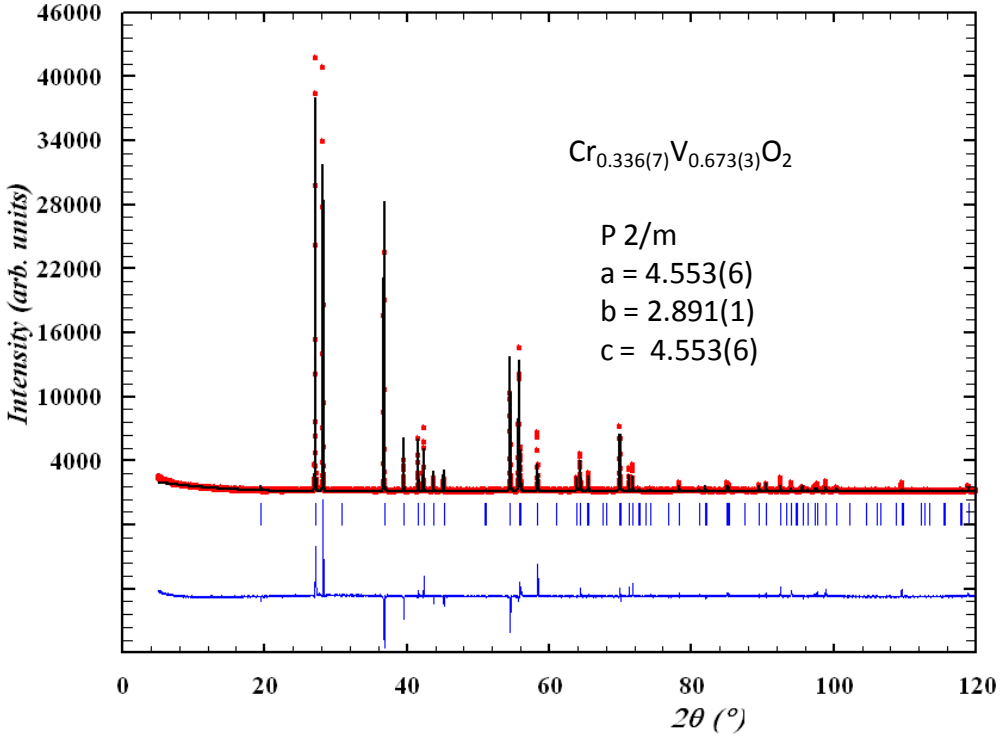

Rietveld refinement of powder x-ray data of $Cr_{0.336(7)}V_{0.673(3)}O_2$

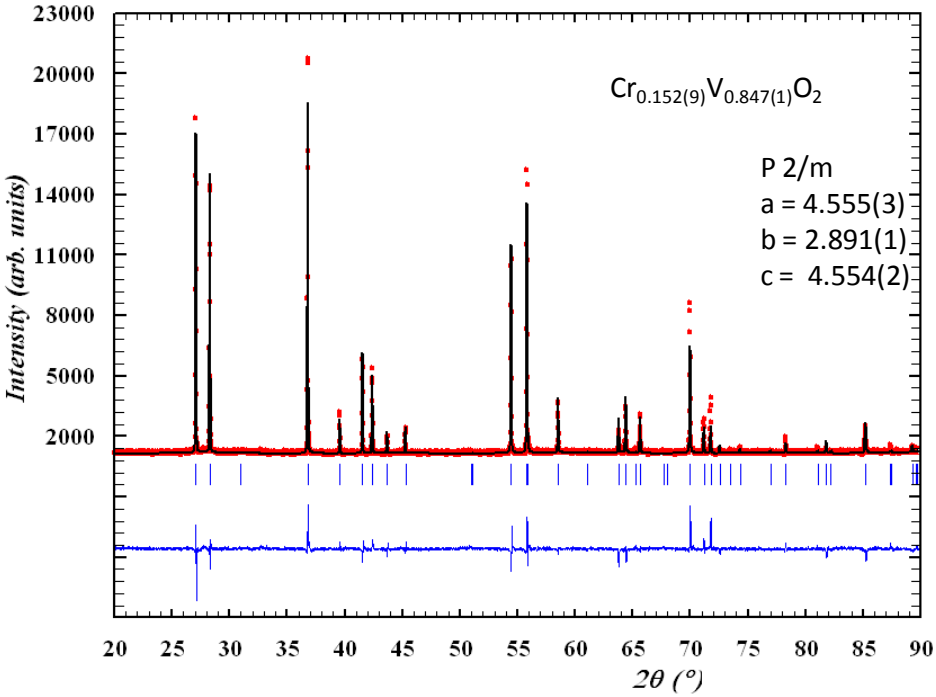

Rietveld refinement of powder x-ray data of $Cr_{0.152(9)}V_{0.847(1)}O_2$

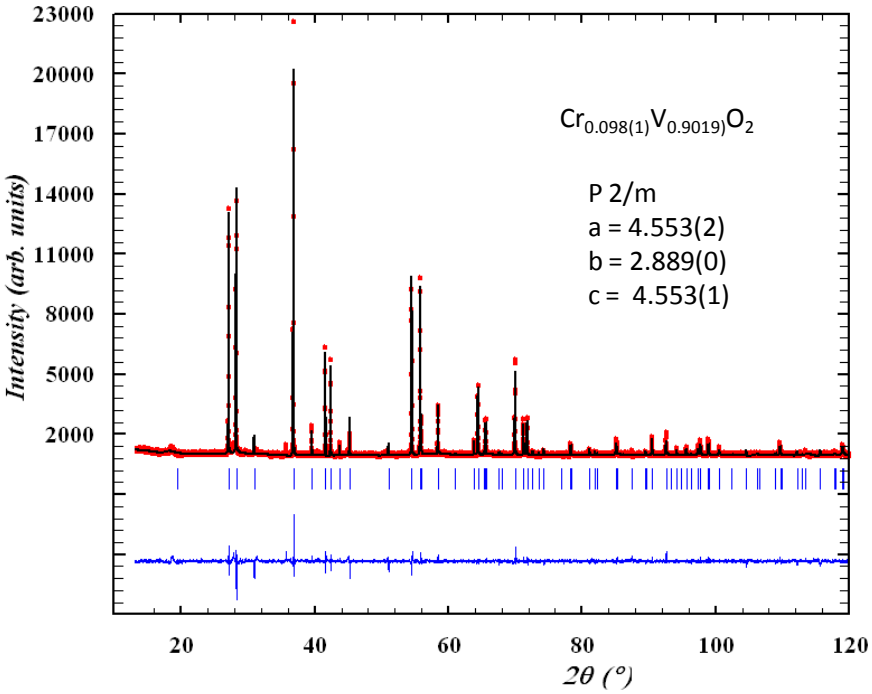

Rietveld refinement of powder x-ray data of $Cr_{0.098(1)}V_{0.9019)}O_2$

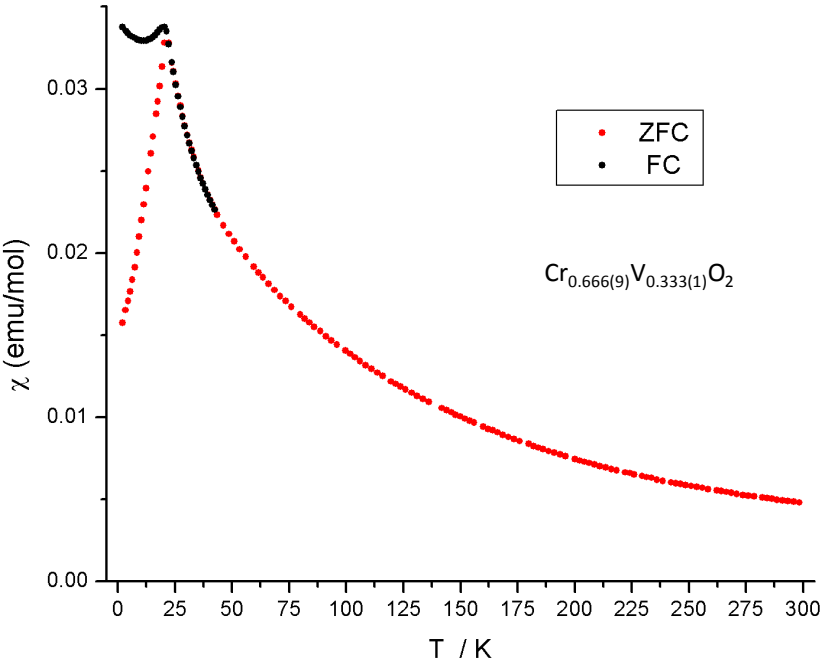

ZFC/FC magneti susceptibility for $Cr_{0.666(9)}V_{0.333(1)}O_2$

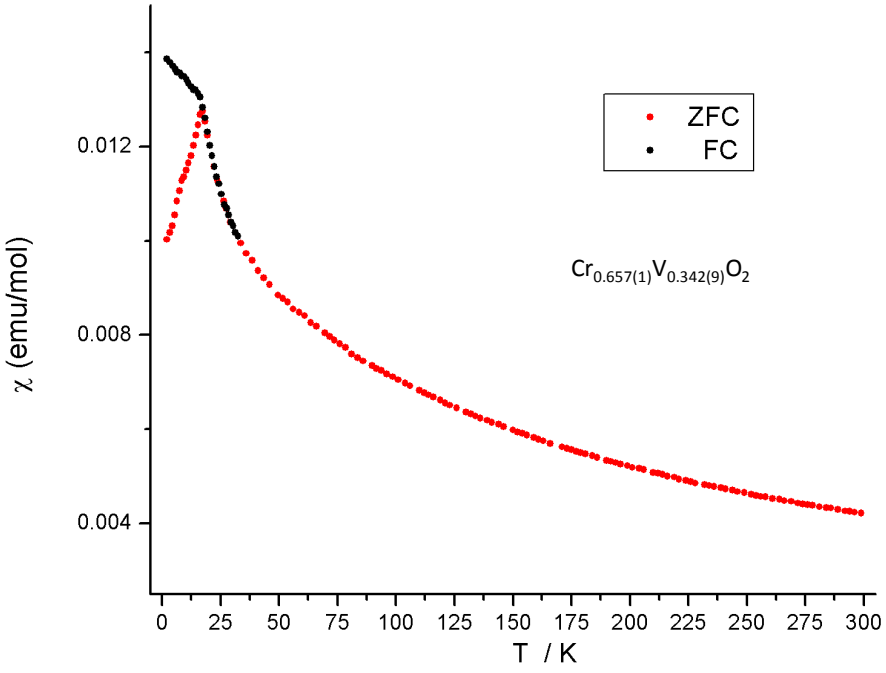

ZFC/FC magneti susceptibility for $Cr_{0.657(1)}V_{0.342(9)}O_2$

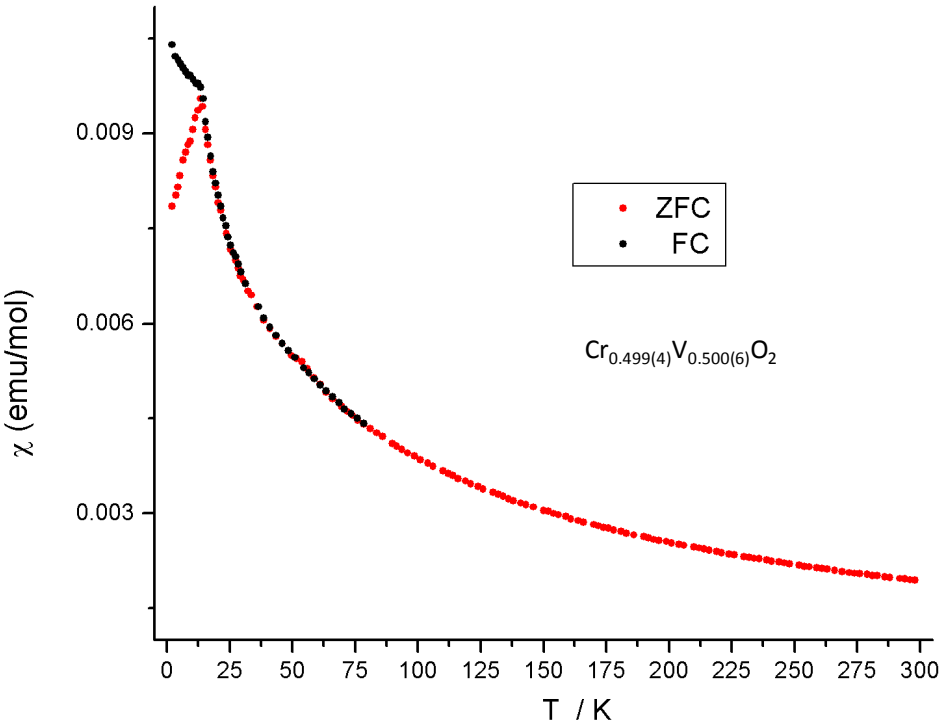

ZFC/FC magneti susceptibility for $Cr_{0.499(4)}V_{0.500(6)}O_2$

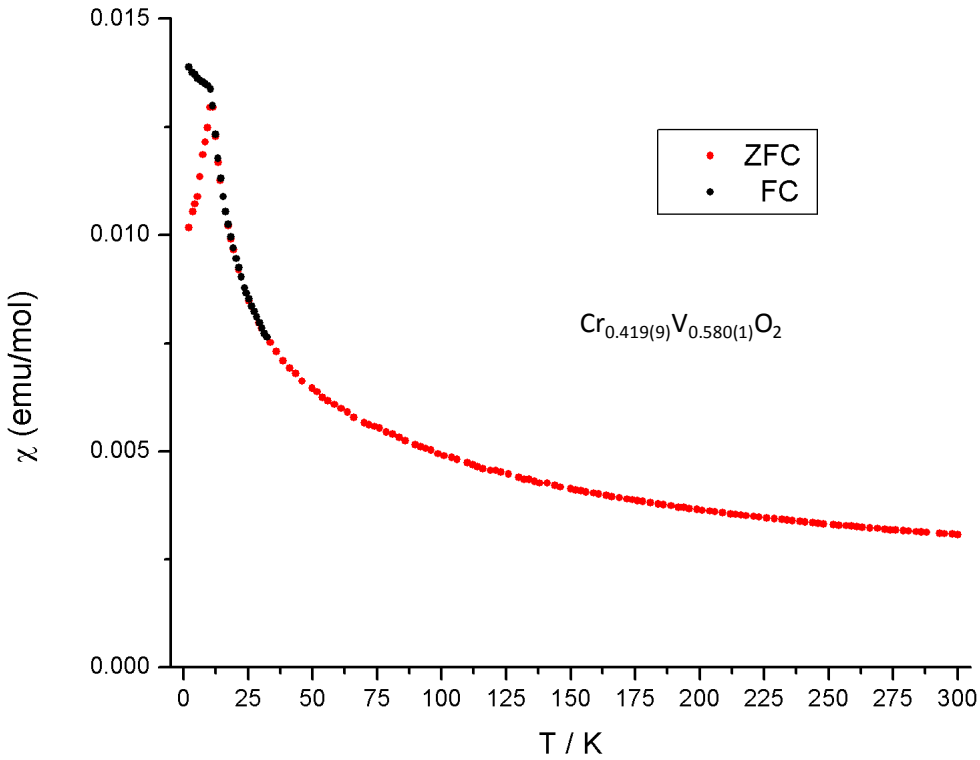

ZFC/FC magneti susceptibility for $Cr_{0.419(9)}V_{0.580(1)}O_2$

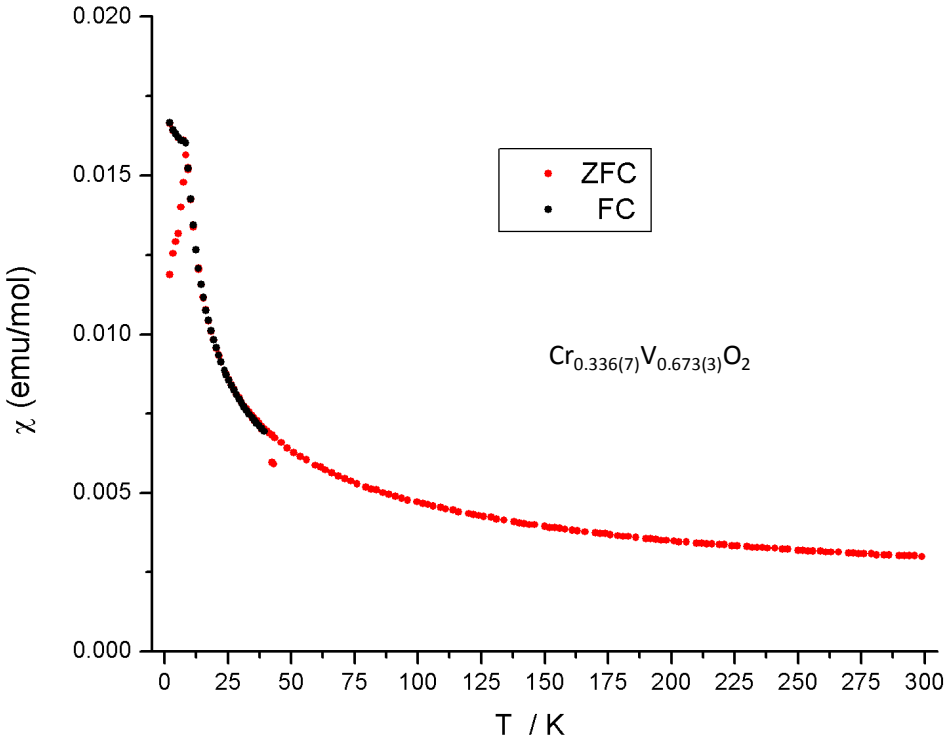

ZFC/FC magneti susceptibility for $Cr_{0.336(7)}V_{0.673(3)}O_2$

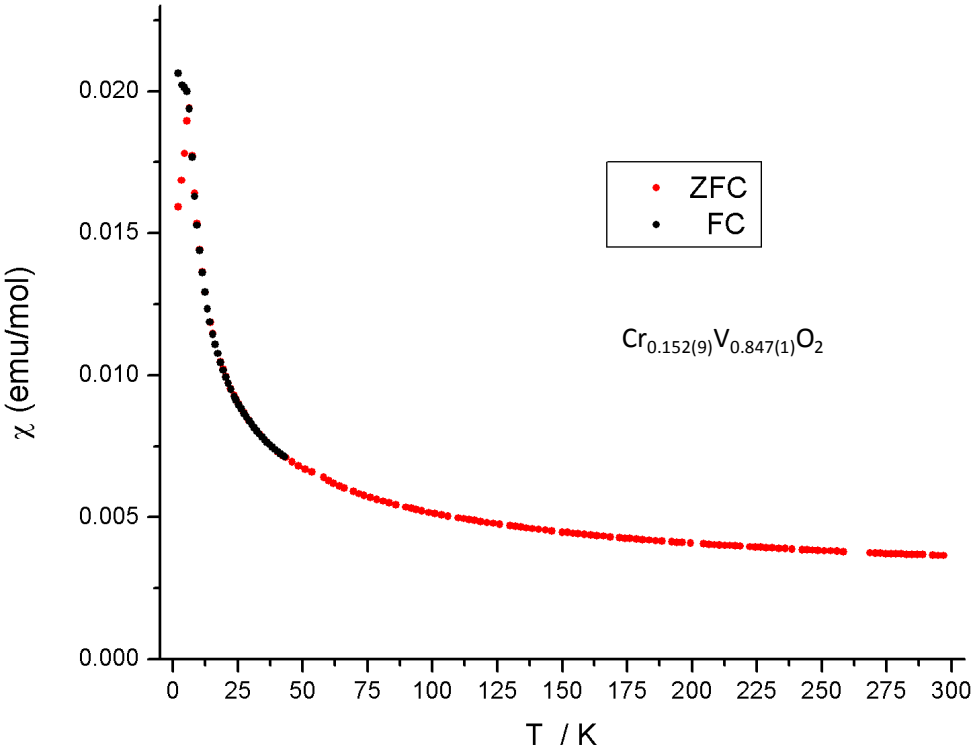

ZFC/FC magneti susceptibility for $Cr_{0.152(9)}V_{0.847(1)}O_2$

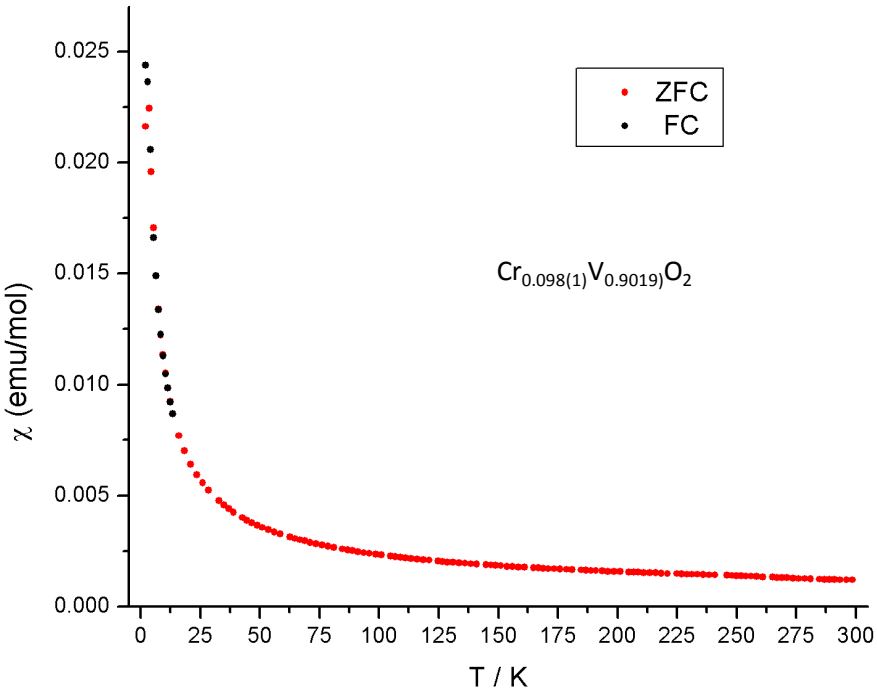

ZFC/FC magneti susceptibility for $Cr_{0.098(1)}V_{0.9019)}O_2$